

Summer 2020

Solid Materials Discovery for Thin Films, Oxide Catalysts, and Polymer Sealants

Benjamin Ruiz-Yi

Follow this and additional works at: <https://scholarcommons.sc.edu/etd>



Part of the [Chemical Engineering Commons](#)

Recommended Citation

Ruiz-Yi, B.(2020). *Solid Materials Discovery for Thin Films, Oxide Catalysts, and Polymer Sealants*. (Doctoral dissertation). Retrieved from <https://scholarcommons.sc.edu/etd/5988>

This Open Access Dissertation is brought to you by Scholar Commons. It has been accepted for inclusion in Theses and Dissertations by an authorized administrator of Scholar Commons. For more information, please contact dillarda@mailbox.sc.edu.

SOLID MATERIALS DISCOVERY FOR THIN FILMS, OXIDE CATALYSTS, AND
POLYMER SEALANTS

by

Benjamin Ruiz-Yi

Bachelor of Science
Massachusetts Institute of Technology 2011

Submitted in Partial Fulfillment of the Requirements
for the Degree of Doctor of Philosophy in
Chemical Engineering
College of Engineering and Computing
University of South Carolina
2020

Accepted by:

Jochen Lauterbach, Major Professor

Christopher Williams, Committee Member

Chang Liu, Committee Member

Anthony Reynolds, Committee Member

Melissa Moss, Committee Member

Cheryl L. Addy, Vice Provost and Dean of the Graduate School

© Copyright by Benjamin Ruiz-Yi, 2020
All Rights Reserved.

DEDICATION

To my family.

ACKNOWLEDGMENTS

I would like to first thank my advisor, Prof. Jochen Lauterbach. Thank you for advising and guiding me for all these years. I appreciate the autonomy you provided and the lessons taught about the field, industry, and life as well. Assisting in teaching your classes was a valuable experience and I am glad you let me contribute. You have been patient and understanding in the tough times, while remaining jovial throughout the best of times as well. I am truly grateful for all that you have done, and I am deeply in your debt.

Thank you to Dr. Kenneth Bunn. You have been a great mentor in and out of the lab, teaching me about academia and industry. The driving trips we took held some of the most enjoyable conversations I can recall. You have been a great friend over all these years, and I appreciate all of your help throughout that time.

To Dr. Travis Williams, thanks for always having a hand with your expertise in coding and indulging me in some of my more eccentric experiments. It was a delight teaching you what I knew about deposition sputtering and working with you on a number of projects. You have also been a wonderful friend and I am blessed to have met you.

To all the former and current members of SAGE, I would like to extend my deepest gratitude toward you all. To Dr. Calvin Thomas, thanks for the long and entertaining conversations. To Dr. Kate Mingle, thanks for setting a strong standard for the lab. To Dr. Juan Jimenez, it was a joy to see your development into a scientist. To Katie McCullough, your curiosity and questions pushes everyone to be thoughtful about their work. To Blake Macqueen, having an opportunity discuss sports with you on

a near daily basis was a small pleasure I rarely get to have, thank you. To Michael Royko, you always have a greeting for the day and can find a way to brighten a day. To Jennifer, Kaveh, and Rasika, it was a pleasure to see you start of your own doctoral pursuits. I am glad to have met you all.

I would like to extend my thanks to the members of my committee: Prof. Christopher Williams, Prof. Chang Liu, Prof. Anthony Reynolds, and Prof. Melissa Moss.

Thank you to Dr. Cun Wen for all of the practical laboratory knowledge you provided alongside teaching the scientific thought process. Thank you to Dr. Jason Hattrick-Simpers for expanding my horizons to different fields of chemistry and engineering. Thank you to Dr. Apurva Mehta and Dr. Fang Ren for your continued help during many of the experiments performed at the synchrotron light source. Thank you to Dr. Brian Benicewicz and Dr. Morgan Stefik for your advice on unfamiliar materials and access and education on your facilities.

To the myriad of undergrads, whom I have had the pleasure to work with and debatably mentor. You have taught me more about myself and what it means to be a teacher and guide than I have probably taught you about the lab or materials. To Alvin Fersner, Layna Frankovich, Cailey Oswald, Jacob Sims, Mark Wichhusen, Patrick Barboun, Kris Hacker, and Ghitte Neethling, thank you.

Finally, I would like to thank my family. To my Mom and Dad, the support you have provided me is immeasurable. Thank you for being there with useful advice when things got difficult. You have endured your stubborn son and continued to be a pillar. There is more I could say, but in the end, thank you. To my sister, Jasmine, thanks for abiding your silly older brother. You are the best sibling I could have asked for, taught me about how to be a responsible brother, and provided an unending friendship. Thank you.

ABSTRACT

Solid materials are made up of multiple classes, including metals, ceramics, and polymers. While each class can be developed for general purpose applications or highly specialized, discovery of new materials in order to improve upon desired properties is a non-trivial task for any type of material. A wide variety of materials encompass expansive design spaces, consisting of parameters such as chemical compositions, synthesis conditions, and post-processing. Due to this, narrowing down the design space to fit within a given figure-of-merit and economic viability becomes time consuming at best and infeasible at worst.

High-throughput experimentation (HTE) is a methodology that can mitigate the difficulties that come with materials discovery. It allows for accelerated exploration of wide parameter spaces by utilizing rapid serial or parallelization synthesis and characterization methods. This generates large data sets that, upon further analysis, can pinpoint regions of interest within a design space for further study. Outside of HTE methods for materials discovery, a statistical design of experiments (DOE) can be conducted in order to minimize the number of experiments needed to sufficiently model and optimize the properties and performance of a given material system.

Various materials were investigated for different applications. HTE was utilized in order to understand the phase stabilization mechanisms of multi-principal element alloys (MPEA) and also to aid in the discovery of oxidation resistant alloy materials. Additionally, two stabilized zirconia systems were studied via thin-film deposition in order to capture specific phase for high-temperature applications. A ceria supported rhena catalyst was characterized with various spectrographic techniques in order to

determine its surface structure. Finally, a thiol-ene curable sealant was optimized using a response surface DOE in order to find conditions that optimize the adhesive strength of the material.

TABLE OF CONTENTS

DEDICATION	iii
ACKNOWLEDGMENTS	iv
ABSTRACT	vi
LIST OF TABLES	xii
LIST OF FIGURES	xiii
CHAPTER 1 INTRODUCTION	1
1.1 Overview	1
1.2 High-Throughput Experimentation	3
1.3 Thesis Results	6
CHAPTER 2 EXPERIMENTAL TECHNIQUES	7
2.1 Magnetron Sputtering	7
2.2 X-Ray Diffraction	12
2.3 Raman Spectroscopy	18
2.4 Fourier Transform Infrared Spectroscopy	22
2.5 Peel Tests	24

CHAPTER 3	PHASE STABILIZATION MECHANISMS OF MULTI-PRINCIPAL ELEMENT ALLOYS	29
3.1	Background and Motivation	29
3.2	Experimental Methodology	36
3.3	Results and Discussion	39
3.4	Conclusions	44
CHAPTER 4	OXIDATION AND PHASE DISCOVERY OF A MULTI-PRINCIPAL ELEMENT ALLOY	48
4.1	Experimental Methodology	51
4.2	Results and Discussion	54
4.3	Conclusions	61
CHAPTER 5	PHASE FORMATION OF YTTRIA-STABILIZED ZIRCONIA VIA MAGNETRON SPUTTERING	64
5.1	Background and Motivation	64
5.2	Experimental Methodology	74
5.3	Results and Discussion	77
5.4	Conclusions	88
CHAPTER 6	REO _x CHARACTERIZATION ON A CeO ₂ SUPPORT	90
6.1	Background and Motivation	90
6.2	Experimental Methodology	93
6.3	Results and Discussion	96
6.4	Conclusions	105

CHAPTER 7	MODELING THE ADHESIVE STRENGTH OF A THIOL-ENE SEALANT VIA RESPONSE SURFACE DESIGN	107
7.1	Background and Motivation	107
7.2	Experimental Methodology	112
7.3	Results and Discussion	118
7.4	Conclusions	126
CHAPTER 8	CONCLUSIONS AND FUTURE WORK	129
8.1	Conclusions	129
8.2	Conclusion: MPEA Phase Stabilization	130
8.3	Conclusion: MPEA Oxidation	132
8.4	Conclusion: Stabilized Zirconia Testing	133
8.5	Conclusion: $\text{ReO}_x/\text{CeO}_2$ Mechanistic Study	136
8.6	Conclusion: Thiol-Ene Peel Test Optimization	137
BIBLIOGRAPHY	139
APPENDIX A	MPEA PHASE STABILIZATION APPENDIX	168
A.1	Ω and δ Values for $(\text{Al}_x\text{Cu}_y\text{Mo}_{1-x-y})\text{FeNiTiVZr}$ Libraries	168
APPENDIX B	MPEA OXIDATION APPENDIX	175
B.1	Ω and δ Values for the $(\text{AlFeNiTiVZr})_{1-x}\text{Cr}_x$ Library	175
B.2	Additional Waterfall Plots of the Post-Annealed MPEA Library	176
B.3	Additional Raman Spectra of the MPEA Library	177
APPENDIX C	STABILIZED ZIRCONIA APPENDIX	181

C.1 Deposited ScSZ Surface Topography	181
APPENDIX D $\text{REO}_x/\text{CeO}_2$ APPENDIX	183
D.1 Catalyst Diffraction Data	183
D.2 Raman Spectra Analysis Validation	184
D.3 Selection Rule Validation	186
APPENDIX E PEEL TEST APPENDIX	188
E.1 Measured Adhesion Data	188
E.2 3D Response Surface Contour Plots	194
E.3 Promoter Adhesion	196
APPENDIX F COPYRIGHT PERMISSIONS	200

LIST OF TABLES

Table 5.1	Deposition Parameters for YSZ Sample Synthesis	75
Table 5.2	Deposition Conditions for ScSZ Sample Synthesis	76
Table 5.3	Indexed Peaks Positions and Phases of YSZ at the Sputtered Conditions	80
Table 6.1	Raman Shifts from the ^{18}O Substitution	102
Table 6.2	Area Ratios of Raman Spectra	103
Table 6.3	Area Ratios of FTIR Spectra	105
Table 7.1	Response Surface Factors for the Thiol-ene Synthesis	115
Table 7.2	Average Peel Strength of the Thiol-Ene Sealants Synthesized at Room Temperature	119
Table 7.3	The Adhesive Strength Transfer Function Coefficients	125
Table A.1	Solubility Table of Binary Constituent Pairs	169
Table A.2	Predictive Values for Alloy Phase Stabilization	170
Table B.1	Predictive Values for Alloy Phase Stabilization	175
Table D.1	Integrated Intensities of the Di-Oxo ReO_x Stretch	187
Table E.1	Average Peel Strength of Thiol-Ene Sealant at the Measured Synthesis Conditions	188

LIST OF FIGURES

Figure 1.1	A visualization of the common elements used in MPEA development. While the previous designs consisted of 36 elements, the most commonly used elements in an alloy consist of Al, Co, Cr, Cu, Fe, Mn, Ni, and Ti.	3
Figure 1.2	(Left) The experimental loop of typical materials discovery. (Right) The experimental design loop utilizing high-throughput methods. While HTE expedites many steps of the scientific process, there is still a bottleneck between data analysis and generation of new hypotheses.	4
Figure 2.1	A cross-sectional schematic of the major magnetron sputter gun components. A copper mesh is typically placed between the target and copper cathode block in order to improve heat conductivity. Oxide materials must be bonded to a copper backing plate to improve conduction.	9
Figure 2.2	A diagram depicting the sputter process when the plasma is ignited over the target. The electrons that are trapped within the magnetic field have high enough energy to collide and ionize neutral Ar atoms.	10
Figure 2.3	An AJA Orion sputtering chamber. This system has five sputter guns, and three target materials can be co-deposited during a single experiment.	11
Figure 2.4	(Left) An example of the co-deposition of a binary system. The sample product concentration varies based on the position relative to the sputter guns. (Right) A colorized example of the co-deposited sample.	12
Figure 2.5	A depiction of X-rays diffracting off a crystal lattice. The Bragg diffraction condition is fulfilled at angles of X-ray constructive interference.	14

Figure 2.6	A representation of the Ewald construction in two dimensions. The Laue condition is a vector analog to the Bragg condition, and is fulfilled when \vec{q} is equal to a lattice vector point that lies on the Ewald construction.	15
Figure 2.7	A generalization of the steps to convert a 2D area diffraction to a 1D pattern. The raw 2D image (Top Left) is from an x-y Cartesian plane image to a polar 2D image (Top Right), via an azimuthal integration. After correction, the image is further integrated along χ in order to collapse the data to a 1D diffraction pattern (Bottom Left). Once the 1D diffraction is acquired it is processed with baseline corrections and normalization in order to analyze the data (Bottom Right).	17
Figure 2.8	An overhead view of the diffraction set up at SLAC. This example includes a Kapton dome used for <i>in situ</i> measurements. The synchrotron light source is seen on the left, and the source X-rays strike the sample. The resulting diffraction is captured by the detector on the left. Any X-rays that participate in fluorescence is captured by the detector that is orthogonal to the substrate plane.	18
Figure 2.9	The Ganesha SAXSLAB X-ray scattering instrument. The vacuum chamber allows for measurements in the small-angle and wide-angle ranges and at grazing incidences. The source on the right generates X-rays in the Cu- $k\alpha$ range, which strikes a tilted sample near the system door. The scattered X-rays are measured by a Dectris Pilatus 300K detector.	18
Figure 2.10	A Jablonski diagram that illustrates possible outcomes after excitation from a laser source. Three scattering events (Rayleigh, Stokes Raman, and Anti-Stokes Raman) and an absorption event (Fluorescence).	20
Figure 2.11	A basic diagram of the Michelson interferometer. The interferometer phase shifts the source beam by first separating light using a beam splitter (typically made with KBr). The two beams are reflected back toward the beam splitter, but at different phases due to a moving mirror that is in the path of one beam, which results in interference between the different IR wavelengths in the beams.	23

Figure 2.12	An example of the conversion from interferogram data to an absorption spectrum. A Fourier transform is done using computational software in order to convert the retardation data into vibrational wavenumber data.	24
Figure 2.13	The DRIFTS cell used for <i>in situ</i> powder measurements. Mirrors reflect the IR source into the sample cell, which can be heated and exposed to desired gases. KBr can be supplemented to save sample material.	25
Figure 2.14	Typical peel data gathered from the Instron. After initial delamination, the load averages out before the sample is fully peeled. The average load divided by the sample width determines the adherent's peel strength.	26
Figure 2.15	The monomers used in the study discussed in Chapter 7. (a) PETMP, (b)TTT, and (c) TMPTA.	27
Figure 2.16	A depiction of the mold and samples for the peel test measurements. (a) The Teflon mold. (b) Example of the sample on the substrate with an aluminum mesh for gripping.	27
Figure 2.17	The Instron 5543A Load Frame that has been outfitted with a 100 N load cell.	28
Figure 3.1	Example of a BCC lattice in an $(Al_xCu_yMo_{1-x-y})FeNiTiVZr$ alloy system. The atoms are randomly assorted within the crystal alloy.	30
Figure 3.2	(Left)An internal view of a gas turbine. (Right)A first stage gas turbine blade with damage around the edges.	31
Figure 3.3	Characteristic diffraction patterns seen in the CCS library. (a) The representative pattern of the as deposited library. (b) The pattern for the same composition after annealing at 733 K for 1 hour in air. (c) The pattern for a similar composition in the LP library after annealing in air for 1 hour at 733 K. The LP library shows oxidation at the composition, while the HP library shows intermetallic phase formation. The patterns were normalized to the alloy peak at 2.91 \AA^{-1}	40

Figure 3.4	HP Pseudoternary phase diagrams. (a) As-deposited CCS. (b) Phase changes after annealing in air at 513 K. (c) Phase changes after annealing in air at 733 K. Black circles represent a solid solution phase. Red open squares represent secondary phase formation.	42
Figure 3.5	LP Pseudoternary phase diagrams. (a) As-deposited CCS. (b) Phase changes after annealing in air at 598 K. (c) Phase changes after annealing in air at 733 K. Black circles represent a solid solution phase. Red open squares represent secondary phase formation. Green triangles represent oxidation.	43
Figure 3.6	Pseudoternary phase diagrams of Al-rich libraries. (a) As-deposited diagram. (b) Vacuum annealed diagram. No intermetallic structures were observed.	44
Figure 3.7	The characteristic diffraction patterns of the Al rich spreads. Coarsening of the alloy peak is observed after vacuum annealing the library for 6 hours at 873 K. The lack of additional peaks indicates that the deposited sample is a highly nanocrystalline sample instead of a metallic glass.	45
Figure 3.8	(a) A graph of the solid solution formation ability, Ω , versus the atomic size difference, δ of multiple samples in the literature. The $(Al_xCu_yMo_{1-x-y})FeNiTiVZr$ libraries inserted for comparison. (b) The diagram is zoomed in to clearly see the HP and LP libraries.	46
Figure 4.1	A representation of passivating oxide development. Near-surface elements that are thermodynamically favorable to be oxidized diffuse to the surface and develop a non-porous layer that prevents further oxidation of the bulk.	51
Figure 4.2	The optical image of the pseudobinary CCS. A visible phase boundary is seen that separates the composition spread into two regions, R_1 and R_2	54

Figure 4.3	Waterfall plots of each samples diffraction patterns across the compositional spread with respect to Cr at.%. Each oxidized sample was also vacuum annealed for 6 hours at 873 K. (a) As-deposited, (b) Vacuum annealed, (c) 1-Hour oxidation, (d) 3-Hour oxidation. (e) 6-Hour oxidation, and (f) 18-Hour oxidation. The black patterns in the oxidized samples correspond with the R_1 phase, while the red patterns are associated with the R_2 phase.	56
Figure 4.4	The peak analysis and indexing of the R_1 and R_2 phase regions. (a) Diffraction patterns measured at 6.4 at.% Cr (R_1). The patterns show an unknown oxide formation along with the growth of a FeSi structure at all oxidation anneals above one hour. (b) Diffraction patterns measured at 35.7 at.% Cr (R_2). The major oxide phase grown was identified as a trigonal Cr_2O_3	58
Figure 4.5	Raman spectra of the 1-hour oxidized sample. (a) R_1 phase (b) R_2 phase. Oxidation is apparent in both regimes, but differentiation is easier in the R_2 region.	60
Figure 4.6	Compositional Raman heat maps. (a) As-deposited library, (b) vacuum annealed library, (c) 1-hour oxidation, and (d) 18-hour oxidation anneal. The phase boundary is visible in the oxidized sample libraries. There is a boundary shift from 25 at.% Cr to 28 at.% Cr as the anneal time increases.	62
Figure 4.7	A meta-image of the 18-hour oxidation that shows the phase boundary using three different measurement techniques. (a) Optical observation. (b) X-ray diffraction heat map. (c) Raman spectroscopy heat map. The phase boundary remains at the same composition across all three observations.	62
Figure 5.1	The cross-sectional schematic of a high-temperature turbine blade. The relevant layers are illustrated, and the thermal barrier coating is responsible for keeping the superalloy over 700 K cooler than the combustion environment.	65
Figure 5.2	An illustration of the components and reactions involved in the layers of a SOFC. At the porous cathode, O_2 molecules are decomposed into O^{2-} ions that travel through the solid electrolyte. At the porous anode these ions synthesize CO_2 and H_2O with the fuel provided to the SOFC. The reaction releases electrons that flow back to the porous cathode via a wire, generating electrical energy.	67

Figure 5.3	Solid electrolytes exhibit Arrhenius behavior with respect to ionic conductivity. The Arrhenius plot shows that within the same temperature regime 9.0 mol.% Sc ₂ O ₃ ScSZ maintains higher ionic conductivity than 9.0 mol.% Y ₂ O ₃ YSZ.	69
Figure 5.4	A basic example of how lattice vacancies cause phonon scattering. (a) The atoms (gray) in the lattice vibrate with a periodicity that can be broken down into several normal modes. (b) The introduction of defect sites (yellow) allow for a scattering effect, which results in higher thermal resistance.	71
Figure 5.5	YSZ phases and transformation. (a and d) c-YSZ, (b) t'-YSZ, (d) t-YSZ, (e) m-YSZ.	72
Figure 5.6	The binary phase diagram of Y ₂ O ₃ and ZrO ₂	78
Figure 5.7	The characteristic diffraction patterns of the YSZ phases. The blue is the cubic (111) plane, purple is characteristic of the mixed tetragonal (002) and cubic (111), while the red shows only the tetragonal (002).	79
Figure 5.8	The deposition phase diagram, using the input synthesis conditions as the axes. The diagram shows that the YSZ phases fall into separate deposition regions.	81
Figure 5.9	The characteristic diffraction patterns of the ScSZ samples deposited at 298 K, 50 W gun power, and with 0 vol.% O ₂ in the chamber atmosphere. These patterns show only that the cubic phase was present at all annealing conditions.	83
Figure 5.10	A visualization of what is looked for when analyzing texture and preferred orientation.	83
Figure 5.11	The ScSZ crystallinity analysis at all synthesis conditions. The red points represent moderate texturing, green points show slight texturing, and the blue points represent disordered crystallites/grains that make up the film.	84
Figure 5.12	The crystallinity ratio between (111) and (220) texturing at each of the synthesis conditions.	85
Figure 5.13	The ScSZ grain size distribution at 923 K, 65 W gun power, and 10 vol.% O ₂ at the different annealing times.	87

Figure 6.1	The proposed possible structural configurations ReO_x on CeO_2 : (a) mono-oxo, (b) di-oxo, and (c) tri-oxo.	91
Figure 6.2	The two major ReO_x species that are proposed. (a) mono-oxo (Xi <i>et al.</i>) and (b) tri-oxo (Ota <i>et al.</i>)	92
Figure 6.3	<i>In situ</i> Raman spectra at each calcination step. The heated sample (e) is a measurement of the 1 wt.% $\text{ReO}_x/\text{CeO}_2$ at 823 K in an Ar environment. Spectra (a-d) were taken with the labeled gas at the same temperature.	97
Figure 6.4	The as-synthesized 1 wt.% $\text{ReO}_x/\text{CeO}_2$ Raman spectrum. At ambient conditions, deconvoluting the monomeric band is a non-trivial task.	98
Figure 6.5	The di-oxo configuration for ReO_x . This structure was supported in the literature by Ota <i>et al.</i>	98
Figure 6.6	Raman spectra comparing the 1 wt.% $\text{ReO}_x/\text{CeO}_2$ before and after the isotope exchange. (a) Fitted sample calcined at 823 K in the $^{16}\text{O}_2$ environment pre-exchange. (b) Calcined in $^{18}\text{O}_2$. (c) The fittings of the exchanged sample mono-oxo and di-oxo structures (d) The fittings of the exchanged sample oxygen bridges and hydroxyl groups.	100
Figure 6.7	The ReO_x structures discovered as a result of the isotope exchange. (a) mono-oxo (b) di-oxo (c) cross-linked structure (d) hydroxyl group.	101
Figure 6.8	The time-resolved FTIR spectra of the 1 wt.% $\text{ReO}_x/\text{CeO}_2$. (a) Initial oxidation under $^{18}\text{O}_2$. (b) Second oxidation under $^{18}\text{O}_2$ after a reduction step.	104
Figure 7.1	The reconstructed wreckage of flight TWA 800.	108
Figure 7.2	The anti-Markovnikov addition of a thiol species to an alkene group. There are two reaction mechanisms: (a) free-radical addition and (b) catalyzed Michael addition.	110
Figure 7.3	The mechanism for a photoinitiated thiol-ene reaction. The reaction is fairly unique due to the step-growth polymerization despite propagating via free-radicals.	111

Figure 7.4	An example of two of the common design spaces for RSM. The red points are experimental conditions and blue point is the center point of the experiment. (a) Three-level Box-Behnken design that utilizes a combination of 2^k factorial design and incomplete block design. (b) Three factor central composite design (CCD) that utilizes axial points (purple).	114
Figure 7.5	Schematic for the (a) Teflon mold and (b) aluminum substrate. The samples were scaled down from the standard.	117
Figure 7.6	Characteristic contour plots of the TTT samples and TMPTA samples. The TTT based samples show a more consistent contour shape from the minimum at the bottom left to the maximum at the top right. The triarcylate has more contour variation with each different filler.	121
Figure 7.7	The main effects plots from the response surface DoE. A steeper slope between the factor indicates a stronger impact of the individual variable to the figure of merit.	123
Figure 7.8	The co-factor interaction between the variables in the DoE. Intersection in the plot the level lines for each pair of factors implies a non-negligible co-factor interaction.	124
Figure B.1	Waterfall plots of the CCS library after annealing in air for 3 hours (Top) and 6 hours (bottom).	178
Figure B.2	The spectrum of the as-deposited $(\text{AlFeNiTiVZr})_{1-x}\text{Cr}_x$. The low intensity of the spectrum is due to the lack of oxides present on the sample surface.	179
Figure B.3	Raman heat map and representative spectra of the CCS after 1 hour.	179
Figure B.4	Raman heat map and representative spectra of the CCS after 6 hours.	180
Figure B.5	Raman heat map and representative spectra of the CCS after 18 hours.	180
Figure C.1	SEM images of ScSZ samples deposited at 923 K, 65 W, and 10 vol.% O_2 concentration. (a)4 hour post-anneal, (b)8 hour post-anneal, (c)12 hour post-anneal.	181

Figure D.1	The diffraction pattern of $\text{ReO}_x/\text{CeO}_2$	183
Figure D.2	A comparison of the SNR between Raman spectra at different points during heating.	185
Figure D.3	A spectrum of the 1 wt.% $\text{ReO}_x/\text{CeO}_2$ between 3000 and 4000 wavenumbers. The O–H stretch has been observed near 3700 cm^{-1} , and a broad band is visible in the spectrum.	186
Figure E.1	3D contour plots of the average adhesive strength. The plot was generated using a regression model that minimized the distance of the contour plot to the data points.	195
Figure E.2	The MTMO promoter. The silane end of the molecule is designed to bond with metal substrates, while the thiol end links with the sealant.	196
Figure E.3	SEM/EDS of the (a) clean Al substrate and (b) promoted Al substrate.	197
Figure E.4	XPS spectra of the (a) clean Al substrate and (b) promoted Al substrate.	198
Figure E.5	XPS spectra of the (a) silicon and (b) sulfur on the promoted Al substrate.	199
Figure F.1	Copyright permission for J.K. Bunn, Development of Novel High-Throughput Methodologies to Evaluate the Thermal Stability of High-Temperature Thin-Film Crystals for Energy Applications. University of South Carolina, 2016	200
Figure F.2	Copyright permission for B. Ruiz-Yi, J. K. Bunn, D. Stasak, A. Mehta, M. Besser, M. J. Kramer, I. Takeuchi, J. R. Hattrick-Simpers, (2016). The Different Roles of Entropy and Solubility in High Entropy Alloy Stability. ACS Combinatorial Science, 18(9), 596-603.	200
Figure F.3	Copyright permission for National Transportation Safety Board. Aircraft accident report - In-flight breakup over the Atlantic Ocean Trans World Airlines Flight 800 Boeing 747-131, N93119, near East Moriches, New York, July 17, 1996. (Report No. PB2000-910403).	201

Figure F.4	Copyright permission for X. Ren, W. Pan (2014). Mechanical properties of high-temperature-degraded yttria-stabilized zirconia. <i>Acta Materialia</i> , 69, 397-406.	202
Figure F.5	Copyright permission for M. Yashima, M. Kakihana, M. Yoshimura, (1996). Metastable-stable phase diagrams in the zirconia-containing systems utilized in solid-oxide fuel cell application. <i>Solid State Ionics</i> , 86-88, 1131-1149.	203
Figure F.6	Copyright permission for B. MacQueen, B. Ruiz-Yi, M. Royko, A. Heyden, Y.J. Pagan-Torres, C. Williams, J. Lauterbach, (2020). In-Situ Oxygen Isotopic Exchange Vibrational Spectroscopy of ReO_x Surface Structures on CeO_2 . <i>The Journal of Physical Chemistry C</i> , 124(13), 7174-7181.	204
Figure F.7	Copyright permission for S. Rani, A.K. Agrawal, V. Rastogi, (2017). Failure analysis of a first stage IN738 gas turbine blade tip cracking in a thermal power plant. <i>Case Studies in Engineering Failure Analysis</i> , 8, 1-10.	205

CHAPTER 1

INTRODUCTION

1.1 OVERVIEW

Solid materials have been utilized in a multitude of industrial sectors, such as energy generation, chemical synthesis, and aeronautics. Each field has highly specific needs unique to their industry. Fortunately, solids can be broken down into various different classes of materials which can suit the needs of an individual industry. Examples range from thin films, heterogeneous catalysts, and polymers, with each type providing distinct functionality in practical application. A material's property is dependent on its phase or structure, which, in turn, is dependent on its synthesis conditions. However, discovery of a material that has a desirable figure of merit for a given function is a non-trivial task, due to the wide array of input variables that are typical during synthesis.

A major branch of materials science that allows for exploration of nanoscale materials in a wide array of compositions is thin-film science. Thin films have multiple different uses within the energy generation sector. Many applications of thin films are as protective coatings for bulk structural materials exposed to corrosive conditions, such as high temperature jet or gas turbines. Thin films can also be applied to the field of high temperature electronic systems, such as in a solid oxide fuel cell (SOFC) or within a high temperature gas sensor. In both of these cases the films can act as either a solid electrolyte or electrode layer. Additionally, they can be utilized as a means of an initial screening of compositions suitable for scaling up into bulk

materials. However, in each of these cases high temperature environments present difficult engineering challenges due to the nature of thin films, such as the delamination of film from substrate due to a difference in thermal expansion coefficients upon heating or interfacial reactions between the film and substrate. Furthermore, a material screened and tested at a thin-film level may not exhibit the same figure of merit for a given property when synthesized a bulk conditions. While these challenges are present, the merits of utilizing thin films for these applications are valuable.

Heterogeneous catalysis has a multitude of applications in the generation of a variety of chemicals. The effectiveness of these catalysts can sometimes be attributed to the surface structure of the catalyst on its given support. Characterization of the surface species is important in determining chemical reaction mechanism steps. At the molecular level characterization involves various spectral observations, from vibrational spectroscopy of the catalyst and support to binding energy measurements that provide insight into oxidation states and can complement other techniques. Understanding potential surface chemistry allows for optimization of future catalysts towards a desired figure of merit.

Polymer sealants represent another type of functional material that have been studied for large scale industrial application. In the aeronautics industry there is a demand for inert, water resistant, and rapid curing sealants. A major application of the sealant is at the stress and contact points of the integrated fuel tank. This prevents the leakage of fuel out of the tank or moisture entering the tank, both of which can lead to catastrophic failure. Ultraviolet (UV) curable sealants are a prominent class of polymer that have been applied due to fast rate of polymerization and ease of application. However, discovery and optimization of the polymerization for a desired figure of merit requires adjustment of a large array of variables.

1.2 HIGH-THROUGHPUT EXPERIMENTATION

A major focus of this thesis is the exploration of multi-principal element alloys (MPEAs) and exploring their composition space. These studies require a paradigm shift in experimental design to efficiently study the wide parameter space. The discovery and characterization of new functional materials have been typically a laborious and time-intensive task. When considering the design space of elements, atomic percentages, and synthesis conditions for MPEAs, the number of variables that need be optimized are effectively limitless. Solely looking at the common of elements used in the synthesis of these alloys, as seen in Figure 1.1, the number of possible five-element equiatomic alloy systems exceeds 400,000. Furthermore, when looking at three to six element systems, the number expands to over two million possible systems. However, current research has roughly only observed slightly more than 100 systems, utilizing only forty-five elements from the periodic table [159, 158].

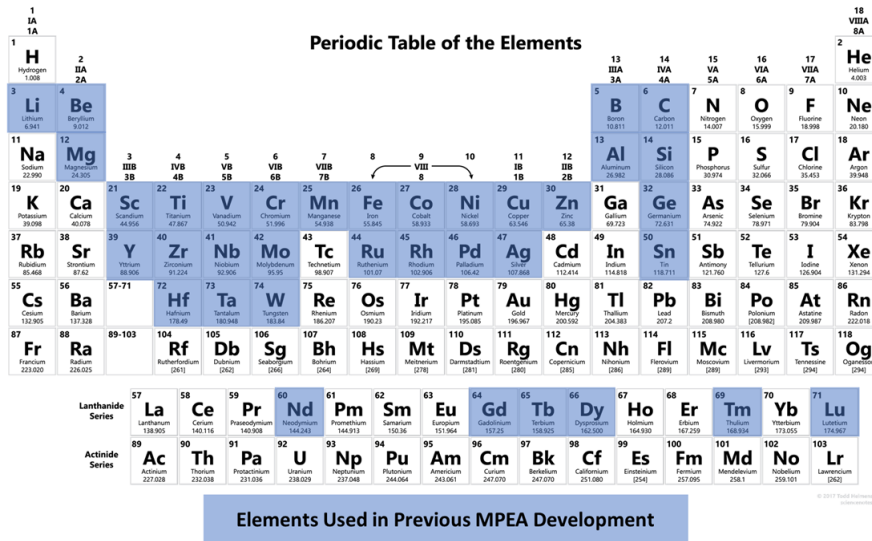


Figure 1.1: A visualization of the common elements used in MPEA development. While the previous designs consisted of 36 elements, the most commonly used elements in an alloy consist of Al, Co, Cr, Cu, Fe, Mn, Ni, and Ti [159].¹

¹The periodic table was adapted courtesy of sciencenotes.org.

Individual sample measurement is not feasible or practical when studying such a tremendous sample space, and a different approach needs to be taken in order to conduct experiments efficiently. High-throughput experimental techniques (HTE) have been utilized in the materials discovery field as more than a means of expediting experimental research. On a national level, the white paper for the Materials Genome Initiative for Global Competitiveness (MGI) was written as an outline for the unification of experimentation, computation, and theory into an efficient framework [214]. Additionally, it seeks to provide data accessibility in an attempt to change the paradigm of materials research and accelerate materials discovery [214]. While the initiative has been fruitful in application of theoretical modeling utilizing CALPHAD and density functional theory (DFT), generation of large quantities of experimental data is still required to contribute toward the goals of MGI. Therefore, HTE techniques are crucial in rapid data creation, which fulfills the goal of MGI.

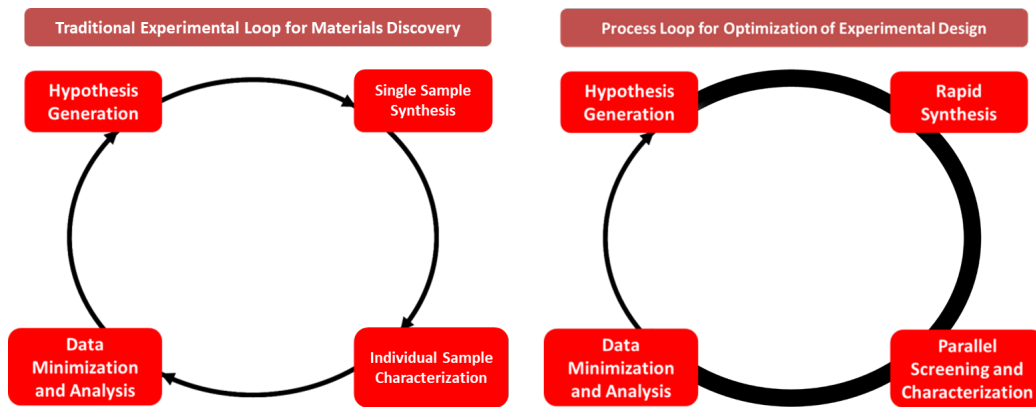


Figure 1.2: (Left) The experimental loop of typical materials discovery. (Right) The experimental design loop utilizing high-throughput methods. While HTE expedites many steps of the scientific process, there is still a bottleneck between data analysis and generation of new hypotheses.

The expansive nature of MPEAs makes them a prime candidate for the deployment of HTE techniques for synthesis and characterization [159]. HTE techniques have already been employed in the discovery of a multitude of solid materials, such as solid powder catalysts [247, 39, 84], optical, magnetic, and electronic materials

[72, 286, 191, 140], and high-temperature alloys [185, 186, 36]. With respect to high temperature alloys, HTE has successfully been utilized to observe phase dynamics and oxidation growth within these materials. Thin-film Ni-Al alloys phase transitions have been observed by Metting *et al.* [154]. Thienhaus *et al.* used high-throughput electrical and optical techniques to identify regions of interest in a Ni-Al thin-film composition spread, and then mechanically measured those regions of interest with nanoindentation [236]. Bunn *et al.* utilized *in-situ* synchrotron diffraction of a highly resolved aluminum rich region of a thin-film FeCrAl alloy, tracking 178 different compositions in order to track phase boundaries and oxidation formation [36]. These studies show how HTE is an ideal tool for tracking and studying phase dynamics in the complicated MPEA composition space.

Many of the aforementioned experiments utilized HTE methodology on continuous composition spread (CCS) libraries for binary or ternary alloy systems, along with the high-temperature oxidation and oxide structure stabilization analysis [186, 145, 85, 74]. Thin-film CCS samples are commonly used in order to accelerate the synthesis, post-processing, and analysis of a sample library. Samples are typically created with deposition methods on a given substrate, such as physical vapor deposition (PVD) of a target material via magnetron sputtering. Once a library is made the physical locations on the sample are correlated to different elemental compositions based off an in-house semi-empirical sputter model [34]. The model utilizes measured deposition rates of targets to estimate composition based off of discrete probability theory and improved with Nelder-Mead optimization [172]. Deposition rates are typically verified through calibration depositions onto a quartz crystal monitor (QCM), which is followed by various experimental techniques, such as physical analysis through profilometry or atomic force microscopy (AFM), or spectrographic investigation via energy/wavelength dispersive spectroscopy (EDS/WDS) [41, 51, 154]. Afterward, the CCS is characterized with rapid-serial or parallel techniques that provides large

quantities of data, from hundreds to thousands of measurements. Timely analysis of large data sets typically require computational methods such as machine learning algorithms. These algorithms can present entirely new problems based off the given data due to the difficulty for computers to interpret patterns in visual data such as spectroscopy, which has subtle nuances that have been honed by human analysis and various empirical heuristics. This has lead to the bottle next of the experimental loop seen in 1.2 transitioning from sample handling (synthesis, processing, and characterization) to data analysis.

1.3 THESIS RESULTS

In this dissertation, the details of different solid materials projects will be discussed. An in depth discussion will be provided for four thin film systems: two multi-principal element alloys (MPEAs) and two variations of stabilized zirconia. The phase identification and characterization of the alloy materials was performed using high-throughput techniques, while the zirconia films were analyzed using discreet methods. With respect to the MPEAs, one study showed that the phase stabilization mechanism for forming a single-phase solid solution is a combination of entropic and solubility mechanisms. Furthermore, an oxide resistant composition was discovered in an alloy doped with chromium after studying a CCS alloy. In the zirconia films, deposition parameters were discovered that were used able to sputter select phases on a given substrate. Additionally, vibrational spectrographic measurements were taken on a $\text{ReO}_x/\text{CeO}_2$ catalyst in order to determine the surface structures of the rhenia and relate that to a calculated reaction mechanism. Four different rhenia structures were discovered on the ceria support. Finally, a transfer function for a thiol-ene polymer system was modeled using a design of experiments (DOE) method in order to provide proof-of-concept for an industrial partner.

CHAPTER 2

EXPERIMENTAL TECHNIQUES

This chapter is dedicated to the major techniques and their principles that were used in this work. Initially, the fundamental science of magnetron sputtering will be discussed. Then a brief description of the sputtering chamber where the synthesis of thin-film continuous composition spreads (CCS) and discrete sample libraries will be introduced. Afterward, an overview on the major characterization techniques, X-ray diffraction, Raman spectroscopy, and Fourier transform infrared spectroscopy (FTIR), that were utilized will be provided, along with the relevance of these techniques to the investigations they were involved. Finally, a short discussion will be had on the simple mechanical technique used to measure the adhesive strength of polymers on substrates. The exact method used in each experiment will be discussed in their respective chapter.

2.1 MAGNETRON SPUTTERING

2.1.1 PRINCIPLES

Magnetron sputtering is a physical vapor deposition (PVD) technique that utilizes the bombardment of directed ionized particles toward a metal target in order to coat a substrate with a desired material. It has been used in industry as a means of synthesizing optical material, thermal coatings, and semiconductors. Sputtering was first described in the mid 1800s, when various metal electrodes targets were discovered to have "disintegrated" (sputtered) in a gas discharge tube [64, 76, 73]. However,

sputtering would not be used on an industrial scale until the development of diode sputtering systems in the 1940s [231, 73]. Additionally, the development of magnetron sputtering increased deposition rates of samples, and greatly reduced impact damage that the thin films received from the high-energy deposition. Radio frequency (RF) sputtering has broadened the range of materials that can be deposited to include insulating materials, such as ceramics and oxides. These have been problematic in the past due to charge buildup on the eroding surface [212].

PVD takes place in an ultra-high vacuum (UHV) chamber with the main components consisting of a sputter source (gun) and a substrate holder. The distance between the gun and holder is known as the throw distance and can be adjusted by moving the holder further from or closer to the source. The sputter gun can be set to use either RF or direct current (DC) voltage depending on the sputtered material (target material), and can also have its tilt adjusted in order to direct the angle of the sputtering plume. Additionally, wattage to the gun can be controlled in order to modify the energetics of the sputtered particles. Sputter sources are composed of three major parts for their function. These include a ground shield (which acts as an anode), a target material that contacts the copper cathode block (which means that the target material acts as a cathode), and a magnetic array, as seen in Figure 2.1. In order to better control the sputter process, a chimney and shutter system are used as a way to prevent cross contamination between targets and control the timing of the material deposition.

In order to begin the sputter process, the sample substrate is locked into position in the UHV chamber. Then the chamber is pressurized with an inert sputtering gas, typically argon. Once at the desired sputter pressure a plasma is generated by applying voltage to the sputter source. The plasma is a glow discharge resulting from the ionization of the sputter gas by a powerful electromagnetic field that ejects an electron from the argon atoms. The Ar^+ ions are accelerated toward the negatively

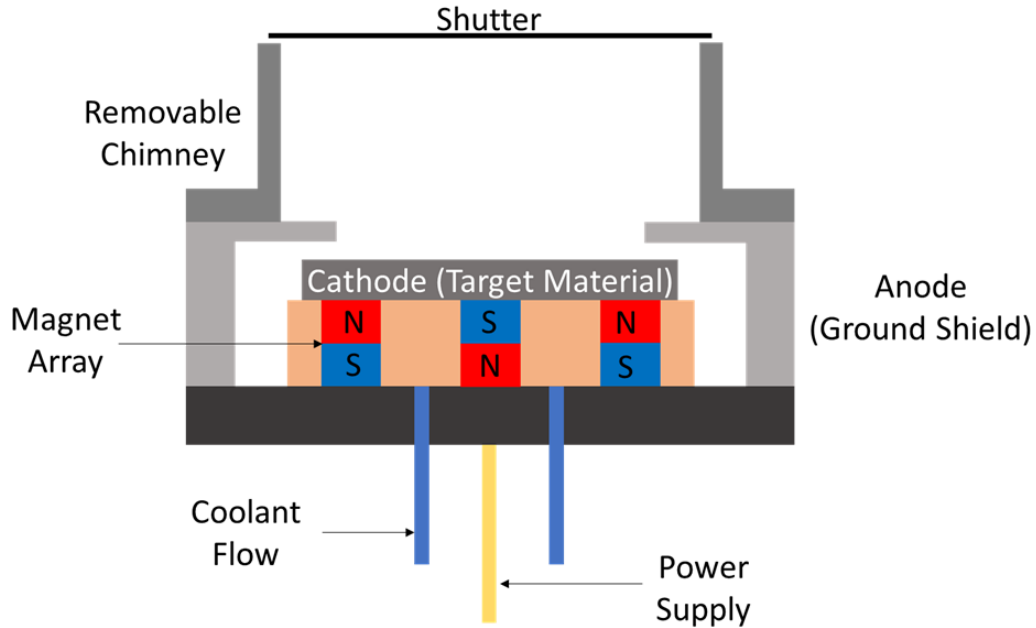


Figure 2.1: A cross-sectional schematic of the major magnetron sputter gun components. A copper mesh is typically placed between the target and copper cathode block in order to improve heat conductivity. Oxide materials must be bonded to a copper backing plate to improve conduction.

charged cathode target with energies that can reach 1000s of eV. As the ions bombard the surface of the target, a linear cascade occurs that causes a chain reaction of atoms to collide and eject a surface atom, which is considered a sputtered atom. The sputtered atom then travels toward the substrate holder, where the atom can either collide with the sputter gas, other sputtered atoms, or the substrate. When colliding with the substrate the atom may eject an atom off it (known as resputtering), deflect off the substrate, or deposit on the surface as an adatom, which is minimized by magnetron sputtering [75]. Another major advantage of magnetron sputtering is the increased deposition rate and reduction in impact damage [222]. This is due to the utilization of a powerful magnetic array that keeps free electrons localized near the target. This allows for consistent ionization of the sputter gas and makes for a denser plasma, which increases the deposition rate due to a more "focused" area of sputter

and a reduction of travel distance for the Ar^+ ions to the target. This process can be seen in Figure 2.2.

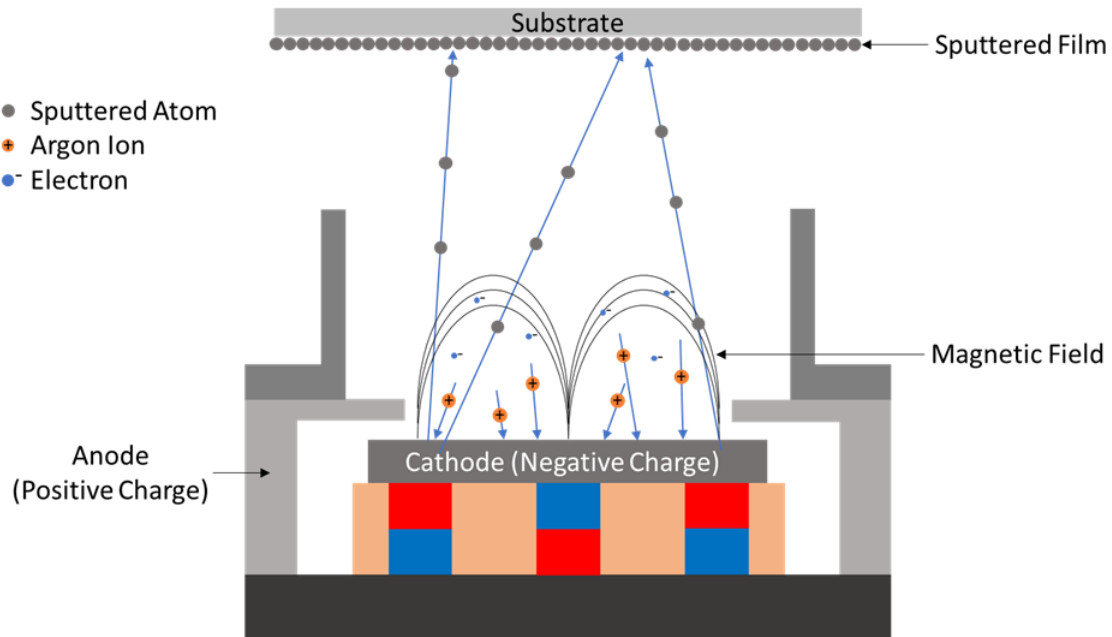


Figure 2.2: A diagram depicting the sputter process when the plasma is ignited over the target. The electrons that are trapped within the magnetic field have high enough energy to collide and ionize neutral Ar atoms.

2.1.2 EXPERIMENTAL EQUIPMENT

All depositions were performed using a 5-gun AJA Orion class sputtering chamber seen in Figure 2.3. This system allows for easily tunable parameters that can adjust the deposition rate of the sputtered material and the energetics of adatoms. Throw distance from target to substrate can be adjusted via the length of the substrate holder and the tilt of the sputter gun, which can affect the deposition rate of the sputtered atoms and the composition spread in a codeposited film. Adjusting the power and voltage of the sputter gun affects the deposition rate of the sputtered atoms along with the energy of the adatom when bombarding the substrate. Controlling the energy of adatoms can modify the crystal phase of the sputtered sample. This is important in preventing lattice mismatch between the grown film and the substrate, which can lead

to spallation. Additionally, depending on the application, the deposition parameters and substrate can be chosen to promote epitaxial growth, which is a type of nucleation where the grown sample preferentially orients to the substrates crystal structure [151].



Figure 2.3: An AJA Orion sputtering chamber. This system has five sputter guns, and three target materials can be co-deposited during a single experiment.

Due to the tilt of the sputter gun, there is variation of the throw distance that causes the film thickness to decrease as the distance of the substrate from the gun increases. In order to have uniform film thickness on the substrate, the holder is able to rotate. This is ideal for studying single sample compositions. However, during co-deposition the substrate remains stationary in order to develop a continuous compositional spread (CCS) thin-film sample. Figure 2.4 illustrates the process of developing a binary CCS. Compositions are generated by determining the deposition rate of each gun material and stoichiometrically calculating the mass of atoms deposited at a given point on the substrate. Deposition rates are estimated using a quartz crys-

tal microbalance (QCM) or monitor, which uses the piezoelectric effect to measure the dampening in the acoustics of a quartz crystal as material is deposited onto its surface, also known as the Sauerbrey relation [210]. However, due to the dependence of geometry on the deposition rates of thin films, additional experiments can be run at different positions in the chamber, and computational modeling can be performed in order to extrapolate deposition rates outside the center of the sputtering chamber. In order to validate the elemental gradients of the composition, elemental analytical techniques such as X-ray fluorescence (XRF) or energy/wavelength dispersive X-ray spectroscopy (EDS/WDS) are applied at different points on the sample. The compositions can then be spatially related to those points on the film and interpolation can determine compositions at other points on the sample.

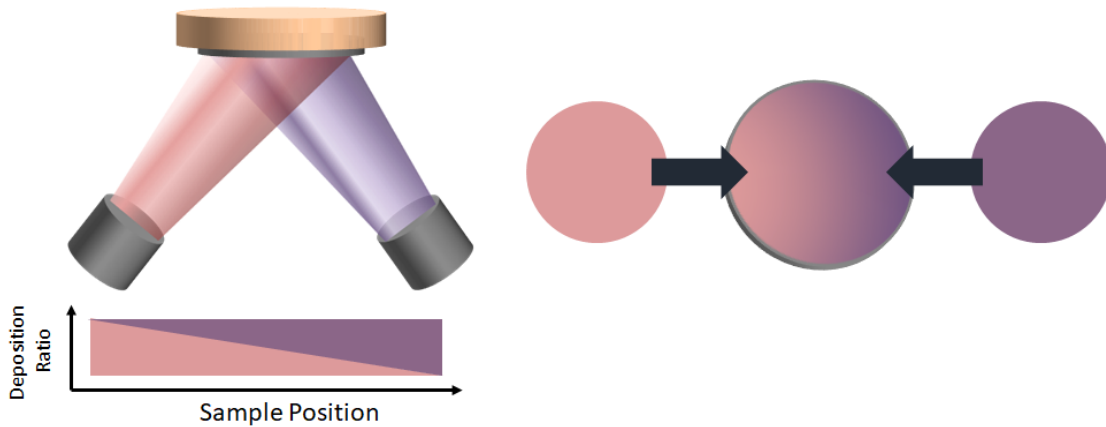


Figure 2.4: (Left) An example of the co-deposition of a binary system. The sample product concentration varies based on the position relative to the sputter guns. (Right) A colored example of the co-deposited sample.

2.2 X-RAY DIFFRACTION

2.2.1 PRINCIPLES

X-rays were discovered by Wilhelm Röntgen in 1895 while experimenting with various discharge tubes [54]. They are considered high-energy electromagnetic radiation with

wavelengths that range from 0.01 to 10 nm [54]. X-rays can be generated in a number of ways depending on application. In many general cases, X-rays are formed in high-voltage vacuum tube where a hot cathode emits electrons via thermionic emission. These electrons accelerate to high velocities and collide with a metal anode, which is typically copper in crystallography. The emitted electrons have high enough energy to eject core shell (1s orbital) electrons from the metal atoms. Electrons from upper shells fill in the vacancy left by the core electron and an X-ray photon is released. These X-rays are characteristic to the anode target material and are referred to as spectral lines. They are named after the shell where the vacancy was filled, which generally the K shell. In the case of copper, the characteristic $K\alpha$ line has a wavelength of 1.54 Å.

One of the discovered applications for X-rays was in crystallography, where their diffraction allowed for characterization of materials. X-ray diffraction (XRD) is a standard technique for crystal phase identification, that was first discovered by Paul Knipping, Walter Friedrich, Max von Laue in 1912 [60]. It is a technique that takes advantage the spacial periodicity and long range ordering of a crystal in order to determine structure. XRD is an elastic scattering technique where monochromatic X-rays are scatter off the electron cloud of the atoms in sample. A majority of the scattered X-rays destructively interfere with each other and are not detected. However, specific scattering angles allow for measurable constructive interference. These angles can be related to the lattice d-spacing and the X-ray wavelength via Bragg's law:

$$n\lambda = 2d \sin \theta \quad (2.1)$$

where n is an integer value, λ is the X-ray wavelength, d is the spacing between the diffracting planes, and θ is the X-ray angle of incident. The angles where constructive interference occurs can be recorded in a diffractogram, generated by a point detector

that moves in the θ direction. Diffracting planes are grouped by families and are identified in a diffraction pattern by Miller indices notation. Figure 2.5 shows an example of diffraction on a crystal lattice.

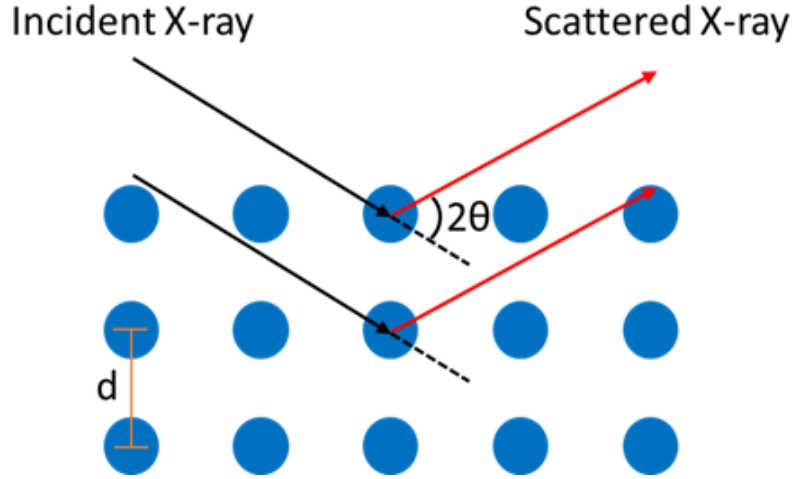


Figure 2.5: A depiction of X-rays diffracting off a crystal lattice. The Bragg diffraction condition is fulfilled at angles of X-ray constructive interference.

Additionally, due to the spatial periodic nature of the crystal lattice, X-ray scattering can be described with vector notation in reciprocal space. The reciprocal lattice, whose primitive vectors $(\vec{b}_1, \vec{b}_2, \vec{b}_3)$, is the Fourier transform of the real space Bravais lattice of the crystal. These primitive vectors can be determined by the following equations:

$$\vec{b}_1 = 2\pi \frac{\vec{a}_2 \times \vec{a}_3}{\vec{a}_1 \cdot (\vec{a}_2 \times \vec{a}_3)} \quad (2.2)$$

$$\vec{b}_2 = 2\pi \frac{\vec{a}_3 \times \vec{a}_1}{\vec{a}_2 \cdot (\vec{a}_3 \times \vec{a}_1)} \quad (2.3)$$

$$\vec{b}_3 = 2\pi \frac{\vec{a}_1 \times \vec{a}_2}{\vec{a}_3 \cdot (\vec{a}_1 \times \vec{a}_2)} \quad (2.4)$$

$$\vec{G} = \nu_1 \vec{b}_1 + \nu_2 \vec{b}_2 + \nu_3 \vec{b}_3 \quad (2.5)$$

where $\vec{a}_1, \vec{a}_2, \vec{a}_3$ are the primitive vectors of the Bravais lattice, ν_1, ν_2, ν_3 are integer values, and \vec{G} is a reciprocal lattice vector. The Fourier transform converts the planes

seen in the real space lattice ($\vec{a}_m \times \vec{a}_n$) into vectors in reciprocal space (\vec{G}), which map to points on the reciprocal lattice. X-rays themselves can be described by their wavevector, where magnitude is its wavenumber and direction is direction of wave propagation. The wavevector for the incident X-ray is known as \vec{k} , and the diffracted wavevector is \vec{k}' . Due to elastic scattering The difference is known as the momentum transfer vector (or scattering vector), \vec{q} . The Bragg diffraction condition is fulfilled when \vec{q} equals \vec{G} , which can be seen in Figure 2.6.

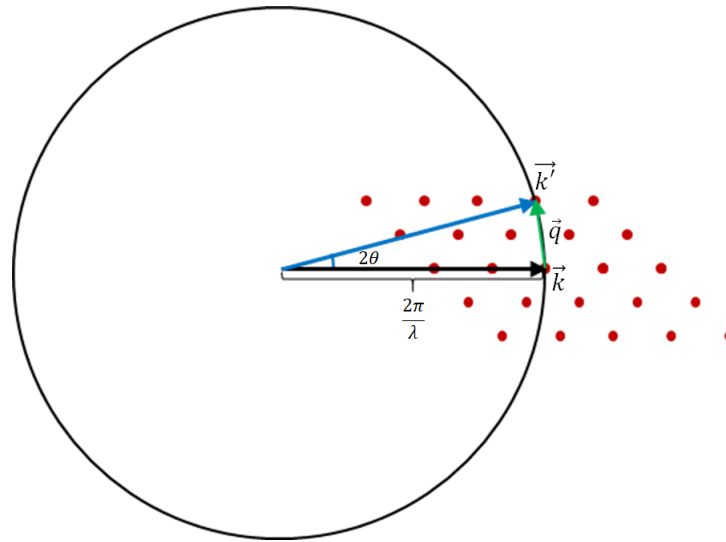


Figure 2.6: A representation of the Ewald construction in two dimensions. The Laue condition is a vector analog to the Bragg condition, and is fulfilled when \vec{q} is equal to a lattice vector point that lies on the Ewald construction.

Analysis in reciprocal space has advantages where the momentum transfer vector is independent from the X-ray wavelength and the detector position, allowing for the use of flux light sources. Furthermore, the momentum transfer vector can be utilized to determine structure factor and form factor, which contribute to the intensity of the diffracted X-ray. This data is typically captured using a 2D area detector that can capture the Debye-Scherrer rings of a diffraction and show the development of texturing, which is the growth of preferential orientations of specific planes, on thin films. Texturing can lead to the absence of peaks during point detector measurements.

This is because thin films do not necessarily have all possible orientations with their grains, which can be missed in a linear scan with a point detector. However, a sufficiently large 2D area detector can capture all possible orientations in χ space. Figure 2.7 the steps to interpret the 2D area diffractogram and has examples of texturing of the film. The momentum transfer vector magnitude, q , is related to θ via the following equation:

$$q = \frac{4\pi}{\lambda} \sin \theta \quad (2.6)$$

where λ is the X-ray wavelength (\AA) and θ is the scattering angle ($^\circ$). A common wavelength that is referenced in the literature is the Cu- α line. From the 1D diffractogram, a cross-reference of the peaks to powder diffraction files (PDF) from the Inorganic Crystal Structure Database (ICSD) [83] can be performed as a means to determine possible structures from previous experiments.

2.2.2 EXPERIMENTAL EQUIPMENT

A majority of the diffraction data was performed at the 1-5 beamline of the Stanford Synchrotron Radiation Lightsource (SSRL) which is a division of Stanford Linear Accelerator Center (SLAC). Synchrotron radiation is generated by accelerating an electron to near the speed of light in a curved magnetic path. The change in angle of the electron path results in an emission of electromagnetic radiation that can be tuned based on the electron energy. Synchrotron data was collected for MPEA samples that will be discussed in Chapter 3 and 4. Additionally, a SAXSLAB Ganesha 200 XL small angle X-ray scattering instrument, seen in Figure 2.9 was utilized to collect additional diffractograms for the oxide samples in Chapter 5.

Both systems utilize 2D area detectors that produces images similarly seen in Figure 2.7 and an x-y sample stage with a tilt capability. Tilting the sample allows for control over the angle of incidence of the incoming X-ray. The experimental set up

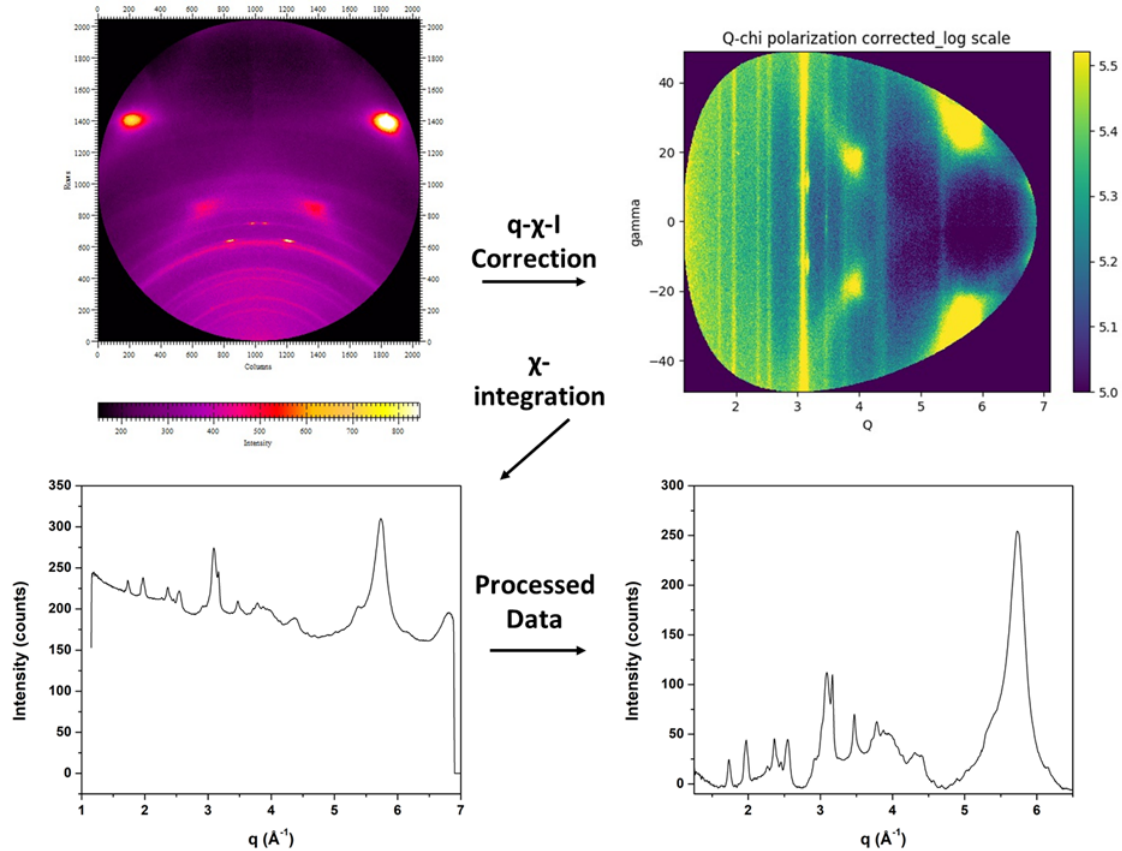


Figure 2.7: A generalization of the steps to convert a 2D area diffraction to a 1D pattern. The raw 2D image (Top Left) is from an x-y Cartesian plane image to a polar 2D image (Top Right), via an azimuthal integration. After correction, the image is further integrated along χ in order to collapse the data to a 1D diffraction pattern (Bottom Left). Once the 1D diffraction is acquired it is processed with baseline corrections and normalization in order to analyze the data (Bottom Right).

for the SLAC system can be seen in Figure 2.8. With the SLAC x-y stage, environmentally controlled *in-situ* experiments can be conducted using an air-tight Kapton dome, plumbed gases, and heating element on the stage. Use of an x-y stage allows for serial measurements across different positions on a thin-film sample. This means that, on a CCS library, rapid serial characterization of multiple compositions can occur with a sufficiently strong light source. Finally, a Rigaku MiniFlex II bench-top X-ray Diffractometer with a 1D silicon strip detector was used for additional measurements.

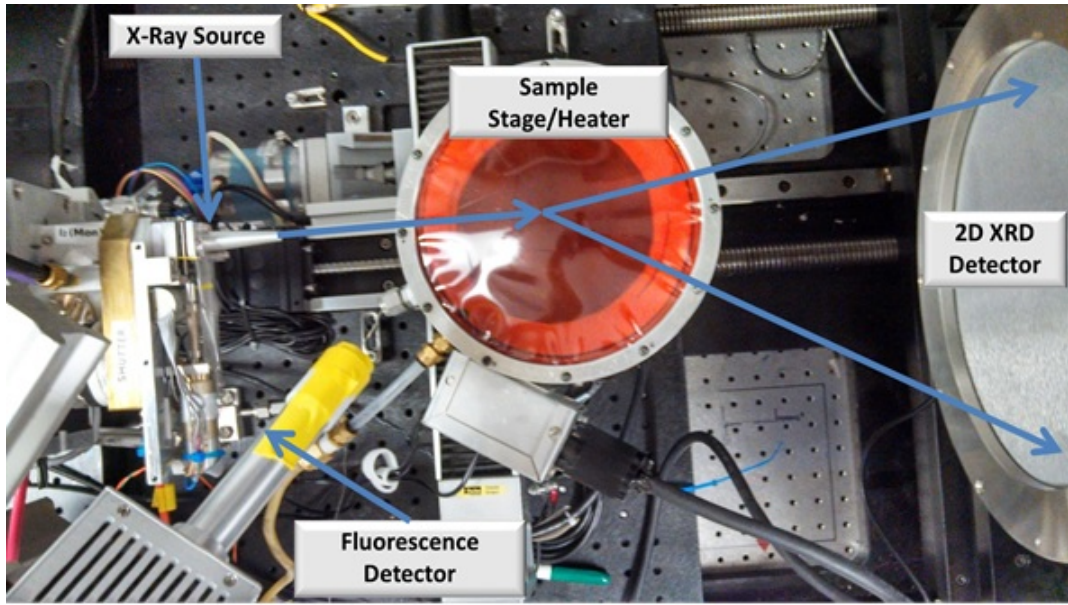


Figure 2.8: An overhead view of the diffraction set up at SLAC. This example includes a Kapton dome used for *in situ* measurements. The synchrotron light source is seen on the left, and the source X-rays strike the sample. The resulting diffraction is captured by the detector on the left. Any X-rays that participate in fluorescence is captured by the detector that is orthogonal to the substrate plane.

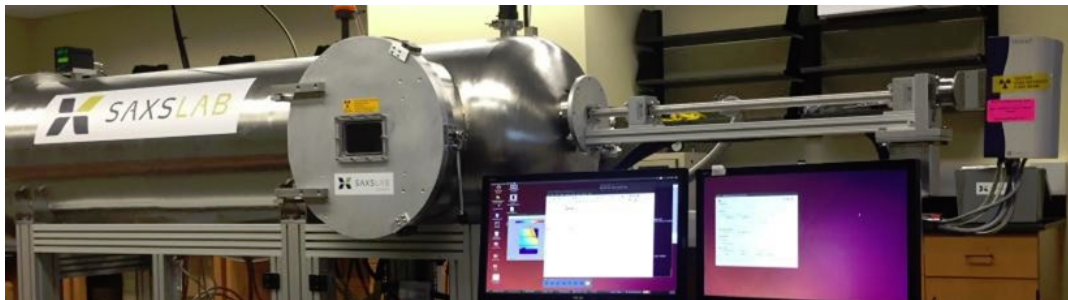


Figure 2.9: The Ganesha SAXSLAB X-ray scattering instrument. The vacuum chamber allows for measurements in the small-angle and wide-angle ranges and at grazing incidences. The source on the right generates X-rays in the $\text{Cu-}\alpha$ range, which strikes a tilted sample near the system door. The scattered X-rays are measured by a Dectris Pilatus 300K detector.

2.3 RAMAN SPECTROSCOPY

2.3.1 PRINCIPLES

Raman spectroscopy is an inelastic scattering technique that utilizes monochromatic light (laser) in order to probe the molecular vibrations of a material, which can

provide insight into structural identification, defect sites, and electronic effects. The Raman scattering effect was discovered by C.V. Raman and K.S. Krishnan in 1928 [196]. Raman spectroscopy is not limited to vibrations of gas or liquid molecules and can be used to excite phonons and magnons of solids. Phonons are quasiparticles that represent the excitation of vibrational modes in the crystal lattice of condensed matter, while magnons are excitations of the electron spin states in a crystal.

When a laser is exposed to a non-metallic sample, the crystal's vibrational energy state excite to a virtual energy state. During the relaxation one of three things can occur: Rayleigh, Stokes Raman, or anti-Stokes Raman scattering. In Rayleigh scattering, the system relaxes to the original state before excitation and light is elastically scattered from the surface. The majority of photons that strike the sample is made up of Rayleigh scattering. Stokes Raman scattering occurs when the excited state relaxes to a vibrational energy level above the ground state and inelastically scatters a photon with less energy than the incident photon. Anti-Stokes Raman scattering occurs when incident photons excite an already excited system (possibly due to a frustrated lattice), and the relaxation from the virtual energy state brings the system back down to the ground state. This results in a scattered photon that has higher energy than the incident laser wavelength. In the Stokes and anti-Stokes situation the difference between the incident laser energy and the emitted photon energy is called the Raman shift, which is expressed in wavenumbers. Each of these situations can be seen in Figure 2.10. During an experiment, approximately one in one million scattered photons will exhibit Raman scattering, while the rest are Rayleigh scattered [246].

A fourth phenomenon can occur when a sample is exposed to the laser, florescence. This occurs when the system is excited from the ground state to a higher electronic state by an electron absorbing a high-energy photon. When the electron relaxes to its ground state, fluorescent light is emitted. Unlike Raman, florescence is a resonant

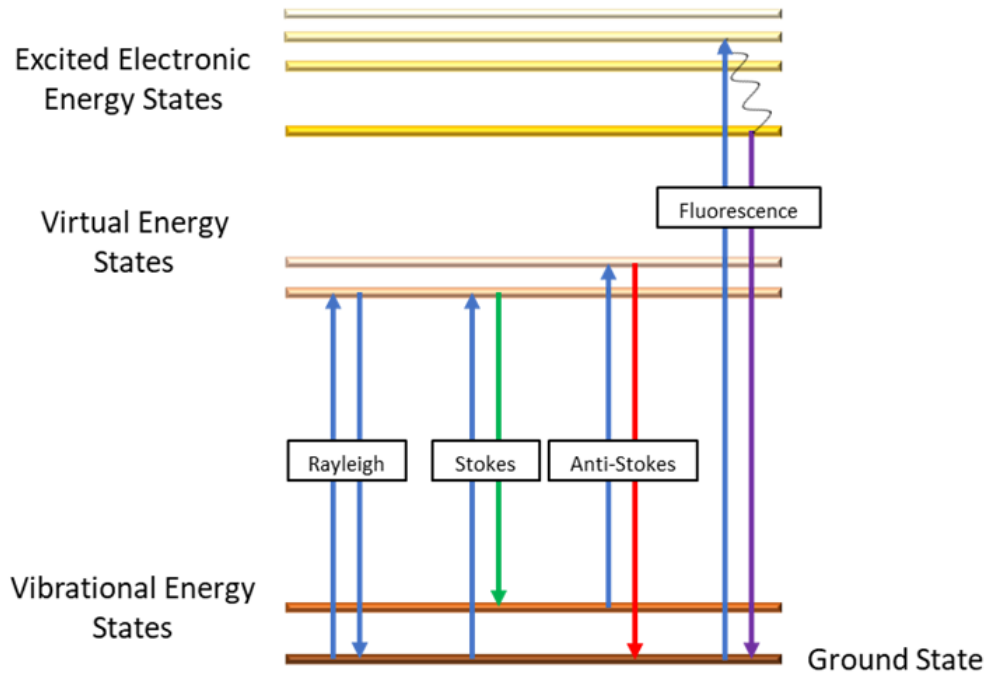


Figure 2.10: A Jablonski diagram that illustrates possible outcomes after excitation from a laser source. Three scattering events (Rayleigh, Stokes Raman, and Anti-Stokes Raman) and an absorption event (Fluorescence).

phenomenon and requires specific wavelengths to electronically excite the system. Raman scattering effects can be observed in any wavelength that does not induce fluorescence, which makes it simple to avoid fluorescence effects from overshadowing Raman bands. Additionally, measured fluorescence peaks are not seen in the anti-Stokes spectral region, which provides another way of differentiating Raman bands from fluorescence peaks.

In order for a vibrational mode to be Raman active, it must exhibit a change in polarizability. This means that the ability to induce dipoles alters with the particular vibrational mode and the following equation is true:

$$\frac{\partial \alpha}{\partial Q} \neq 0 \quad (2.7)$$

where α is the polarizability and Q is the normal coordinate. Pure metals are effectively infinitely polarizable, and thus they do not exhibit Raman scattering because

there can be no change in polarizability. Due to the metallic bonding between atoms, excited light is reflected off the surface as the electrons in a metal generate an electromagnetic field to oppose the excitation source. However, ceramic materials generated with metals can be Raman active and studied with this technique.

A typical Raman instrument utilizes a monochromatic laser source that is focused on a sample using an optical microscope. The microscope objective collimates the laser and doubles as a way of imaging the sample during experimentation. The spot size of the incident light can be calculated using the Airy disk diameter (D_{Airy} (μm)) equation:

$$D_{Airy} = \frac{1.22\lambda}{NA} \quad (2.8)$$

where λ is the laser wavelength (nm) and NA is the numerical aperture of the objective. Rayleigh and Raman scattered light is returned through the objective lens, where a majority of the Rayleigh light is filtered out. The rest of the chromatic Raman light is separated through a prism or holographic grating and detected via a charge-coupled device (CCD).

2.3.2 EXPERIMENTAL EQUIPMENT

Raman spectroscopy was performed using a Horiba XploRA PLUS confocal Raman microscope on the oxidized MPEA discussed in Chapter 4 and the $\text{ReO}_x/\text{CeO}_2$ catalyst in Chapter 6. The system is equipped with a 638 nm, 30 mW red diode laser and a 473 nm, 25 mW blue solid state laser. A selection of four microscope objectives are provided, which are capable of 10, 20, 50, and 100 times magnification. Additionally, diffraction gratings of 600, 1200, 1800, and 2400 lines per millimeter are accessible, which vary the wavenumber range and resolution. The detector is a thermoelectric air cooled CCD, with an area of 1024 by 256 pixels.

The system is also equipped with a programmable, motorized x-y translation stage. This allows for rapid, automated, serial measurements across a sample in order to generate a spectral map. In an oxidized CCS library, the Raman map provides structural and phase boundary information. In order to perform *in situ* experiments, a Linkam environmental cell is available that can be plumbed with gases and heated up to 1073 K.

2.4 FOURIER TRANSFORM INFRARED SPECTROSCOPY

2.4.1 PRINCIPLES

Fourier transform infrared spectroscopy (FTIR) is an absorption spectrographic technique that utilizes broadband IR source to measure the absorption or emission spectrum of a sample. IR spectroscopy relies on the principle that molecular bonds absorb light characteristic to their vibrational frequencies. The absorption spectrum can be used to identify types of bonds and estimate relative quantities of bonds in the spectrum. Molecular vibrations can be approximated with Lagrangian mechanics and Hooke's law, using simple mass and spring calculations to model atoms and bonds [199, 259]. This provides a range of frequencies for which families of bonds lie. Similar to Raman spectroscopy, selection rules indicate whether or not a vibration is IR active. A major rule for IR spectroscopy requires that the bond vibration have a change in the dipole moment of the system, whereas Raman requires a change in the polarizability. Due to their similarities and ability to probe different aspects of molecular vibrations, Raman spectroscopy and FTIR are seen as complementary techniques.

Instead of using monochromatic light to measure the bond absorption (typical to dispersive spectroscopy), FTIR uses a Michelson interferometer to measure the absorption from a broadband IR source, a diagram of which can be seen in Figure 2.11. As the name suggests, it provides a wave interference pattern by adjusting the phase of two IR beams, which results in different wavelengths constructively or destructively

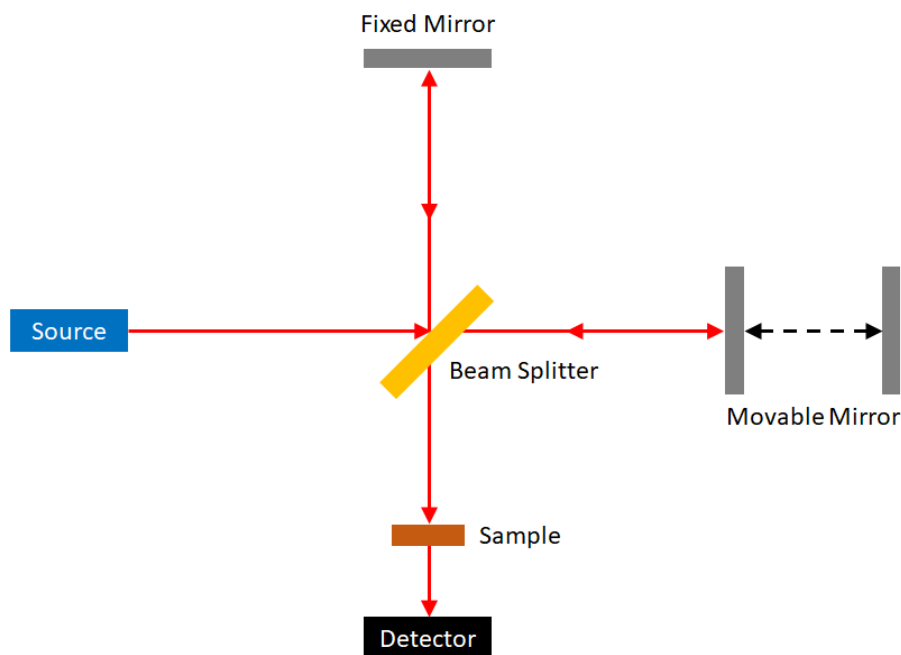


Figure 2.11: A basic diagram of the Michelson interferometer. The interferometer phase shifts the source beam by first separating light using a beam splitter (typically made with KBr). The two beams are reflected back toward the beam splitter, but at different phases due to a moving mirror that is in the path of one beam, which results in interference between the different IR wavelengths in the beams.

interfering. This allows for screening of a sample with multiple IR wavelengths at once, which accelerates the data collecting process. As the interfered IR beam passes through the sample, an interferogram is generated as a function of the optical path retardation (which is related to the mirror position). A Fourier transform is performed on the data, and transforms the interferogram into an absorption spectra, which can be seen in Figure 2.12.

2.4.2 EXPERIMENTAL EQUIPMENT

Time-resolved FTIR was taken for the $\text{ReO}_x/\text{CeO}_2$ study described in Chapter 6. This experiment was performed to determine the rate of exchange between the ^{18}O and the surface ReO_x . In order to perform the FTIR *in situ*, a diffuse reflectance infrared Fourier transform spectroscopy (DRIFTS) cell was used, which can be seen

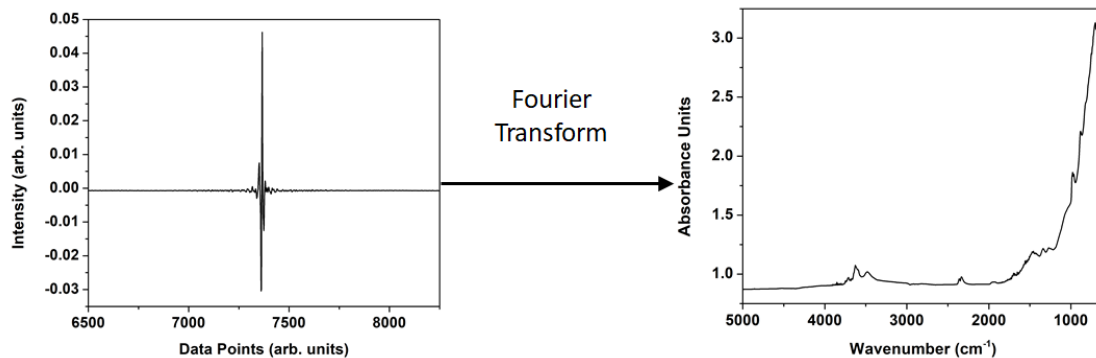


Figure 2.12: An example of the conversion from interferogram data to an absorption spectrum. A Fourier transform is done using computational software in order to convert the retardation data into vibrational wavenumber data.

in Figure 2.13. This cell allowed for bulk measurements of a powder sample without additional preparation. Additionally, it can be plumbed with gases and heated to a limit of 1073 K.

In order to detect the IR signal, a mercury cadmium telluride (MCT) detector was used. MCT is a commonly used material for IR photodetectors because it spans a large range of detection wavelengths at a high detectivity. However, it must be cooled to liquid nitrogen temperatures (77 K) in order to reduce the noise from thermal excitation.

2.5 PEEL TESTS

2.5.1 PRINCIPLES

Peel testing is a special type of cleavage test that is utilized to measure the adhesive strength and fracture energy of materials. The test has been standardized, and for the study in Chapter 7, an American Society for Testing and Materials (ASTM) D3330 standard was used for a 180° peel test [55]. The peel adhesion value (peel/adhesive strength) is determined as the average load during an extension divided by the sample

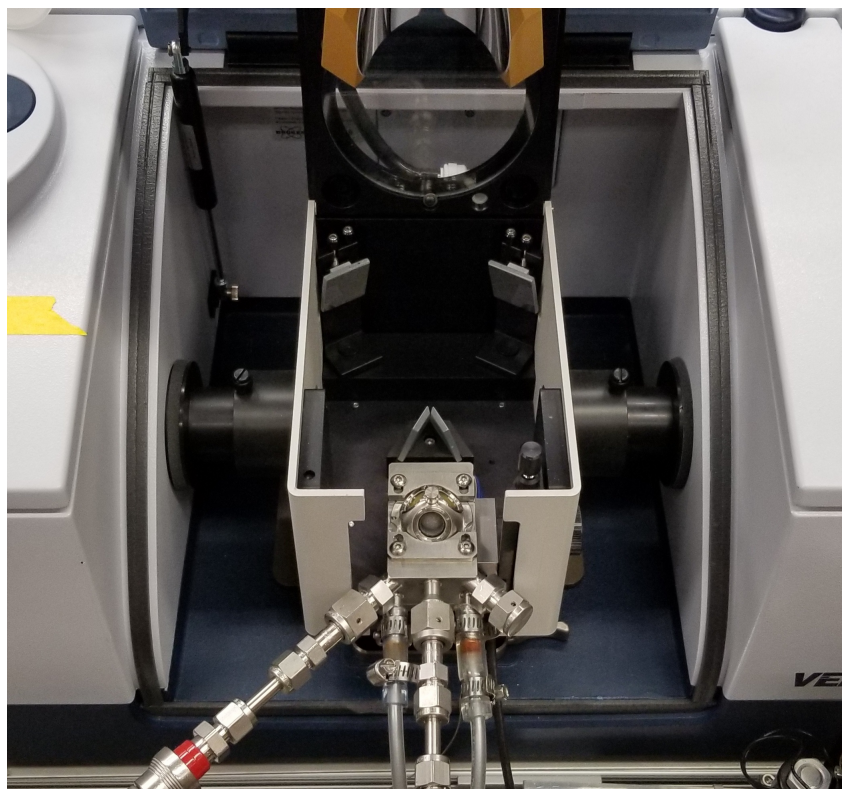


Figure 2.13: The DRIFTS cell used for *in situ* powder measurements. Mirrors reflect the IR source into the sample cell, which can be heated and exposed to desired gases. KBr can be supplemented to save sample material.

width seen in Figure 2.14. Fracture energy can be calculated by considering additional energy from the sample bending angle, which is seen in Equation 2.9:

$$\Gamma = \frac{F}{l}(1 - \cos(\theta)) \quad (2.9)$$

where Γ is the fracture energy ($\text{J}\cdot\text{m}^{-2}$), F is the peel load (N), l is the sample width (mm), and θ is the peel angle ($^{\circ}$). The F/l term is typically recorded when discussing the adhesive strength of a material.

2.5.2 EXPERIMENTAL EQUIPMENT

To fulfill the Thiol-Ene click chemistry reaction a series of monomers were selected for the synthesis, seen in Figure 2.15. The thiol monomer tested was pentaery-

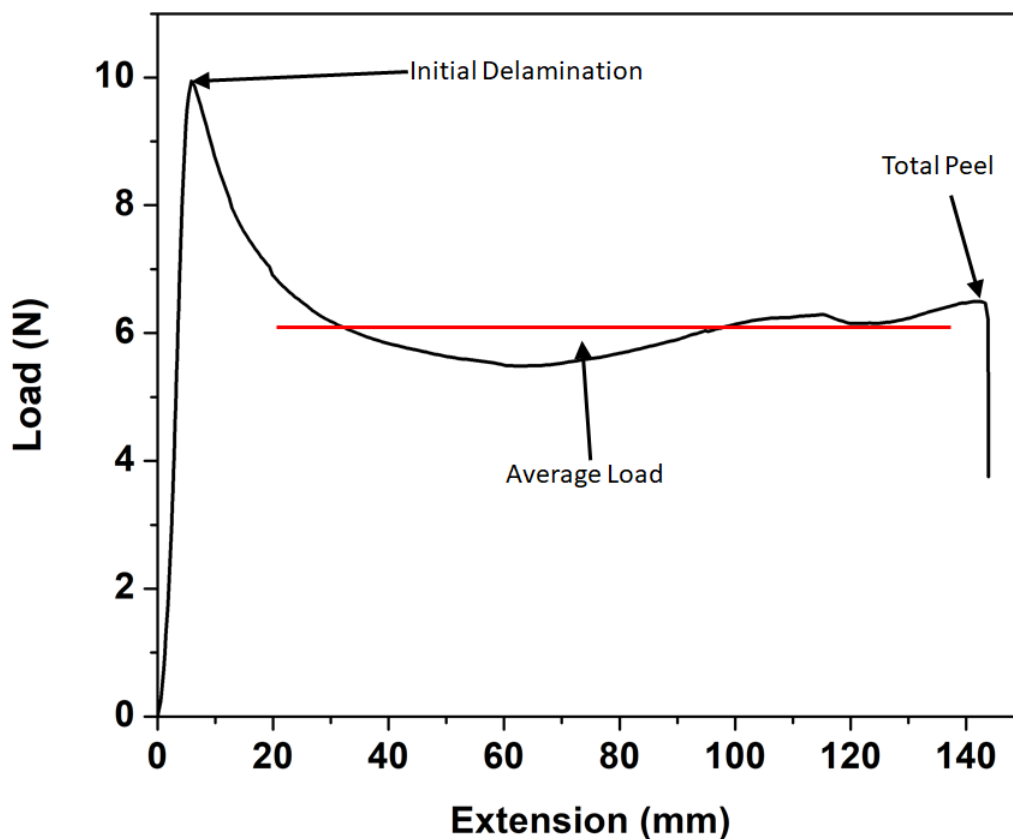


Figure 2.14: Typical peel data gathered from the Instron. After initial delamination, the load averages out before the sample is fully peeled. The average load divided by the sample width determines the adherent's peel strength.

thritol tetrakis(3-mercaptopropionate) (PETMP), which has four functional thiol groups. The allyl monomers that were tested consist of 1,3,5-triallyl-1,3,5-triazine-2,4,6(1H,3H,5H)-trione (TTT) and trimethylolpropane triacrylate (TMPTA), which both have three functional allyl groups. This allows for a cross-linked system with various backbones to test for structural and adhesive properties. These were selected due to their use in previous literature [40, 171, 59, 52, 280, 225, 226].

In order to create peelable samples, the polymer had to be molded into a specific shape for use in an Instron 5543 load frame. The mold and sample shape can be seen in Figure 2.16, where the mold was made of Teflon. The samples were cured on an aluminum 2024 substrate and had an aluminum mesh placed during synthesis to allow for the Instron grips to peel the sample. Aluminum 2024 was used as a

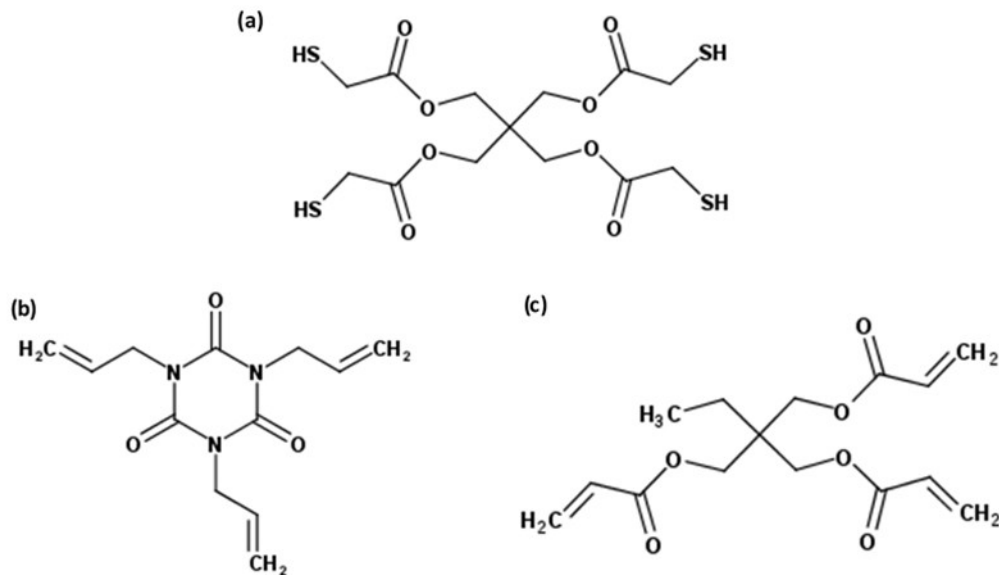


Figure 2.15: The monomers used in the study discussed in Chapter 7. (a) PETMP, (b)TTT, and (c) TMPTA.

substrate because it is a similar material used in the aerospace applications discussed in Chapter 1. Thiol-ene samples were cured under a UVP XX-15S bench lamp, and temperature was controlled via a 4-pass, 305 mm Hi-Contact Liquid Cold Plate.



Figure 2.16: A depiction of the mold and samples for the peel test measurements. (a) The Teflon mold. (b) Example of the sample on the substrate with an aluminum mesh for gripping.

In order to take adhesive strength measurements, samples were placed in an Instron 5543 A load frame equipped with a 100 N load cell and flat plane grips, as seen in Figure 2.17. Peel angles and speed are adjusted using a proprietary Bluehill Fracture software package. Measurements are also recorded using the software, which is then transferred to other data processing software.



Figure 2.17: The Instron 5543A Load Frame that has been outfitted with a 100 N load cell.

CHAPTER 3

PHASE STABILIZATION MECHANISMS OF MULTI-PRINCIPAL ELEMENT ALLOYS

3.1 BACKGROUND AND MOTIVATION

Multi-principal element alloys (MPEAs) are a relatively new class of materials that were first hypothesized and worked on in the 70s and 90s, but were expanded on into the current era with works by Cantor *et al.* and Yeh *et al.* [38, 275, 276, 167]. These materials are of interest due to the complexity of new ideas that they bring into alloy discovery, by inciting the exploration of a vast compositional space. MPEAs, as their name implies, are alloy systems that utilize relatively large proportions of elements into a base alloy. Traditionally, alloys were synthesized with a base element in mind, such as iron for stainless steel, and introduced smaller quantities of elements as dopants for a given figure-of-merit [56, 57]. This was done because the implications of the phase rule:

$$F = C - P + 2 \quad (3.1)$$

Parts of chapter adapted from: B. Ruiz-Yi, J. K. Bunn, D. Stasak, A. Mehta, M. Besser, M. J. Kramer, I. Takeuchi, J. R. Hattrick-Simpers, (2016). *The Different Roles of Entropy and Solubility in High Entropy Alloy Stability*. ACS Combinatorial Science, 18(9), 596-603, with permission from ©(2016) American Chemical Society. See Figure F.2 for copyright permission.

Where, F is the degrees of freedom, C is the components, and P is the number of phases. This implied a large upper bound of ordered phases would be seen upon an attempt to synthesize an alloy system with many principal elements [287, 238, 283, 240]. While ordered intermetallic phases are desirable for some systems, such as the precipitation hardening of super alloys [157, 89, 98], the potential for alloy embrittlement makes them a concern for industrial application.

However, early studies done by Cantor showed that when combining a 20-element system, few phases were actually formed, and a FeCrMnNiCo solid solution was created [38]. These solid solutions were originally identified as "High-Entropy Alloys" (HEAs), due to the proposed method of phase stabilization, where an increase in configurational entropy allowed for the free energy of the solid solution phase to dominate over the free energy of any intermetallic structures [276]. Additionally, HEAs were traditionally defined as multi-principal element systems consisting of at least five elements with the concentrations ranging from 5 at.% to 35 at.% [95]. These solid solutions consist of a random assortment of the principal elements within the lattice to typically form body-centered or face-centered cubic structures [275].

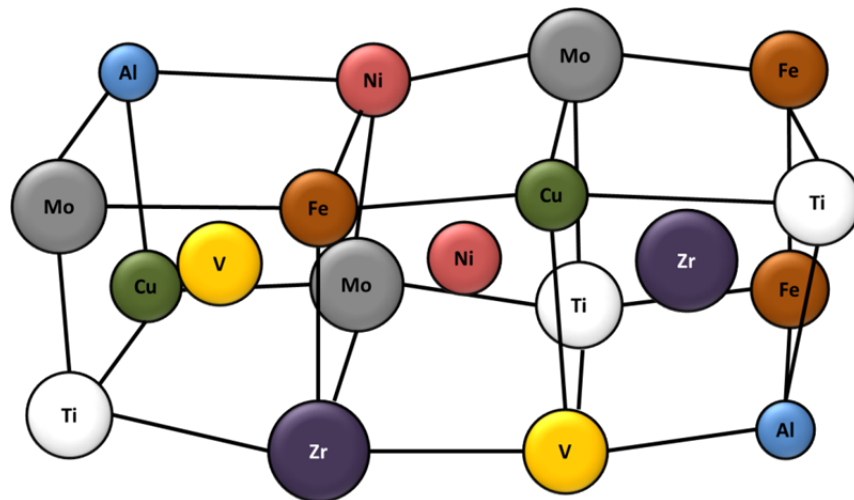


Figure 3.1: Example of a BCC lattice in an $(Al_xCu_yMo_{1-x-y})FeNiTiVZr$ alloy system. The atoms are randomly assorted within the crystal alloy.

On a functional level, these materials have been proposed to exhibit many desirable physical properties from the "cocktail effect." This is a colloquial term for the expression of desirable alloy properties as a result of the combination of elements within it [197]. These properties include increased hardness, compressibility, and microstructural stability, sluggish diffusion rates, and low density [92, 106, 133, 254, 243, 241, 279]. Furthermore, at high temperatures they have been theorized to retain properties such as high yield strength, elasticity, and corrosion resistance [71, 93, 94, 239]. Many of these properties match up favorably to desired strengths of gas turbine blades, where failure can result in damage seen in Figure [198].

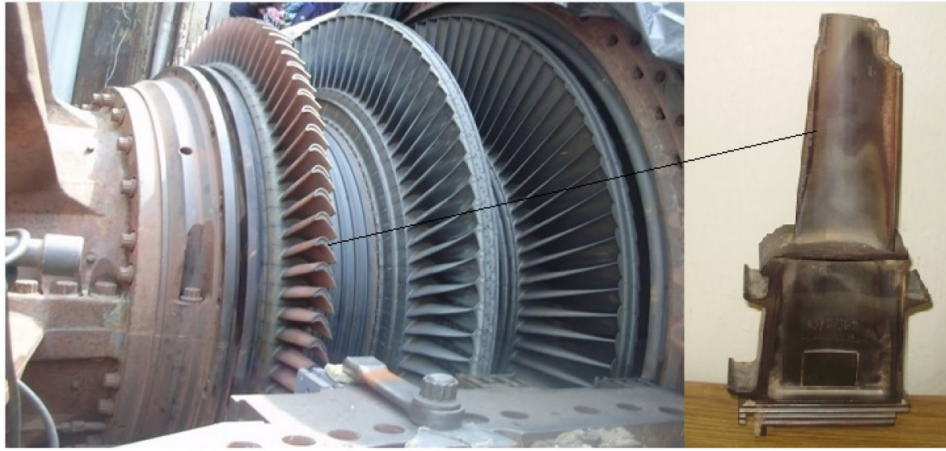


Figure 3.2: (Left)An internal view of a gas turbine. (Right)A first stage gas turbine blade with damage around the edges [198].¹

However, MPEAs expand the definition away from single-phase solid solution alloys, driven by configuration entropy and to a broader set of alloys consisting of multiple major constituent elements. When considering the utility of MPEAs and

¹Image reprinted from S. Rani, A.K. Agrawal, V. Rastogi, (2017). Failure analysis of a first stage IN738 gas turbine blade tip cracking in a thermal power plant. Case Studies in Engineering Failure Analysis, 8, 1-10, with permission from ©(2017) Elsevier. See Figure F.7 for copyright permission.

HEAs, they present a new avenue for alloy discovery by presenting a broader search scope for scientific study [159].

3.1.1 PHASE STABILIZATION OF MPEAS

During the early stages of MPEA study, there was a range of hypotheses on why single phase solid solutions arose from these multi-metal mixtures. Two of the most predominant explanations were the originally proposed entropy driving mechanisms of HEAs and the mutual solubility of the constituents within a common structure. The traditional entropy driven argument claims that configurational entropy was the driving factor toward the phase stabilization of the material [275, 132]. The free energy of mixing can be determined via the following equations:

$$\Delta S_{mix} = \Delta S_{conf} = -R \sum_i^j c_i \ln(c_i) \quad (3.2)$$

$$\Delta H_{mix} = 4 \sum_{\substack{i=1 \\ i \neq j}}^n H_{ij}^{mix} c_i c_j \quad (3.3)$$

$$T_m = \sum_i^n c_i (T_m)_i \quad (3.4)$$

$$\Delta G_{ss} = \Delta H_{mix} - T_m \Delta S_{mix} \quad (3.5)$$

Where R is the gas constant ($\text{J}\cdot\text{K}^{-1}\cdot\text{mol}^{-1}$), c_i and c_j are the atomic fractions of the principal elements, H_{ij}^{mix} is the binary mixing enthalpy of the i^{th} and j^{th} constituent elements ($\text{J}\cdot\text{mol}^{-1}$), and T_m is the melting temperature of the alloy based off the rule of mixtures (K) [132, 272, 158, 112]. The binary mixing enthalpies were calculated by using the Miedema model, which is a "semi-empirical approach" for calculating heats of formation of alloys [155]. Using this thermodynamic framework, a tabulated list of binary enthalpies of formations have been calculated thanks to Takeuchi *et al.* [232] Based off these calculations, increasing the number of elements within the system would provide higher probabilities for the stabilization of a solid solution.

Similarly related to the metal alloy development, Rost *et al.* utilized thermodynamic models and a multicomponent oxide system to determine that entropic effects and configurational disorder were dominant in the stabilization of oxide systems, which provides a new axis for determining stabilized oxide materials. [202].

However, it has been shown that adding constituent elements, does not guarantee the development of a solid solution. This has been with CoCrFeMnNi destabilization by the addition of elements (such as Ge and Cu) or the substitution of elements (such as V for Fe) [38, 182]. Therefore, work has been done that considers mutual solubility of the constituents into a common crystal structure as a possible driver for phase stabilization [132]. Zhang *et al.* hypothesized that immiscibility between binary mixtures in the alloy contributes to secondary phase formation. They utilized CALculation of PHase Diagrams (CALPHAD) in order to calculate the binary phase diagrams of the destabilized alloys [281, 108]. It was discovered that in the CoCr-FeMnNi system, the binary element pairs maintained a mutual FCC crystal structure. However, calculations also showed that the introduction the addition or substitution of elements caused secondary phases, due to a miscibility gap between new binary pairs within the system.

Unfortunately, CALPHAD calculations are an extrapolation of existing phase diagrams, which can result in inaccurate predictions when utilizing incomplete phased diagrams. Additionally, the calculations are performed at equilibrium conditions, which does not account for metastable phases or the effects of sample processing. These constraints are particularly difficult due to the metastable nature of the solid solution alloys at low temperatures [21], which implies that secondary phase formation is possible if sample quench rates are too low. This can complicate comparisons between alloys of varying constituents and processing techniques. Therefore, in order to determine the driving factor of phase stability, simultaneous probing of entropic and solubility effects is required at identical synthesis and processing conditions.

The thermodynamic entropic model describes the driving mechanism of single phase solid solution formation as an increase in configurational entropy. This pushes the Gibbs free energy of mixing to be lower than the Gibbs free energy of intermetallic formation. It was initially proposed by Yeh *et al.* has been expounded upon by Yang *et al.* [272]. A common factor that is discussed during the formation of a solid solution is the energetic ratio, Ω , which seen in the following equation:

$$\Omega = \frac{T_m \Delta S_{mix}}{|\Delta H_{mix}|} \quad (3.6)$$

where T_m is the alloy melting temperature (K), ΔS_{mix} is the change in mixing entropy ($\text{J}\cdot\text{K}^{-1}\cdot\text{mol}^{-1}$), and $|\Delta H_{mix}|$ is the change in mixing enthalpy ($\text{J}\cdot\text{mol}^{-1}$). Calculations for alloy melting temperature, mixing entropy, and mixing enthalpy are seen in Equations 3.4, 3.2, and 3.3 respectively. A solid solution phase is considered favorable to form when the Ω is greater than or equal to 1.1, which is when the entropic effects on Gibbs free energy dominate over the enthalpic contribution [272, 113].

Another factor that has been considered is the disparity between atomic sizes of the components. A large difference can cause significant lattice distortion in the alloy, which increases strain. However, it has also been theorized that the variation in size contributes toward sluggish diffusion [283]. Atomic size difference, δ , is calculated with the following equations:

$$\delta = \left(\sqrt{\sum_{i=1}^n c_i \left(1 - \frac{r_i}{\bar{r}}\right)^2} \right) \times 100\% \quad (3.7)$$

$$\bar{r} = \sum_{i=1}^n c_i r_i \quad (3.8)$$

where c_i is the atomic percentage of the i^{th} element out of n constituent elements and r_i is the atomic radius taken from Kittel [115]. A δ less than 6.6% has been used as an arbitrary limit for solid solution formation, based on previous empirical data. The atomic size difference is a heuristic taken from the Hume-Rothery rules for substi-

tutional solid solution formation [97, 162]. Additional rules include the constituents having similar electronegativities, valencies, and crystal structures. However, these rules are only accurate (with a 90% accuracy) at predicting poor solubility [285, 155]. The combination of Ω and δ provide a set of criteria toward the selection of a solid solution. However, many compositions fulfill both criteria for solid solution formation, yet precipitate ordered structures [272, 113, 159]. Thus, there must be an additional criterion for the development of an alloy phase.

Ensuring mutual solubility between constituents is an additional approach toward understanding the stabilization mechanisms of the solid solution phase. This hypothesis is based off of calculation of phase diagrams (CALPHAD) models done by Zhang *et al.*, where phase diagrams of failed alloy systems were calculated [281]. When modeling the CoCrFeMnNi system, which had a base FCC structure, and adding elements (such as Ge or Cu) or substituting elements (such as V for Fe), the calculated phase diagrams showed miscibility gaps in the or predicted insolubility. This implies that maintaining solubility between binary pairs in a system can lower the chance for phase destabilization. CALPHAD calculations are a thermodynamic model, but this hypothesis introduces a new parameter in order to explain observed secondary phase phenomena in various alloys. To determine if this parameter is consistent, a new alloy system needs to be systematically probed that can take into account entropy and solubility.

$(Al_xCu_yMo_{1-x-y})FeNiTiVZr$ is selected as a model system for the simultaneous probing of the entropic effects and mutual solubility. This is because it fulfills both criteria for the formation of a single phase solid solution. The alloy is generated from a combination of AlFeNiTiVZr, CuFeNiTiVZr, and MoFeNiTiVZr alloys. These materials were selected because the individual systems have been observed as MPEA, and they share 5 common elements between each other [275]. The combined system contains enough elements to fulfill the classic entropic definition of an MPEA, while it

both passes and fails the mutual solubility heuristic described above. A binary alloy of Al and Cu form a face-centered cubic (FCC) structure, while an Al and Mo alloy forms a body-centered cubic (BCC) structure. The Cu-Mo binary are immiscible within one another. Additionally, pairings of the common elements (FeNiTiVZr) can form BCC, ordered B2 phases, or closed packed structures [147, 148, 149]. This is seen in Appendix A with Table A.1. These properties allow the $(Al_xCu_yMo_{1-x-y})FeNiTiVZr$ to act as a reasonable model to perform high-throughput experimentation (HTE) that simultaneously examines the effects of entropy and miscibility in phase stabilization.

The large parameter space of the $(Al_xCu_yMo_{1-x-y})FeNiTiVZr$ makes high-throughput experimental (HTE) methodology a prime candidate for the exploration of the system. It is an established methodology for alloys with less constituents as described in Subsection 1.2. An increase in the multidimensional space from the number of constituent elements in an MPEA is a straightforward addition to synthesis and characterization techniques used in HTE. Additionally, continuous composition spread (CCS) libraries are also an optimal means of synthesizing and screening a large number of compositions, while providing a means to assess any phase changes caused by variations to the stabilization criteria.

3.2 EXPERIMENTAL METHODOLOGY

3.2.1 CONTINUOUS COMPOSITION SPREAD LIBRARY SYNTHESIS AND VERIFICATION

Section 2.1 discusses the standard methodology for synthesis of CCS libraries. Films were deposited by co-sputtering AlFeNiTiVZr, CuFeNiTiVZr, and MoFeNiTiVZr alloy targets of 99% purity on single crystal 7.62 cm diameter Si substrates. The resulting deposition generates an eight element "pseudoternary" CCS. A pseudoternary phase diagram takes a higher order composition space (with dimensions 4 or greater) and condenses the data down to a three dimensional space by restricting compositional changes to three elements. Two sample libraries were synthesized. One library

consisted of each target receiving 150 W of sputter gun power and is designated as a "high power" (HP) sample. While the other library had each target receive 50 W of power and has been labeled as a "low power" (LP) sample. The different sputtering powers were used in order to observe effects of processing energetics. All targets were sputtered using radio frequency (RF) modulation magnetron sputtering. Both samples were synthesized at an 0.667 Pa Ar environment at room temperature. Deposition rates were determined by synthesizing a calibration sample of each individual target material at each synthesis condition and then measuring the thickness profile using a Tencor Alpha-Step 200 profilometer. The thickness data was then used in conjunction with an in house sputter model to approximate synthesis time [34]. The HP sample was sputtered for 48 minutes and had an average film thickness of 300 nm, while the LP sample was sputtered for 345 minutes and had an average film thickness of 500 nm.

Elemental composition predictions were confirmed using wavelength dispersive X-ray spectroscopy (WDS). The procedure was performed on 177 points across the library using pure metal standards. Due to peak spectral overlap between Ti and V, a correction procedure was utilized. The maximum standard deviation of the experiment was 0.10 at.%. From the WDS data, compositions were correlated to spacial points on the sample and then used to construct the pseudoternary phase diagram.

3.2.2 *IN SITU* INTERMEDIATE TEMPERATURE DIFFRACTION STUDIES

The *in situ* diffraction studies were performed at the 1-5 beamline at SLAC has been described in Section 2.2 and the experimental set up is seen in Figure 2.8 [74]. Each sample was mounted onto the x-y translation stage that had been equipped with a substrate heater. A Kapton dome was placed over the sample to control the environment. The stage was aligned with the X-ray source to have an incident

angle of 8° (grazing incidence). The X-ray source energy was 15 keV (0.8266 \AA). The samples were scanned at room temperature across an evenly spaced grid of 107 points in series. Afterwards the samples were heated in air and allowed to equilibrate for 15 minutes before the next set of measurements. Heated measurements were taken at 438, 598, 733 K for the LP library, while the HP library had measurements taken at 513 and 733 K. Each scan took approximately 75 minutes to complete, including time to ramp and equilibrate. This additional annealing time may be attributed to the fact that oxidation occurred in the LP library and not the HP library.

In order to analyze the 2D area diffractograms, a calibration was performed using a LaB_6 standard. The diffractograms were then processed using the techniques discussed in Section 2.2 and seen in Figure 2.7. The azimuthal integration was done using the Fit2D software package [81, 80]. The 1D diffraction patterns were processed using a cubic spline baseline correction and normalized to the alloy peak. The CombiView clustering analysis package was used to cluster the compositions based off of the phases observed in the diffraction patterns [138].

Additional measurements were taken in regions of high Al concentration, due to phase observations made from the LP and HP sample. New samples were sputtered by applying 150 W RF to the AlFeNiTiVZr target, while the CuFeNiTiVZr and MoFeNiTiVZr were sputtered with 50 W RF. The libraries were deposited at 0.667 Pa Ar on a 7.62 cm diameter Si wafers. Then one sample was annealed in vacuum for 6 hours at 873 K. This was done to coarsen the nanocrystalline MPEA and ensure that the structure was not a metallic glass. The SAXSLAB Ganesha system described in section 2.2 was used to measure the diffraction patterns of this Al-rich library. The measurement was taken at the wide-angle X-ray scattering (WAXS) detector distance, with an incidence angle of 8° and a source wavelength of 1.5418 \AA^{-1} .

3.3 RESULTS AND DISCUSSION

3.3.1 *IN-SITU* PHASE MAPPING OF THE $(\text{Al}_x\text{Cu}_y\text{Mo}_{1-x-y})\text{FeNiTiVZr}$ ALLOY

Two separate $(\text{Al}_x\text{Cu}_y\text{Mo}_{1-x-y})\text{FeNiTiVZr}$ CCS libraries were synthesized to observe differences in the processing effects. Representative diffraction patterns of the observed phases across the samples were seen in Figure 3.3. The as-deposited pattern in Figure 3.3(a) was classified as the single phase MPEA. The broad peak was fitted at 2.91 \AA^{-1} and has been determined to most likely be a single phase solid solution. Unfortunately, the entire data set shows only a single broad, nanocrystalline peak related to the metal alloy, which makes determining the crystal structure difficult to conclude. Based on previous heuristics, it was determined that the alloy is potentially a BCC structure. This is due to the preference of the common constituent elements to form a BCC structure based off their binary alloy structures. Additionally, the valence electron concentration (VEC) is a term used to predict phases based off the Hume-Rothery rule of valency [77]. Based off the compositions measured, the VECs of each library ranged from 5.70 to 6.10, less than the 6.87 cut off for the formation of BCC structures. With this knowledge the d-spacing for the disordered alloy was estimated to be 2.16 \AA with local ordering on the (110) BCC plane. Using calculations based off of Vegard's law, the theoretical d-spacing would be 2.21 \AA . Comparing the experimental value with the theory gives a 2% error.

Different regions of the CCS had patterns with ordered and sharp peaks that were not attributed to the MPEA phase, seen in Figure 3.3(b). These peaks were attributed to an unidentified intermetallic structure, while the structure's presence is important in determining compositional phase regimes, determining the identity of the structure was outside the scope of the study. The stochastic distribution of intermetallic phases in certain regions on the library was likely a result of the non-equilibrium nature of the deposition process, which have quench rates greater than

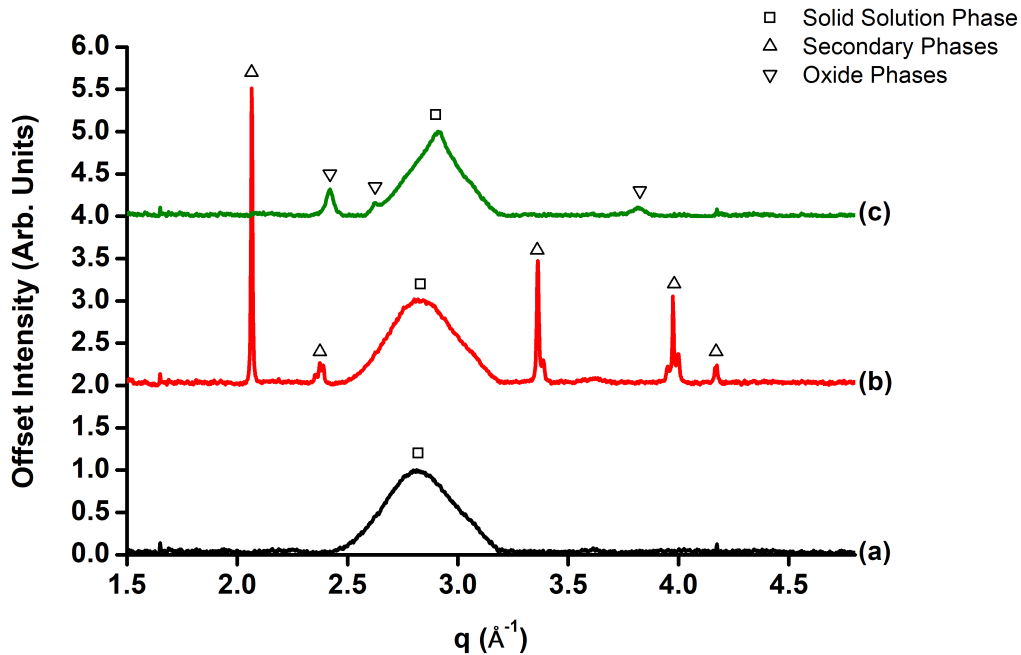


Figure 3.3: Characteristic diffraction patterns seen in the CCS library. (a) The representative pattern of the as deposited library. (b) The pattern for the same composition after annealing at 733 K for 1 hour in air. (c) The pattern for a similar composition in the LP library after annealing in air for 1 hour at 733 K. The LP library shows oxidation at the composition, while the HP library shows intermetallic phase formation. The patterns were normalized to the alloy peak at 2.91 \AA^{-1} .

1000 K/s. These intermetallic phases are highly ordered complexes that do not share the same crystal structure as any of their constituent elements. While intermetallic precipitates have been used to strengthen some materials, it has been hypothesized that they can result in sample embrittlement. Traditionally, studies on MPEAs have desired to only see the alloyed phases.

Furthermore, oxidation was seen in the LP CCS library. after annealing in air for over 6 hours. These oxide structures can be seen in Figure 3.3(c), but they have not been indexed. Based off of the Ellingham diagram for oxides, Ti, Zr, and Al are potentially oxidizing [209]. However, due to the large number of elements it is likely that they are forming mixed metal oxide structures.

Figures 3.4 and 3.5 show the phase mapping of the pseudoternary phase diagram in relative atomic percentages. Both samples show a significant regions of MPEA formation. However, the differing deposition conditions produce different results after annealing. The as-deposited HP library in Figure 3.4(a) shows secondary phase formations along the Cu-Mo edge of the ternary phase diagram. After annealing the sample at 513 K, Figure 3.4(b) shows that additional secondary phases form along the 50 relative at.% Mo line of the phase diagram. Further annealing at 733 K, as seen in Figure 3.4(c) reveals that the secondary phases dominate the Mo-rich regime, and an intermetallic phase growth begins to form at 37.5 relative at.% Al. These regions of instability imply that a phase boundary formed as the sample was annealing and resulted in a highly unstable phase regime. The exaggeration of the immiscible region as annealing temperature and time increased also suggests some level of metastability for the alloy. This destabilization originates at the Cu-Mo composition edge, which was identified as the binary pairing that has low miscibility between each other. This implies that constituent solubility is a relevant factor for phase stabilization.

Unlike the HP library, the as-deposited LP library in Figure 3.5(a) does not exhibit the same regions of instability that seen on along the Cu-Mo edge. Furthermore, Figure 3.5(b) shows that as the sample library was annealed at 598 K, the alloy phase remained constant throughout the CCS. However, once the library was annealed in air at 733 K, a oxide phases were prevalent throughout the sample, as seen in Figure 3.5(c). There is a region of oxide suppression that corresponds closely to the Al-Mo binary edge. Al and Mo mixtures develop into BCC alloys based on their phase diagram [147]. This common structure corresponds with the assumed $Al_xCu_yMo_{1-x-y}FeNiTiVZr$ BCC structure and hints toward a solubility parameter. Additionally, regions of high Al may suppress oxide formation due to Al oxides performing as excellent passivating oxides. However, $\alpha-Al_2O_3$ does not form unless annealed at temperatures above 1323 K.

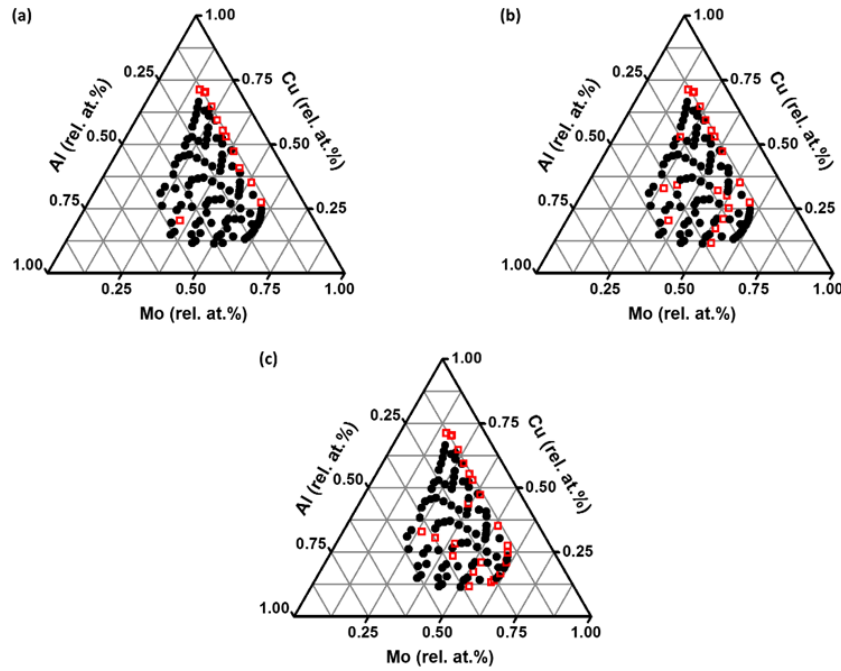


Figure 3.4: HP Pseudoternary phase diagrams. (a) As-deposited CCS. (b) Phase changes after annealing in air at 513 K. (c) Phase changes after annealing in air at 733 K. Black circles represent a solid solution phase. Red open squares represent secondary phase formation.

Differences between the HP and LP samples illustrate the effects of deposition energetics on phase stability. Adjustments in sputtering power not only affects the deposition rates but also the thermodynamic equilibrium. Since the as-deposited LP sample library solely forms an alloy phase, it would imply entropic effects are sufficient to stabilize the alloy. However, the HP library shows secondary phases were deposited along a composition edge, instead of showing the pure alloy phase across the entire wafer. Higher sputtering power supplies additional energy to the surface adatoms, which provides mobility. The adatoms are then able to diffuse and settle into thermodynamically stable intermetallic phases, resulting in the observed secondary phase regions in the HP library [235, 233]. Therefore, the LP adatoms are quenched too rapidly and form a metastable alloy phase. This is evidenced by the destabilizing effect caused by heightened concentrations of Mo in the presence of

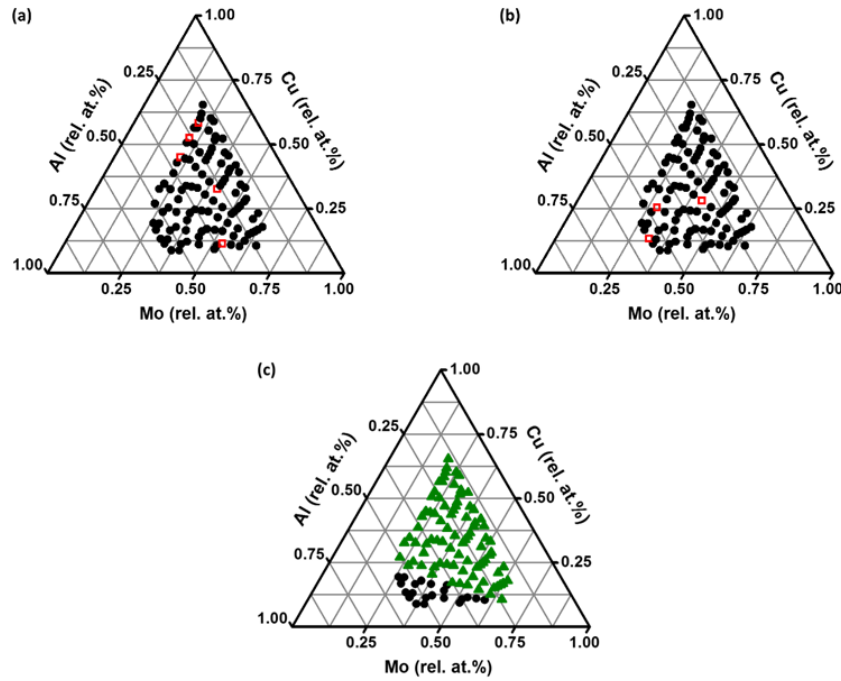


Figure 3.5: LP Pseudoternary phase diagrams. (a) As-deposited CCS. (b) Phase changes after annealing in air at 598 K. (c) Phase changes after annealing in air at 733 K. Black circles represent a solid solution phase. Red open squares represent secondary phase formation. Green triangles represent oxidation.

Cu. This has is consistent with observations made by Zhu *et al.*, where there is a phase destabilization in their AlCoCrCuFeNiMo_y FCC system, due to the insolubility between Cu and Mo [290]. At that composition it is likely more favorable to have intermetallic phases grown, when provided with additional energy.

3.3.2 CHARACTERIZATION OF THE AL-RICH REGION

Additional data was taken at an Al-rich region of the $(\text{Al}_x\text{Cu}_y\text{Mo}_{1-x-y})\text{FeNiTiVZr}$ alloy, phase stability seen in this region from both the HP and LP libraries. This data was taken in order to ensure that the alloy system studied maintained an alloy phase, and a vacuum anneal was performed to ensure that the material was a nanocrystalline alloy structure instead of a metallic glass with low local ordering. Two libraries were deposited with a composition greater than 62.5 relative at.% Al. One remained as-

deposited and the other was vacuum annealed at 873 K for 6 hours. The composition spreads can be seen in Figure 3.6.

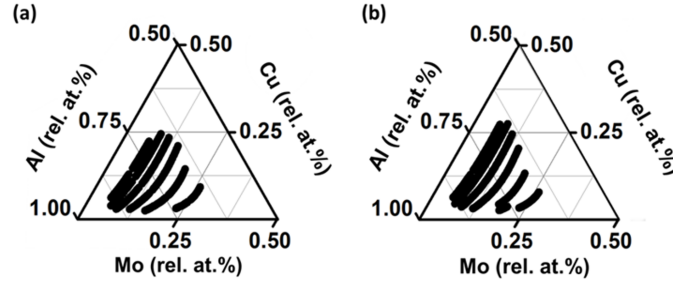


Figure 3.6: Pseudoternary phase diagrams of Al-rich libraries. (a) As-deposited diagram. (b) Vacuum annealed diagram. No intermetallic structures were observed.

Both libraries showed no secondary phase formation, indicating that the destabilizing effects of the Cu-Mo edge had minimal impact at these compositions. The characteristic diffraction of both sample libraries shows coarsening of the MPEA peak, with a full-width half-max (FWHM) change from 0.389 \AA^{-1} in the as-deposited sample to 0.063 \AA^{-1} . Additionally, after the vacuum anneal no secondary peaks formed, supporting the argument that the broad peak is an alloy phase instead of a glass structure.

3.4 CONCLUSIONS

Figure 3.8 shows the application of the solid solution ability energy ratio (Ω) and atomic size difference (δ) to the $(\text{Al}_x\text{Cu}_y\text{Mo}_{1-x-y})\text{FeNiTiVZr}$ alloy. This particular system has an Ω range of approximately 1.05 to 1.61 and a δ between 9.1% and 10.5%. Calculated values for the HP and LP samples can be seen in Appendix A.1 Tables A.2. These values fall outside the numbers suggested by Yang *et al.*, but the system is still able to form a solid solution phase [272]. Furthermore, $(\text{Al}_x\text{Cu}_y\text{Mo}_{1-x-y})\text{FeNiTiVZr}$ system is in a region that would predict intermetallics and metallic glass formation,

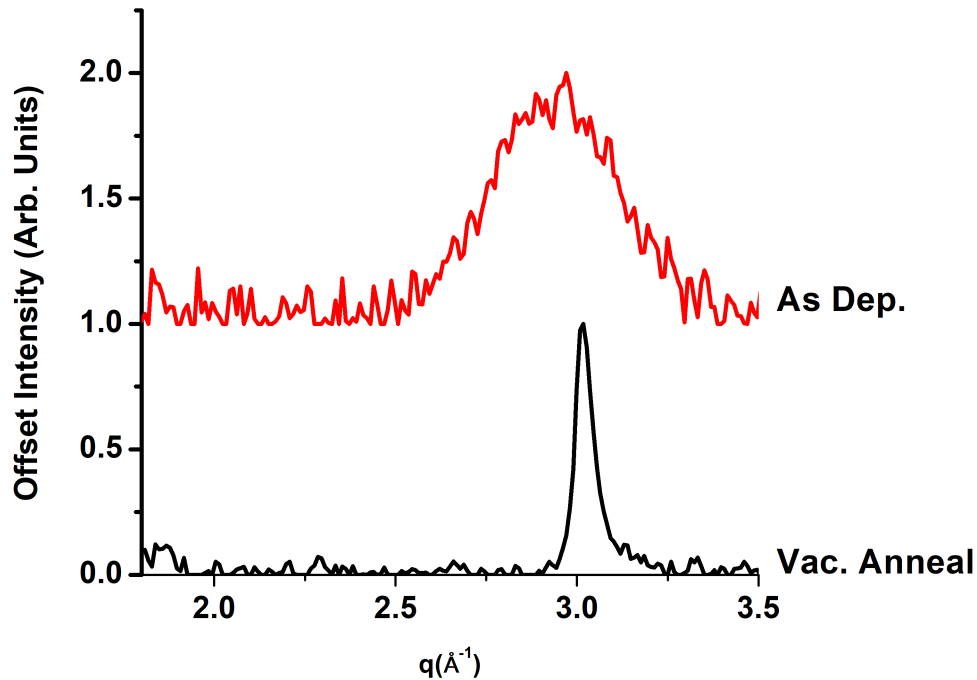


Figure 3.7: The characteristic diffraction patterns of the Al rich spreads. Coarsening of the alloy peak is observed after vacuum annealing the library for 6 hours at 873 K. The lack of additional peaks indicates that the deposited sample is a highly nanocrystalline sample instead of a metallic glass.

but has been shown to be a solid solution. Therefore, additional solubility factors contribute toward predicting phase stabilization outside of Ω and δ .

While, the previous heuristics would indicate that the $(Al_xCu_yMo_{1-x-y})FeNiTiVZr$ sample spread would mostly consist of intermetallic phases, we show that the development of a solid solution phase is possible. Therefore, additional factors outside of entropic effects contribute toward phase stabilization. The traditional MPEA predictive model has dictated alloy synthesis, but additional analysis shows binary solubility contributes greatly to phase destabilization and poor retention after processing. This can be related back to Hume-Rothery solid solution rules, which have previously stated that crystal structures of solute and solvent should be similar. Therefore, it can be said that entropic thermodynamic effects explain the development of an MPEA but mutual solubility is vital for the retention of the solid solution phase.

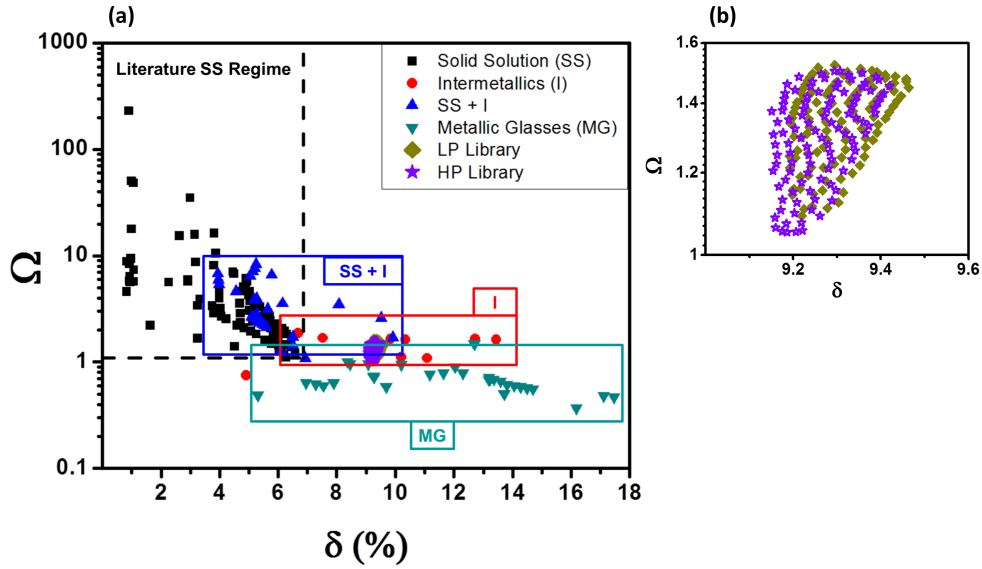


Figure 3.8: (a) A graph of the solid solution formation ability, Ω , versus the atomic size difference, δ of multiple samples in the literature. The $(Al_xCu_yMo_{1-x-y})FeNiTiVZr$ libraries inserted for comparison. (b) The diagram is zoomed in to clearly see the HP and LP libraries. [272]

This study also highlights how integral HTE is toward the discovery of materials in this large composition space. HTE methodologies allowed for systematic and rigorous probing of a large number of samples that have been synthesized and processed in identical manners. Additionally, it provided a means of examining unexplored compositional regions rapidly. These factors remove uncertainties and difficulties of extrapolating data from various other sources that utilizes different synthesis and processing techniques.

The above HTE methodology for alloy discovery provides a path toward utilization of any found alloys in larger scale applications. However, thin-film properties do not necessarily directly correlate to bulk systems. Therefore, investigations into the bulk materials requires additional mechanical and characterization studies of bulk MPEA alloys. If these properties are maintained in a macro-sized material, then studies on the mechanical properties would be an important next step toward applying these alloys in an industrial setting.

Furthermore, new computational modeling methods for predictive alloys can now be applied based off of the new set of heuristics. These would not only be based off of the Hume-Rothery rules of solid solution formation but also the entropic information and mutual solubility conditions. Early interpretations of a database have been implemented but can be further enhanced with the solubility condition [3, 146, 43].

Despite the consistent use of Ω as a way to determine ratio the Gibbs energy of the solid solution, a new energetic ratio has been suggested that accounts for the Gibbs energy of intermetallic formation. Historically, the Gibbs free energy of intermetallic formation (ΔG_{int}) had not been considered when predicting solid solution formation of MPEAs. However, it can be assumed that ΔG_{int} is equivalent to ΔH_{int} due to the lack of configurational entropy in an ordered structure. Φ is a term that is a ratio between the Gibbs energy of these structures and can be seen in the following equation:

$$\Phi = \frac{\Delta G_{ss}}{-|\Delta G_{max}|} \quad (3.9)$$

where ΔG_{ss} is the Gibbs free energy of solid solution formation. ΔG_{max} is the maximum Gibbs energy of intermetallic formation based off the binary pairs in the studied system. If the solid solution Gibbs energy is high enough to overcome the highest possible energy of intermetallic formation of a binary pair, then it would dominate any ordered structure [113]. Future studies should involve the use of Φ in order to increase accuracy of predictions.

CHAPTER 4

OXIDATION AND PHASE DISCOVERY OF A MULTI-PRINCIPAL ELEMENT ALLOY

4.0.1 BACKGROUND AND MOTIVATION

While MPEAs have been hypothesized to have desirable high-temperature properties, there have been a limited number of experiments on applications and oxidation of these materials at temperatures greater than 773 K. Previous studies investigated single sample compositions or over a narrow range of discrete compositions. Gorr *et al.* introduced Ti into an oxidation resistant MoWAlCr base alloy in order to lower the total density of the system [71]. The CoCrFeMnNi system was used as a base for eight compositionally different samples and had their oxidation resistance compared to Ni-based superalloys and austenitic stainless steel [87]. Butler *et al.* oxidized AlCoCrFeNi samples at 1323 K in order to determine structural stability and the development of Al₂O₃ [37].

In these cases, the number of different compositions explored is low, never going above ten compositions. This is due to the application of traditional experimental techniques toward the discovery of new materials. Gorr *et al.* observed a single equiatomic system, while Holcomb *et al.* and Butler *et al.* studied eight and six

Parts of chapter adapted from manuscript submitted for publication: B. Ruiz-Yi, T. Williams, J. K. Bunn, F. Ren, N. Al Hasan, I. Takeuchi, J. R. Hattrick-Simpers, A. Mehta (2020). *Phase stabilization and oxidation of a continuous composition spread multi-principal element (AlFeNiTiVZr)_{1-x}Cr_x alloy.*

samples respectively [71, 87, 37]. While discreet bulk sample measurement is useful in functional studies, determining phase stabilization requires more nuanced approaches due to the narrow atomic percentages where phase boundaries can occur in a phase diagram of the system. Therefore, an approach that can examine a wide set of compositions with rich structural information can provide more insight into phase stability during the oxidation process.

Studies have been limited for the oxidation of multi-principle element alloy (MPEA) systems. Subsection 4.0.1 discusses some of the previous experiments performed on these complex alloys, but it also details limitation of discreet studies in this complex space. Similar to the difficulty of first discovering stable compositions, finding alloys with high-temperature functionality is a non-trivial task.

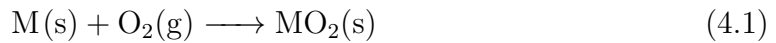
A major application for an oxide resistant alloy is as the bulk material in high temperature applications. Turbine blades coatings typically need to provide a temperature differential of over 873 K to prevent plasticizing or oxidation of the traditional superalloy used as the bulk blade material [49, 187]. MPEAs have been proposed to maintain oxidation resistance and high temperature strength based on the "cocktail effect" [197]. Therefore, discovering new materials in this class of alloys has been an ongoing effort.

However, the traditional approach for discovery of these materials is not feasible for such a large design space. MPEAs as a material class can easily contain over 100 million compositions, which makes discreet analysis extremely inefficient. In order to expedite the discovery process, high-throughput experimental (HTE) methodologies that develop large compositional libraries and utilize rapid characterization techniques are necessary.

This study focused on the oxidation resistance of the $(\text{AlFeNiTiVZr})_{1-x}\text{Cr}_x$ system. HTE techniques provided information on phase formation and oxidation growth as a function of annealing time. This particular system was chosen because AlFeNi-

TiVZr is a known MPEA system and contain Al and Ni, which are known to promote oxidation resistance [275, 154]. The other elements are often used in alloy synthesis for to structurally strengthen the material. However, elements like Zr have been observed readily oxidize and degrade resistance. The introduction of Cr as a dopant into the base AlFeNiTiVZr alloy creates a pseudobinary alloy system.

Cr has been used as a means to promote the development of passivating oxide layers in alloy. Cr_2O_3 itself acts as a passivating oxide layer at temperatures below 1273 K [137]. However, if it is exposed to temperatures above 1273 K or humid environments at temperatures around 873 K, the oxide layer fails, due to high volatility in those environments [278, 15]. While it can fail under certain conditions, the presence of Cr_2O_3 has been shown to promote the growth of $\alpha\text{-Al}_2\text{O}_3$, which is another passivating oxide that is more resilient than Cr_2O_3 at the aforementioned conditions. The $\alpha\text{-Al}_2\text{O}_3$ phase is typically only attainable at temperatures above 1273 K, but when Cr and Cr_2O_3 is present, the temperature needed to form $\alpha\text{-Al}_2\text{O}_3$ can be suppressed all the way down to 573 K [14]. This is because Cr_2O_3 is isomorphic with $\alpha\text{-Al}_2\text{O}_3$ and is able to nucleate growth of the structure [10, 205]. While $\alpha\text{-Al}_2\text{O}_3$ is preferred, the presence of Cr_2O_3 or $\alpha\text{-Al}_2\text{O}_3$ is desirable once the $(\text{AlFeNiTiVZr})_{1-x}\text{Cr}_x$ is oxidized.



In order for a metal oxide to form, as seen in Equation 4.1, the chemical potential of the oxygen in the atmosphere is greater than the equilibrium partial pressure of oxygen with the oxide [110, 216]. Thermodynamically, the standard Gibbs free energy of oxide formation, ΔG° , can be determined by the following equation:

$$\Delta G^\circ = -RT \ln K = -RT \ln \frac{a_{\text{MO}_2}}{a_{\text{M}} \cdot p_{\text{O}_2}} \quad (4.2)$$

where K is the equilibrium constant, a_{MO_2} and a_{M} are the activities of the oxide and metals respectively, and p_{O_2} is the partial pressure of oxygen gas. In an ideal

scenario, the ratio of the activities can be taken as unity. From the resulting idealized equation, the Ellingham diagrams are constructed for oxidation [209].

However, the growth of a passivating oxide is also a highly kinetic process, which is not explicit from the energetic calculations. Slow kinetics can delay the formation of an oxide, despite the thermodynamics stating otherwise. A major type of kinetic equation for the development of a passivating oxide is related to the parabolic law:

$$\frac{dx}{dt} = \frac{K_p}{x} \quad (4.3)$$

$$x^2 = 2K_p t + C \quad (4.4)$$

where x is the thickness of the oxide, t is the time, and K_p is the parabolic rate constant [131, 206]. As the oxide becomes thicker, the rate of oxidation decreases, which is preferable for a passivating layer. Furthermore, diffusion within the alloy can contribute toward oxidation limitations. Figure 4.1 shows a simple schematic illustrating the oxidation of a material.

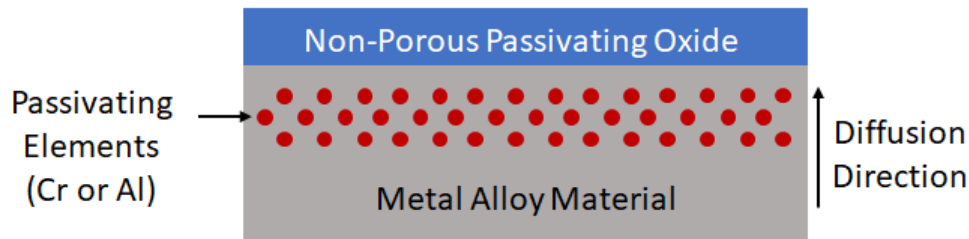


Figure 4.1: A representation of passivating oxide development. Near-surface elements that are thermodynamically favorable to be oxidized diffuse to the surface and develop a non-porous layer that prevents further oxidation of the bulk.

4.1 EXPERIMENTAL METHODOLOGY

4.1.1 CONTINUOUS COMPOSITION SPREAD SYNTHESIS AND POST-PROCESSING

Section 2.1 discusses the standard methodology for synthesis of continuous composition spread (CCS) libraries. Physical vapor deposition via magnetron sputtering was

used to co-sputter a CCS sample library using a 99% pure AlFeNiTiVZr alloy and Cr targets on a 7.62 cm Si wafer. This resulted in the $(\text{AlFeNiTiVZr})_{1-x}\text{Cr}_x$ "pseudobinary" system. Similar to the pseudoternary system described in Chapter 3, the pseudobinary system is one where the higher order compositional space is reduced down to a two dimensional space where the variation in composition is between two constituents. In this case the AlFeNiTiVZr acts as a single constituent along with the Cr. Before library synthesis, calibration depositions were performed in order to determine deposition rates of each target at the synthesis conditions. The AlFeNiTiVZr target was sputtered using a radio frequency (RF) sputter source with 150 W of power applied, while the Cr target was sputtered with 15 W from a direct current (DC) source. Both depositions were done in 0.667 Pa Ar. The calibration samples had their thickness measured using a Tencor Alpha-Step 200 profilometer, and the resulting thickness data was used in conjunction with the in-house sputter model to determine the deposition time and approximate the composition spread [34]. Afterward the CCS library was synthesized by co-deposition of the AlFeNiTiVZr and Cr targets for 60 minutes at the aforementioned conditions. The resulting average film thickness was 100 nm. For the post-processed libraries, the film was annealed in vacuum for 6 hours at 873 K. The composition stoichiometry was verified using wavelength dispersive X-ray spectroscopy (WDS) measurements across 45 points along the pseudobinary space using pure metal standards for calibration.

Post-annealing in an oxidizing environment was performed in order to determine regions of oxidation resistance across the CCS. Five libraries were synthesized and vacuum annealed under the same conditions as mentioned above. The samples were separately placed into a furnace that was preheated to 873 K in an air environment and annealed for 1, 3, 6, 12, and 18 hours. The samples were then removed from the furnace and cooled in a room temperature environment.

4.1.2 *EX SITU* SYNCHROTRON DIFFRACTION STUDIES

Ex situ X-ray diffraction (XRD) studies were performed at the 1-5 beamline of SLAC [74]. The experimental set up has been described in Section 2.2 and seen in Figure 2.8. The CCS sample libraries were mounted onto an x-y transnational stage, which was aligned with the source at a incidence angle of 6° . The X-ray source energy was 12.7 keV (0.9762 Å). The samples were scanned at room temperature, in series, across an evenly spaced grid of 441 points. Sample to detector distance and sample angle was calibrated using a LaB₆ standard. The 2-D diffractograms were converted into 1D patterns by an azimuthal integration using an "on-the-fly data assessment" Python script by Ren *et al.* [200]. This script was designed to process high-throughput quantities of diffractogram data. The 1D patterns were baseline reduced using a cubic spline, and the CombiView clustering analysis package was used to determine phase regions across the binary [138].

4.1.3 *EX SITU* RAMAN SPECTROSCOPY MAPPING

Raman spectroscopy was performed using the Horiba XploraPLUS Raman microscope described in Section 2.3. The excitation source was a 25 mW, 473 nm blue solid state laser. Additionally, the 30 mW, 638 red diode laser was used to ensure no fluorescence was observed by the using blue source. The 2400 lines/mm grating was to separate the Raman light, and a 20x objective (numerical aperture (NA) = 0.40 working distance (WD) = 12 mm) was used to focus the source. The spot size was approximately 1.44 μm . Measurements were captured using a thermoelectrically air cooled Syncerity charged couple device (CCD) detector. Raman spectra were taken over a 5 second acquisition time and averaged with 3 spectral accumulations. Sample measurements were taken in serial using an x-y motorized stage programmed to move at 0.4 mm intervals over a total of 191 points. The change in composition of each point was approximately 0.2 at.% Cr.

4.2 RESULTS AND DISCUSSION

4.2.1 CHARACTERIZATION OF THE PSEUDOBINARY CCS VIA DIFFRACTION

The thin film CCS libraries were synthesized and processed in order to determine the phase dynamics and oxidation behaviors of a $(\text{AlFeNiTiVZr})_{1-x}\text{Cr}_x$ composition. The $(\text{AlFeNiTiVZr})_{1-x}\text{Cr}_x$ pseudobinary composition resulted with an x between 0.064 and 0.357. A phase boundary was optically observed at all oxidation annealing times, as seen in Figure 4.2, where variation in color is indicative of two separate phases. This is due to differing refractive indices, which is a result of different oxide phases on the surface. Therefore, there is strong evidence that the increase in Cr at.% results in phase change. The region with a lower Cr content was labeled as R_1 and the higher Cr content was labeled R_2 .

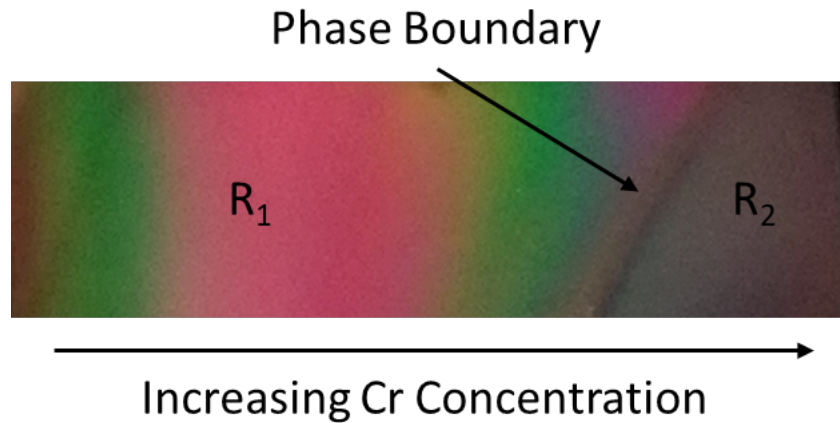


Figure 4.2: The optical image of the pseudobinary CCS. A visible phase boundary is seen that separates the composition spread into two regions, R_1 and R_2 .

Ex situ synchrotron measurements were taken over 441 evenly spaced points along the entire CCS sample wafer. After initial analysis of the 441 diffraction patterns, the total number of examined patterns was narrowed down to 23 that were specifically along the pseudo-binary spread. Figure 4.3 displays a waterfall plot of each the diffraction patterns of all sample libraries with respect to the Cr content. The

as-deposited film (Figure 4.3a). shows two broad peaks that have typically been associated with bulk metallic glass materials, but the patterns can also be attributed to highly polycrystalline structure that has short range ordering. After annealing the grains coarsen into ordered structures seen, which can be seen in the additional plots. Figure 4.3(b) is a plot of the vacuum annealed sample library, and it shows that structure of material is identical across all observed compositions, with some variations in the intensity ratio of the main peak at 3.04 \AA^{-1} . There are some slight variations in the peak positions, which indicates minor changes with the lattice. However, this is consistent with variations in composition and are not indicative of any full phase change. Bragg's law and d-spacing calculations were performed in order to determine the structure and spacing of the vacuum annealed composition. The results revealed that the crystal structure was a BCC solid solution with a lattice parameter of 2.92 \AA [54]. Compared to the theoretical Vegard's law calculations, the lattice constant would fall between 3.25 and 3.14 \AA , based on the material's composition [215]. This results in an error of 7% between the measured and theoretical values, but Vegard's law is also a heuristic estimate and will not always be in full agreement [114]. Furthermore, the calculated BCC crystal structure is consistent with the valence electron concentration (VEC) heuristic. A VEC that is less than 6.87 indicates that a BCC solid solution is more favorable to form, while a system that has a VEC that is greater than 8.0 prefers an FCC structure. Values in between result in a mixed structure [77]. The VEC of $(\text{AlFeNiTiVZr})_{1-x}\text{Cr}_x$ falls within 5.79 and 5.69 depending on the pseudo-binary compositions, which places the material firmly in the BCC range.

Figures 4.3(c-f) show a progression of oxidation in air at 873 K as a function of time. After 1-hour of oxidation, seen in Figures 4.3(c), there is a clear phase transition between 23.6 and 25.4 at.% Cr, which arises from the formation of low Q-space peaks. The phase transition provides additional evidence toward the optical boundary

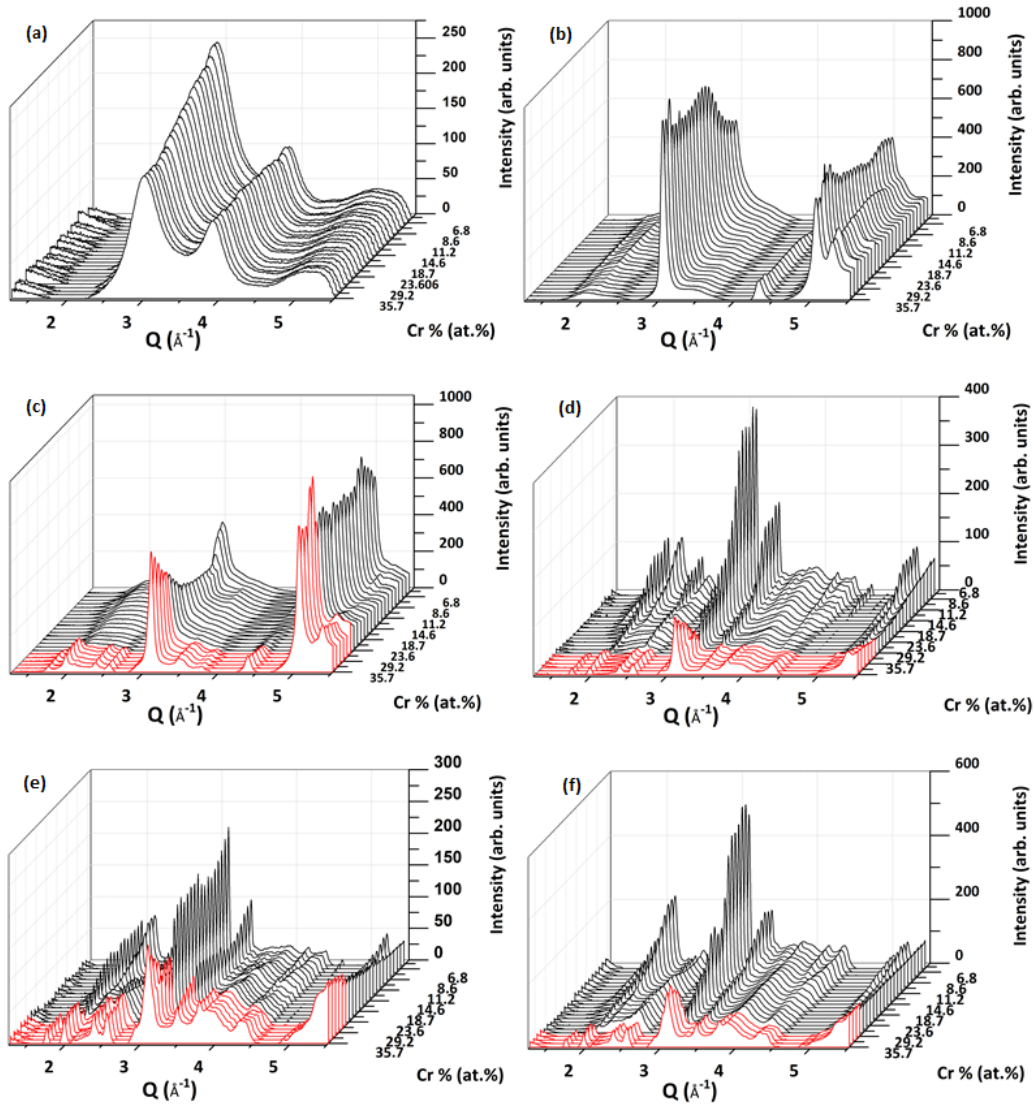


Figure 4.3: Waterfall plots of each samples diffraction patterns across the compositional spread with respect to Cr at.%. Each oxidized sample was also vacuum annealed for 6 hours at 873 K. (a) As-deposited, (b) Vacuum annealed, (c) 1-Hour oxidation, (d) 3-Hour oxidation. (e) 6-Hour oxidation, and (f) 18-Hour oxidation. The black patterns in the oxidized samples correspond with the R_1 phase, while the red patterns are associated with the R_2 phase.

representing different phases in Figure 4.2. Therefore, the diffraction patterns on the different sides of the boundary can be linked to the R_1 and R_2 regions. As the sample is annealed further, we can different oxide phases form. However, Figure 4.3(f) shows that the phase boundary has shifted to between 27.3 and 29.2 at.% Cr, which indicates

that the R_1 phase shifts towards regions of higher Cr as anneal time increases. This could indicate that R_2 is a metastable phase.

The characteristic diffraction patterns associated with extreme end of each phase region can be seen in Figure 4.4. Figure 4.4(a) shows the representative patterns of the R_1 phase region (6.4 at.% Cr), while Figure 4.4(b) contains patterns that represent compositions in the R_2 region (35.7 at.% Cr). After the 6-hour vacuum anneal, the BCC crystal structure is readily apparent in both phases. Both graphs show the Si (311) substrate peak only with the vacuum annealed library and 1 hour oxidized library. This is due to slight variations in the synchrotron tilt angles as a result of measurements taken on different days.

Analysis starting with the R_1 phase (Figure 4.4(a)) shows that after 3 hours of oxidation, the BCC MPEA structure has fully destabilized. The Ellingham diagram for oxide formation shows Zr, Al, and Ti as likely candidates for the formation of oxides, with Ni and Fe closely following [209]. However, the peaks at 1.45, 1.75, and 2.05 \AA^{-1} can be attributed to multiple oxide phases (ZrO_2 PDF# 88-2390, TiO_2 PDF# 78-2486, 75-1582, 88-1174). Since the library deposition was on a silicon substrate, silicides must be considered as possible candidates for indexing. In particular, a cubic FeSi structure fits very well with peaks in the R_1 phase (FeSi PDF# 76-1748). Notably FeSi is not present during the vacuum anneal and only forms after oxidation. This could indicate that oxidation provides a nucleation point for the formation of FeSi, or the sample was not annealed long enough for FeSi to form.

The R_2 phase, seen in 4.4(b), shows different oxide structures. In particular, the oxide formed is proposed to be an eskolaite (Cr_2O_3 PDF# 74-0326), which is a trigonal form of Cr_2O_3 . While the eskolaite appears to continuously grow with anneal time, no Al_2O_3 structures were visible in the diffraction patterns (Al_2O_3 PDF# 83-2080). There were also two unidentified peaks within the region at 1.96 and 3.01 \AA^{-1} . These may correspond to mix metal oxides but require further analysis to

verify their identity. Outside of the unknown peaks, it appears that Cr_2O_3 prevented the formation of other oxide species on the surface, while preserving the BCC MPEA. Furthermore, the R_2 does not show the FeSi structure at any time during oxidation. This is potentially due to the oxide structures grown in the R_2 region not providing nucleation sites for the growth of FeSi, or a reduction of the Fe at.% relative to the increase Cr at.%, which supports the lack of anneal time during vacuum, in the R_1 region.

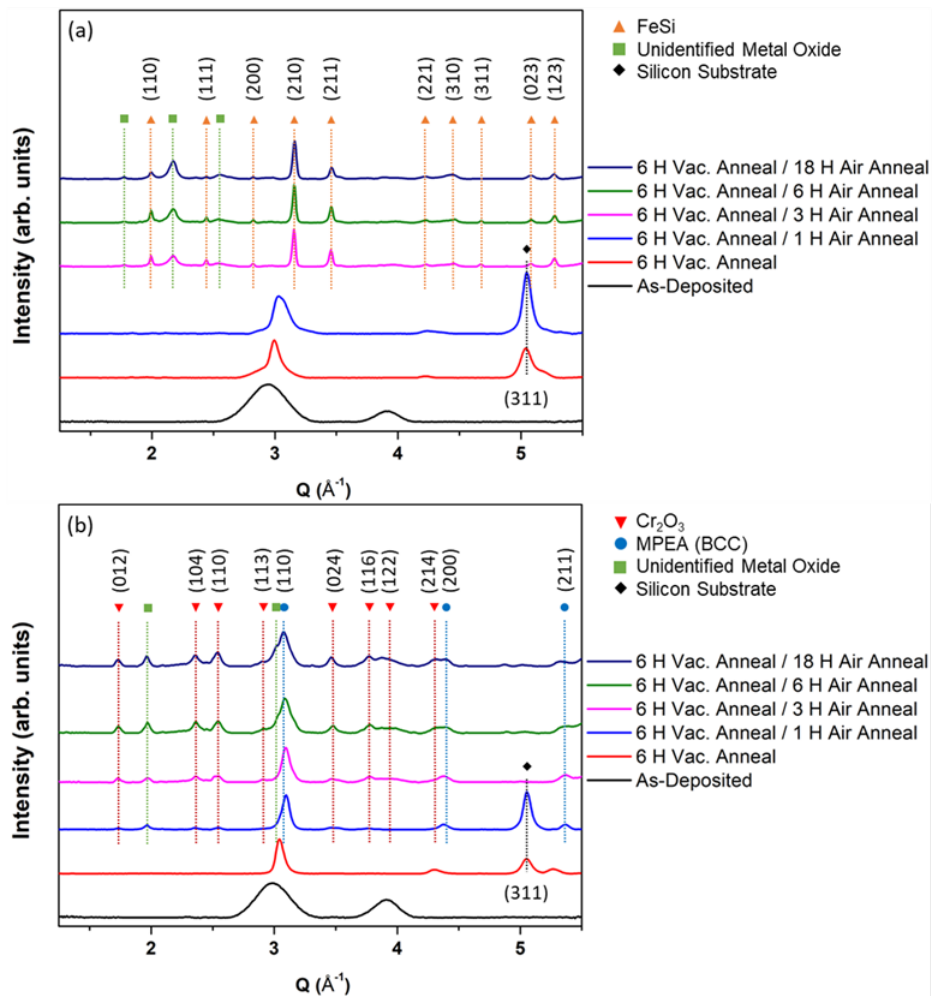


Figure 4.4: The peak analysis and indexing of the R_1 and R_2 phase regions. (a) Diffraction patterns measured at 6.4 at.% Cr (R_1). The patterns show an unknown oxide formation along with the growth of a FeSi structure at all oxidation anneals above one hour. (b) Diffraction patterns measured at 35.7 at.% Cr (R_2). The major oxide phase grown was identified as a trigonal Cr_2O_3 .

4.2.2 OXIDE IDENTIFICATION VIA RAMAN SPECTROSCOPY

Phase mapping via Raman spectroscopy was performed as an additional characterization technique to identify the oxide structures. The mapping was performed in a 1D line corresponding to the change in Cr concentration in the library. Figure 4.5 shows the spectra of the R_1 and R_2 regions after the 1-hour oxidation. A literature search based off the possible oxide constituents and FeSi was performed. FeSi was observable in the diffraction data, and the Raman modes are associated with the A(212 and 392 cm^{-1}), E (225 and 353 cm^{-1}), and T (224, 255, 332, 384, and 464 cm^{-1}) symmetries [192, 193]. However, the modes are not visible in Figure 4.5(a), which indicates that FeSi is at the interface between the sputtered film and the substrate. Many different oxide bands were gathered when considering oxide formation. Al_2O_3 has two major polymorphs α and γ . The γ polymorph has no visible Raman bands [8, 120, 166]. However, α - Al_2O_3 has seven known Raman active bands corresponding to A_{1g} and E_g modes. These bands are located at 378, 418, 432, 451, 578, 648, and 755 cm^{-1} [8, 160, 120]. CrO_2 has four Raman modes at 149 cm^{-1} (B_{1g}), 458 cm^{-1} (E_g), 570 cm^{-1} (A_{1g}), and 682 cm^{-1} (B_{2g}) [99]. Additionally, there it has been reported to have a band at 633 cm^{-1} , but it can be considered a convolution of the A_{1g} and B_{2g} modes [227]. Other Cr oxides have also been studied, such as Cr_8O_{21} , which is an intermediate between CrO_3 and Cr_2O_3 and has been reported to have a band at 838 cm^{-1} [227, 100]. Cr_2O_3 was observed in the XRD, and the bands for Cr_2O_3 are visible at 307, 350, 550, and 614 cm^{-1} [82, 19]. CrO_3 bands have been reported at 300, 400, 600, 760, 880, 935, and 1005 cm^{-1} [248]. For Ti based oxides, rutile TiO_2 has Raman modes at 142, 195, 395, 515, and 637 cm^{-1} . The anatase polymorph of TiO_2 only has the single band at 614 cm^{-1} [230]. A major V oxide is V_2O_5 , which has a single band at 992 cm^{-1} . This band can shift to 1040 cm^{-1} when the oxide is supported on SiO_2 [164, 264]. Fe has many different oxide structures, which include FeO, α - Fe_2O_3 , γ - Fe_2O_3 , and Fe_3O_4 . Most of the bands associated with these Fe oxide

structures lie near 250 and 630 cm^{-1} [139]. The Ni-O stretch has been measured at 505 cm^{-1} [129]. Zr oxides are typically seen at 267 and 644 cm^{-1} [17]. Outside of single metal oxides, there were possible mixed metal oxides to consider. Chromites and ferrites, such as FeCr_2O_4 , NiCr_2O_4 , and NiFe_2O_4 have been shown to have the A_{1g} band at 650 and 750 cm^{-1} [88]. Additionally, certain spinels, such as $\text{FeCr}_{3-x}\text{O}_4$ and $\text{NiFe}_x\text{Cr}_{2-x}\text{O}_4$ have been shown to have bands at the same locations [88].

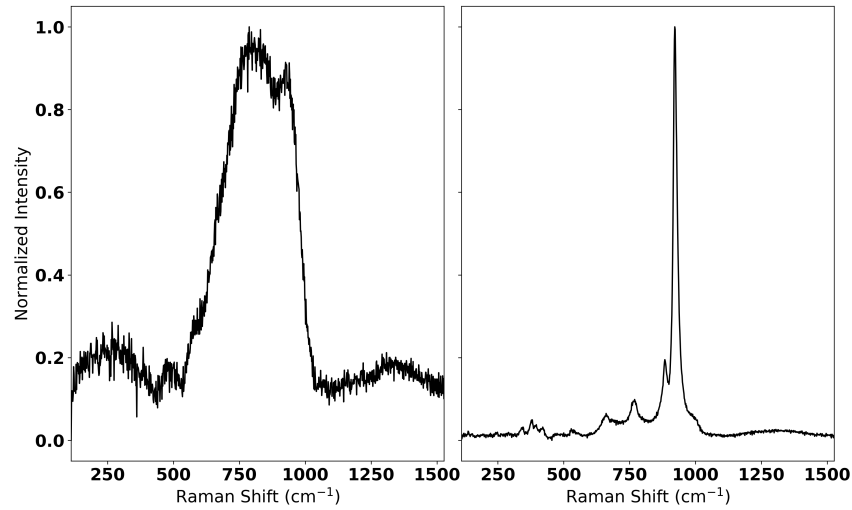


Figure 4.5: Raman spectra of the 1-hour oxidized sample. (a) R_1 phase (b) R_2 phase. Oxidation is apparent in both regimes, but differentiation is easier in the R_2 region.

After exhausting the vast potential oxides through a literature search, it became clear that labeling the bands was a difficult proposition. Many of the oxide bands overlap between structures, which makes it nearly impossible to distinguish what oxides are forming via Raman spectroscopy. Figure 4.5(a) is a broad convolution of these bands. Furthermore, Figure 4.5(b) does not readily show the known Cr_2O_3 , despite the observations in the XRD. Therefore, the previously indexed eskolaite may be a similarly sized trigonal mixed metal oxide that inherited passivating properties from Cr_2O_3 . While exact identification of peaks is not possible at the moment, mapping via Raman spectroscopy can still be used to track phase changes by watching for the development of new bands as a function of composition.

Figure 4.6 shows a heat map of the Raman spectra as a function of composition. These maps include the as-deposited, vacuum annealed, 1-hour oxidation, and 18-oxidation libraries. As expected with the as-deposited and vacuum annealed samples, there is very little discernible signal from the metal. The formation of a thin surface oxide shows slight signal, but overall there is a lack of information. However, the heat maps support the observation seen in the XRD and optically that a phase boundary develops with two distinct phase regions after oxidation. In the 1-hour oxidized library, a very sharp band forms at 920 cm^{-1} , at the Cr concentrations greater than 25 at.% (R_2). However, this band has not been indexed to any known peak and could correspond to the unknown mixed metal oxide seen in the diffraction patterns at the same composition region. Additional bands form at 380, 662, 770, and 884 cm^{-1} , which correspond well with CrO_3 . At concentrations below 25 at.% (R_1), broader band formations are seen between 500 and 1000 cm^{-1} . These two differing areas on the map highlight the distinct phases, which are a result of changing Cr concentrations. After annealing for 18 hours, the broad bands between 500 and 1000 cm^{-1} grow more intense, which indicates oxidation is continuous with anneal time in the R_1 region. The phase boundary is observed to have shifted from approximately 25 at.% to 28 at.%, which agrees with the XRD analysis. At concentrations between 15 and 20 at.% Cr, the Raman intensity drops slightly with the formation of a new band at 718 cm^{-1} , which is a result of the development of new oxides from the continuous oxidation in the region.

4.3 CONCLUSIONS

Each type of characterization shows a consistent phase boundary that separates the clearly distinct R_1 and R_2 phases. Figure 4.7, is a meta-image that compiles these observations of the 18-hour oxidized library. Each image shows that the phase transition is approximately at 29.2 at.% Cr. Additionally, the images provide a means of

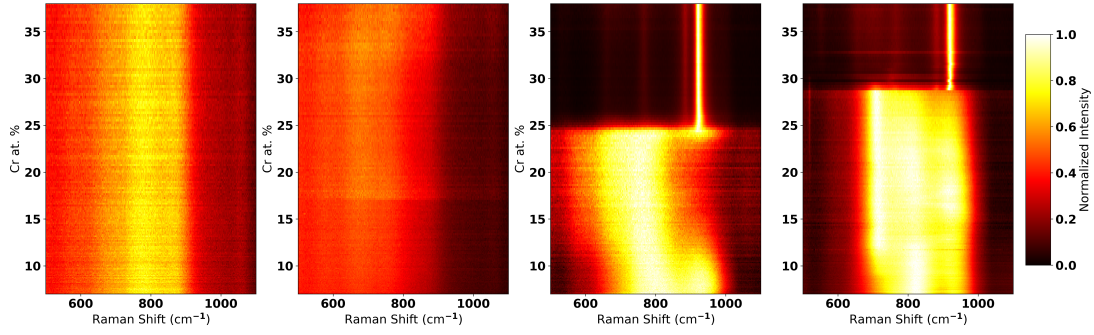


Figure 4.6: Compositional Raman heat maps. (a) As-deposited library, (b) vacuum annealed library, (c) 1-hour oxidation, and (d) 18-hour oxidation anneal. The phase boundary is visible in the oxidized sample libraries. There is a boundary shift from 25 at.% Cr to 28 at.% Cr as the anneal time increases.

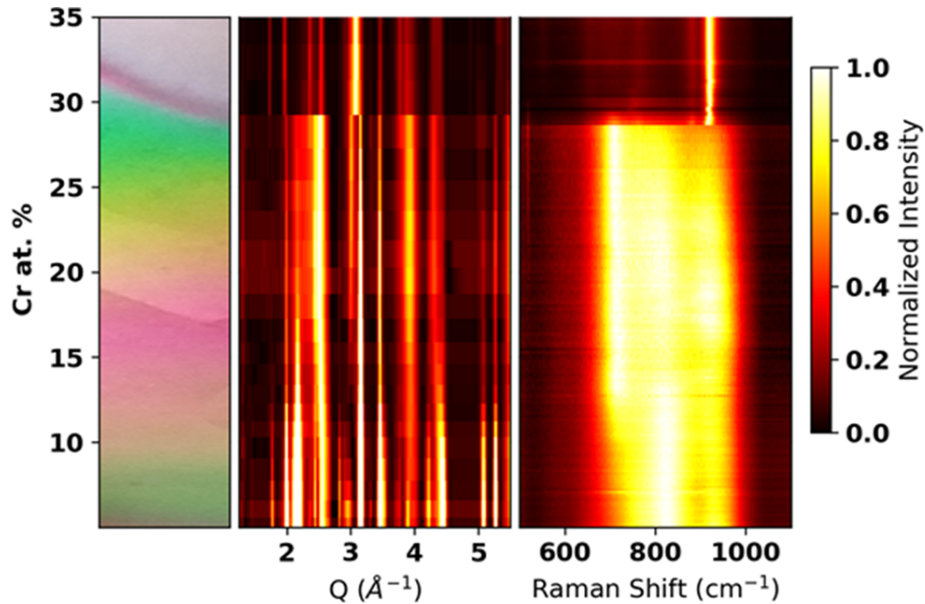


Figure 4.7: A meta-image of the 18-hour oxidation that shows the phase boundary using three different measurement techniques. (a) Optical observation. (b) X-ray diffraction heat map. (c) Raman spectroscopy heat map. The phase boundary remains at the same composition across all three observations.

focusing the large amount of data gained using HTE methods in order to present the phase boundary in different ways.

Taking a deeper look into the samples as a whole, the BCC structure was favored post-vacuum anneal. However, at the region of low Cr content (R_1), the crystal

was destabilized after oxidation with the formation of an FeSi and various different oxides. At regions with more Cr (R_2), the BCC structure is retained along with the suppression of oxides seen in the R_1 phases. After continued oxidation past 18 hours, the boundary separating the R_1 and R_2 phases shifted from approximately 25 at.% Cr to 28 at.% Cr. Overall, this highlights HTE as an effective method for the rapid top down investigations of MPEA materials, which can narrow down regions of interest for further analysis.

Future analysis of materials of interest include characterization and mechanical testing of bulk samples, in order to ensure the scalability of the properties. Mechanical studies include hardness tests and cyclic fatigue measurements. Furthermore, electron microscopy studies can help determine the kinetics and rate of oxidation growth by measuring oxide thickness via cross-sectional analysis, which can verify if parabolic growth is seen on the oxide suppressing phase. Additionally, energy dispersive X-ray spectroscopy (EDS) measurements, performed in conjunction with the electron microscopy measurements, can supply composition information on the surface oxides and provide insight into the make up of the unknown oxides.

CHAPTER 5

PHASE FORMATION OF YTTRIA-STABILIZED ZIRCONIA VIA MAGNETRON SPUTTERING

5.1 BACKGROUND AND MOTIVATION

As global energy demand rises, the need for materials that are optimal for the generation of electricity is amplified. Solid oxide materials have had many applications in this field from energy storage to acting as catalysts and catalyst supports for the synthesis of biofuels or conversion of CO [121, 252, 253]. Two applications for solid oxides include use as thermal barrier coatings in high-temperature gas turbine blade applications and as solid electrolytes in electrochemical fuel cell systems [44, 207, 126, 261].

5.1.1 THERMAL BARRIER COATING APPLICATION

Ceramic materials also have applications as thermal barrier coatings (TBC) for turbine blade systems. Typical turbine blades are made of nickel-based superalloys such as Inconel [244, 96]. These alloys are chosen due to their oxidation, creep stress, and cyclic fatigue resistance and high hardness at temperatures above 1173 K [16, 123, 152]. However, the operating environment for gas and jet turbine applications are often over 1873 K, which exceeds the melting point for these superalloys [274, 183, 125]. Therefore, TBCs are required in order to suppress the temperature at the superalloy during operation. The thermal barrier coating is applied to the superalloy with a bond coating and thermally grown oxide as seen in Figure 5.1. This

is done in order to prevent lattice mismatch and spallation of the ceramic TBC from the difference in expansion coefficient between the layers [217, 22, 105].

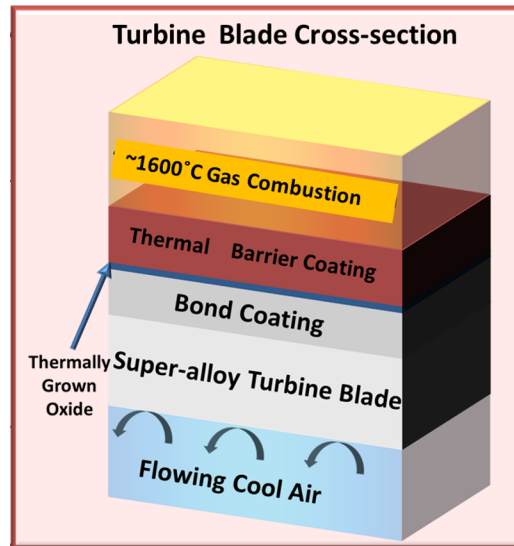


Figure 5.1: The cross-sectional schematic of a high-temperature turbine blade. The relevant layers are illustrated, and the thermal barrier coating is responsible for keeping the superalloy over 700 K cooler than the combustion environment [35].¹

Yttria-stabilized zirconia (YSZ) is the standard material used in TBC applications. It has high thermal resistance, as a result of the same interstitial oxygen vacancies that provide its ionic conductivity. Incorporation of Y_2O_3 into the base structure of ZrO_2 creates oxygen vacancies within the lattice due to the introduction of cations with lower valency than Zr. These vacancies are positive charge holes, which balance the anion lattice charge [271, 109, 124]. Additionally, the vacant sites in the lattice provide locations where phonon scattering occurs, which results in an increase of the thermal resistance of the material [213, 211, 270]. Phonons are the

¹Image reprinted from: J.K. Bunn, Development of Novel High-Throughput Methodologies to Evaluate the Thermal Stability of High-Temperature Thin-Film Crystals for Energy Applications. PhD Thesis, University of South Carolina, 2016, with permission from ©(2016) Jonathan Kenneth Bunn. See Fig. F.1 for copyright permission.

vibrational excitation modes of particles (atoms or molecules) in a lattice and their scattering results in a disruption of heat transfer in a material [251, 260]. The thermal conductivity, with respect to the phonons, can be expressed as the following equation, which arises from the kinetic theory of gases [211, 260]:

$$k = \frac{1}{3}Cv\Lambda \quad (5.1)$$

where k is the thermal conductivity of the material ($\text{W}\cdot\text{m}^{-1}\cdot\text{K}^{-1}$), C is the heat capacity per unit volume ($\text{J}\cdot\text{K}^{-1}\cdot\text{m}^{-3}$), v is the phonon velocity ($\text{m}\cdot\text{s}^{-1}$), and Λ is the phonon mean free path (m).

While YSZ has been used often in TBC applications, the crystal structure of the oxide is extremely important in these applications. Zirconia exhibits multiple structural polymorphs, monoclinic (m), tetragonal (t), and cubic (c) and the introduction of dopant oxides, such as yttria, present a means of stabilization of specific phases at different temperature conditions [237]. The monoclinic structure has been avoided due to resulting in a lattice mismatch between a non- Al_2O_3 TBC and the bond coating that can result in spallation and failure of the blade material [288, 262]. Therefore, t-YSZ has been studied extensively. However, using YSZ as a TBC in other applications, without introducing structural defects, such as pin holing, is a challenging procedure that require a different approach to synthesis.

5.1.2 ELECTROCHEMICAL APPLICATIONS

One of the major electrochemical systems that utilizes solid oxides is the fuel cell. In this field, a prominent technology is the solid oxide fuel cell (SOFC). Typical SOFCs are operated at relatively high temperatures ranging from 773 K to 1273 K [101, 250]. While other fuel cell systems, such as the proton exchange membrane fuel cell (PEMFC), can operate at much lower temperatures, SOFCs have an advantage because they can utilize a wide variety of fuels to generate electricity, such as biofuels,

light hydrocarbon fuels, H₂ and liquefied petroleum [78, 277]. Additionally, SOFCs have been demonstrated to have a high combined heat and power efficiency of up to 85% [224, 169, 150]. By contrast, PEMFCs require H₂ as their fuel source, which reduces their overall flexibility. Additionally, H₂ is a costly energy source that requires precious metal oxygen reduction reaction (ORR) catalysts or industrial gasification to generate, which drives up expenses [224, 169, 150].

Figure 5.2 illustrates the components of a typical SOFC, with the major parts consisting of an anode, cathode, and solid oxide electrolyte. SOFCs convert chemical energy into electrical energy by flowing gaseous fuel over an anode and oxygen over a cathode. Oxygen molecules are reduced to O²⁻ ions that travels through the cathode, solid oxide electrolyte, and anode. There the ions react with the fuel to generate H₂O, CO₂, and free electrons. These electrons travel via a wire back to the cathode, completing the circuit and electrical energy is harnessed from this circuit.

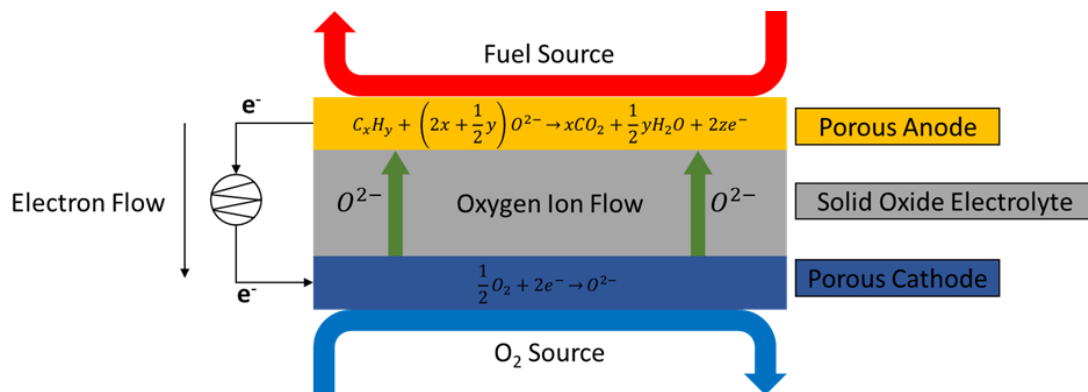


Figure 5.2: An illustration of the components and reactions involved in the layers of a SOFC. At the porous cathode, O₂ molecules are decomposed into O²⁻ ions that travel through the solid electrolyte. At the porous anode these ions synthesize CO₂ and H₂O with the fuel provided to the SOFC. The reaction releases electrons that flow back to the porous cathode via a wire, generating electrical energy.

Mixed-potential gas sensors are another electrochemical device that utilize solid oxide electrolytes. These gas sensors have potential application for the detection of toxic and flammable gases [161, 65, 136] These gases have been closely monitored in automotive exhaust due to environmental legislation enforced in the USA, Eu-

rope, and Japan [161]. Typically, automotive exhaust sources use potentiometric and impedancemetric gas sensors to detect harmful emissions. However, mixed-potential sensors have an advantage over the standard sensors due to their ability in harsh, high temperature (723 K to 1173 K) combustion environments [161, 31]. The operating principle is similar to SOFCs, with two electrodes connected via a wire and solid electrolyte. A reduction or oxidation half-reaction occurs at the working electrode, while the opposite reaction occurs at the counter electrode. The potential difference between the electrodes is read by a potentiometer that can translate voltage to the concentration of the reactive species [161, 195]. Both electrode half-reactions are rate limited by Butler-Volmer kinetics and exhibit Tafel-type behavior as seen in the following equation [63, 184]:

$$i = i_0 \exp(\pm \alpha F \frac{\eta}{RT}) \quad (5.2)$$

where i is the current density ($\text{A}\cdot\text{m}^{-2}$) from one half reaction, i_0 is the exchange current density ($\text{A}\cdot\text{m}^{-2}$), α is the charge transfer coefficient from 0 to 1, F is the Faraday constant ($\text{J}\cdot\text{V}^{-1}\cdot\text{mol}^{-1}$), η is the overpotential (V), R is the gas constant ($\text{J}\cdot\text{mol}^{-1}\cdot\text{K}^{-1}$), and T is the temperature (K). Similarly to SOFCs, the solid electrolyte provides a medium for the transfer of oxygen ions between electrodes during sensing.

In both of these situations, operating temperatures range from 723 K to 1273 K [101, 250, 61]. While for mixed-potential sensors this is typical for the environment, in a SOFC it can be a major disadvantage. High temperatures increase costs due to a requirement for sturdy materials that are resistant to thermal shock and the environment. Additionally, expensive heat exchangers are required to control the SOFC temperature. Furthermore, inter-diffusion can cause additional wear on the already expensive materials and can promote reactions between the parts of the SOFC [101]. Lowering the operating temperature of the SOFC can mitigate many of these

costs and potential points of failure. However, the current material that is traditionally used as a solid electrolyte is yttria-stabilized zirconia (YSZ). YSZ is capable of allowing oxygen ion diffusion through vacant sites within its lattice [4, 70, 124]. However, it only has optimal ionic conductivity at temperatures between 1073 K to 1273 K [70, 128, 269]. Therefore, studies for an alternative material that can function at lower temperatures or has a higher ionic conductivity have been performed [156, 221, 257].

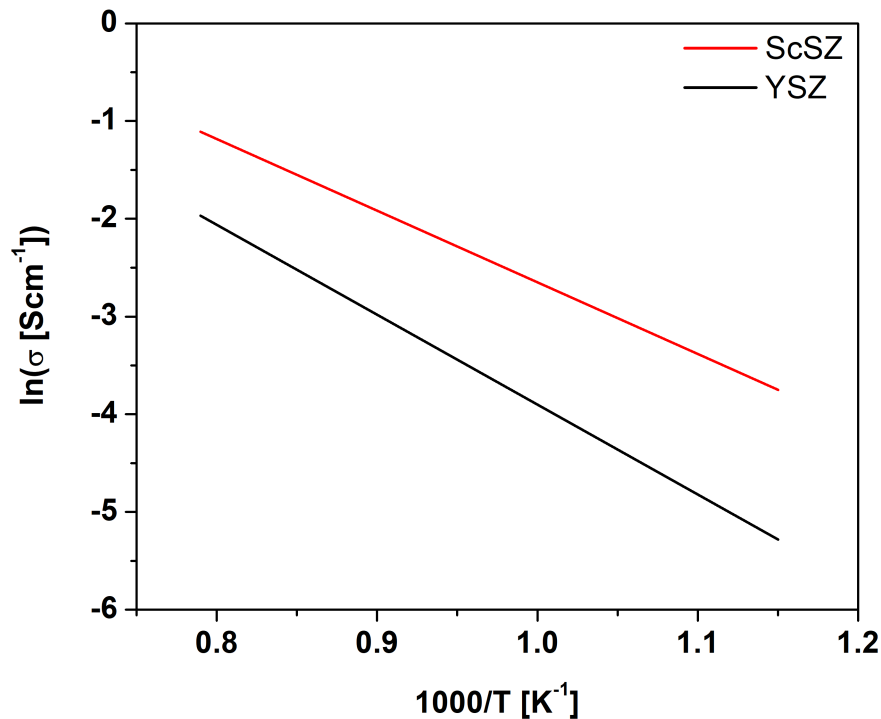


Figure 5.3: Solid electrolytes exhibit Arrhenius behavior with respect to ionic conductivity. The Arrhenius plot shows that within the same temperature regime 9.0 mol.% Sc₂O₃ ScSZ maintains higher ionic conductivity than 9.0 mol.% Y₂O₃ YSZ. [228, 267]

One of material that has been studied is scandia-stabilized zirconia (ScSZ). Similar to YSZ, the addition of Sc into Zr₂O₃ stabilizes the cubic zirconia phase [173, 245, 265, 268]. ScSZ utilizes the same interstitial oxygen vacancy mechanism for ionic transport as YSZ, but has higher ionic conductivity at lower temperatures (973 K to 1123 K). Compared to YSZ, in the same temperature regime, oxygen ion conductivity

of ScSZ is higher as seen in the Arrhenius plot in Figure 5.3 [1, 26, 122, 284]. However, the synthesis of ScSZ for use in these applications is a non-trivial task. Traditionally, synthesis of oxides involved spin coating and is a fairly inexpensive technique. However, oxides created in this manner are relatively thick ($>1\mu\text{m}$) for this particular application. It is preferable for these electrolytes to be thinner than 500 nm because it lowers the constriction effect that increases ionic resistivity linearly with thickness [103, 119, 284]. However, it is not possible to spin coat ceramic electrolytes this thin because of mechanical failure [144]. Therefore, other synthesis techniques need to be explored in order to achieve optimal efficiency for the electrolyte.

5.1.3 SPUTTERING SYNTHESIS AND CRYSTAL PHASE STABILIZATION

Thin-film deposition is a good candidate technique for the synthesis of these oxide materials onto their desired surfaces. Deposition techniques have been utilized in the past to investigate ScSZ and YSZ electrolyte performance [219, 218]. Physical vapor deposition (PVD) is a potentially viable technique due to its ability to scale up to quality thin-films industrial levels, such as in semi-conductor materials [258, 223]. However, a major issue that can present itself during magnetron sputtering is the development of undesirable metastable phases due to the high-energy particle bombardment along with the rapid quench rate of the technique [42, 23]. A rigorous inquiry into the adjustment of sputtering conditions, such as the gun power, gun tilt, and deposition pressure, can provide insight into the a pseudo-phase diagram based off thin-film deposition.

5.1.4 STABILIZED ZIRCONIA STRUCTURES

Historically, cubic and tetragonal phases zirconia are stabilized by oxides such as yttria or scandia to prevent the material from adopting the monoclinic phase upon

cooling [190]. The functionality of these stabilized zirconium oxides as an electrolyte or thermal barrier can be dependent on the phase of the material.

Oxygen vacancies in the stabilized zirconia systems provide sites for the transport of oxygen ions during when the material is used as a solid electrolyte. Additionally, oxygen vacancies are also the main contributor to the high thermal resistance of the stabilized zirconia systems because of the phonon scattering effect [211, 116, 251]. In a simple sense, heat travels through solid materials via the phonon vibrations in the crystal lattice, and because of disruptions in the lattice due to the introduction of a dopant oxide, phonon vibrations are scattered and heat flow is disrupted, increasing thermal resistance. A basic example of the phonon scattering due to vacancies can be seen in Figure 5.4.

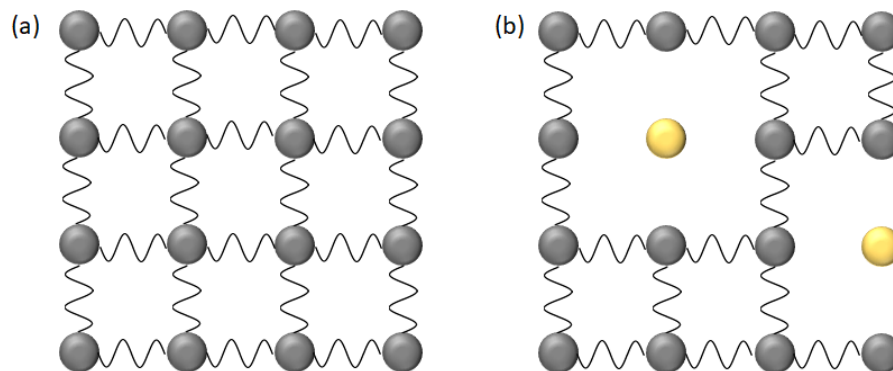


Figure 5.4: A basic example of how lattice vacancies cause phonon scattering. (a) The atoms (gray) in the lattice vibrate with a periodicity that can be broken down into several normal modes. (b) The introduction of defect sites (yellow) allow for a scattering effect, which results in higher thermal resistance.

While the cubic YSZ (c-YSZ) and tetragonal YSZ (t-YSZ) maintain oxygen defect sites that contribute to their high ionic conductivity and thermal resistance, there are preferences between the two structures in various applications due to the necessity of preventing lattice mismatch between the coated material and substrate. Additionally, while the metastable t'-YSZ has been shown to have high thermal resistance due to the formation of microstructural tweed boundaries, the metastability of the crystal

phase means that phase separation is a potential concern [141, 153, 102, 201]. The t'-YSZ can phase separate at high enough temperatures (>1473 K) over many hours of operation into c-YSZ and t-YSZ, which leads to m-YSZ upon cooling, defeating the purpose of stabilizing the material. This can lead to a mechanical failure from the stresses caused by changes in volume [201, 262, 45].

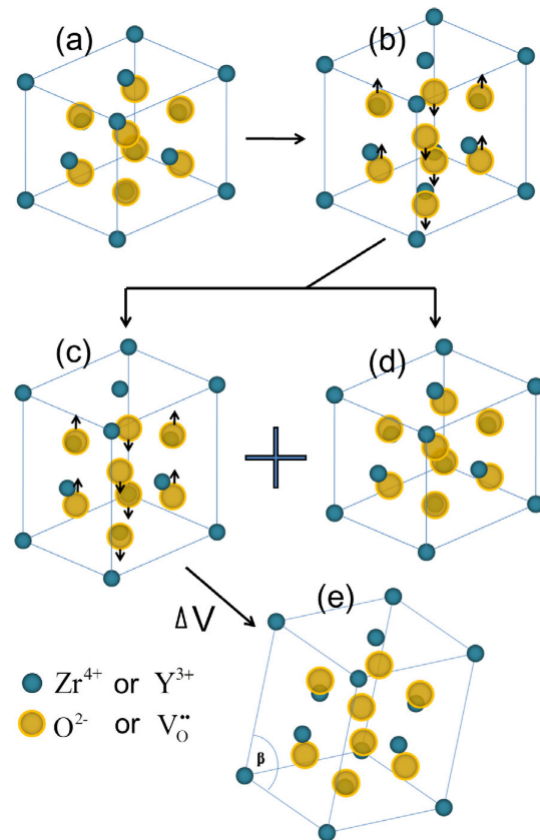


Figure 5.5: YSZ phases and transformation. (a and d) c-YSZ, (b) t'-YSZ, (d) t-YSZ, (e) m-YSZ [201].²

The polymorphs of stabilized zirconia and how they phase separate can be seen in Figure 5.5. The tetragonal phases are distinguished by the degree of oxygen displacement in the structure. Differentiating the tetragonal structures can be difficult with

²Image reprinted from: X. Ren, W. Pan. *Mechanical properties of high-temperature degraded yttria-stabilized zirconia*. Acta Materialia, 69, 397-406, with permission from ©(2014) Elsevier. See Figure F.4 for copyright permission.

only diffraction because they belong in the same space group $P4_2/nmc$, while c-YSZ is $Fm3m$ [273, 201]. A way to parse t-YSZ and t'-YSZ (along with the additional t''-YSZ phase) is to measure the displacement of oxygen in the lattice, which is outside the scope of this work. While, further analysis of the crystal structures requires additional experiments and data collection, the current work is a proof of concept in order to show the ability to develop a phase diagram system using estimated sputter energy.

Scandia stabilized zirconia (ScSZ) has similar structural considerations, but has been observed to form rhombohedral structures at temperatures above 1373 K [130]. Additionally, it has also been shown to have better application as a solid electrolyte than YSZ due to higher ion conductivity (0.30 S/cm) compared to YSZ at operating conditions (<1123 K) [1, 26, 122, 284].

In this chapter, phase analysis is performed on YSZ and ScSZ samples that have been synthesized via R.F. magnetron sputtering. Sputtering was chosen because traditional synthesis methods have difficulties when developing thin ceramics due to the development of pinholes and fractures [144]. Both applications of the zirconia films also benefit from synthesis as thin materials. The thermal barrier coating reduces additional parasitic mass on the structural material it is applied to, and the solid electrolyte has increased conductivity with less mass in the direction of ion flow. An investigation of the effects of synthesis conditions on the phase formation of YSZ thin films was conducted, utilizing tools discussed in sections 2.1 and 2.2. High-throughput methodology was applied to the ScSZ studies, where a four factor, three level design space was utilized to determine synthesis and post-processing conditions associated with analyzed crystal phases and texturing of the films.

5.2 EXPERIMENTAL METHODOLOGY

5.2.1 YTTRIA-STABILIZED ZIRCONIA EXPERIMENTAL DESIGN, SYNTHESIS, AND CHARACTERIZATION

One of the major goals of sputtering YSZ at various conditions was to develop a "pseudo-phase diagram" for the deposition of the oxide at various energetic conditions. Studies on the effects of deposition parameters on the properties of YSZ have been performed in the past, but have not developed a visualization of the phase boundaries based on the parameter space [203]. Gun power directly correlates to adatom energy but with sputter pressure. As for sputter gas pressure, the energy of the adatom decreases with increased pressure. This is due to the higher number of gas atoms that are directly in the path between the adatom and substrate. Collisions with these atoms decreases the energy the adatom carries to the substrate during deposition. After identifying the phases associated with each deposition parameter, the deposition phase diagram can be compared to the traditional binary phase diagram for YSZ, with the goal of estimating deposition conditions required for the synthesis of desired phases, in particular metastable structures that are observable in the traditional phase diagram. Additionally, this approach can also be to transfer operating knowledge for the deposition parameters used for other sputtering systems.

However, using deposition phase diagram has unique difficulties because different sputter systems often have varying geometries, which result in different energetics within the system. Oftentimes a way to mitigate the different geometry is to use the voltage applied to the gun for energy measurements, but ceramics can have difficulties with presenting the potential on the surface. Therefore, estimations have to be made based on deposition rates, sputter power, and sputter gas pressure.

In order to determine the sputtering conditions YSZ requires for a particular crystal structure to be synthesized, a synthesis design space was chosen based off the

previous deposition rate calibrations... An 8 mol.% Y_2O_3 YSZ target with 99.9% purity was RF sputtered with the AJA sputtering system discussed in 2.1. The RF magnetron source was used in order to prevent charge buildup on the insulating target material. The deposition sputter power and argon pressure conditions are based off of permutations of the conditions seen in Table 5.1. Depositions were performed at room temperature with the *in situ* tilt of the YSZ target at 7 mm. Twelve samples were deposited on 1 cm² single crystal Si substrates with the <100> orientation. The substrates were cleaned with acetone and mounted on the substrate holder with Kapton tape.

Table 5.1: Deposition Parameters for YSZ Sample Synthesis

Factors	Variables			
Gun Pow. (W)	150	100	75	50
Argon Press. (mTorr)	10	5		2

Post-deposition thickness measurements were performed using a Filmetrics reflectometer. This uses the differences in refractive index, n , and extinction coefficient, k , between the measuring medium (air), sample (YSZ), and substrate (Si) in order to determine thickness based off the constructed wavelength of light that returns to the detector [176, 177]. The input refractive index of the YSZ is 2.15, and the approximate average thickness of each sample is 200 nm.

Crystallographic measurements were collected using XRD with a Rigaku MiniFlex benchtop X-ray diffractometer, with a Cu- $k\alpha$ source and scintillating detector. Measurements were taken between 20 to 65° 2θ at a scan rate of 0.5 °/min. This created a 1D diffraction pattern for the samples, which allowed for an ease of measurement, but prevented critical analysis of sample texturing on the Si substrate surface.

5.2.2 SCANDIA-STABILIZED ZIRCONIA EXPERIMENTAL DESIGN, SYNTHESIS, AND CHARACTERIZATION

An 11 mol.% Sc₂O₃ ScSZ target was RF sputtered using the AJA sputtering system outlined in Section 2.1. The deposition parameters were varied over a series of factors with high, medium, and low levels, seen in Table 5.2, with samples being synthesized via each arrangement of conditions. Out of the 27 possible permutations, the samples with the conditions at 35 W with both 5 and 10 vol.% O₂ and at 773 and 973 K were not synthesized due to the extremely low deposition rates (≈ 0.1 Å/min). Deposition rates were calibrated using a quartz crystal monitor and profilometry in conjunction with the in-house sputter model, as described in Section 2.1. The remaining samples were deposited onto 7.62 cm by 2.54 cm single crystal Si substrates with a <100> surface orientation. The Si substrates were cleaned using acetone and were mounted onto the substrate holder using silver paste as an adhesive, due to the deposition being performed at temperatures above 773 K. After deposition, film thickness was measured using Filmetrics reflectometry, and the average film thickness on the sample strip was found to be 30.24 ± 2.80 nm. The samples were then cut into three equal area square pieces (2.54 cm by 2.54 cm) for the post-annealing study. One sample was left as-deposited, while the remaining two were annealed in air at 1273 K for 4 and 8 hours. This is a typical temperature for a solid electrolyte to experience, in particular during deposition of an electrode onto it.

Table 5.2: Deposition Conditions for ScSZ Sample Synthesis

Factor Level	Variable Factors			
	Gun Pow.	O ₂ Conc.	Deposition Temp.	Annealing Time
	W	vol.%	K	Hours
High	65	10	923	8
Medium	50	5	773	4
Low	35	0	297	0

Crystal structure measurements were taken using the SAXSLab Ganesha system outlined in Section 2.2. This was used in order to determine the crystal phase and texturing of the material with the help of a 2D area detector. The 2D diffractograms were converted to 1D diffraction patterns via an integration with respect to χ . Microstructural data, such as continuity, uniformity, and grain size was measured using scanning electron microscopy (SEM), which uses an electron beam to sample the surface topography. The microscopy used was a Zeiss Ultraplus Thermal Field Emission SEM with 10 keV electron beam intensity, a 4.6 nm working distance, and secondary detector. All analysis of the grain size distributions was performed using Nano Measurer [266].

5.3 RESULTS AND DISCUSSION

5.3.1 YTTRIA-STABILIZED ZIRCONIA CHARACTERIZATION AND PHASE REGIMES

The standard phase diagram of YSZ can be seen in Figure 5.6 [273]. Typically 8 mol.% of Y_2O_3 is used to stabilize the cubic zirconia phase, but it has been shown that the material destabilizes at temperatures above 1273 K, and operating conditions for thermal barrier coatings can exceed 1873 K [18, 229]. This is due to the phase separation the cubic structure into a mixture of the tetragonal and cubic phases. However, Yashima *et al.* have also shown a metastable tetragonal prime structure for that exists at temperatures above 1273 K. The metastable structure has been hypothesized to be a result of sluggish diffusion, and with a rapid quench rate, it can be captured during synthesis [273]. Thin-film deposition is a technique that can provide the rapid quench rate (1000 K/s) alongside depositing a structurally sound ceramic material [219]. However, as previously mentioned, despite t'-YSZ retaining its structure at high temperatures, due to its metastable nature it can still phase separate into t-YSZ and c-YSZ after continued heating. However, it is still worth

determining the conditions for the synthesis of each phase in order to develop a link between deposition and the binary phase diagram.

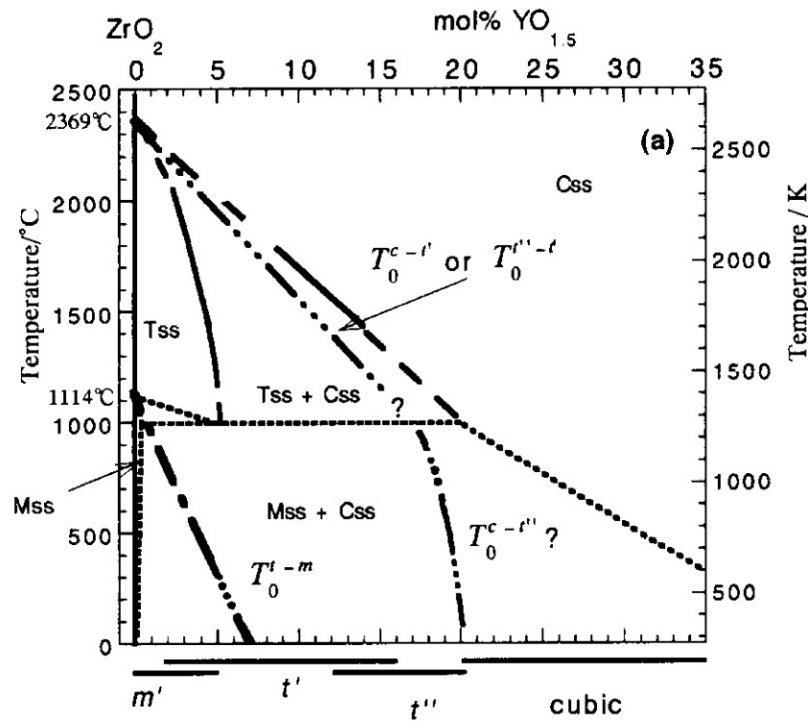


Figure 5.6: The binary phase diagram of Y_2O_3 and ZrO_2 [273].³

Characteristic diffraction patterns of samples measured with the design space outlined in Table 5.1 can be seen in Figure 5.7. The diffraction patterns show the cubic and tetragonal structures that have been observed in the samples. Preliminary analysis of the structures are based off of PDF cards from the Inorganic Crystal Structure Database (ICSD) and the fitting of the diffraction peaks [83]. The cubic space group was Fm-3m as seen in PDF# 82-1246 and the tetragonal space group was P42/nmc from PDF# 82-1245. The $\text{C}(111)$ has an average peak position of

³Image reprinted from: M. Yashima, M. Kakihana, M. Yoshimura. *Metastable phase diagrams in the zirconia-containing systems utilized in solid-oxide fuel cell application*. Solid State Ionics, 86-88, 1131-1149, with permission from ©(1996) Elsevier. See Figure F.5 for copyright permission.

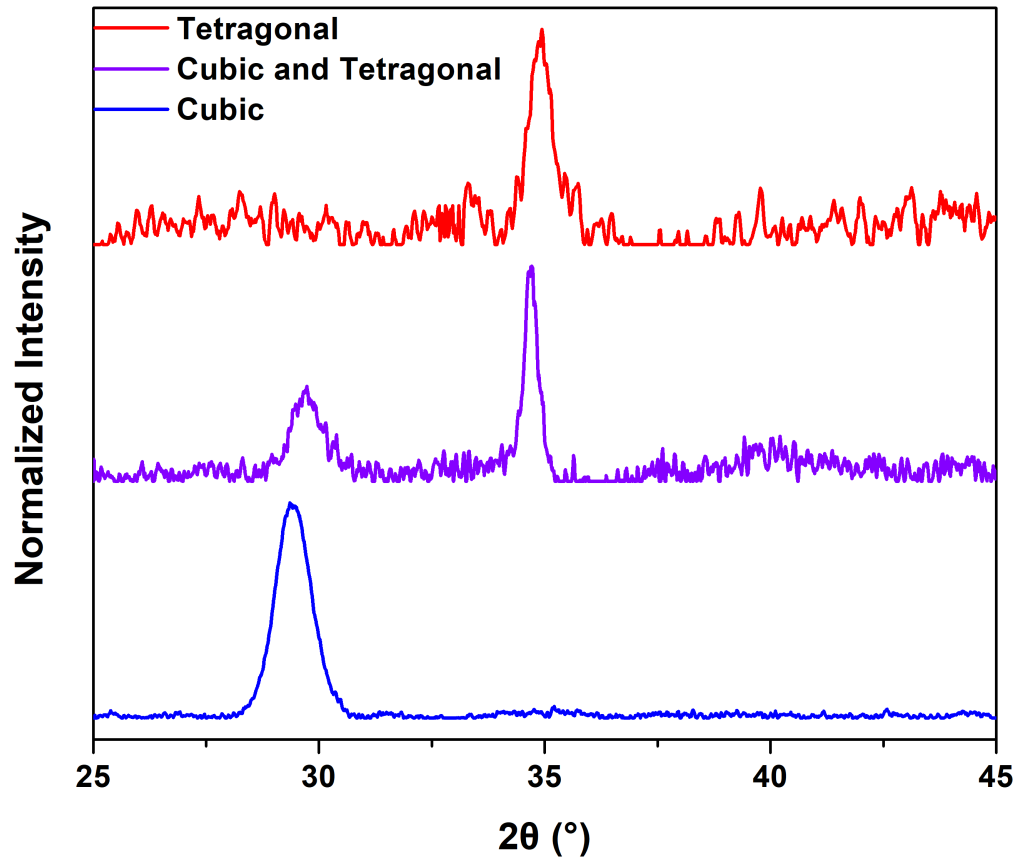


Figure 5.7: The characteristic diffraction patterns of the YSZ phases. The blue is the cubic (111) plane, purple is characteristic of the mixed tetragonal (002) and cubic (111), while the red shows only the tetragonal (002).

29.7° 2θ , while the T(002) has an average peak position of 35.0 . Variations in the peak positions for the same phases can be attributed to oxygen deficiency during deposition, and mix phases can cause expansion with the lattice. It can be argued that the two observable peaks are multiple orientations of either c-YSZ or t-YSZ, but based on the reference diffraction patterns, it is reasonable to assume that different phases exist, due to the slight variations in peak position. Additional experiments are required in order to validate the phase formations, and will be performed in a future work.

Reorganizing the data in Table 5.3 into a deposition phase diagram results in Figure 5.8. The phases can be divided into distinct regions based off of estimated energy

Table 5.3: Indexed Peaks Positions and Phases of YSZ at the Sputtered Conditions

Argon Press.	Sputter Pow.	Main Peak Position	Phase and Index
mTorr	W	$2\theta(^{\circ})$	(hkl)
2	50	29.5	C(111)
2	75	29.3	C(111)
2	100	29.3	C(111)
2	150	29.5	C(111)
5	50	35.1	T(002)
5	75	35.0	T(002)
5	100	29.9 & 34.9	C(111) & T(002)
5	150	29.7 & 34.9	C(111) & T(002)
10	50	34.9	T(002)
10	75	35.0	T(002)
10	100	30.1 & 35.0	C(111) & T(002)
10	150	30.1 & 34.9	C(111) & T(002)

contribution from the sputter gas (Ar) pressure and the gun power. In particular, the solo c-YSZ phase is seen at gun powers with the sputter gas pressure at 2 mTorr. The t-YSZ only structures are seen at sputter gun powers below 75 W and Ar pressures of 5 mTorr and higher. Finally, the mixed phases are observed after the sample has been synthesized at sputter gun powers 100 W and greater, when the chamber is exposed to Ar pressures at 5 mTorr and greater. Cubic YSZ is seen at regions that would be considered high energy based on sputtering heuristics, and the cubic-only structure is at pressures less than 5 mTorr. Low Ar pressure reduces the number of molecules in the direct path of the adatoms, which reduces the number of collisions that decrease the energy of the adatoms. Tetragonal-only samples are seen in regions considered lower energy, where Ar pressure lowers adatom energy and the deposition power is moderate. It can be reasonably assumed that there is an pressure threshold between 2 and 5 mTorr that acts as a phase boundary during synthesis between the

cubic and tetragonal structures. Additionally, there is a second boundary at sputter powers between 75 and 100 W when the Ar pressure is at or above 5 mTorr. This boundary separates the tetragonal-only samples from the mixed structure samples, indicating that there is a sort of dome where the mixed YSZ phases exist. This is semi-analogous to the traditional binary phase diagram for YSZ, where higher temperatures during synthesis contribute toward the development of a cubic phase, and lower energy leans toward tetragonal and eventually monoclinic structures.

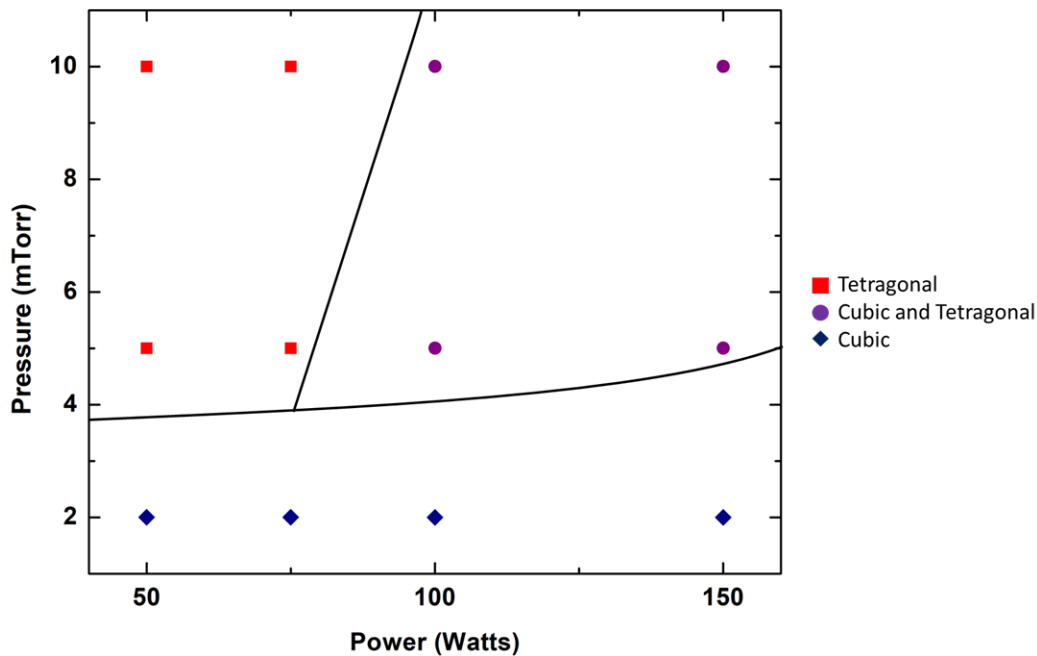


Figure 5.8: The deposition phase diagram, using the input synthesis conditions as the axes. The diagram shows that the YSZ phases fall into separate deposition regions.

During all measurements it is unclear whether or not the metastable t' -YSZ structure was synthesized, and additional experiments will be required to possibly differentiate the structures. However, from the newly formed deposition phase diagram, we can make reasonable assumptions on where a potential metastable phase will form when translating phase boundaries from the traditional phase diagram to the new one. Additionally, in order to fully validate the deposition phase diagram, additional structural analysis, annealing tests, and energetic calculations via the sputter model

are required and will be discussed below, but this is a promising first step toward translating the binary phase diagram to the deposition space.

5.3.2 SCANDIA-STABILIZED ZIRCONIA CHARACTERIZATION AND ANALYSIS

Scandia has been shown to stabilize bulk cubic zirconia at temperatures below 1373 K, but thin-film phase studies have been limited. Figure 5.9 shows characteristic diffraction patterns of the ScSZ sample at 50 W, unheated and with no reactive gas (O_2) in the sputtering chamber. The as-deposited sample shows the c-ScSZ phase was synthesized and remained in the sample after post annealing the sample at 1273 K for both 4 and 8 hours. The planes observed were cubic (111), (200), and (220) at 30.0, 34.5, and 48.9° 2θ , respectively [208, 86]. Additionally, there is a lack of secondary phases seen in the diffraction patterns of all measured samples, which indicates that c-ScSZ is stable up to 1273 K and insensitive to changes in the synthesis conditions. While, the cubic phase remained post-anneal, all peaks showed a visible shift of approximately -0.5° 2θ , which is indicative of lattice expansion. This is likely due to the addition of oxygen in the ScSZ system during the air anneal. During deposition of oxide ceramic materials, it has been shown that oxygen deficiencies can be seen in the lattice of the deposited material [204]. Annealing in air reintroduces oxygen into the lattice that was lost during deposition, which forms a stoichiometric ScSZ material.

Crystallinity was determined after confirming the cubic phase of ScSZ in the samples, and the characteristic texturing differences can be seen in Figure 5.10. Samples were determined to be polycrystalline (disordered), nanocrystalline (slightly-textured), or textured based on the imaging of the Debye-Scherrer rings in the 2D area diffractogram. When a textured system develops the rings compress to intense points in the same 2θ , because all grains in the film orient to the preferred direction

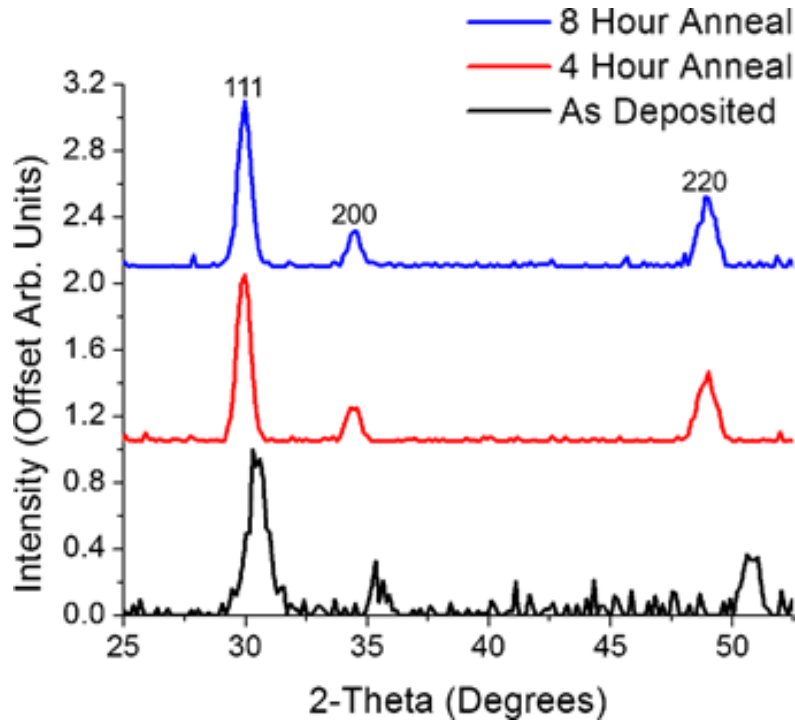


Figure 5.9: The characteristic diffraction patterns of the ScSZ samples deposited at 298 K, 50 W gun power, and with 0 vol.% O_2 in the chamber atmosphere. These patterns show only that the cubic phase was present at all annealing conditions.

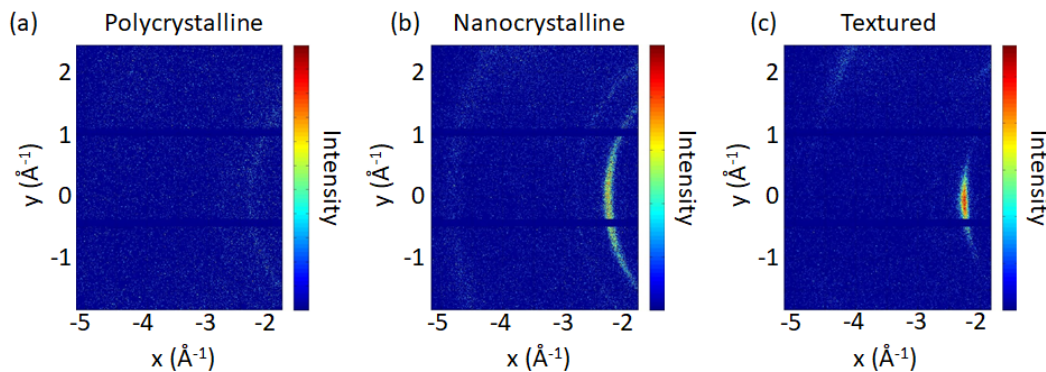


Figure 5.10: A visualization of what is looked for when analyzing texture and preferred orientation.

without randomization like in a powder diffraction. This makes 2D area diffraction vital when determining the extent of crystallinity in a sample.

A multilayer graph, seen in Figure 5.11, was developed to show crystallinity trends in the factorial design space. The samples that were sputtered at room temperature

and with no post-anneal showed broad peaks at 30.5 (111) and 50.8° (220) 2θ , which are indicative of disordered crystals in the film [208]. After a post-anneal in oxygen the peaks began to sharpen alongside an increase of signal-to-noise, which corresponds to increasing crystallinity and texture formation. The increase in crystallinity is typically associated with grain growth and coarsening, which is a typical phenomenon during annealing, or the reintroduction of oxygen into the deficient ScSZ system.

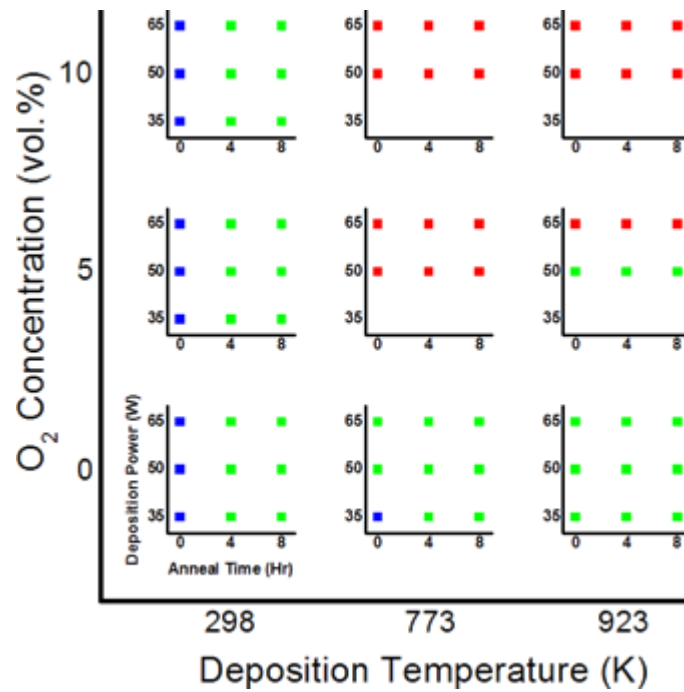


Figure 5.11: The ScSZ crystallinity analysis at all synthesis conditions. The red points represent moderate texturing, green points show slight texturing, and the blue points represent disordered crystallites/grains that make up the film.

Figure 5.11 also shows the reduction of lattice disorder when heating during deposition. When the substrates are heated to 773 to 923 K during deposition, all samples showed at the minimum slightly-textured orientations. Furthermore, when the vol.% of O₂ and deposition temperature are increased a textured film is form. Therefore, it can be determined that when the substrate temperature increase, the surface energy is higher and allows the adatoms to deposit on its preferred orientation [9]. Furthermore, heating and application of the reactive gas (O₂) restores the oxygen atoms that

were lost during deposition providing a higher textured surface. Finally, deposition power can also affect texturing by adjusting adatom energy, which can be seen at the 923 K and 5 vol.% O₂ sample point. However, the largest contributor to texturing is the substrate temperature during deposition.

The development of a textured film, where the material develops in a preferred orientation, is also an important factor when improving the performance and ionic conductivity of a solid electrolyte when operating as a SOFC [220]. Film texture analysis was performed by fitting the diffraction peaks with a pseudo-Voigt profile and calculating the ratio of the intensities between the (111) and (200) peaks. That ratio is used as a qualitative way to determine the preferential orientation of the ScSZ on the Si substrate and is seen in the multilayer graphs in Figure 5.12. Unfortunately four of the measured samples showed silver contamination and were not used in the texture analysis.

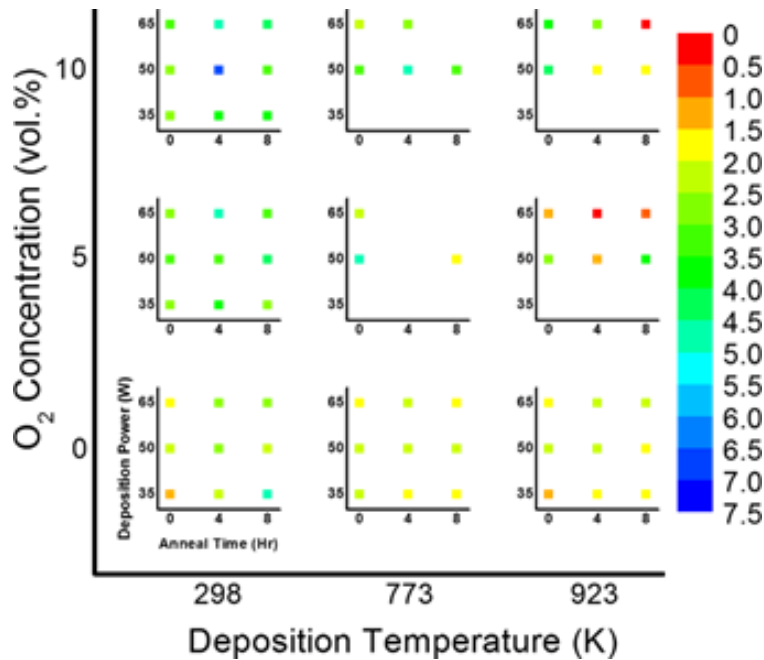


Figure 5.12: The crystallinity ratio between (111) and (220) texturing at each of the synthesis conditions.

As the samples are subject to post-processing we see different changes in the texture ratio. The film synthesized with no additional O₂ and with 5 vol.% O₂, increased texturing in the (111) orientation after annealing for 4 hours, while after 8 hours the (111)/(220) texturing ratio decreases slightly. However, the samples that were deposited at 10 vol.% O₂ and at 50 or 65 W had preferential texturing in the (220) direction after post-annealing for 4 hours, which became exacerbated after 8 hours of processing. One explanation for this phenomenon is that with the additional oxygen introduced to the system, Stoichiometric ScSZ has a preferential orientation with a plane that includes the atoms and will reorient during annealing. In any event, the retention of the (220) orientation indicates a stable film after post-processing.

Finally, the samples with the theoretically largest grains, deposited at 923 K, 65 W deposition power, and 10 vol.% O₂ concentration, were studied via SEM. Furthermore, the 4 and 8 hour post-annealed samples were imaged with SEM alongside an additional 12 hour post anneal to investigate any microstructural effects of post-processing the deposited sample. The SEM imaging showed no structural damage of the ScSZ film, with no visible cracking or delamination.

After imaging, the as-deposited sample grain sizes were too small to be resolved. The post-annealed sample had over 300 grains measured for their sizes to observe how the grains grew as a function of anneal time. The grain sizes were estimated as ellipsoid in shape and were measured by taking the short length (L_S) and long length (L_L) of each grain. Then a pseudo-diameter scalar value, D , was calculated by using Equation 5.3.

$$D = \sqrt{L_S * L_L} \quad (5.3)$$

Using this equation and the 300 measured grains in each sample, the average grain sizes was 23.9, 25.8, and 27.4 nm for the 4, 8, and 12 hr annealed samples, respectively. Figure 5.13 shows the grain distribution across the sample conditions at

the various annealing times. While the average grain sizes increased, the average of the 12 hr sample is only 15% larger than the 4 hour sample. This increase is likely due to large grains consuming smaller grains and skewing the grain size, as seen by the slightly higher number of large grains of the 12 hr sample in Figure 5.13. However, the mode and average is still largely weight to the same region as the 4 ad 8 hr samples. Therefore, without increasing the temperature to the destabilization point, the grains are stabilized at approximately 26 nm for ScSZ from this deposition parameter.

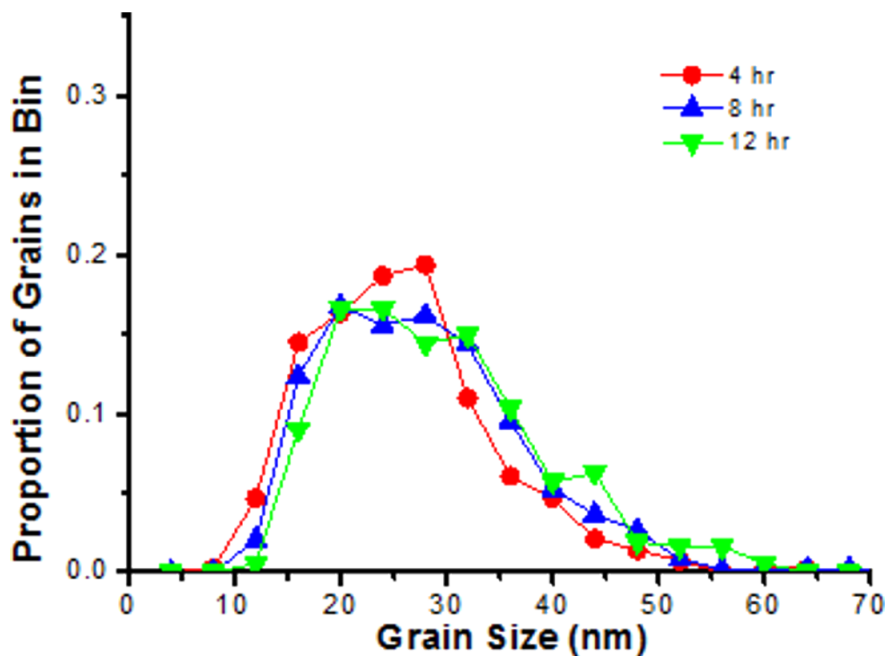


Figure 5.13: The ScSZ grain size distribution at 923 K, 65 W gun power, and 10 vol.% O₂ at the different annealing times.

With respect to the crystallinity and texturing of the ScSZ thin films, the post-anneal after depositions allows for the crystal grains to grow and reduce the oxygen deficiencies born from stripping during the sputtering process. The degree of texturing, seen in Figure 5.10c, tends to increase with respect to deposition power, deposition temperature, oxygen concentration, and annealing time. The deposition parameters most likely increases texturing due to providing the adatoms enough en-

ergy to deposit in their preferred lattice orientation. The post-anneal increases the grain size of the crystals in each sample and reduces grain boundary effects on conductivity, in addition to reintroducing oxygen into the ScSZ lattice [32]. ScSZ films that were deposited at higher powers and at high temperatures (>65 W and at 923 K) under 10 vol.% O_2 showed texturing in the cubic (220) orientation, while lower powers showed little texturing or preference to the (111) orientation pre-anneal. The development of a stable cubic phases, larger grains, and strong texturing can lead to higher ionic conductivity, which is promising in SOFC applications.

5.4 CONCLUSIONS

Oxide stabilized zirconia have a large multitude of applications, and two of the major applications exist within a high-temperature environment, thermal barrier coatings and solid electrolytes. This requires specific crystal structures and for the material to retain its phase during operation when exposed to the high-temperature stressors. YSZ and ScSZ are ideal ceramics for these applications due to the oxygen vacancies providing both ionic conductivity and thermal resistance. However, each material needs careful study in order to synthesize the proper phase and microstructure for their given application.

YSZ has been used as a thermal barrier coating in jet turbines. However, because the exhaust can reach temperatures above 1873 K, phase destabilization is a possibility when the material cools down. While the t' -YSZ phase is favorable for this application, synthesizing the phase via thin-film deposition requires a precise set of input parameters. A phase diagram was developed with the sputter gas pressure and deposition power, and different phase regions can be delineated from the parameters. However, the metastable t' -YSZ is difficult to differentiate from regular t -YSZ. In order to ensure the synthesis of t' -YSZ, additional studies are required. First the exact energetics of the thin-film deposition need to be correlated to the energies of

the different YSZ phase formations. That can provide reference starting point for deposition parameters required for t'-YSZ development. Finally, oxygen displacement needs to be observable in order to differentiate between t'-YSZ and t-YSZ. Raman spectroscopy, *in situ* high-temperature XRD, and transmission electron microscopy (TEM) can be used to help differentiate the different tetragonal structures for future studies.

The ScSZ thin film cubic structures were optimized (increased texturing and stability) using HTE methodology with a 4-factor 3-level design space for synthesis and post-processing. XRD allowed for the analysis of the crystal phase, crystallinity, and texturing. The cubic phase was sole observed phase and was stable at temperatures up to 1273 K after 8 hours of annealing in air. When the deposition temperature and deposition oxygen concentration increased, samples showed higher ordering. Additionally, the ScSZ samples had an increased degree of texturing in the (200) orientation. The (111) orientation was transient with respect to increased post-processing, deposition power, and higher deposition oxygen concentration. Analysis of the ScSZ SEM images showed that grain growth was minimal with respect to annealing time. The thin films that were synthesized at 65 W, 10 vol.% O₂, and with substrate temperatures at room temperature, exhibited a highly stable c-ScSZ film that was highly crystalline with a preference for the (220) orientation. Therefore, the samples synthesized at these conditions make excellent candidates for use as the solid electrolyte in a SOFC application.

CHAPTER 6

REO_x CHARACTERIZATION ON A CeO₂ SUPPORT

6.1 BACKGROUND AND MOTIVATION

Simultaneous hydrodeoxygenation (S-HDO) is a reaction to generate value-added chemicals by conversion from oxygen-rich biomass chemicals [180, 181, 143]. S-HDO utilizes two steps. The first is a deoxydehydration (DODH) step that is followed by a hydrogenation step [263]. A recently designed ReO_x-Pd/CeO₂ catalyst has been used, where the ReO_x/CeO₂ catalyzes the DODH step, while the palladium catalyzes hydrogen dissociation. This results in hydrogen spillover onto the surface, which promotes hydrogenation [181].

Early calculated reaction mechanisms propose that the S-HDO initiates with an isolated Re^{VI} species, where the ReO_x starts with a tri-oxo structure that is reduced to a di-oxo structure. This causes the oxidation state to change from Re^{VI} to Re^{IV}. Once the alcohol, 1,4-anhydroerythritol, is introduced, the vicinal OH groups coordinate to the Re^{IV} species. Hydrogenation occurs and the Re^{VI} is regenerated [181].

Another proposed mechanism states that the mono-oxo Re species is the initiating site, due to calculations indicating that the mono-oxo structure is the most

Parts of chapter adapted from: B. MacQueen, B. Ruiz-Yi, M. Royko, A. Heyden, Y. Pagan-Torres, C. Williams, J. Lauterbach (2020). *In-situ Oxygen Isotopic Exchange Vibrational Spectroscopy of Rhenium Oxide Surface Structures on Cerium Oxide*. The Journal of Physical Chemistry C, 124(13), 7174-7181, with permission from ©(2020) American Chemical Society. See Figure F.6 for copyright permission.

energetically favorable at reaction conditions on a fully hydroxylated CeO_2 support [263]. Initially, 1,4-anhydroerythritol adsorbs and the DODH step occurs, resulting in a di-oxo Re, which regenerates back to the mono-oxo structure through a hydrogen migration process.

From the aforementioned theoretical calculations, there are three candidate structures for the isolated ReO_x . These structures are mono-oxo, di-oxo, and tri-oxo, which are seen in Figure 6.1. "Oxo" designation refers to the number of donor groups or terminal oxygen double bonds on the Re. While ReO_x species with various double bonded oxide structures are most commonly reported, cross-linked bridge structures, where Re atoms are linked together with O atoms, have been experimentally observed in 3 wt.% $\text{Re}_2\text{O}_7/\text{ZrO}_2$ and have been proposed to exist in $\text{ReO}_x\text{-Pd}/\text{CeO}_2$ [255, 181]. Unfortunately the surface structures of ReO_x on CeO_2 have not been confirmed by vibrational spectroscopy. Spectral analysis of ReO_x has been performed of other metal oxide supports, such as the previous mentioned ZrO_2 , along with Al_2O_3 , TiO_2 , and Cr_2O_3 and SiO_2 [255, 256, 142, 127, 12]. However, extensive spectrographic analysis is necessary for the $\text{ReO}_x/\text{CeO}_2$ in order to determine which proposed S-HDO mechanism is accurate.

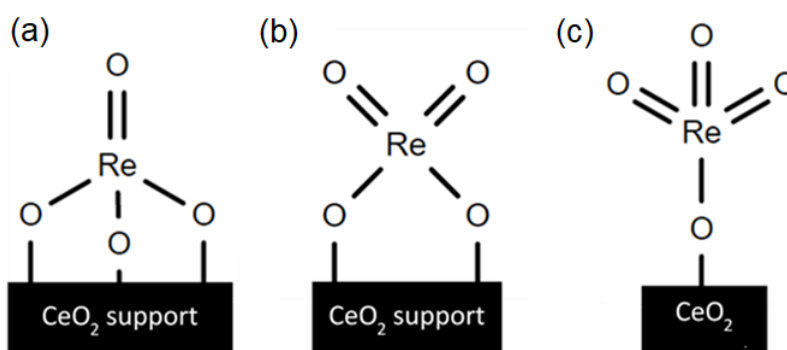


Figure 6.1: The proposed possible structural configurations ReO_x on CeO_2 : (a) mono-oxo, (b) di-oxo, and (c) tri-oxo.

$\text{ReO}_x\text{-Pd}/\text{CeO}_2$ has been developed as a state-of-the-art catalyst for simultaneous hydrodeoxygenation (S-HDO). This reaction removes vicinal hydroxyl groups of sugar

alcohols in order to generate new platform chemicals. The value in this process comes from the ability to take fermented lignocellulosic biomass, which is typically made from plant waste, and generate useful biofuels and chemicals [5, 181]. S-HDO is a culmination of two reaction mechanisms, the deoxydehydration (DODH) an alcohol, and the hydrogenation of the resulting double alkene bonds [7, 234, 180]. Understanding the way ReO_x is oriented on the support can allow us to have a better understanding of the fundamental steps of S-HDO and optimize the reaction for the generation of the value added chemicals.

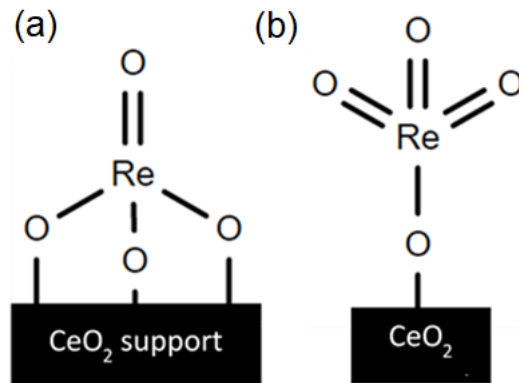


Figure 6.2: The two major ReO_x species that are proposed. (a) mono-oxo (Xi *et al.*) and (b) tri-oxo (Ota *et al.*)

The potential structures that Xi *et al.* and Ota *et al.* proposed are the mono-oxo and tri-oxo structures, respectively, and are seen in Figure 6.2 [263, 181]. Isotope exchange of the oxygen is a way to determine what species the ReO_x exhibits while supported by CeO_2 . Multiple isotope exchange experiments on ReO_x have been done to determine speciation on supports other than CeO_2 , such as Al_2O_3 , Cr_2O_3 , SiO_2 , TiO_2 , and ZrO_2 [256, 255, 142, 127, 12]. The principle relies on the modeling of bond vibrations between the atoms via Hooke's law [188]. After reduction of the ReO_x on CeO_2 , $^{18}\text{O}_2$ is introduced and bonds to the Re. The increase in mass from ^{16}O to ^{18}O causes the Re and O bond vibration to dampen, which shows a redshift in the bands representing the bond vibration in spectral images. This change in vibration can be

seen when utilizing a model for a simple rigid diatomic molecule [255, 242, 282, 69]. Equation 6.1 is a generalized form of the vibrational change between a metal-oxygen bond based off the isotope exchange:

$$\frac{\nu_{16O}}{\nu_{18O}} = \sqrt{\frac{\frac{1}{m_M} + \frac{1}{m_{16O}}}{\frac{1}{m_M} + \frac{1}{m_{18O}}}} \quad (6.1)$$

where, $\frac{\nu_{16O}}{\nu_{18O}}$ is the isotope exchange ratio, which is a ratio of the vibrational frequencies of the bond in wavenumbers (cm^{-1}). The masses of the metal, ^{16}O isotope and ^{18}O isotope are represented by m_M , m_{16O} , and m_{18O} respectively (amu). Utilizing this ratio allows us to observe what structure is present on the surface, because each possible species has different theoretical values for the vibration change based on the isotope exchange. Additionally, it has been shown that multiple different species can exist on the surface, which can complicate the post-exchange spectral analysis and reaction hypotheses. ReO_x on TiO_2 has been shown to exhibit both mono-oxo and di-oxo structures at 823 K [12]. Additionally, mono-oxo metal oxide species on ZrO_2 have been shown to co-exist with the oxygen bridge cross-links [255].

6.2 EXPERIMENTAL METHODOLOGY

6.2.1 1 WT.% $\text{REO}_x/\text{CeO}_2$ SYNTHESIS

The catalyst utilized 1 wt.% loading of ReO_x on CeO_2 in order to easily observe the surface structures in Raman spectroscopy and to provide a low enough loading to minimize cross-linking bridge structures. Sample synthesis was performed via the methods described by Ota *et al.* and MacQueen *et al.* [181, 143]. Cerium (IV) oxide (CeO_2) was acquired by Daiichi (CAS No. 1306-38-3). Ammonium perrhenate (NH_4ReO_4) (CAS No. 13598-5-7) and the $^{18}\text{O}_2$ isotope (CAS No. 32767-18-3) were both obtained by Sigma-Aldrich. The isotope had 99% purity.

The CeO₂ was calcined in air at 873 K for 3 hours. It was then impregnated with ReO_x by wet impregnation using an aqueous solution of NH₄ReO₄. This was dried at 383 K for 12 hours to remove all water from the precipitate. The leftover ReO_x/CeO₂ solid was then calcined in air at 773 K for 3 hours. Afterwards a mortar and pestle were used to ground the catalyst into a powder.

6.2.2 IN-SITU RAMAN SPECTROSCOPY OF THE ISOTOPE EXCHANGE

An *in situ* Raman spectroscopy was performed on the 1 wt.% sample in order to determine the extent of isotope exchange and the effects on the molecular vibrations. All measurements were taken using the Horiba XploRA Plus Raman microscope described in Section 6.1. The excitation laser source was a red 638 nm diode laser with a power of 30 mW. The Raman measurements were calibrated against a polystyrene standard and detected using the charge-coupled detector (CCD), which was cooled to 223 K. Preliminary scans of the 1 wt.% ReO_x/CeO₂ sample were taken at ambient conditions to measure the baseline bond vibrations. Afterward the sample was calcined by heating to 823 K at a rate of 50 K/min. The sample was exposed to a flow of 20 sccm ultra-high purity (UHP) O₂ (99.9993% O₂) in a Linkham cell. Calcination was performed for 30 minutes in this environment, and a Raman measurement was taken. Afterwards, the O₂ was purged from the *in situ* cell using Ar, and the samples were reduced for 10 minutes under 20 sccm of H₂ at the same temperature. A measurement was taken in order to ensure complete reduction. This calcination and reduction cycle was repeated with Raman measurements taken between each step.

In order to introduce ¹⁸O₂ into the system, a sample cylinder cell was set up that had a volume of 25 cm³. The sample cylinder was purged using a roughing vacuum pump while with heating the cylinder at 473 K over night. The 2 bar of the isotope was transferred to a the sample cylinder. This allowed for a batch introduction of the isotope gas to the reduced sample, but also required a purged environment

for the *in situ* cell. After the second reduction the Linkham cell was purged using a roughing vacuum pump, taking careful consideration to not disturb the powder sample. The sample cylinder containing $^{18}\text{O}_2$ was connected to the Linkham cell via a quick connect and introduced to the 1 wt.% $\text{ReO}_x/\text{CeO}_2$. A calcination was performed in the $^{18}\text{O}_2$ environment at 823 K for 30 minutes, and spectral measurement was taken. The sample was reduced again in the same H_2 condition as the previous reduction and recalcined using $^{18}\text{O}_2$, with spectral measurements taken after each step. This calcination temperature was chosen due to previous experiments done on similar catalysts, where the calcinations were performed at temperatures between 723 to 823 K [255, 256, 248]. High temperature calcination allowed for faster oxidation with the $^{18}\text{O}_2$, preventing any residual oxygen from the support from transferring to the bare Re metal, thus ensuring sufficient isotope exchange within the studied time frame.

6.2.3 TIME-RESOLVED *IN-SITU* FTIR SPECTROSCOPY OF THE ISOTOPE EXCHANGE

Fourier transform infrared spectroscopy (FTIR) was performed as a complement to the Raman spectral data, and as a way to take rapid time-resolved measurements with a good signal-to-noise ratio. The *in situ* FTIR measurements were taken at near identical conditions to the Raman spectroscopic measurements. Spectra were taken using a Bruker Vertex 70 FTIR spectrometer that was equipped with a mercury cadmium telluride (MCT) detector and KBr beam splitter. The 1 wt.% $\text{ReO}_x/\text{CeO}_2$ sample was loaded into a diffuse reflectance infrared Fourier Transform spectroscopy (DRIFTS) cell and was heated to 823 K at 50 K per minute, under a flowing 20 sccm N_2 environment. Due to a lack of flowing O_2 to the FTIR, calcination was performed using the 25 cm^3 sample cylinder with a pressure of 1.4 bar. The system was purged of N_2 and the sample cylinder was connected to the DRIFTS cell. Calcination was performed at 823 K for 30 minutes with spectral measurements taken every minute.

Afterward the sample was reduced with 20 sccm H₂ for 30 minutes at 773 K, and the cell was purged again with N₂. Finally, the sample cylinder was filled with 1.4 bar ¹⁸O₂ and attached to the DRIFTS cell for the isotope exchange. Time-resolved measurements were taken for 30 minutes. The process was repeated after a reduction cycle with H₂

6.3 RESULTS AND DISCUSSION

6.3.1 IN-SITU RAMAN SPECTROSCOPY OF THE ISOTOPE EXCHANGE

Baseline measurements of the ¹⁶O at the above calcination conditions were taken in order to provide a point of comparison for the isotope ReO_x. Two sets of ¹⁸O ReO_x/CeO₂ Raman spectra data were captured in order to observe how the isotope exchanged proceeded [127, 256]. The individual spectrum were baseline corrected then normalized to the total area under the curve, resulting in a total spectrum area of unity, which allowed for comparisons between spectra to calculate the amount of isotope exchange [13]. Figure 6.3 is the normalized spectra of the 1 wt.% ReO_x/CeO₂ at each of the calcination steps during the isotope exchange.

Figure 6.3(f) is the spectrum of the as-synthesized sample, and shows three primary bands. These Raman bands are seen in Figure 6.4 and include a convolution of the symmetric and asymmetric stretches of di-oxo ¹⁶O=Re=¹⁶O (972 and 961 cm⁻¹), the asymmetric stretch of the bridge Re-¹⁶O-Re (881 cm⁻¹), and the bending of the hydroxyl Re-¹⁶OH (834 cm⁻¹) [12, 11, 20]. As the sample is heated, there is visible shifting of the peaks along with splitting of the ReO_x band. This separation reveals that another Raman mode with a higher wavenumber was present in the region that contained the di-oxo species, seen in Figure 6.3(e). After reduction and calcination in ¹⁶O, the band separation is more distinctive, as seen in 6.3(c) and (d). After the isotope is introduced to the reduced ReO_x/CeO₂, new bands appear at lower wavenumbers (900-950 cm⁻¹), seen in 6.3(b). These bands are the isotope exchanged

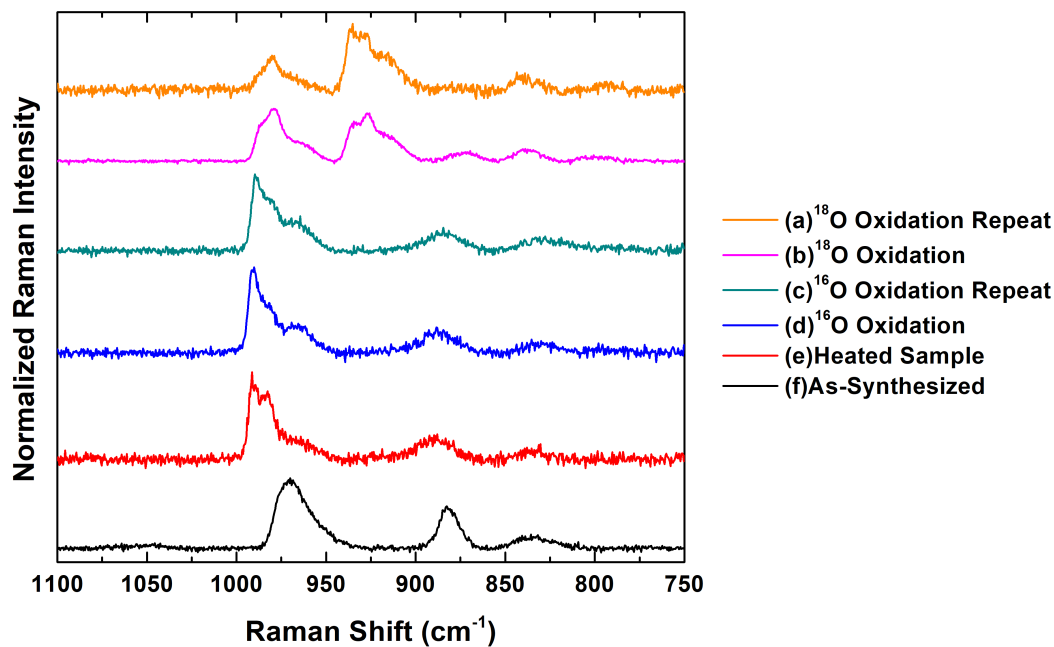


Figure 6.3: *In situ* Raman spectra at each calcination step. The heated sample (e) is a measurement of the 1 wt.% $\text{ReO}_x/\text{CeO}_2$ at 823 K in an Ar environment. Spectra (a-d) were taken with the labeled gas at the same temperature.

bands of the previously labeled bands and are redshifted as a result of the increase in mass [111]. After an additional reduction and oxidation cycle in the isotope, the ^{18}O bands increased in intensity, indicating further substitution. The leftover ^{16}O bands are potentially a result of ^{16}O transfer from the CeO_2 support, or a minor leak of atmospheric air into the stage when using the quick connect.

Additional Raman mode analysis of the as-synthesized sample is shown in Figure 6.4. All bands were fitted using a Gaussian band shape due to measurements of a solid material [30]. As previously mentioned, the di-oxo ReO_x symmetric and asymmetric stretches were labeled to the 972 and 961 cm^{-1} bands, respectively. These bands actually support an older S-HDO mechanism that Ota *et al.* described, where the reaction begins with a di-oxo ReO_x , seen in Figure 6.5 instead of the tri-oxo structure [180]. The asymmetric stretch of the $\text{Re}-\text{O}-\text{Re}$ was seen at 881 cm^{-1} and is has been reported to be an oxygen bridge that cross-links two separate ReO_x structures [20]. This bridge has been reported to have no effect on the S-HDO reaction [181].

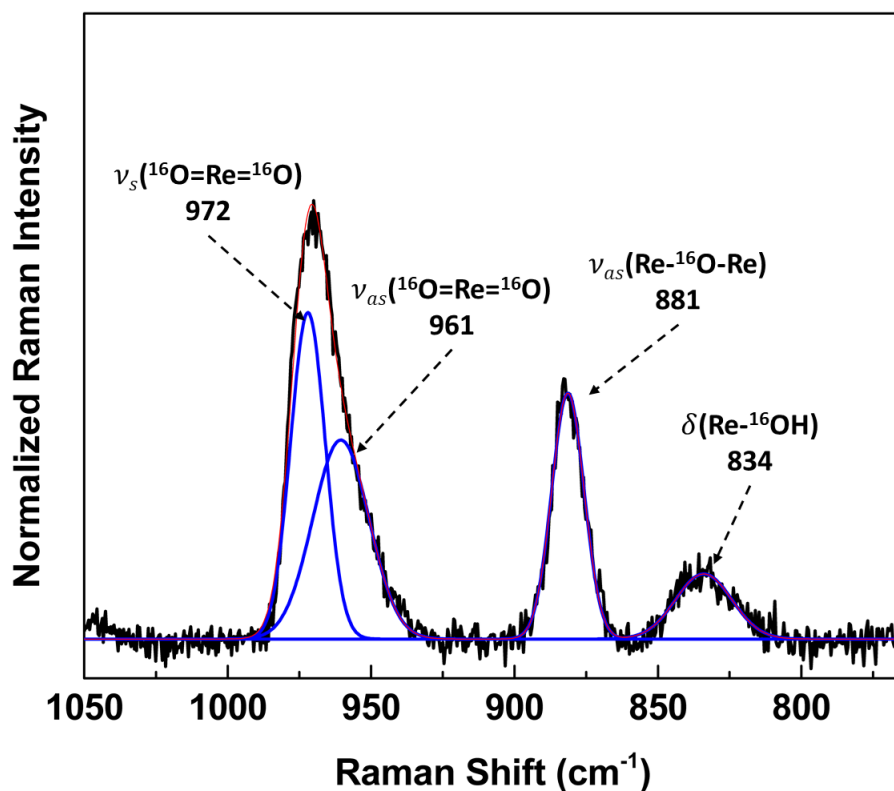


Figure 6.4: The as-synthesized 1 wt.% $\text{ReO}_x/\text{CeO}_2$ Raman spectrum. At ambient conditions, deconvoluting the monomeric band is a non-trivial task.

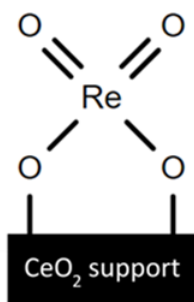


Figure 6.5: The di-oxo configuration for ReO_x . This structure was supported in the literature by Ota *et al.* [180]

The hydroxyl species have been reported by Xi *et al.* as a terminal group on Re [263]. While the mono-oxo $\text{Re}=\text{O}$ species proposed by Xi *et al.* is clearly not visible in the as-synthesized sample, the observed hydroxyl group was seen in their density functional theory (DFT) calculations. The hydroxyl group has been proposed to reduce during

the hydrogen migration, and regenerates into the mono-oxo $\text{Re}=\text{O}$ [263]. This along with the heated samples, indicate that the mono-oxo species is likely present in the as-synthesized sample as well. It should be noted that because the mechanisms incorporate hydrogen migration there is a low chance for the structures to remain measurable in reaction conditions [263, 181].

Figure 6.6, compares the calcination of the sample in $^{16}\text{O}_2$ versus $^{18}\text{O}_2$. Initial investigation into the ^{16}O condition implies the mono-oxo and di-oxo structures are present, which are seen in Figure 6.2. The isotope exchange validates this, due to the number of bands present after an incomplete isotope exchange. In a mono-oxo structure, there are two stretching modes ($\text{M}=\text{}^{16}\text{O}$ and $\text{M}=\text{}^{18}\text{O}$). With a di-oxo structure, there are three major stretching modes ($\text{M}=(\text{}^{16}\text{O})_2$, $\text{}^{16}\text{O}=\text{M}=\text{}^{18}\text{O}$, and $\text{M}=(\text{}^{18}\text{O})_2$). Finally, with a tri-oxo species, there are 4 major modes ($\text{M}=(\text{}^{16}\text{O})_3$, $\text{}^{18}\text{O}=\text{M}=(\text{}^{16}\text{O})_2$, $\text{}^{16}\text{O}=\text{M}=(\text{}^{18}\text{O})_2$, and $\text{M}=(\text{}^{18}\text{O})_3$) [255]. Additionally, the symmetric and asymmetric stretches can be differentiated with each of these species. Before the isotope exchange, the bands are limited to the symmetric and asymmetric stretches of the ^{16}O chemistry and Figure 6.6 (a), shows that three peaks were present. These are labeled as $\nu(\text{Re}=\text{}^{16}\text{O})$ (991 cm^{-1}), $\nu_s(\text{}^{16}\text{O}=\text{Re}=\text{}^{16}\text{O})$ and $\nu_{as}(\text{}^{16}\text{O}=\text{Re}=\text{}^{16}\text{O})$ (985 and 966 cm^{-1}). Furthermore, the cross-linked oxygen bridge $\nu_{as}(\text{Re}-\text{}^{16}\text{O}-\text{Re})$ (888 cm^{-1}) and hydroxyl bend $\delta(\text{Re}-\text{}^{16}\text{OH})$ (830 cm^{-1}) are still present at calcination conditions. These visualization of these structures on the support can be seen in Figure 6.7.

After the exchange a total of eight peaks are associated with the ReO_x speciation. These bands have been labeled in Figure 6.6(c-d). The at band 936 cm^{-1} corresponds with the redshifted mono-oxo stretch mode, $\nu(\text{Re}=\text{}^{18}\text{O})$. The exchanged di-oxo modes are seen at 958 , 933 , 927 , and 913 cm^{-1} and correspond to $\nu_s(\text{}^{18}\text{O}=\text{Re}=\text{}^{16}\text{O})$, $\nu_{as}(\text{}^{18}\text{O}=\text{Re}=\text{}^{16}\text{O})$, $\nu_s(\text{}^{18}\text{O}=\text{Re}=\text{}^{18}\text{O})$, and $\nu_{as}(\text{}^{18}\text{O}=\text{Re}=\text{}^{18}\text{O})$ respectively. The single exchanged vibrations ($\nu_s(\text{}^{18}\text{O}=\text{Re}=\text{}^{16}\text{O})$ and $\nu_{as}(\text{}^{18}\text{O}=\text{Re}=\text{}^{16}\text{O})$) were deconvoluted

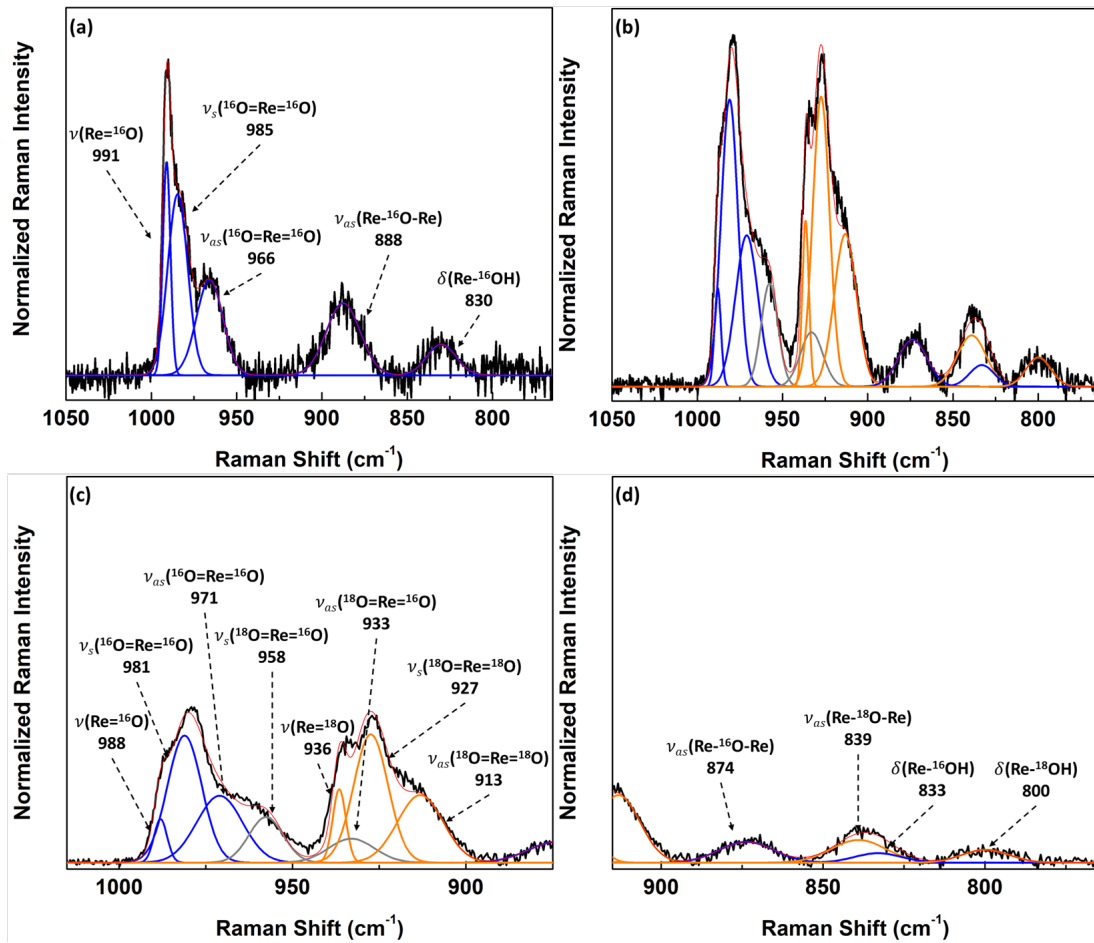


Figure 6.6: Raman spectra comparing the 1 wt.% ReO_x/CeO₂ before and after the isotope exchange. (a) Fitted sample calcined at 823 K in the ¹⁶O₂ environment pre-exchange. (b) Calcined in ¹⁸O₂. (c) The fittings of the exchanged sample mono-oxo and di-oxo structures (d) The fittings of the exchanged sample oxygen bridges and hydroxyl groups.

via fitting based off of calculations from Equation 6.1, the results of which are seen in Table 6.1. It has been reported that the single substitution asymmetric stretch of the di-oxo structure is difficult to parse from the data, which can be corroborated with our results [127]. Utilizing the theoretical values for as the fitting start point allowed for a better fit among all the spectra and for the identification of the single substitution bands at 958 (symmetric stretch) and 933 (asymmetric stretch) cm⁻¹. The full-width half-max was properly constrained for bands with the same speciation

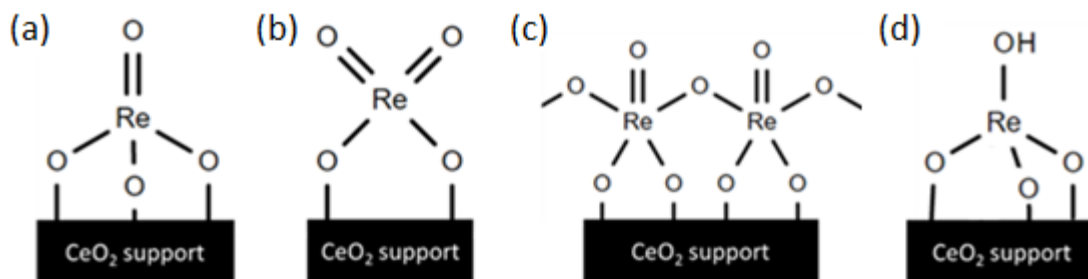


Figure 6.7: The ReO_x structures discovered as a result of the isotope exchange. (a) mono-oxo (b) di-oxo (c) cross-linked structure (d) hydroxyl group.

during fitting. Additionally, the area ratio of the symmetric to asymmetric stretches of the di-oxo ReO_x was constrained for the fitting as well.

$$\frac{\nu_{18\text{O}}}{\nu_{16\text{O}}} \approx \sqrt{\frac{m_{16\text{O}}}{m_{18\text{O}}}}, m_M \gg m_{18\text{O}}, m_{16\text{O}} \quad (6.2)$$

As previously mentioned in Section 6.1, the simple rigid diatomic molecule model was used to determine the theoretical band shift isotope exchange ratio. The isotope exchange ratio ($\frac{\nu_{16\text{O}}}{\nu_{18\text{O}}}$) from Equation 6.1 can be simplified to Equation 6.2. However, this is only holds in scenarios where the metal, M, has a much higher atomic mass than the oxygen isotopes. Rhenium has approximately eleven times more mass than oxygen isotopes, so the approximation holds. The isotope exchange ratio provides a scaling factor determine the redshift that would be seen based of the mass change. It should be noted that since this is a diatomic model, it does not fully account for vibrational changes from multiple isotope substitutions in higher level speciation. Such modeling require *ab initio* or DFT calculations to make a more accurate assessment [291]. However, the rigid diatomic model is a good first approximation that has been utilized in literature [255, 256, 282, 69]. The average difference between the theory and calculated peak shift of the vibrational stretches is 3.33 cm^{-1} with a standard error of 0.61 cm^{-1} . The bending mode, $\delta(\text{Re}-\text{OH})$, had a difference of 14 cm^{-1} between the theoretical and experimental values, but this was a result utilizing the diatomic model, which is developed for stretching modes, on a bending vibrational mode.

Table 6.1: Raman Shifts from the ^{18}O Substitution

Vibrational Mode	Raman Shifts (cm^{-1})			
	$^{18}\text{O}_2$ Theoretical		$^{18}\text{O}_2$ Measured	
	Single Sub.	Double Sub.	Single Sub.	Double Sub.
ν ($Re = O$)	939	N/A	936	N/A
ν_s ($O = Re = O$)	955	933	958	927
ν_{as} ($O = Re = O$)	937	915	933	913
ν_{as} ($Re - O - Re$)	841	N/A	839	N/A
δ ($Re - OH$)	786	N/A	800	N/A

The extent of the isotope exchange can be seen in Table 6.2. These values were determined by taking the fitted areas of the single and double substitution bands and dividing the sum of those areas by the area of the leftover non-substituted ReO_x . The initial ^{18}O exchange shows that each observable species had a ratio greater than one, which means that at least fifty percent of the bonds substituted with the isotope oxygen. After the first exposure to $^{18}\text{O}_2$, the mono-oxo structure experienced the highest extent of exchange at about 62% substitution. After a reduction and second exposure to $^{18}\text{O}_2$, the efficacy reached over 90%, while the di-oxo structure reached approximately 70%. The bands for the oxygen bridge and hydroxyl modes show a near complete exchange after the second exposure cycle, despite exchanging less than the mono-oxo structure did after the first cycle. The high substitution efficacy of the mono-oxo structure implies higher reactivity to oxygen than the di-oxo species. This suggests that a change in the oxidation state of this structure is likely, which is favorable to the S-HDO reaction mechanism progression, which makes the Xi *et al.* mechanism a strong candidate for S-HDO. The di-oxo structure still is a potential active site for S-HDO, because it had a significant extent of isotope exchange, but it would possibly be a slower reaction mechanism.

Table 6.2: Area Ratios of Raman Spectra

Vibrational Mode	Raman Spectral Area Ratios	
	$^{18}\text{O}/^{16}\text{O}$ Ratio	
	^{18}O First Cycle	^{18}O Second Cycle
ν ($Re = O$)	1.68	9.86
ν_s ($O = Re = O$)	1.37	2.45
ν_{as} ($O = Re = O$)	1.37	2.45
ν_{as} ($Re - O - Re$)	1.09	Near Complete
δ ($Re - OH$)	1.36	Near Complete

6.3.2 TIME-RESOLVED *IN-SITU* FTIR SPECTROSCOPY OF THE ISOTOPE EXCHANGE

Time-resolved *in situ* FTIR data was taken in order to measure the isotope band formation and determine the rate of isotope exchange. Figure 6.8 shows two exposure cycles of $^{18}\text{O}_2$ to the 1 wt.% $\text{ReO}_x/\text{CeO}_2$, with Figure 6.8(a) as the first cycle and 6.8(b) is the second cycle. The reduced catalyst was exposed to the $^{18}\text{O}_2$ environment for 25 minutes at 823 K. The peak positions were fitted and similarly labeled to the positions seen in the Raman. FTIR and Raman spectroscopy are considered complementary techniques and measure similar phenomenon using different properties. The ReO_x structures and oxygen bridge ($\text{Re}-\text{O}-\text{Re}$) band redshifts are clearly visible in the IR spectra, but the hydroxyl species is more difficult to measure. Figure 6.8(a) shows that the hydroxyl species at 828 cm^{-1} vanishes and is no longer seen during isotope uptake. This may be due to a weak intensity of the bending modes. As for the other modes, the band intensities of the isotope exchanged structures increase with time and per cycle.

The increase in intensity of the bands associated with the isotope allows us to determine the amount and rate of the isotope exchange. These bands are redshifted similarly to the Raman vibrations seen in the Raman spectra and the peaks can be labeled the same. The first cycle shows that the substitution reaches steady state

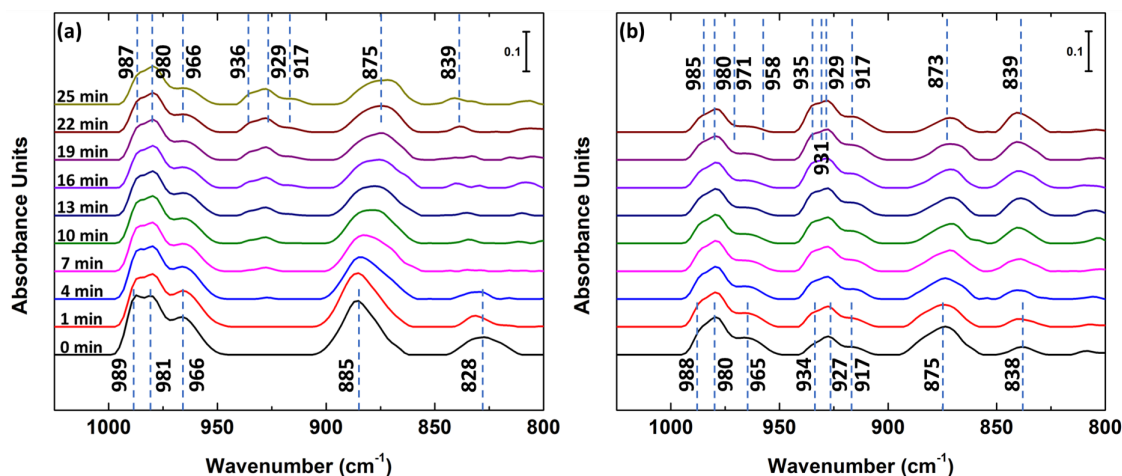


Figure 6.8: The time-resolved FTIR spectra of the 1 wt.% $\text{ReO}_x/\text{CeO}_2$. (a) Initial oxidation under $^{18}\text{O}_2$. (b) Second oxidation under $^{18}\text{O}_2$ after a reduction step.

after approximately 15 minutes of calcination in 823 K. The amount of exchange is calculated the same way as with the Raman spectra, by calculating the ratio of the band area of the ^{18}O over the ^{16}O structures. After the second 25 minutes of exposure, the $^{18}\text{O}/^{16}\text{O}$ area ratio is approximately 1.534. This leads to an overall exchange of about 61% from the ^{16}O to the ^{18}O . Furthermore, the pre-steady-state $^{18}\text{O}/^{16}\text{O}$ exchange rate was calculated from the 1, 7, and 13 minute spectra, which was determined to be 2.3% exchange per minute. After the two cycles of ^{18}O exposure, the di-oxo structure had a higher area ratio than the mono-oxo, seen in Table 6.3. This is different than what was observed in the Raman areas in Table 6.2. This variance could be a result of difference in measurement technique used in analysis. However, the overall trend of increasing isotope exchange is still observed, but is not nearly as extreme as was observed in the Raman spectra. The similar $^{18}\text{O}/^{16}\text{O}$ area ratios between the mono-oxo and di-oxo imply that both species may have similar reactivity to oxygen and will both undergo separate S-HDO reactions on the surface, instead of having a dominant mechanism.

Table 6.3: Area Ratios of FTIR Spectra

Vibrational Mode	FTIR Spectral Area Ratios	
	$^{18}\text{O}/^{16}\text{O}$ Ratio	
	^{18}O First Cycle	^{18}O Second Cycle
ν ($\text{Re} = \text{O}$)	0.243	1.467
ν_s ($\text{O} = \text{Re} = \text{O}$)	0.350	1.873
ν_{as} ($\text{O} = \text{Re} = \text{O}$)	0.350	1.873
ν_{as} ($\text{Re} - \text{O} - \text{Re}$)	0.148	1.873

6.4 CONCLUSIONS

The *in situ* ^{18}O isotope exchange vibrational spectroscopy showed that 1 wt.% $\text{ReO}_x/\text{CeO}_2$ contained multiple structures. These structures were seen in Figure 6.7 and included two structures (mono-oxo $\text{Re}=\text{O}$ and di-oxo $\text{O}=\text{Re}=\text{O}$), the oxygen bridge ($\text{Re}-\text{O}-\text{Re}$), and a hydroxyl species ($\text{Re}-\text{OH}$). This also verifies that multiple species are possible [249, 127, 12, 111]. The Raman and FTIR spectra both show that the efficacy of the isotope exchange was approximately 60%. Time-resolved FTIR showed that the rate of change for the $^{18}\text{O}/^{16}\text{O}$ ratio was 2.3% per minute.

Due to the multiple species and similar rate of exchange between them, there has not been a definitive determination on which of the two proposed S-HDO mechanisms is dominant [180, 263]. The di-oxo reduction (Re^{VI} to Re^{IV}) and the mono-oxo mechanism are still possible and additional reaction studies are required in order to determine which mechanism is preferred during S-HDO. Furthermore, additional isotope exchanges on different weight loadings (0.5, 2, 5 wt.%) of ReO_x can provide information on if the speciation stays consistent at different loadings.

Finally, DFT can provide a more rigorous computational theory for the vibrational predictions. This not only provides a link between computational and experimental methods, but allows for further understanding of the fundamental chemistry behind the exchange and can make fitting for specific modes a less time intensive task. A DFT

model of Raman prediction has been suggested by using the Lagrangian approach towards vibration prediction [199]. However, *ab initio* and DFT calculations of IR and Raman modes have been predicted using calculations based off of polarizability and dipole moment derivatives [291]. Applying these to isotope exchange predictions can further validate laboratory experiments.

CHAPTER 7

MODELING THE ADHESIVE STRENGTH OF A THIOL-ENE SEALANT VIA RESPONSE SURFACE DESIGN

7.1 BACKGROUND AND MOTIVATION

In the field of aviation, there has been a demand for strong polymer sealant materials. Modern aircraft use integral fuel tanks and are typically located in the wings and fuselage. These tanks can contain fuel quantities of over 250,000 liters and are one of the primary drivers for the polymer sealants. The sealant acts as a preventative measure for the leak of fuel into the electrical components of the aircraft or the introduction of moisture into the tank, both of which can lead to catastrophic failure [66, 68, 67]. An example of the danger with the lack of proper sealing is the Trans World Airlines Flight 800 (TWA 800) accident. This incident was a tragic loss of life that was a result of an ignition of fuel that was leaking due to overpressurization in the tank [175]. Following the accident, updates to fuel-tank protections were ordered by the Department of Transportation in 2008.

Parts of chapter adapted from manuscript submitted for publication: B. Ruiz-Yi, C. Oswald, L. Frankovich, A. Fersner, B. Kandapallil, J. Lauterbach (2020). *Response Surface Design of a Thiol-Ene Polymer Sealant to Model Adhesive Strength*.



Figure 7.1: The reconstructed wreckage of flight TWA 800. [175].¹

Sealant is typically applied to stress or contact points, such as metal-metal interfaces, rivet points, and joints [68]. Desired properties for these types of sealants are high adhesion strength, fast cure speeds, corrosion resistance, and high fracture resistance [66, 24, 58]. Common polymers for this application consist of epoxies, polyurethanes, and silicones, with application conditions being optimized for room temperature applications [58, 179, 48]. Despite improvements to cure speed for these types of polymers, tack-free time still range from 4 to 64 hours, with full cure time ranging from 7 to 136 hours [58, 50, 189]. Additionally, application to the fuel tank is sometimes done in environments with temperatures as low as 283 K. Alternative

¹Image reprinted from: National Transportation Safety Board. Aircraft accident report - In-flight breakup over the Atlantic Ocean Trans World Airlines Flight 800 Boeing 747-131, N93119, near East Moriches, New York, July 17, 1996. (Report No. PB2000-910403). See Figure F.3 for copyright permission.

materials have been considered in order to decrease cure time and be utilized at low temperatures.

A prominent synthesis technique for these materials is the ultraviolet (UV) curing, which uses UV radiation to initiate polymerization. UV curing is a rapid synthesis technique that utilizes a UV active photoinitiator that generates a free-radical group to propagate a reaction that can complete on the order of minutes [33]. The rate of polymerization is variable based on input variables such as choice of monomer, photoinitiator, and irradiance, but UV curing has an ease of set-up and application, which makes labor faster and easier [33]. However, optimization of the curing process is difficult, due to the wide range of processing conditions that affects the synthesis process and material property.

While low cure times are a desirable trait in fuel tank sealants, high adhesion strength must also be considered due to the caustic environments and high loads they are exposed to. Adhesion is a complex, system dependent property, where a majority of the strength comes from dissipation of stress [2]. Adhesive failure tends to be a result of weak bonding at the sealant-substrate interface and when fracture stress energy does not dissipate into the bulk [163, 194, 67]. However, adhesive properties can be adjusted through synthesis conditions of a UV curable sealant, instead of completely changing the material system.

Thiol-ene is polymer system that is UV curable, and is an example of click chemistry, which is a term for a class of reactions that mimic examples seen in nature. It performs polymer synthesis via the linking of carbon-heteroatoms bonds, which is a similar reaction that is seen in DNA polymerization and RNA translation[117]. Click reactions are advantageous over other types of reactions due to their high yields and selectivity, modular nature, and insensitivity to water [117, 118, 25].

The thiol-ene click reaction takes place between a monomer that contains a thiol group, R-SH, and an alkene. There are two reaction pathways that have been studied:

the radical addition and Michael addition [91]. Due to the click chemistry nature of the reaction, it is regioselective and produces near quantitative yields based off the reactant monomers [117]. Additionally, the reaction can be done in batch, is insensitive to air and water, and can utilize a wide range of thiols and alkenes. Thiol-enes are of interest because of their applicability in shape memory polymers, lithography, and adhesives, which has been attributed to their low volume shrinkage, low shrinkage stress, and their ability to form homogeneous networks [170]. These properties are a result of the basic structure of the thiols, which include four prominent structures, alkyls, phenols, proprionates, and glycolates [91, 90].



Figure 7.2: The anti-Markovnikov addition of a thiol species to an alkene group. There are two reaction mechanisms: (a) free-radical addition and (b) catalyzed Michael addition [91].

The hydrothiolation mechanism via free-radical chemistry can be seen in the Figure 7.3 [46]. Initiation begins with photolysis of a photoinitiator via UV radiation, which forms the thiyl radical, R_1-S^\bullet . Propagation occurs with the thiyl radical directly adds to the $C=C$ bond with an anti-Markovnikov orientation. The new oligomer yields a carbon centered radical that chain transfers to a new thiol molecule, which gives rise to a new thiyl radical. Termination occurs when two of the carbon centered radical oligomers combine or when one combines with a thiyl radical [91, 170, 46, 107]. Oxygen does not inhibit the reaction because if present, it will incorporate into the polymer as a peroxy radical species and regenerate the thiyl [46]. It should be noted that the propagation of the reaction is not the standard chain polymerization but a unique radical step-growth polymerization [174, 6].

The ideal reaction results in thiol-ene copolymerization with no homopolymer units [178, 40, 135]. Aside from mass transfer limitations, the reaction has near complete conversion. Additionally, due to the chain transfer to the thiol monomer, the reaction requires all monomers to have multi-functionality. The most common thiol-ene polymers develop cross-linked networks that develops a relatively strong system [107].

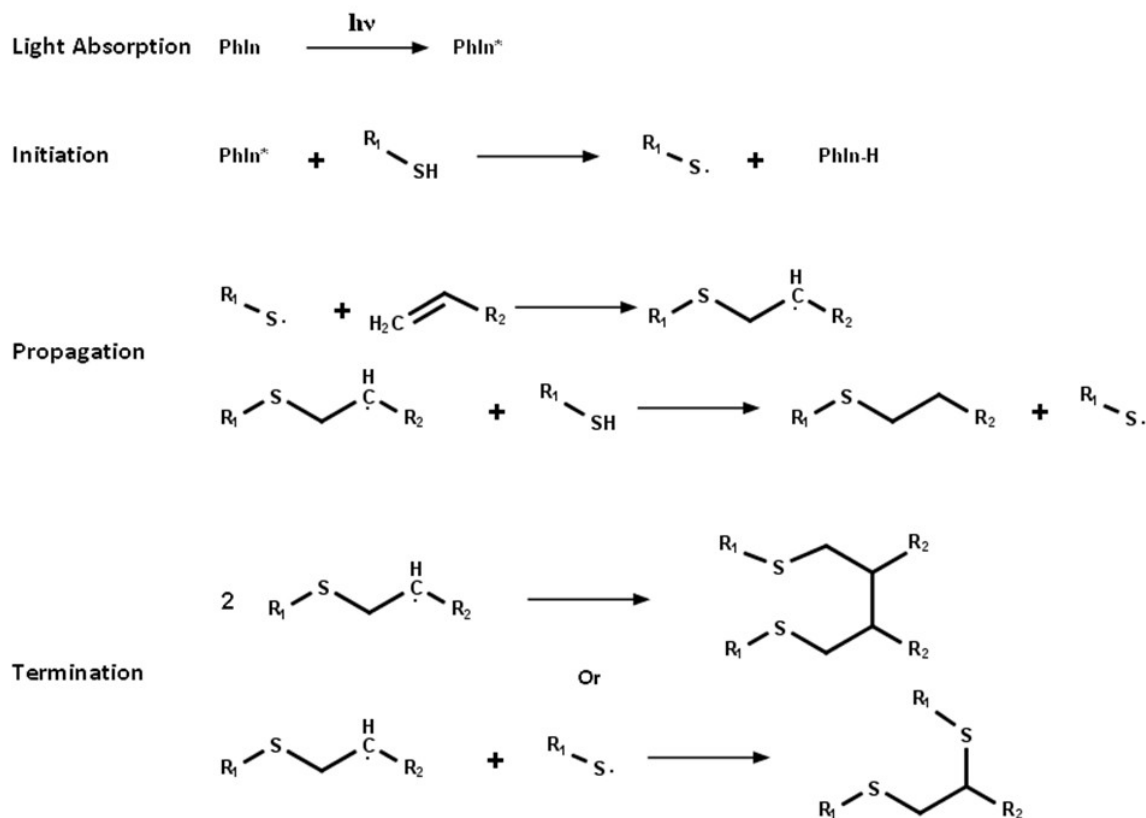


Figure 7.3: The mechanism for a photoinitiated thiol-ene reaction. The reaction is fairly unique due to the step-growth polymerization despite propagating via free-radicals [46].

Despite the advantages presented by UV curable thiol-ene sealant systems, selecting optimized synthesis conditions for a given figure-of-merit remains difficult. This is due to a lack of predictive models for material properties given a set of input variables. A way to predict properties of a given system at unexplored synthesis conditions is desired because of the time consuming nature of testing every individual condition.

A systematic Design of Experiment (DOE) approach can provide an optimized set of conditions for a system, model that predicts properties with given variables, and insight into co-factor effects on the desired response.

7.2 EXPERIMENTAL METHODOLOGY

Section 7.1 discussed the importance of having a strong adhesive lining the fuel tank of an airliner. In particular, the high stress environment of a fuel tank requires a material to retain its adhesive properties to prevent catastrophic failure [66]. However, there has been limited research performed utilizing a systematic design of experiments in order to optimize and predict the synthesis conditions for a given figure-of-merit. Design of experiments (DOE) have been applied to click chemical reactions in the field of biology. Here the development of magnetic microspheres were optimized using response surface methodology in order to enrich glycoproteins via click chemistry [53]. Additionally, a thiol-ene click reaction was used to synthesize cationic carbosilane dendrimers, and a response surface methodology was used to analyze the stability of the dendrimers at varying pHs, temperatures, and incubation times [62]. These examples show that this approach can be used to optimize and develop a function for to predict mechanical properties of a thiol-ene reaction, such as adhesive strength.

7.2.1 DESIGN OF EXPERIMENTS

Response surface methodology (RSM) utilizes mathematical and statistical techniques in order to design a set of experiments that will optimize a response based off of the influence of several independent variables [165]. The expected response, η , for a set of variables, ξ , can typically be expressed through the following low-order polynomial equations:

$$\eta = \beta_0 + \sum_{i=1}^k \beta_i \xi_i + \epsilon \quad (7.1)$$

$$\eta = \beta_0 + \sum_{i=1}^k \beta_i \xi_i + \sum_{i=1}^k \beta_{ii} \xi_i^2 + \sum_{i < j} \beta_{ij} \xi_i \xi_j + \epsilon \quad (7.2)$$

where Equation 7.1 is a first-order linear function, while Equation 7.2 is a second-order model. The ϵ term represents any error or noise seen in the response. An expression is chosen based off of the presence of curvature in the system, which requires the second-order polynomial function to model the data. Models with a higher order than two can be used. However, this can lead to an expression that over fits the data. These, models use the method of least squares in order to determine the polynomial parameters, which are seen as the coefficients, β_i . These expressions are not a true physical model and do not fully describe the response-variable relationship outside the measurement region. While they cannot be used to extrapolate and predict the response outside of the measurement region, they do provide a good first approximation when constrained to a relatively small localized region. Furthermore, they can provide a guide to optimize the process for a given figure of merit. Utilizing the method of steepest ascent, the experimental conditions can be optimized using a sequential process that moves in the direction of the gradient toward a determined optimum, which provides a model function that can predict within region of the optimum [27, 29, 168]. RSM tend to employ design spaces that maintain orthogonality (each factor can vary independently of one another), rotatability (the variance of the predicted values are only dependent on the distance from the center), and uniformity (where the number of center point experiments is controlled to maintain uniform precision across all experiments), which can be seen in the spaces in Figure 7.4.

RSM can be designed using a Box-Behnken design or central composite design (CCD). The Box-Behnken design is a design space that provides a design space for three or more factors. Have no embedded factorial design, but is typically sufficient enough to model a quadratic system and is seen in Figure 7.4a. A CCD is similar to a factorial design but focuses around a center point in the design space that is equidistant to axial experimental points. These axial points are similar to the center points

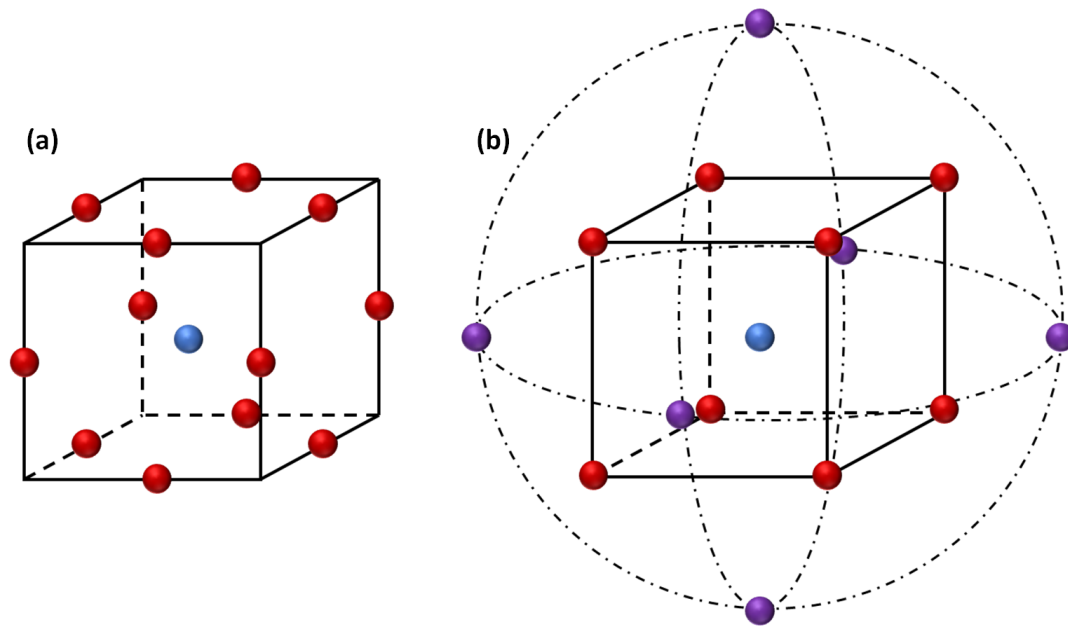


Figure 7.4: An example of two of the common design spaces for RSM. The red points are experimental conditions and blue point is the center point of the experiment. (a) Three-level Box-Behnken design that utilizes a combination of 2^k factorial design and incomplete block design. (b) Three factor central composite design (CCD) that utilizes axial points (purple). [134]

but provide experimental runs that measure a maximum and minimum setting for a factor, which can aid in extrapolation outside the space. This type of design space can be seen in Figure 7.4b. Center point repeats provide a check against experimental instability and determine the internal variance in each experiment (uniformity). Both designs are used to reduce the number of experiments needed to provide an reasonable estimate of a model that optimizes a desired figure-of-merit. are used with coded variable levels, which are numerically coded with -1, 0, and 1 and represent the low, middle, and high quantities in this design [28]. Coding variables allow for centering of the design space and ease of interpretation. For the peel test experiment, the design factors used were the quantitative variables: the cure time and the synthesis temperature. The qualitative (categorical) variables that were used (cross-linking monomer and filler material) provided categorical systems that were measured using the quantitative variables. The categorical variables provided multiple different design spaces

for the quantitative variables. However, if the experiment needed to compress into a singular space, a way to quantify the categorical variables would be necessary. While both of these design spaces are typical for a response surface experiment, the peel test experiment did not employ an exact version of a central composite design.

7.2.2 THIOL-ENE SAMPLE SYNTHESIS

The factors and levels can be seen in Table 7.1. From the table, it can be seen that the levels for each factor was chosen atypically from the major response surface methodology designs. The number of synthesis experiments were increased to a larger than average set of levels for cure time synthesis, because overexposure can result in weak adhesion as well. Therefore, there was a need to increase experimental resolution in order to optimize the exposure time of the synthesis toward the adhesive figure-of-merit. Thus an adjusted factorial design, which does not precisely follow the CCD, was implemented in order to carry out the experiment.

Table 7.1: Response Surface Factors for the Thiol-ene Synthesis

Factors	Levels						
Cure Time (minutes)	3	5	7	10	20	40	60
Cure Temperature (°C)	10			15.56		21.11	
Cross-linking Monomer	TTT			TMPTA			
Filler	None	Sand		Al ₂ O ₃		SiO ₂	

Synthesis was performed using each combination of the levels from Table 7.1. After accounting for each permutation 168 sets of five samples were synthesized using a response surface that varied the cure time, cure temperature, functionality of the alkene monomer, and the solid filler material. This allowed for a rapid assessment of the relevant factors that contributed to the adhesion strength figure-of-merit. The main monomers used have been shown in Figure 2.15 and consist of pentaerythritol tetrakis(3-mercaptopropionate) (PETMP) as the thiol and two different allyl

monomers, 1,3,5-Triallyl-1,3,5-triazine-2,4,6(1H,3H,5H)-trione (TTT) and trimethylolpropane triacrylate (TMPTA). These monomers were chosen because they had been used previously in the literature and as a commercial product [289, 226, 225]. Additionally, they are able to provide a cross-linked network because they have an average functionality greater than two. As mentioned in Section 7.1 the thiol-ene reaction used in these sets of experiments utilized ultraviolet curing as a way to accelerate synthesis and adhesion. In order to initialize and propagate the reaction, a 2,2-dimethoxy-2-phenylacetophenone (DMPA) radical photoinitiator was used. DMPA had been used previously as a photoinitiator and has an optimal UV absorbance at 254 nm and secondary absorbance at 340 nm. Three different solid filler material were used in order to strengthen the adhesive material and also observe their effects on the adhesive on the substrate. The fillers used were 60 Å Al_2O_3 with a surface area of 150 m^2/g (CAS: 1344-28-1), 0.007 μm fumed SiO_2 (CAS: 112945-52-5), and washed sand with varying particle sizes (CAS: 14808-60-7).

The bulk polymers were synthesized on Al plates using a Teflon mold for shaping and easy removal after curing. The dimensions of the molds allowed for 4 by 0.5 inch (11.43 by 1.27 cm) samples. The Al substrate plates used 2024 grade aluminum and were 5 by 1.5 by 0.1 inches (12.7 by 3.81 by 0.254 cm). These can be seen in Figure 7.5. Each plate was cleaned with acetone and roughened with P150 grit sandpaper after each experiment.

The viscous liquid monomers were measured out by volume using macro pipettes. The volumes were determined by calculating the quantities required for a one-to-one ratio of the thiol functional group and allyl functional group. The weight percent of the different fillers to the total mass of the system was 0.5 wt.%. For the DMPA 0.05 wt.% was used for all synthesis conditions. The system was mixed vigorously until the mixture was visually uniform. Five samples were prepared using 8 mL of the mixed solution, which resulted in 6 mm thick samples. The samples were

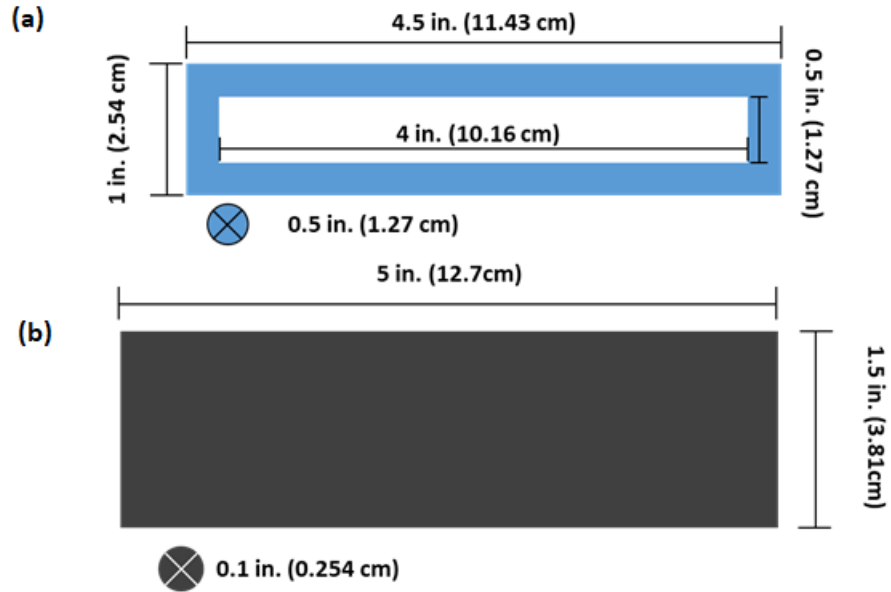


Figure 7.5: Schematic for the (a) Teflon mold and (b) aluminum substrate. The samples were scaled down from the standard.

placed on a 4-pass, 305 mm Hi-Contact Liquid Cold Plate. This plate was made with unfinished aluminum and was plumbed with 9.5 mm copper tubing and cooled with an attached water chiller. The samples were cured at 10, 15.56, and 21.11 °C. Temperatures lower than 21.11 °C were chosen because it was desired to observe curing behaviors where aircraft sealant replacement conditions may be sub-optimal. UV curing took place between three to sixty minutes using a UVP XX-15S bench lamp, which provided a region where over-curing may potentially be observed. The lamp exhibited wavelengths between 254 to 365 nm and had an irradiance of 4500 $\mu\text{W}/\text{cm}^2$. The molds were then removed off the plates and the samples were peel tested.

7.2.3 180° PEEL TEST

Adhesive strength measurements were taken using an Instron 5543A Load Frame with a 100 N load cell. The measurement protocol followed the ASTM D3330 standard for 180° peel test, with the samples scaled down to fit the system [55]. Due to the intrinsic

nature of adhesive strength the sample was safely scaled down. Measurements were taken sequentially while installing the samples into a pair of square hydraulic grips. The peel speed was 10 mm/s and load versus extension graphs were taken as seen in Figure 2.14. From these graphs the average load was for each sample was calculated and peel strength was determined by dividing that value by the width of the sample. Finally, the repeat measurements were used to determine the average peel strength at each experimental point. These values were used to calculate the response surfaces of the categorical pairs in the design space.

7.3 RESULTS AND DISCUSSION

Based of the design space seen in 7.1, there were 168 conditions with five repeat samples, resulting in a total of 840 measurements. As described in 7.2.3, the average peel strength was calculated from taking the average load over sample width while ignoring the delamination region. An average was taken over repeat experiments. For example, after a three-minute cure at 21.11 °C using the TTT monomer and no filler, the average peel load was 1.450 N. All sample widths are 12.7 mm. Therefore, the average peel strength is 0.114 N/mm. Table 7.2 shows the average peel strengths of the thiol-ene trials that were synthesized at room temperature (21.1 °C) with a cure time between 3 and 7 minutes. Additional adhesive strength values can be seen in Appendix E under Table E.1. We see that the TTT based polymer has an average adhesive strength that is higher by approximately a factor of two when compared to the TMPTA based polymer. However, when performing the peel test, all samples de-adhered from the substrate cleaning with no cohesive failure.

Table 7.2: Average Peel Strength of the Thiol-Ene Sealants Synthesized at Room Temperature

Alkene	Time	Temp.	Filler	Peel Strength	Std. Err.
	min.	°C		N/mm	N/mm
TTT	3	21.1	None	0.114	0.011
TTT	3	21.1	Sand	0.297	0.051
TTT	3	21.1	Al ₂ O ₃	0.042	0.042
TTT	3	21.1	SiO ₂	0.064	0.064
TTT	5	21.1	None	0.202	0.034
TTT	5	21.1	Sand	0.127	0.032
TTT	5	21.1	Al ₂ O ₃	0.588	0.058
TTT	5	21.1	SiO ₂	0.522	0.063
TTT	7	21.1	None	0.917	0.079
TTT	7	21.1	Sand	0.385	0.041
TTT	7	21.1	Al ₂ O ₃	0.736	0.067
TTT	7	21.1	SiO ₂	1.035	0.127
TMPTA	3	21.1	None	0.166	0.069
TMPTA	3	21.1	Sand	0.143	0.039
TMPTA	3	21.1	Al ₂ O ₃	0.102	0.007
TMPTA	3	21.1	SiO ₂	0.150	0.025
TMPTA	5	21.1	None	0.284	0.096
TMPTA	5	21.1	Sand	0.136	0.017
TMPTA	5	21.1	Al ₂ O ₃	0.163	0.046
TMPTA	5	21.1	SiO ₂	0.284	0.046
TMPTA	7	21.1	None	0.189	0.034
TMPTA	7	21.1	Sand	0.118	0.018

Alkene	Time	Temp.	Filler	Peel Strength	Std. Err.
	min.	°C		N/mm	N/mm
TMPTA	7	21.1	Al ₂ O ₃	0.102	0.027
TMPTA	7	21.1	SiO ₂	0.207	0.015

Response surfaces were modeled and contour plots, which visualize the RSM function, can be seen in Figure 7.6. Three-dimensional images of the response surfaces can be seen in Appendix E, Figure E.1. From an initial evaluation no optimum was observable in either alkene (TTT and TMPTA) system. A general observable trend shows an increase in adhesive strength as cure temperature and cure time increases. As temperature increase the reaction rate is higher. However, in the TTT system, the gradient of the adhesive strength is in the direction of cure time, initially indicating cure time is a dominant parameter. The TMPTA system shows a greater effect of the cure temperature when silica and alumina is added to the mixture, but visually there is a less consistent trend and shape to the contours when observing the gradient of adhesive strength. The increase in cure time also can allow for the thiol-ene sealants to set into the substrate with the polymerization going to completion, which results in a sample less prone to cohesion failure and has properly adhered to the substrate. However, overexposure to UV radiation can stiffen the sample too much, to the point where the high elastic modulus prevents dissipation of energy within the sealant due to the rigidity of polymer strands. This reduction in energy dissipation has been seen as a detriment to adhesion [2].

The RSM DOE also allows for scrutinization of the individual effects of the factors on the overall figure-of-merit. Figure 7.7 shows the fitted means of the each variable. A non-zero slope of the fitted means represents higher effects of the variable on the figure-of-merit. Cure time and cure temperature have a highly non-zero slope seen in the main effects plots, which is expected due to how influential those variables are to

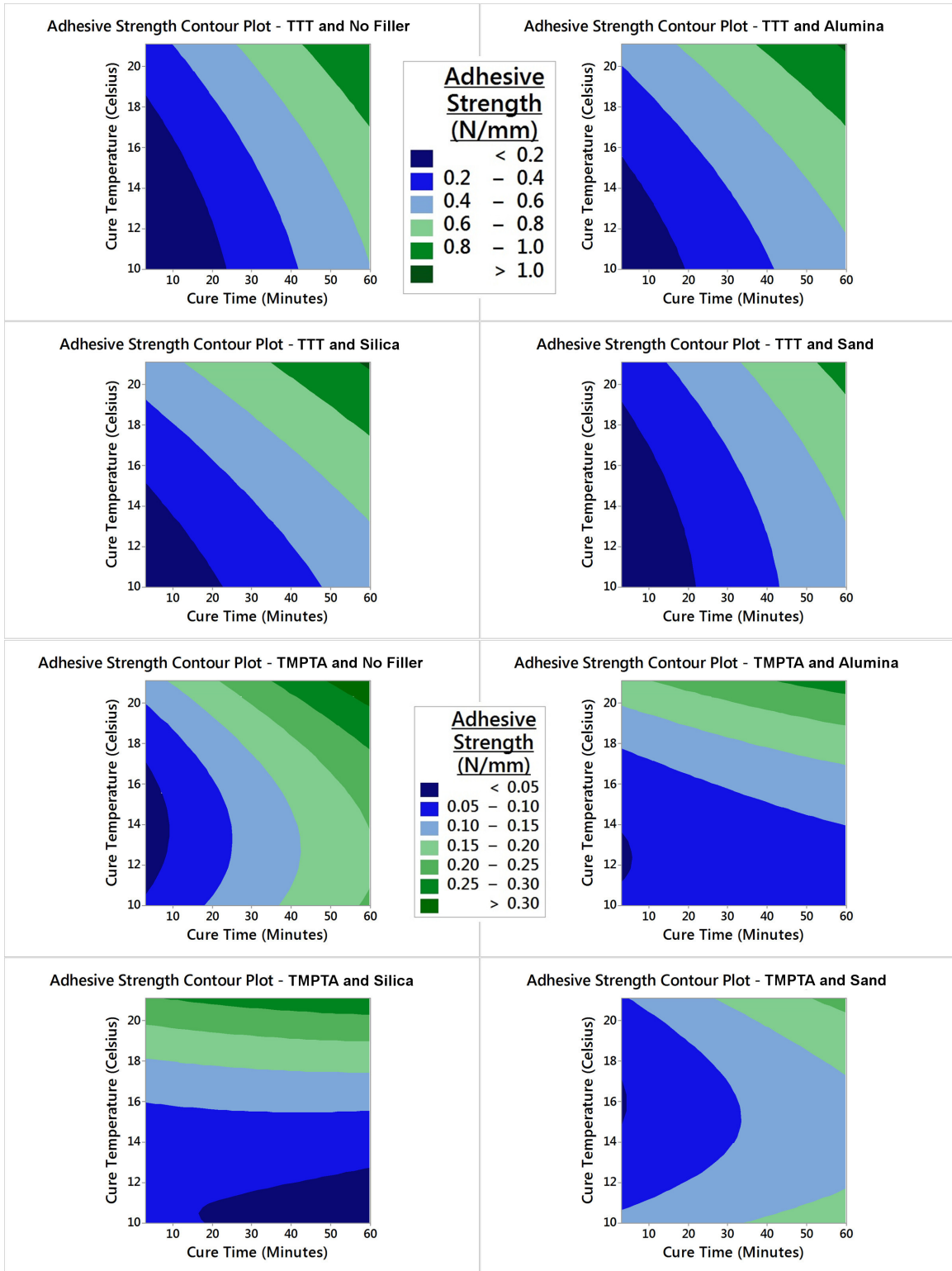


Figure 7.6: Characteristic contour plots of the TTT samples and TMPTA samples. The TTT based samples show a more consistent contour shape from the minimum at the bottom left to the maximum at the top right. The triarcylate has more contour variation with each different filler.

the kinetics of the thiol-ene reaction. It has been shown that temperature does not affect the development of homopolymers in the thiol-ene system, but does affect the conversion of the reaction due to the dependency of rate constants on temperature [104]. Additionally, increased cure time provides continued exposure to UV radiation, which can ensure complete activation of the photoinitiator. However, the additional exposure can cause structural instability by embrittling the sample due to high energy UV damage.

The categorical variables fitted means show that the type of alkene monomer has a significant effect on the adhesive strength, while the filler additives do not show a strong distinction between factors and the fitted means. Different alkene monomers result in a polymer structure that has different backbones based off the structure of the molecule, and the different backbones affect the material property. The TTT and TMPTA molecules both contain electronegative heteroatoms that support hydrogen bonding, but TTT contains a cyclic structure that can strengthen the polymer structure, leading to a more rigid sample. This is counter to the previous idea that an increase in stiffness lowers adhesive strength, due to the inability to dissipate fracture energy [2]. However, a strong material may also be resistant to the delamination from the substrate because of decreased flexibility. The sample strengthening also applies toward the filler additives, which can provide particles for the polymer structure to wrap around and tangle itself, increasing the material strength. However, looking at the individual factor effect there is no clear change in the fitted means by the filler material.

While individual factor effects on the figure-of-merit can shed a light on the contribution each factor provides, RSM allows for the study of co-factor interaction on the figure-of-merit. This provides insight on how the adjustment of multiple variables at the same time affects the peel strength and allows for further understanding on how the interactions work on a fundamental level to improve adhesive strength during

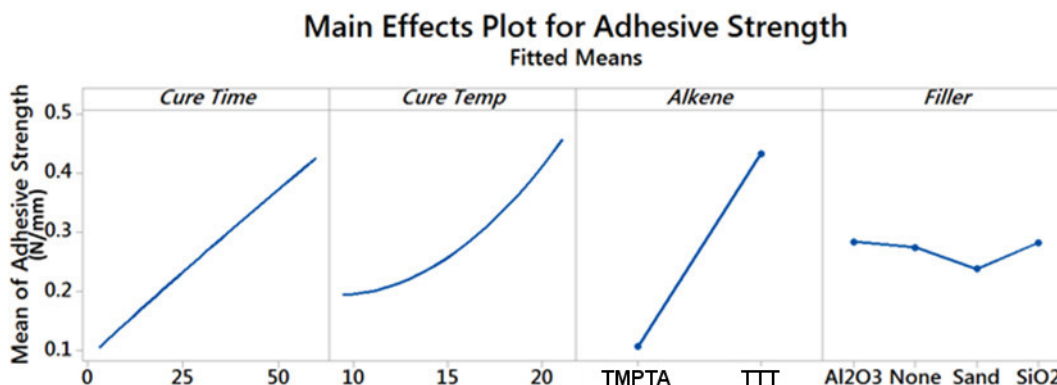


Figure 7.7: The main effects plots from the response surface DoE. A steeper slope between the factor indicates a stronger impact of the individual variable to the figure of merit.

synthesis. Figure 7.8 shows plots of the co-factor fitted means. From the graphs we can see that cure temperature and cure time do not have strong direct interaction when measuring adhesive strength. This can be seen from the parallel lines of the fitted means plot. While, both cure time and cure temperature can be argued to have influences on the kinetics of the reaction, the main influence of the temperature is on the rate constants and cure time is just the additional exposure of the UV toward the photoinitiator.

When observing the co-factor effects of the categorical and quantitative factors there are more potential interactions that contribute toward the adhesive strength, which can be seen by the intersection of the fitted means lines. Cure time and temperature do not have strong co-factor interaction with the different alkene monomers. However, the filler material has noticeable co-factor interaction with each of the other variables. Therefore, while the main effects plot of the filler additive do not show significant effects on the adhesive strength, when varying multiple factors in the experiment, additives exhibit an interactive effect on the peel strength alongside other changing conditions. They may contribute to changes with exposure, due to the presence of a powder filler blocking UV photons from radicalizing the photoinitiator.

Additionally, the change in the cure temperature also affects the viscosity of the mixture, which can affect the suspension of the filler additives in the solution. Finally, as mentioned above, the different alkene monomers create differing backbones to the cross-linked structure. Variations on the polymer chain may interact differently to the various sizes, surface areas, and materials of the powder filler.

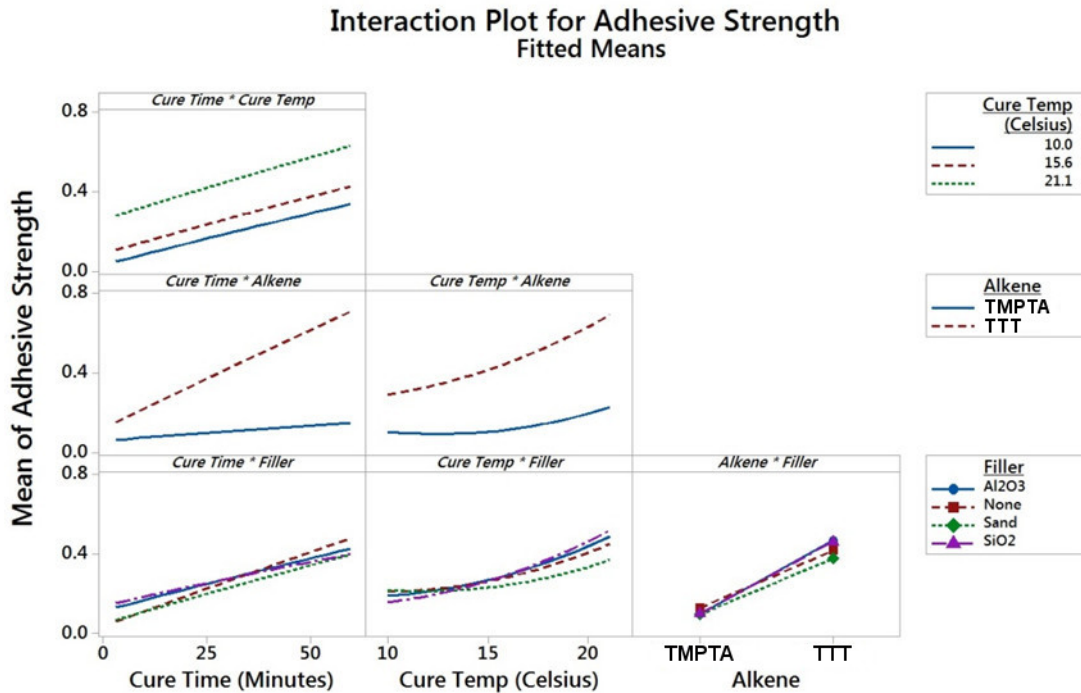


Figure 7.8: The co-factor interaction between the variables in the DoE. Intersection in the plot the level lines for each pair of factors implies a non-negligible co-factor interaction.

Coefficients for the second order model of the adhesive strength response surfaces can be seen in Table 7.3. These are based off a regression model from the experimental averages for peel strength. While there are no changes in the coefficient values for the nonlinear terms (β_3 , β_4 , and β_5), the linear terms of the model show a noticeable trend. All instances of the TTT monomer system had positive coefficients for the time coefficient (β_1), while the TMPTA monomers had a majority of negative coefficients. While all pairs of monomers and filler additive had negative coefficient values with

respect to the first-order temperature term (β_2), adhesive strength generally increased with respect to temperature in all cases, which is attributed to the positive coefficients with the second-order terms that contain temperature.

Table 7.3: The Adhesive Strength Transfer Function Coefficients

Adhesive Strength (N/mm) = $\beta_0 + \beta_1\mathbf{t} + \beta_2\mathbf{T} + \beta_3\mathbf{t}^2 + \beta_4\mathbf{T}^2 + \beta_5\mathbf{tT}$							
Cross Linker	Filler	β_0	β_1	β_2	β_3	β_4	β_5
<i>(-Ene)</i>	<i>Type</i>	$\frac{N}{mm}$	$\frac{N}{mm \times min}$	$\frac{N}{mm \times ^\circ C}$	$\frac{N}{mm \times min^2}$	$\frac{N}{mm \times ^\circ C^2}$	$\frac{N}{mm \times min \times ^\circ C}$
TTT	None	0.015	0.0104	-0.051	-6.0×10^{-6}	1.8×10^{-3}	9.7×10^{-5}
TTT	Al ₂ O ₃	0.053	0.0089	-0.021	-6.0×10^{-6}	1.8×10^{-3}	9.7×10^{-5}
TTT	SiO ₂	-0.017	0.0073	-0.015	-6.0×10^{-6}	1.8×10^{-3}	9.7×10^{-5}
TTT	Sand	0.149	0.0088	-0.034	-6.0×10^{-6}	1.8×10^{-3}	9.7×10^{-5}
TMPTA	None	0.377	0.0020	-0.051	-6.0×10^{-6}	1.8×10^{-3}	9.7×10^{-5}
TMPTA	Al ₂ O ₃	0.332	-0.0002	-0.046	-6.0×10^{-6}	1.8×10^{-3}	9.7×10^{-5}
TMPTA	SiO ₂	0.271	-0.0010	-0.040	-6.0×10^{-6}	1.8×10^{-3}	9.7×10^{-5}
TMPTA	Sand	0.518	0.00042	-0.059	-6.0×10^{-6}	1.8×10^{-3}	9.7×10^{-5}

RSM design was able to determine a approximate function for this particular system, and the same principles can be applied to many other polymer systems to model a function that is localized to the experimental conditions. However, this methodology is limited in terms extrapolation. The calculated model function is a regression based off the points in the design space, and though extrapolation beyond the experimental regime is possible, the accuracy of the calculations typically is far off from the experimental data in the new regime. This is due to interactions not captured within the original parameter space. The method of steepest ascent is used with RSM to determine where an optimum is for the desired figure-of-merit, and a new set of model equations is calculated after an additional round of experiments. RSM is results based to estimate a model and does not use theory to model the physical interactions in the curing process. In order to determine a global model,

more rigorous first principles analysis is required, but RSM experimental design is a good approximation for optimization of a figure-of-merit.

7.4 CONCLUSIONS

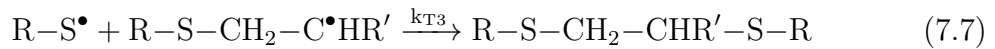
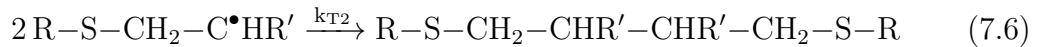
Response surface methodology provides insight into optimization of a figure-of-merit based off of a design space that reduces the number of experiments in order to increase efficiency. In the thiol-ene sealant system, a localized model was developed from the RSM experimental design that quantifies the adhesive strength in the experimental region. This can be expanded to other UV cured sealants as a first approximation to optimize the peel strength. However, the regression model is not only restricted to the experimented region, but also the categorical factors (monomer structure and filler additive). Quantification of the categorical variables based off of chemical properties, such as energetics, diffusive constants, and other first principles values can further optimize the model and allow for some predictive flexibility when choosing different chemicals for future experiments. High-throughput techniques for synthesis and characterization is also a key means to gather large experimental datasets in an efficient manner. This allows for an expedition of predictive model development for the curable systems.

Further studies into kinetics via *in situ* high-throughput FTIR is another avenue of fundamental study. As mentioned previously, thiol-ene click chemistry is unique because it is a radical step growth polymerization [47]. Therefore, determining the kinetics of the thiol-ene reaction requires careful analysis of the chemical system, and techniques like FTIR can be used for these studies. For a general thiol-ene reaction seen in Equation 7.3, the rate-determining step is determined by the ratio of the propagation rate constant, k_p , and the chain-transfer rate constant, k_{CT} . From the ratio, the reaction order can be determined, as seen in Equation 7.4 [174].



$$\frac{k_p}{k_{CT}} = \begin{cases} \gg 1; & R_p \propto [\text{SH}]^1 \\ \approx 1; & R_p \propto [\text{SH}]^{1/2}[\text{C}=\text{C}]^{1/2} \\ \ll 1; & R_p \propto [\text{C}=\text{C}]^1 \end{cases} \quad (7.4)$$

When the rate constant ratio is greater than 1, the overall reaction is first order with respect to the thiol, and the rate limiting step is chain transfer. When it is less than 1, the reaction is first order with respect to the alkene, and the rate limiting step is propagation. Both the propagation and chain transfer steps are seen in Figure 7.3. When the ratio is approximately equal to one, the reaction half order with respect to both monomers. However, these reactions can be broken down into multiple rate equations that can be manipulated in order to determine the rates of the elementary steps. In particular the termination steps seen in the following equations, are an area of study that can shed insight on the way the polymer network goes to completion.



However, the photoinitiated thiol-ene reaction has been seen as a second order reaction [47, 79]. In this instance the rate equations can be expressed as the following:

$$\frac{dx}{dt} = k(1-x)^2 \quad (7.8)$$

$$\frac{1}{1-x} = kt + 1 \quad (7.9)$$

where x is the thiol conversion, t is the time, and k is the rate constant. At the beginning of the reaction (initial condition: $t = 0, x = 0$), Equation 7.8 can be integrated

into Equation 7.9. The second order behavior has been attributed to impurities that modify the termination step [47]. However, more study is required on multiple different systems in order to fully understand the rate kinetics, and high-throughput techniques would be appropriate for data collection and analysis. Understanding the kinetics of the thiol-ene reaction can further optimize the cure time required for a given sealant system, further cutting down the number of experiments required in a DOE modeled system.

CHAPTER 8

CONCLUSIONS AND FUTURE WORK

8.1 CONCLUSIONS

Solid materials are utilized in a wide variety of applications. In order for functional materials to be optimized in each application, different classes of solid materials are required. These classes are typically categorized based on the way the material is chemically bonded. These include metallic, covalent, and ionic bonds, which make up metals, minerals (and ceramics), and salts respectively. Organic solids, such as wood and polymers, utilize covalent bonds and intermolecular forces such as hydrogen bonding and van der Waals forces. The properties of these different solids are highly dependent on their structures, which the bonding can have influence over. In general, the types of materials themselves and the way they are processed lead to properties that affect their usefulness in a bevy of applications, ranging from energy storage, thermal coatings, corrosion resistance, and structural stability.

This thesis explored a variety of metals, oxides, and polymers for a wide range of applications. Various MPEAs, stabilized zirconias, Re_x/CeO_2 catalysts, and thiol-ene polymers were created and studied. These materials were often synthesized and processed at conditions applicable for use in whatever industrial or commercial setting they are used in. For example, the MPEAs were post-processed in oxygen environments at high temperatures to test their corrosion resistant properties. Testing often utilized *in situ* and *ex situ* characterization techniques to understand the structure of these materials during synthesis, processing, or reaction conditions and gain a better

understanding of how the material changes in response to different conditions. Additionally, High-throughput experimental (HTE) methodologies were used in a number of these studies as a design scheme. This experimental set up allowed for the exploration of large parameter spaces using serial or parallel techniques for synthesis and characterization, which expedited data collection and provided more time for analysis of the given data.

8.2 CONCLUSION: MPEA PHASE STABILIZATION

HTE methodologies were applied to a novel $(Al_xCu_yMo_{1-x-y})FeNiTiVZr$ alloy system for synthesis via deposition and characterization via diffraction. These methods have been utilized in a number of other simple ternary compositions. This particular elemental composition was used because it was made with separate systems with known histories as MPEA systems. Multiple continuous composition spread (CCS) thin film libraries were deposited using magnetron sputtering of $AlFeNiTiVZr$, $CuFeNiTiVZr$, and $MoFeNiTiVZr$ alloy targets, and sputtering conditions were varied in order to observe effects of adatom energies on the phase of the finalized alloy. Using *in situ* synchrotron X-ray diffraction, a pseudo-ternary phase diagram was developed that illustrated clear phase boundaries as a function of composition. It was found that a body-centered cubic (BCC) structure was dominant throughout the composition spread, but at compositions where there were greater concentrations of elements that did not share binary solubility (Cu-Mo), secondary phases were more prevalent. This indicates that the alloy phase begins to destabilize and no longer behaves as a single phase solid solution. Additionally, while the thermodynamics of increased entropy allows for a metastable alloy phase to exist, when the sample is annealed over long periods of time, it will begin to destabilize if there is a lack of solubility between constituent elements.

8.2.1 FUTURE WORK

While it was shown that the binary solubility between constituents is an important factor to consider when developing new MPEA systems, these behaviors were identified in a thin film scale. Scaling up to a bulk system and observing crystallographic changes is necessary for to ensure that this heuristic is applicable at a macro scale. Additionally, bulk measurement testing can determine the structural applicability of stable alloy compositions that have been identified in a CCS on the thin materials scale. These studies measure the mechanical properties at this scale and involve tensile tests, impact strength experiments, hardness studies, and various other evaluations, in addition with high-temperature studies.

The traditional thermodynamic ratio that assist in predicting viable phase stable compositions, which is the enthalpic and entropic ratio, Ω , has been hypothesized to be limited in its predictive power. This is due to its only consideration being the alloy phase rather than considering potential the thermodynamics of the secondary phases that have been observed within the material's elemental constituents. Thus a term has been developed that is the ratio between the free energy of solid solution formation in a composition and the lowest potential free energy of intermetallic formation (between binary constituents), Φ .

$$\Phi = \frac{\Delta G_{ss}}{-|\Delta G_{max}|} \quad (8.1)$$

While these thermodynamic ratios provide a useful first pass toward alloy prediction, additional insight into the need for mutually soluble constituents in an alloy system can provide further predictive refinement. A major predictive methodology is CALPHAD (computation of phase diagrams) which requires previously available experimental data, phase diagrams, and thermodynamic information in order fit a model that will predict phase diagrams for new systems where no data is available. The large data sets that have been provided with the HTE methodology are valuable

for these computational diagrams. However, for future theoretical works, using the thermodynamic ratios, along with the solubility consideration when selecting constituents, is key for developing systems for testing. This can provide a computational method to plan experiments that further refine the predictive process.

8.3 CONCLUSION: MPEA OXIDATION

Similarly to the $\text{Al}_x\text{Cu}_y\text{Mo}_{1-x-y}\text{FeNiTiVZr}$ system, HTE methodologies were again applied to the $(\text{AlFeNiTiVZr})_{1-x}\text{Cr}_x$ alloy system in order to synthesize and characterize a CCS thin film library. The introduction of Cr was an attempt to promote the growth of passivating oxide phases that protect the MPEA structure from destabilizing via oxygen consumption. The CCS library was post-processed via annealing in oxygen at 873 K for various times and was characterized using synchrotron X-ray diffraction and Raman spectroscopy. These techniques, in conjunction with optical observations, show that the base phase of the alloy at all compositions is a BCC structure. However, once exposed to oxidizing conditions, a phase or behavioral boundary within the $(\text{AlFeNiTiVZr})_{1-x}\text{Cr}_x$ system at approximately 23.6 at.% Cr. At concentrations below 23.6 at.% Cr, the crystal structure of the material is destabilized and various unknown oxides and iron silicides form. Once the Cr concentration increases past 23.6 at.%, the BCC structure is retained with a suppressive oxide not seen in the compositions with lower Cr concentration. However, it is important to note that when the sample is annealed for longer than 18 hours, the boundary shifts to the 29.2 at.% Cr concentration, indicating that the BCC structure is either metastable or the silicides are able to destabilize the sample upon further annealing.

8.3.1 FUTURE WORK

The discovery of the phase boundary in the $\text{AlFeNiTiVZr}_{1-x}\text{Cr}_x$, where a potential oxidation resistant alloy resides is a first step toward application of additional

techniques to study the oxidation resistant properties of the $\text{AlFeNiTiVZr}_{1-x}\text{Cr}_x$ alloy. Outside of the bulk mechanical studies that were mentioned in Subsection 8.2.1, cross-sectional scanning electron microscopy (SEM) studies would be performed to measure the kinetic rate of the oxide formation and determine if parabolic growth can be seen at the compositions. Parabolic kinetics is a preferred growth rate of an oxide that is used as a suppressing oxide layer.

Additionally, there is a need to determine the compositions of the unknown suppressing oxide that grew on the surface of the high Cr concentration $\text{AlFeNiTiVZr}_{1-x}\text{Cr}_x$. Energy dispersive X-ray spectroscopy (EDS) can be used to help determine the composition of the unknown oxides and link them to known oxides in the materials database. Having the compositional data available can lead us to understanding the fundamentals of development of this particular mixed-metal suppressive oxide and how the introduction of high amounts of Cr promote its formation.

The study performed on the current $\text{AlFeNiTiVZr}_{1-x}\text{Cr}_x$ alloy system was performed at 873 K. This is not typically considered high temperature, which are generally accepted to be above 1273 K. However, the original study was performed in hopes of developing Al_2O_3 at moderate temperature conditions. Additional studies on the high-temperature (1273 K) stabilization of the $\text{AlFeNiTiVZr}_{1-x}\text{Cr}_x$ alloy are another step to determine the applicability of the material system.

8.4 CONCLUSION: STABILIZED ZIRCONIA TESTING

8.4.1 YTTRIA STABILIZED ZIRCONIA (YSZ) PHASE REGIONS

A deposition phase diagram was developed for the YSZ system with the intention of linking deposition parameters to the existing YSZ phase diagram. Thin films of YSZ were synthesized using magnetron sputtering with an 8 mol.% Y_2O_3 YSZ target on Si substrates. A design space was created that varied the deposition parameters of the YSZ films, and the samples were characterized using XRD. After analyzing

the diffraction data, it was discovered that two common YSZ crystal structures, cubic (c-YSZ) and tetragonal (t-YSZ), were the preferred structures to form during synthesis. In particular, the cubic phase was seen at synthesis conditions suspected of high energy bombardment, while tetragonal phases developed at lower energy conditions. Additionally, a mixture of cubic and tetragonal phases can be seen as well. While it has been previously understood that phases can be controlled via the adjustment of deposition parameters, utilizing this design of experiments generated data that provided a graphical representation in the form of a pseudo-phase diagram, seen in Figure 5.8. This diagram utilized the deposition parameters as its axes, and helps to visualize regions of higher energy. From this we can tune deposition parameters to desired phases and eventually capture metastable structures after determining the required synthesis conditions.

8.4.2 FUTURE WORK - YSZ

One of the main goals of developing the YSZ deposition phase diagram was to connect it to the standard phase diagram of YSZ, which would ease the determination of input deposition parameters for a desired phase. Additionally, the phase diagram would be applicable to various other deposition geometries. However, to generate an accurate transferable diagram requires modeling the adatom energy during deposition. In order to do this, calculations of using the in-house sputtering model can be utilized, but additional work is necessary to determine the energetics provided by the sputter gun, due to the insulating nature of the YSZ material. This would be combined with additional deposition experiments to fill in the phases and structures missing from the currently explored deposition conditions. Furthermore, post-processing studies are necessary to determine metastability of deposited films. This provides additional kinetic data outside of any calculated information from *ab initio* thermodynamic calculations, which can finalize the deposition phase diagram.

In order to differentiate between the standard tetragonal YSZ (t-YSZ) and metastable tetragonal prime (t'-YSZ), the oxygen displacement in the t' phase must be observed. The t' phase of YSZ has oxygen ion displaced on the c-axis in its unit cell compared to t-YSZ. While diffraction has been used to identify cubic, monoclinic, and tetragonal YSZ structures, it is difficult to differentiate between the metastable tetragonal phases of YSZ because the main differentiation is due to the oxygen displacements. While higher angle peaks can help differentiate the structures, there are conflicting diffracting peak positions in the literature. Therefore, in order to determine if t'-YSZ can be synthesized and labeled on the deposition phase diagram additional characterization through Raman spectroscopy and transmission electron microscopy (TEM) will be necessary.

8.4.3 SCANDIA STABILIZED ZIRCONIA (ScSZ) PHASE, CRYSTALLINITY, AND TEXTURE SYNTHESIS CONDITIONS

An analysis of ScSZ was performed on samples synthesized via magnetron sputtering using a factorial design and then post-processed using high-temperature annealing. This was done in order to determine synthesis conditions that lead toward optimal structures for the use as the electrolyte in a solid oxide fuel cell (SOFC). Utilizing XRD, the texturing, crystallinity, and phase of the ScSZ at different deposition conditions were cataloged. All samples showed a cubic phase in the diffraction patterns that remained stable after annealing at 1273 K for up to 8 hours. At higher deposition temperatures and oxygen concentrations, the ScSZ samples showed increased crystallinity in the 2D diffractograms. Furthermore, the preferred texture orientation increased from the (111) orientation to (200). Imaging the grains using SEM showed that there was limited grain growth as anneal times increased. The film synthesized at 65 W, 10 vol.% O₂, and with a room temperature deposition, showed a c-ScSZ film

that preferred the (220) orientation, which is a phase and faceting that is desirable for use in SOFCs.

8.4.4 FUTURE WORK - ScSZ

While these samples were processed at temperature close to operating conditions of a SOFC, the next steps are to apply the ScSZ thin film layer in actual fuel cell application. Initially, after deposition of the ScSZ onto the preferred electrodes, SEM of the fuel cell cross-section is a way to visualize the . Additionally, measurements should be performed post-anneal to ensure that the electrolyte and electrodes do not undergo any spallation, which will delaminate and destroy the fuel cell. Afterward, tests with different fuels should be performed at temperatures below 1273 K in order to determine the efficiency of the fuel cell and the efficacy of ScSZ as an electrolyte at lower operating temperatures.

8.5 CONCLUSION: $\text{ReO}_x/\text{CeO}_2$ MECHANISTIC STUDY

$\text{ReO}_x/\text{CeO}_2$ structures were determined with *in situ* vibrational spectroscopy studies using oxygen isotope exchange. The Raman and diffuse reflectance infrared Fourier transform spectroscopy (DRIFTS) showed evidence via red shift of the mono-oxo ($\text{Re}=\text{O}$), di-oxo ($\text{O}=\text{Re}=\text{O}$), oxygen bridge ($\text{Re}-\text{O}-\text{Re}$), and hydroxyl species ($\text{Re}-\text{OH}$) on the 1 wt.% $\text{ReO}_x/\text{CeO}_2$. Additionally, the spectroscopy showed that the extent of the isotope exchange to be approximately 60%. Time resolved DRIFTS showed that the ^{18}O exchanged with ^{16}O at a rate of 2.29% per minute.

8.5.1 FUTURE WORK

Additional isotope exchange experiments can provide information on if the same speciation occurs at higher weight loadings. Due to the discovery of multiple potential initiation structures for the simultaneous hydrodeoxygenation (S-HDO) reaction, the

dominant mechanism is still not fully determined. This is because the current candidate mechanisms have separate starting species for the ReO_x , which we see with the mono-oxo and di-oxo structures. Therefore, in order to determine which mechanism is dominant, future studies should include *in situ* vibrational spectroscopy on the $\text{ReO}_x/\text{CeO}_2$ using the S-HDO reaction conditions.

Application of computational modeling was limited to determining the potential reaction mechanisms for S-HDO on $\text{ReO}_x/\text{CeO}_2$. However, there has been limited work on using *ab initio* methodologies in predicting the band positions of the different potential species that ReO_x can form on the various support surfaces. Utilizing previous approaches to Raman band predicting models on these catalysts can expedite and validate the analysis of spectrographic data after experiments have been conducted.

8.6 CONCLUSION: THIOL-ENE PEEL TEST OPTIMIZATION

Utilizing a variation of the response surface methodology (RSM) on various thiol-ene mixtures allowed for the development of a model localized to the studied parameters. This model was used to optimized the figure-of-merit, adhesive strength, with respect to the synthesis parameters. The use of RSM is transferable to other ultraviolet (UV) curable sealant systems.in order to optimize a given property. In the case of pentaerythritol tetrakis(3-mercaptopropionate) (PETMP), synthesized with 1,3,5-Triallyl-1,3,5-triazine-2,4,6(1H,3H,5H)-trione (TTT) or trimethylolpropane triacrylate (TMPTA), the quantitative parameters of cure temperature and cure time showed an optimum adhesive strength at longer cure times and higher temperatures. However, when adjusting for additive filler the adhesive strength only increased slightly, which may be a result of the increased elastic modulus of the polymer systems. Application of high-throughput techniques toward synthesis and characterization can expedite the data acquisition process, analysis, and model development.

8.6.1 FUTURE WORK

A major concession toward the development of the RSM modeling function was the utilization of categorical variables in the design space. While these the type of alkene and filler material are necessary in studying the adhesive strength of the material, they do not readily lend themselves to a numerical value that can be applied to a calculated model. Therefore, when applying a design of experiments and computational modeling to future peel samples, determining quantitative values that can be related to the categorical variables is an exploratory path. For example, using energy of formations, extents of polymerization, and intermolecular bond strengths can be factors that are applied to the thiol and alkene interaction, and these factors can adjust the model away from an estimation and closer to a developed function. However, there is a risk of overparameterization when applying these factors and addition studies will be required to determine relevant input variables.

Outside of the RSM for estimating thiol-ene adhesive strength, the fundamental reaction has additional avenues of study. In particular, the kinetic information of the polymerization for these particular reactions can be determined utilizing known rate equations and high-throughput experimentation. Spectrographic techniques, such as Fourier transform infrared spectroscopy (FTIR) and Raman spectroscopy can be applied to the thiol-ene reaction *in situ* and the resulting spectral data can provide a timeline of consumption of different bonds during the polymerization. In order to expedite these experiments, characterization can be parallelized using a zinc selenide (ZnSe) prism. This prism is IR transparent and allows for multiple samples to be measured in a single experiment with the use of a specialized focal plane array (FPA) area detector. The end results in the novel analysis of reaction kinetics of a polymerization reaction using high-throughput spectral techniques.

BIBLIOGRAPHY

- [1] Hussien Ahmed Abbas, Christos Argirusis, Martin Kilo, Hans Dieter Wiemhöfer, Fadua Fwad Hammad, and Zeinab Mohamed Hanafi. Preparation and conductivity of ternary scandia-stabilised zirconia. *Solid State Ionics*, 184(1):6–9, 2011.
- [2] S Abbott. *Adhesion Science: Principles and Practice*. DEStech Publications, Lancaster, 1 edition, 2015.
- [3] A. Abu-Odeh, E. Galvan, T. Kirk, H. Mao, Q. Chen, P. Mason, R. Malak, and R. Arróyave. Efficient exploration of the High Entropy Alloy composition-phase space. *Acta Materialia*, 152:41–57, 2018.
- [4] C. Ahamer, A. K. Opitz, G. M. Rupp, and J. Fleig. Revisiting the temperature dependent ionic conductivity of yttria stabilized zirconia (YSZ). *Journal of the Electrochemical Society*, 164(7):F790–F803, 2017.
- [5] David Martin Alonso, Stephanie G. Wettstein, and James A. Dumesic. Bimetallic catalysts for upgrading of biomass to fuels and chemicals. *Chemical Society Reviews*, 41(24):8075–8098, 2012.
- [6] Filipa Alves and Ivo Nischang. Radical-mediated step-growth: Preparation of hybrid polymer monolithic columns with fine control of nanostructural and chromatographic characteristics. *Journal of Chromatography A*, 1412:112–125, 2015.
- [7] Yasushi Amada, Nobuhiko Ota, Masazumi Tamura, Yoshinao Nakagawa, and Keiichi Tomishige. Selective hydrodeoxygenation of cyclic vicinal diols to cyclic alcohols over tungsten oxide-palladium catalysts. *ChemSusChem*, 7(8):2185–2192, 2014.
- [8] A. Aminzadeh. Excitation frequency dependence and fluorescence in the Raman spectra of Al₂O₃. *Applied Spectroscopy*, 51(6):817–819, 1997.
- [9] R. Ananthakumar, B. Subramanian, S. Yugeswaran, and M. Jayachandran. Effect of substrate temperature on structural, morphological and optical prop-

- erties of crystalline titanium dioxide films prepared by DC reactive magnetron sputtering. *Journal of Materials Science: Materials in Electronics*, 23(10):1898–1904, oct 2012.
- [10] Piers S. Anderson, Xin Wang, and Ping Xiao. Effect of isothermal heat treatment on plasma-sprayed yttria-stabilized zirconia studied by impedance spectroscopy. *Journal of the American Ceramic Society*, 88(2):324–330, 2005.
- [11] Chrysanthi Andriopoulou, Ioannis Anastasiou, and Soghomon Boghosian. Di-oxo and tri-oxo Re(VII)-oxosulfato complexes in the Re₂O₇-K₂S₂O₇ molten system. Molecular structure, vibrational properties and temperature-dependent interconversion. *Vibrational Spectroscopy*, 100(September 2018):14–21, 2019.
- [12] Chrysanthi Andriopoulou and Soghomon Boghosian. Molecular structure and termination configuration of Oxo-Re(VII) catalyst sites supported on Titania. *Catalysis Today*, (June):1–13, 2019.
- [13] Chrysanthi Andriopoulou and Soghomon Boghosian. Tuning the configuration of dispersed oxometallic sites in supported transition metal oxide catalysts: A temperature dependent Raman study. *Catalysis Today*, 336(January):1–10, 2019.
- [14] D. E. Ashenford, F. Long, W. E. Hagston, B. Lunn, and A. Matthews. Experimental and theoretical studies of the low-temperature growth of chromia and alumina. *Surface and Coatings Technology*, 116-119:699–704, 1999.
- [15] H. Asteman, J. E. Svensson, M. Norell, and L. G. Johansson. Influence of water vapor and flow rate on the high-temperature oxidation of 304L; effect of chromium oxide hydroxide evaporation. *Oxidation of Metals*, 54(1):11–26, 2000.
- [16] Mohammad Azadi and Mahboobeh Azadi. Evaluation of high-temperature creep behavior in Inconel-713C nickel-based superalloy considering effects of stress levels. *Materials Science and Engineering A*, 689(September 2016):298–305, 2017.
- [17] P. Barberis, T. Merle-Méjean, and P. Quintard. On Raman spectroscopy of zirconium oxide films. *Journal of Nuclear Materials*, 246(2-3):232–243, 1997.
- [18] W Baukal. Über die kinetik der alterung eines zro₂-festelektrolyten in abhängigkeit vom sauerstoff-partialdruck. *Electrochimica Acta*, 14(11):1071–1080, 1969.

- [19] I. R. Beattie and T. R. Gilson. The Single-crystal Raman Spectra of nearly Opaque Materials. Iron (III) Oxide and Chromium (III) Oxide. *Journal of the Chemical Society A: Inorganic, Physical, Theoretical*, pages 980–986, 1970.
- [20] I. R. Beattie, T. R. Gilson, and P. J. Jones. Vapor Phase Vibrational Spectra for Re_2O_7 and the Infrared Spectrum of Gaseous HReO_4 . Molecular Shapes of Mn_2O_7 , Tc_2O_7 , and Re_2O_7 . *Inorganic Chemistry*, 35(5):1301–1304, 2002.
- [21] John Bechhoefer, Hartmut Löwen, and Laurette Tuckerman. Dynamical mechanism for the formation of metastable phases. *Physical Review Letters*, 67(10):1266–1269, 1991.
- [22] A Bennett. Properties of thermal barrier coatings. *Materials Science and Technology*, 2(3):257–261, 1986.
- [23] Robert Beyers and Robert Sinclair. Metastable phase formation in titanium-silicon thin films. *Journal of Applied Physics*, 57(12):5240–5245, jun 1985.
- [24] G. P. Bierwagen and D. E. Tallman. Choice and measurement of crucial aircraft coatings system properties. *Progress in Organic Coatings*, 41(4):201–216, 2001.
- [25] Wolfgang H. Binder and Robert Sachsenhofer. 'Click' chemistry in polymer and materials science. *Macromolecular Rapid Communications*, 28(1):15–54, 2007.
- [26] O. Bohnke, V. Gunes, K. V. Kravchyk, A. G. Belous, O. Z. Yanchevskii, and O. I. V'Yunov. Ionic and electronic conductivity of 3 mol% Fe_2O_3 -substituted cubic yttria-stabilized ZrO_2 (YSZ) and scandia-stabilized ZrO_2 (ScSZ). *Solid State Ionics*, 262:517–521, 2014.
- [27] G. E. P. Box and J. S. Hunter. Multi-Factor Experimental Designs for Exploring Response Surfaces. *The Annals of Mathematical Statistics*, 28(1):195–241, 1957.
- [28] George EP Box and Donald W Behnken. Some new three level designs for the study of quantitative variables. *Technometrics*, 2(4):455–475, 1960.
- [29] George EP Box and Norman R Draper. *Response surfaces, mixtures, and ridge analyses*, volume 649. John Wiley & Sons, 2007.
- [30] Michael S. Bradley and Cheryl Bratu. Vibrational line profiles as a probe of molecular interactions. *Journal of Chemical Education*, 74(5):553–555, 1997.

- [31] A.D. Brailsford and E.M. Logothetis. Selected aspects of gas sensing. *Sensors and Actuators B: Chemical*, 52(1-2):195–203, sep 1998.
- [32] I. Brodnikovska, N. Korsunska, L. Khomenkova, Yu Polishchuk, S. Lavoryk, M. Brychevskiy, Y. Brodnikovskiy, and O. Vasylyev. Grains, grain boundaries and total ionic conductivity of 10Sc1CeSZ and 8YSZ solid electrolytes affected by crystalline structure and dopant content. *Materials Today: Proceedings*, 6(January):79–85, 2019.
- [33] Kevin Bruen, Kurt Davidson, Daniel F E Sydes, and Peter M. Siemens. Benefits of UV-curable coatings. *European Coatings Journal*, 49(4):42–48, 2004.
- [34] J K Bunn, C J Metting, and J R Hattrick-Simpers. Development of an Accurate Semi-Empirical Model for Tilted-Gun Planer Magnetron Sputtering Accounting for Chimney Shadowing. *Journal of the Minerals, metals and Materials*, 67(1):154–163, 2015.
- [35] Jonathan Kenneth Bunn. *Development of Novel High-Throughput Methodologies to Evaluate the Thermal Stability of High-Temperature Thin-Film Crystals for Energy Applications*. PhD thesis, University of South Carolina, 2016.
- [36] Jonathan Kenneth Bunn, Randy L Fang, Mark R Albing, Apurva Mehta, Matthew J Kramer, Matthew F Besser, and Jason R Hattrick-Simpers. A high-throughput investigation of Fe–Cr–Al as a novel high-temperature coating for nuclear cladding materials. *Nanotechnology*, 26(27):274003–1–9, 2015.
- [37] Todd M. Butler and Mark L. Weaver. Oxidation behavior of arc melted AlCoCr-FeNi multi-component high-entropy alloys. *Journal of Alloys and Compounds*, 674:229–244, 2016.
- [38] B. Cantor, I.T.H. Chang, P. Knight, and A.J.B. Vincent. Microstructural development in equiatomic multicomponent alloys. *Materials Science and Engineering: A*, 375-377:213–218, jul 2004.
- [39] J. M. Caruthers, J. A. Lauterbach, K. T. Thomson, V. Venkatasubramanian, C. M. Snively, A. Bhan, S. Katare, and G. Oskarsdottir. Catalyst design: Knowledge extraction from high-throughput experimentation. *Journal of Catalysis*, 216(1-2):98–109, 2003.
- [40] Justin W. Chan, Bing Yu, Charles E. Hoyle, and Andrew B. Lowe. The nucleophilic, phosphine-catalyzed thiol-ene click reaction and convergent star synthesis with RAFT-prepared homopolymers. *Polymer*, 50(14):3158–3168, 2009.

- [41] JF Chang, HH Kuo, IC Leu, and MH Hon. The effects of thickness and operation temperature on zno: Al thin film co gas sensor. *Sensors and actuators B: Chemical*, 84(2-3):258–264, 2002.
- [42] Keke Chang, Denis Music, Moritz to Baben, Dennis Lange, Hamid Bolvardi, and Jochen M. Schneider. Modeling of metastable phase formation diagrams for sputtered thin films. *Science and Technology of Advanced Materials*, 17(1):210–219, dec 2016.
- [43] Hai Lin Chen, Huahai Mao, and Qing Chen. Database development and Calphad calculations for high entropy alloys: Challenges, strategies, and tips. *Materials Chemistry and Physics*, 210:279–290, 2018.
- [44] LB Chen. Yttria-stabilized zirconia thermal barrier coatings—a review. *Surface Review and Letters*, 13(05):535–544, 2006.
- [45] Jérôme Chevalier, Laurent Gremillard, Anil V. Virkar, and David R. Clarke. The tetragonal-monoclinic transformation in zirconia: Lessons learned and future trends. *Journal of the American Ceramic Society*, 92(9):1901–1920, 2009.
- [46] B S Chiou, J Robert, and S A Khan. Rheology and photo-cross-linking of thiol-ene polymers. *Macromolecules*, 29(16):5368–5374, 1996.
- [47] Bor-sen Chiou, Saad a Khan, and North Carolina. Real-Time FTIR and in Situ Rheological Studies on the UV Curing Kinetics of Thiol-ene Polymers. *Macromolecules*, 9297(97):7322–7328, 1997.
- [48] Leslie J. Clark and Michael A. Cosman. Use of Permapol® P3.1 polymers and epoxy resins in the formulation of aerospace sealants. *International Journal of Adhesion and Adhesives*, 23(5):343–348, 2003.
- [49] David R. Clarke and Simon R. Phillpot. Thermal barrier coating materials. *Materials Today*, 8(6):22–29, 2005.
- [50] J. Comyn, J. Day, and S. J. Shaw. Durability of aluminium-sealant joints in jet-fuel, water and antifreeze. *International Journal of Adhesion and Adhesives*, 17(3):213–221, 1997.
- [51] C Corbella, M Vives, A Pinyol, E Bertran, C Canal, MC Polo, and JL Andújar. Preparation of metal (w, mo, nb, ti) containing ac: H films by reactive magnetron sputtering. *Surface and Coatings Technology*, 177:409–414, 2004.

- [52] Neil B. Cramer and Christopher N. Bowman. Kinetics of thiol-ene and thiol-acrylate photopolymerizations with real-time Fourier transform infrared. *Journal of Polymer Science, Part A: Polymer Chemistry*, 39(19):3311–3319, 2001.
- [53] Qingxin Cui, Yuanyuan Hou, Jie Hou, Pengwei Pan, Lu-Yuan Li, Gang Bai, and Guoan Luo. Preparation of Functionalized Alkynyl Magnetic Microspheres for the Selective Enrichment of Cell Glycoproteins Based on Click Chemistry. *Biomacromolecules*, 14(1):124–131, jan 2013.
- [54] Bernard Dennis Cullity and Stuart R. Stock. *Elements of X-Ray Diffraction*. Prentice Hall, New York, 3 edition, 2001.
- [55] ASTM D3330/D3330M-04(2018). Standard Test Method for Peel Adhesion of Pressure-Sensitive Tape. Standard, ASTM International, West Conshohocken, PA, 2018.
- [56] Joseph R Davis. *ASM Handbook*, volume 1. ASM International, 1990.
- [57] Joseph R Davis. *ASM Handbook*, volume 2. ASM International, 1990.
- [58] A. A. Donskoi and N. V. Baritko. Fluorosiloxane sealants for aviation industry. *Polymer Science Series C*, 49(2):182–187, 2007.
- [59] Olivia Z. Durham and Devon A. Shipp. Suspension “click” polymerizations: thiol-ene polymer particles prepared with natural gum stabilizers. *Colloid and Polymer Science*, 293(8):2385–2394, 2015.
- [60] M. Eckert. Max von Laue and the discovery of X-ray diffraction in 1912. *Annalen der Physik*, 524(5):83–85, 2012.
- [61] J Fergus. Materials for high temperature electrochemical NO_x gas sensors. *Sensors and Actuators B: Chemical*, 121(2):652–663, feb 2007.
- [62] Elena Fuentes-Paniagua, José Manuel Hernández-Ros, María Sánchez-Milla, M. Alejandra Camero, Marek Maly, Jorge Pérez-Serrano, José Luis Copa-Patiño, Javier Sánchez-Nieves, Juan Soliveri, Rafael Gómez, and F. Javier de la Mata. Carbosilane cationic dendrimers synthesized by thiol-ene click chemistry and their use as antibacterial agents. *RSC Adv.*, 4(3):1256–1265, 2014.
- [63] Fernando H Garzon, Rangachary Mukundan, and Eric L Brosha. Solid-state mixed potential gas sensors : theory , experiments and challenges. *Solid State Ionics*, 137:633–638, 2000.

- [64] John Peter Gassiot. The Bakerian Lecture - On the stratifications and dark bands in electrical discharges as observed in torricellian vacuums. *Proceedings of the Royal Society of London*, 9:145–150, dec 1859.
- [65] Ho Truong Giang, Ha Thai Duy, Pham Quang Ngan, Giang Hong Thai, Do Thi Anh Thu, Do Thi Thu, and Nguyen Ngoc Toan. High sensitivity and selectivity of mixed potential sensor based on Pt/YSZ/SmFeO₃ to NO₂ gas. *Sensors and Actuators, B: Chemical*, 183(2):550–555, 2013.
- [66] S. Giannis, R. D. Adams, L. J. Clark, and M. A. Taylor. Investigation of the Water and Fuel Exposure Characteristics of Aircraft Fuel Tank Sealants and the Effect on their Glass Transition Temperature. *Journal of Applied Polymer Science*, 108(5):3073–3091, 2008.
- [67] S. Giannis, R. D. Adams, L. J. Clark, and M. A. Taylor. Peel behaviour of aircraft fuel tank sealants: The effect of peel angle, sealant layer thickness and peel rate. *Journal of Adhesion Science and Technology*, 22(13):1495–1522, 2008.
- [68] S. Giannis, R. D. Adams, L. J. Clark, and M. A. Taylor. The use of a modified peel specimen to assess the peel resistance of aircraft fuel tank sealants. *International Journal of Adhesion and Adhesives*, 28(4-5):158–175, 2008.
- [69] Philippe Gillet, Paul McMillan, Jacques Schott, James Badro, and Andrzej Grzechnik. Thermodynamic properties and isotopic fractionation of calcite from vibrational spectroscopy of ¹⁸O-substituted calcite. *Geochimica et Cosmochimica Acta*, 60(18):3471–3485, 1996.
- [70] J. Goff, W. Hayes, S. Hull, M. Hutchings, and K. Clausen. Defect structure of yttria-stabilized zirconia and its influence on the ionic conductivity at elevated temperatures. *Physical Review B*, 59(22):14202–14219, 1999.
- [71] B. Gorr, M. Azim, H.-J. J. Christ, T. Mueller, D. Schliephake, and M. Heilmaier. Phase equilibria, microstructure, and high temperature oxidation resistance of novel refractory high-entropy alloys. *Journal of Alloys and Compounds*, 624:270–278, mar 2015.
- [72] Martin L. Green, Ichiro Takeuchi, and Jason R. Hattrick-Simpers. Applications of high throughput (combinatorial) methodologies to electronic, magnetic, optical, and energy-related materials. *Journal of Applied Physics*, 113(23):231101–1–53, 2013.

- [73] J. E. Greene. Review Article: Tracing the recorded history of thin-film sputter deposition: From the 1800s to 2017. *Journal of Vacuum Science & Technology A: Vacuum, Surfaces, and Films*, 35(5):05C204, 2017.
- [74] J. M. Gregoire, D. G. Van Campen, C. E. Miller, R. J. R. Jones, S. K. Suram, and a. Mehta. High-throughput synchrotron X-ray diffraction for combinatorial phase mapping. *Journal of Synchrotron Radiation*, 21(6):1262–1268, 2014.
- [75] JM Gregoire, MB Lobovsky, MF Heinz, FJ DiSalvo, and RB Van Dover. Resputtering phenomena and determination of composition in codeposited films. *Physical Review B*, 76(19):195437, 2007.
- [76] William Robert Grove. VII. On the electro-chemical polarity of gases. *Philosophical Transactions of the Royal Society of London*, 142:87–101, dec 1852.
- [77] Sheng Guo, Chun Ng, Jian Lu, and C. T. Liu. Effect of valence electron concentration on stability of fcc or bcc phase in high entropy alloys. *Journal of Applied Physics*, 109(10):0–5, 2011.
- [78] K. Haga, S. Adachi, Y. Shiratori, K. Itoh, and K. Sasaki. Poisoning of SOFC anodes by various fuel impurities. *Solid State Ionics*, 179(27-32):1427–1431, 2008.
- [79] Peter J Halley and Michael E Mackay. Chemorheology of thermosets-an overview. *Polymer Engineering & Science*, 36(5):593–609, mar 1996.
- [80] A. P. Hammersley. FIT2D: A multi-purpose data reduction, analysis and visualization program. *Journal of Applied Crystallography*, 49:646–652, 2016.
- [81] AP Hammersley et al. Fit2d: an introduction and overview. *European Synchrotron Radiation Facility Internal Report ESRF97HA02T*, 68:58, 1997.
- [82] Franklin D. Hardcastle, Israel E. Wachs, John A. Horsley, and Grayson H. Via. The structure of surface rhenium oxide on alumina from laser raman spectroscopy and x-ray absorption near-edge spectroscopy. *Journal of Molecular Catalysis*, 46(1-3):15–36, 1988.
- [83] Mariette Hellenbrandt. The Inorganic Crystal Structure Database (ICSD)—Present and Future. *Crystallography Reviews*, 10(1):17–22, jan 2004.
- [84] Reed J. Hendershot, Paul T. Fanson, Christopher M. Snively, and Jochen A. Lauterbach. High-throughput catalytic science: Parallel analysis of transients in

- catalytic reactions. *Angewandte Chemie - International Edition*, 42(10):1152–1155, 2003.
- [85] S. J. Henderson, J. A. Armstrong, A. L. Hector, and M. T. Weller. High-throughput methods to optically functional oxide and oxide-nitride materials. *Journal of Materials Chemistry*, 15(15):1528–1536, 2005.
- [86] Masanori Hirano, Takayuki Oda, Kenji Ukai, and Yasunobu Mizutani. Effect of Bi₂O₃ additives in Sc stabilized zirconia electrolyte on a stability of crystal phase and electrolyte properties. *Solid State Ionics*, 158(3-4):215–223, 2003.
- [87] Gordon R. Holcomb, Joseph Tylczak, and Casey Carney. Oxidation of CoCr-FeMnNi High Entropy Alloys. *Jom*, 67(10):2326–2339, 2015.
- [88] Brian D Hosterman. *Raman Spectroscopic Study of Solid Solution Spinel Oxides*. PhD thesis, University of Nevada, Las Vegas, 2011.
- [89] Paul R. Howell. The pearlite reaction in steels: Mechanisms and crystallography. *Materials Characterization*, 40(4-5):227–260, 1998.
- [90] Charles Hoyle, Tolecial Clark, Tai Yeon Lee, Todd Roper, Bo Pan, Huanyu Wei, Hui Zhou, and Joe Lichtenhan. Thiol-Enes : Fast Curing Systems with Exceptional Properties. In *Radtech Eur. 05*, pages 2–6, 2005.
- [91] Charles E. Hoyle and Christopher N. Bowman. Thiol-ene click chemistry. *Angewandte Chemie - International Edition*, 49(9):1540–1573, 2010.
- [92] Chin-You Hsu, Tsing-Shien Sheu, Jien-Wei Yeh, and Swe-Kai Chen. Effect of iron content on wear behavior of AlCoCrFexMo0.5Ni high-entropy alloys. *Wear*, 268(5-6):653–659, feb 2010.
- [93] Chin-you Hsu, Jien-wei Yeh, Swe-kai Chen, and Tao-tsung Shun. Wear Resistance and High-Temperature Compression Strength of Fcc CuCoNiCrAl 0.5 Fe Alloy with Boron Addition. *Metallurgical and Materials Transactions A*, 35A:1465–1469, 2004.
- [94] P.-K. Huang, J.-W. Yeh, T.-T. Shun, and S.-K. Chen. Multi-Principal-Element Alloys with Improved Oxidation and Wear Resistance for Thermal Spray Coating. *Advanced Engineering Materials*, 6(12):74–78, feb 2004.
- [95] Yuan Sheng Huang, Ling Chen, Hong Wei Lui, Ming Hong Cai, and Jien Wei Yeh. Microstructure, hardness, resistivity and thermal stability of sputtered

- oxide films of AlCoCrCu_{0.5}NiFe high-entropy alloy. *Materials Science and Engineering A*, 457(1-2):77–83, 2007.
- [96] J. Huebner, D. Kata, J. Kusiński, P. Rutkowski, and J. Lis. Microstructure of laser cladded carbide reinforced Inconel 625 alloy for turbine blade application. *Ceramics International*, 43(12):8677–8684, 2017.
- [97] William Hume-Rothery, Gilbert W M Abbott, and K. M. Channel-Evans. The freezing points, melting points, and solid solubility limits of the alloys of silver and copper with the elements of the b sub-groups. *Philosophical Transactions of the Royal Society of London. Series A, Containing Papers of a Mathematical or Physical Character*, 233(721-730):1–97, may 1934.
- [98] C. R. Hutchinson, X. Fan, S. J. Pennycook, and G. J. Shiflet. On the origin of the high coarsening resistance of Ω plates in Al-Cu-Mg-Ag alloys. *Acta Materialia*, 49(14):2827–2841, 2001.
- [99] M. N. Iliev, A. P. Litvinchuk, H. G. Lee, C. W. Chu, A. Barry, and J. M.D. Coey. Raman spectroscopy of ferromagnetic CrO₂. *Physical Review B - Condensed Matter and Materials Physics*, 60(1):33–36, 1999.
- [100] P. G. Ivanov, S. M. Watts, and D. M. Lind. Epitaxial growth of CrO₂ thin films by chemical-vapor deposition from a Cr₈O₂₁ precursor. *Journal of Applied Physics*, 89(2):1035–1040, 2001.
- [101] Allan J. Jacobson. Materials for solid oxide fuel cells. *Chemistry of Materials*, 22(3):660–674, 2010.
- [102] Kuo Jiang, Songbai Liu, and Xin Wang. Phase stability and thermal conductivity of nanostructured tetragonal yttria-stabilized zirconia thermal barrier coatings deposited by air-plasma spraying. *Ceramics International*, 43(15):12633–12640, 2017.
- [103] San Ping Jiang. Dependence of cell resistivity on electrolyte thickness in solid oxide fuel cells. *Journal of Power Sources*, 183(2):595–599, 2008.
- [104] Peter M. Johnson, Jeffrey W. Stansbury, and Christopher N. Bowman. High-throughput kinetic analysis of acrylate and thiol-ene photopolymerization using temperature and exposure time gradients. *Journal of Polymer Science Part A: Polymer Chemistry*, 46(4):1502–1509, feb 2008.

- [105] DW Jordan and KT Faber. X-ray residual stress analysis of a ceramic thermal barrier coating undergoing thermal cycling. *Thin Solid Films*, 235(1-2):137–141, 1993.
- [106] Chien-Chang Juan, Chin-You Hsu, Che-Wei Tsai, Woei-Ren Wang, Tsing-Shien Sheu, Jien-Wei Yeh, and Swe-Kai Chen. On microstructure and mechanical performance of AlCoCrFeMo_{0.5}Nix high-entropy alloys. *Intermetallics*, 32:401–407, jan 2013.
- [107] Matthew J. Kade, Daniel J. Burke, and Craig J. Hawker. The Power of Thiol-ene Chemistry. *Journal of Polymer Science, Part A: Polymer Chemistry*, 48:743–750, 2009.
- [108] Larry Kaufman and Harold Bernstein, editors. *Computer Calculation of Phase Diagrams*. Academic Press Inc, 1970.
- [109] Koutaro Kawata, Hideki Maekawa, Takahiro Nemoto, and Tsutomu Yamamura. Local structure analysis of YSZ by Y-89 MAS-NMR. *Solid State Ionics*, 177(19-25 SPEC. ISS.):1687–1690, 2006.
- [110] A. S. Khanna. High Temperature Oxidation. In *Handbook of Environmental Degradation of Materials: Second Edition*, pages 127–194. Elsevier Inc., second edition, 2012.
- [111] Du Soung Kim and Israel E. Wachs. Surface rhenium oxide-support interaction for supported Re₂O₇ catalysts, 1993.
- [112] D. M. King, S. C. Middleburgh, L. Edwards, G. R. Lumpkin, and M. Cortie. Predicting the Crystal Structure and Phase Transitions in High-Entropy Alloys. *Jom*, 67(10):2375–2380, 2015.
- [113] D.J.M. J M King, S.C. C. Middleburgh, A.G. G. McGregor, and M.B. B. Cortie. Predicting the formation and stability of single phase high-entropy alloys. *Acta Materialia*, 104:172–179, 2016.
- [114] H. W. King. Quantitative size-factors for metallic solid solutions. *Journal of Materials Science*, 1(1):79–90, 1966.
- [115] Charles Kittel and Paul McEuen. *Introduction to Solid State Physics*. John Wiley & Sons, Inc, Hoboken, NJ, 8th edition, 2005.

- [116] P. G. Klemens. Phonon scattering and thermal resistance due to grain boundaries. *International Journal of Thermophysics*, 15(6):1345–1351, nov 1994.
- [117] Hartmuth C Kolb, M G Finn, and K Barry Sharpless. Click chemistry: Diverse Chemical Function from a Few Good Reactions. *Angewandte Chemie - International Edition*, 40:2004–2021, 2001.
- [118] Hartmuth C. Kolb and K. Barry Sharpless. The growing impact of click chemistry on drug discovery. *Drug Discov. Today*, 8(24):1128–1137, 2003.
- [119] Igor Kosacki, Harlan U. Anderson, Yasunobu Mizutani, and Kenji Ukai. Non-stoichiometry and electrical transport in Sc-doped zirconia. *Solid State Ionics*, 152-153:431–438, 2002.
- [120] R. Krishnan, R. Kesavamoorthy, S. Dash, A. K. Tyagi, and Baldev Raj. Raman spectroscopic and photoluminescence investigations on laser surface modified α -Al₂O₃ coatings. *Scripta Materialia*, 48(8):1099–1104, 2003.
- [121] Harold H. Kung and Edmond I. Ko. Preparation of oxide catalysts and catalyst supports - A review of recent advances. *Chemical Engineering Journal and the Biochemical Engineering Journal*, 64(2):203–214, 1996.
- [122] Rainer K ngas, Fred Bidrawn, Eyas Mahmoud, John M. Vohs, and Raymond J. Gorte. Evidence of surface-reaction rate limitations in SOFC composite cathodes. *Solid State Ionics*, 225:146–150, 2012.
- [123] Ludv k Kunz, Petr Luk s, and Radomila Kone n . High-cycle fatigue of Ni-base superalloy Inconel 713LC. *International Journal of Fatigue*, 32(6):908–913, 2010.
- [124] M. Kurumada, H. Hara, and E. Iguchi. Oxygen vacancies contributing to intragranular electrical conduction of yttria-stabilized zirconia (YSZ) ceramics. *Acta Materialia*, 53(18):4839–4846, 2005.
- [125] M. Lachowicz, W. Dudziński, K. Haimann, and M. Podrez-Radziszewska. Microstructure transformations and cracking in the matrix of γ - γ' superalloy Inconel 713C melted with electron beam. *Materials Science and Engineering A*, 479(1-2):269–276, 2008.
- [126] M. A. Laguna-Bercero, J. A. Kilner, and S. J. Skinner. Development of oxygen electrodes for reversible solid oxide fuel cells with scandia stabilized zirconia electrolytes. *Solid State Ionics*, 192(1):501–504, 2011.

- [127] Edward L. Lee and Israel E. Wachs. In situ Raman spectroscopy of SiO₂-supported transition metal oxide catalysts: An isotopic ¹⁸O-¹⁶O exchange study. *Journal of Physical Chemistry C*, 112(16):6487–6498, 2008.
- [128] Eunseok Lee, Friedrich B. Prinz, and Wei Cai. Enhancing ionic conductivity of bulk single-crystal yttria-stabilized zirconia by tailoring dopant distribution. *Physical Review B - Condensed Matter and Materials Physics*, 83(5):1–4, 2011.
- [129] Se Hee Lee, Hyeonsik M. Cheong, Nam Gyu Park, C. Edwin Tracy, Angelo Mascarenhas, David K. Benson, and Satyen K. Deb. Raman spectroscopic studies of Ni-W oxide thin films. *Solid State Ionics*, 140(1-2):135–139, 2001.
- [130] Ze Lei and Qingshan Zhu. Low temperature processing of dense nanocrystalline scandia-doped zirconia (ScSZ) ceramics. *Solid State Ionics*, 176(37-38):2791–2797, 2005.
- [131] Kirsten Leistner, Charles Toulemonde, Boubakar Diawara, Antoine Seyeux, and Philippe Marcus. Oxide film growth kinetics on metals and alloys ii. numerical simulation of transient behavior. *Journal of the Electrochemical Society*, 160(6), 2013.
- [132] Anmin Li and Xiyan Zhang. Thermodynamic analysis of the simple microstructure of AlCrFeNiCu high-entropy alloy with multi-principal elements. *Acta Metallurgica Sinica (English Letters)*, 22(3):219–224, 2009.
- [133] B.S. Li, Y.P. Wang, M.X. Ren, C. Yang, and H.Z. Fu. Effects of Mn, Ti and V on the microstructure and properties of AlCrFeCoNiCu high entropy alloy. *Materials Science and Engineering: A*, 498(1-2):482–486, dec 2008.
- [134] Binbin Lian, Tao Sun, and Yimin Song. Parameter sensitivity analysis of a 5-DoF parallel manipulator. *Robotics and Computer-Integrated Manufacturing*, 46(December 2015):1–14, 2017.
- [135] Meina Liu, Beng Hoon Tan, Robert P. Burford, and Andrew B. Lowe. Nucleophilic thiol-Michael chemistry and hyperbranched (co)polymers: synthesis and ring-opening metathesis (co)polymerization of novel difunctional exo-7-oxanorbornenes with in situ inimer formation. *Polymer Chemistry*, 4(11):3300, 2013.
- [136] Tao Liu, Xiaofang Zhang, Lei Yuan, and Jingkun Yu. A review of higherature electrochemical sensors based on stabilized zirconia. *Solid State Ionics*, 283:91–102, 2015.

- [137] Zhenyu Liu, Wei Gao, Karl Dahm, and Fuhui Wang. The effect of coating grain size on the selective oxidation behaviour of Ni-Cr-Al alloy. *Scripta Materialia*, 37(10):1551–1558, 1997.
- [138] C. J. Long, J. Hattrick-Simpers, M. Murakami, R. C. Srivastava, I. Takeuchi, V. L. Karen, and X. Li. Rapid structural mapping of ternary metallic alloy systems using the combinatorial approach and cluster analysis. *Review of Scientific Instruments*, 78(7):072217–1 – 072217–6, 2007.
- [139] Maïke Lübbe, Alexander M. Gigler, Robert W. Stark, and Wolfgang Moritz. Identification of iron oxide phases in thin films grown on Al₂O₃(0 0 0 1) by Raman spectroscopy and X-ray diffraction. *Surface Science*, 604(7-8):679–685, 2010.
- [140] Alfred Ludwig, Robert Zarnetta, Sven Hamann, Alan Savan, and Sigurd Thienhaus. Development of multifunctional thin films using high-throughput experimentation methods. *International Journal of Materials Research*, 99(10):1144–1149, 2008.
- [141] Vanni Lughì and David R. Clarke. High temperature aging of YSZ coatings and subsequent transformation at low temperature. *Surface and Coatings Technology*, 200(5-6):1287–1291, 2005.
- [142] Soe Lwin, Christopher Keturakis, Jaros'Aw Handzlik, Philippe Sautet, Yuanyuan Li, Anatoly I. Frenkel, and Israel E. Wachs. Surface ReO_x sites on Al₂O₃ and their molecular structure-reactivity relationships for olefin metathesis. *ACS Catalysis*, 5(3):1432–1444, 2015.
- [143] Blake MacQueen, Elizabeth Barrow, Gerardo Rivera Castro, Yomaira Pagan-Torres, Andreas Heyden, and Jochen Lauterbach. Optimum Reaction Conditions for 1,4-Anhydroerythritol and Xylitol Hydrodeoxygenation over a ReO_x-Pd/CeO₂ Catalyst via Design of Experiments. *Industrial & Engineering Chemistry Research*, 58:8681–8689, 2019.
- [144] Neelima Mahato, Amitava Banerjee, Alka Gupta, Shobit Omar, and Kantesh Balani. Progress in material selection for solid oxide fuel cell technology: A review. *Progress in Materials Science*, 72:141–337, 2015.
- [145] Wilhelm F. Maier, Klaus Stowe, and Simone Sieg. Combinatorial and high-throughput materials science. *Angewandte Chemie - International Edition*, 46(32):6016–6067, 2007.

- [146] Huahai Mao, Hai Lin Chen, and Qing Chen. TCHEA1: A Thermodynamic Database Not Limited for “High Entropy” Alloys. *Journal of Phase Equilibria and Diffusion*, 38(4):353–368, 2017.
- [147] Thaddeus B. Massalski, Okamoto Hiroaki, P.R. Subramanian, and Linda Kacprzak. *Binary alloy phase diagrams*. ASM International, Materials Park, OH, 2 edition, 1990.
- [148] Thaddeus B. Massalski, Okamoto Hiroaki, P.R. Subramanian, and Linda Kacprzak. *Binary alloy phase diagrams vol. 2*. ASM International, Materials Park, OH, 2 edition, 1990.
- [149] Thaddeus B. Massalski, Okamoto Hiroaki, P.R. Subramanian, and Linda Kacprzak. *Binary alloy phase diagrams vol. 3*. ASM International, Materials Park, OH, 2 edition, 1990.
- [150] Yoshio Matsuzaki, Yuya Tachikawa, Takaaki Somekawa, Toru Hatae, Hiroshige Matsumoto, Shunsuke Taniguchi, and Kazunari Sasaki. Effect of proton-conduction in electrolyte on electric efficiency of multi-stage solid oxide fuel cells. *Scientific Reports*, 5:1–10, 2015.
- [151] John Matthews. *Epitaxial growth*. Elsevier, 2012.
- [152] Z. Mazur, A. Luna-Ramírez, J. A. Juárez-Islas, and A. Campos-Amezcu. Failure analysis of a gas turbine blade made of Inconel 738LC alloy. *Engineering Failure Analysis*, 12(3):474–486, 2005.
- [153] C. Mercer, J. R. Williams, D. R. Clarke, and A. G. Evans. On a ferroelastic mechanism governing the toughness of metastable tetragonal-prime (t') yttria-stabilized zirconia. *Proceedings of the Royal Society A: Mathematical, Physical and Engineering Sciences*, 463(2081):1393–1408, 2007.
- [154] Christopher Jason Metting, Jonathan Kenneth Bunn, Ellen Underwood, Stephen Smoak, and Jason Hattrick-Simpers. Combinatorial approach to turbine bond coat discovery. *ACS Combinatorial Science*, 15(8):419–424, 2013.
- [155] A. R. Miedema. A Simple Model for Alloys. *Philips Technical Review*, 33(6):149–160, 1973.
- [156] K. Minami, T. Masui, N. Imanaka, L. Dai, and B. Pacaud. Redox behavior of CeO₂-ZrO₂-Bi₂O₃ and CeO₂-ZrO₂-Y₂O₃ solid solutions at moderate temperatures. *Journal of Alloys and Compounds*, 408-412:1132–1135, 2006.

- [157] D. B. Miracle. High entropy alloys and their development as structural materials. *Materials Science and Technology*, 31(10):1142–1147, 2015.
- [158] Daniel B. Miracle, Jonathan D. Miller, Oleg N. Senkov, Christopher Woodward, Michael D. Uchic, and Jaimie Tiley. Exploration and development of high entropy alloys for structural applications. *Entropy*, 16(1):494–525, 2014.
- [159] D.B. Miracle and O.N. Senkov. A critical review of high entropy alloys and related concepts. *Acta Materialia*, 122:448–511, 2016.
- [160] A. Misra, H. D. Bist, M. S. Navati, R. K. Thareja, and J. Narayan. Thin film of aluminum oxide through pulsed laser deposition: A micro-Raman study. *Materials Science and Engineering B: Solid-State Materials for Advanced Technology*, 79(1):49–54, 2001.
- [161] Norio Miura, Tomoaki Sato, Sri Ayu Anggraini, Hiroshi Ikeda, and Serge Zhuiykov. A review of mixed-potential type zirconia-based gas sensors. *Ionics*, 20(7):901–925, 2014.
- [162] Uichiro Mizutani and Hirokazu Sato. The physics of the Hume-Rothery electron concentration rule. *Crystals*, 7(1), 2017.
- [163] AK Moidu, AN Sinclair, and JK Spelt. Analysis of the Peel Test: Prediction of Adherend Plastic Dissipation and Extraction of Fracture Energy in Metal-to-Metal Adhesive Joints. *Journal of Testing and Evaluation*, 23(4):241, 1995.
- [164] Jorge Moncada, William R. Adams, Raj Thakur, Michael Julin, and Carlos A. Carrero. Developing a Raman Spectrokinetic Approach to Gain Insights into the Structure-Reactivity Relationship of Supported Metal Oxide Catalysts. *ACS Catalysis*, 8(10):8976–8986, 2018.
- [165] D C Montgomery. *Design and Analysis of Experiments*. Design and Analysis of Experiments. John Wiley & Sons, 7th edition, 2008.
- [166] A. Mortensen, D. H. Christensen, O. Faurskov Nielsen, and E. Pedersen. Raman spectra of amorphous Al₂O₃ and Al₂O₃/MoO₃ obtained by visible and infrared excitation. *Journal of Raman Spectroscopy*, 22(1):47–49, jan 1991.
- [167] BS Murty, Jien-Wei Yeh, and S Ranganathan. *High-Entropy Alloys*. Butterworth-Heinemann, 2014.

- [168] Raymond H. Myers, Douglas C. Montgomery, G. Geoffrey Vining, Connie M. Borror, and Scott M. Kowalski. Response Surface Methodology: A Retrospective and Literature Survey. *Journal of Quality Technology*, 36(1):53–78, 2004.
- [169] E. J. Naimaster and A. K. Sleiti. Potential of SOFC CHP systems for energy-efficient commercial buildings. *Energy and Buildings*, 61:153–160, 2013.
- [170] Devatha P. Nair, Neil B. Cramer, Timothy F. Scott, Christopher N. Bowman, and Robin Shandas. Photopolymerized thiol-ene systems as shape memory polymers. *Polymer*, 51(19):4383–4389, 2010.
- [171] Charles Nason, Todd Roper, Charles Hoyle, and John A. Pojman. UV-induced frontal polymerization of multifunctional (meth)acrylates. *Macromolecules*, 38(13):5506–5512, 2005.
- [172] J. A. Nelder and R. Mead. A Simplex Method for Function Minimization. *The Computer Journal*, 7(4):308–313, jan 1965.
- [173] K Nomura. Aging and Raman scattering study of scandia and yttria doped zirconia. *Solid State Ionics*, 132(3-4):235–239, 2000.
- [174] Brian H. Northrop and Roderick N. Coffey. Thiol-ene click chemistry: Computational and kinetic analysis of the influence of alkene functionality. *Journal of the American Chemical Society*, 134(33):13804–13817, 2012.
- [175] National Transportation Safety Board (NTSB). Aircraft accident report - In-flight breakup over the Atlantic Ocean Trans World Airlines Flight 800 Boeing 747-131, N93119, near East Moriches, New York, July 17, 1996. Technical report, 1996.
- [176] Ivan Ohlídal. Immersion spectroscopic reflectometry of multilayer systems I Theory. *Journal of the Optical Society of America A*, 5(4):459, apr 1988.
- [177] Ivan Ohlídal, Frantisek Vizard, and Miloslav Ohlídal. Optical analysis by means of spectroscopic reflectometry of single and double layers with correlated randomly rough boundaries. *Optical Engineering*, 34(6):1761, jun 1995.
- [178] Oguz Okay and Christopher N. Bowman. Kinetic modeling of thiol-ene reactions with both step and chain growth aspects. *Macromolecular Theory and Simulations*, 14(4):267–277, 2005.

- [179] Nese Orbey. UV-Curable Aerospace and Aircraft Coatings. Technical Report August, 2006.
- [180] Nobuhiko Ota, Masazumi Tamura, Yoshinao Nakagawa, Kazu Okumura, and Keiichi Tomishige. Hydrodeoxygenation of vicinal OH groups over heterogeneous rhenium catalyst promoted by palladium and ceria support. *Angewandte Chemie - International Edition*, 54(6):1897–1900, 2015.
- [181] Nobuhiko Ota, Masazumi Tamura, Yoshinao Nakagawa, Kazu Okumura, and Keiichi Tomishige. Performance, Structure, and Mechanism of ReO_x-Pd/CeO₂ Catalyst for Simultaneous Removal of Vicinal OH Groups with H₂. *ACS Catalysis*, 6(5):3213–3226, 2016.
- [182] F. Otto, Y. Yang, H. Bei, and E. P. George. Relative effects of enthalpy and entropy on the phase stability of equiatomic high-entropy alloys. *Acta Materialia*, 61(7):2628–2638, 2013.
- [183] Nitin P Padture. Thermal Barrier Coatings for Gas-Turbine Engine Applications. *Science*, 296(5566):280–284, 2002.
- [184] Jinsu Park, B.Y. Yoon, C.O. Park, Won-Jun Lee, and C.B. Lee. Sensing behavior and mechanism of mixed potential NO_x sensors using NiO, NiO(+YSZ) and CuO oxide electrodes. *Sensors and Actuators B: Chemical*, 135(2):516–523, jan 2009.
- [185] Matthew A. Payne, James B. Miller, and Andrew J. Gellman. High-throughput characterization of early oxidation across Al_xFeyNi_{1-x-y} composition space. *Corrosion Science*, 91:46–57, 2015.
- [186] Matthew A. Payne, James B. Miller, Martin E. Oliveros, Geronimo Perez, Cristol P. Gouvea, Bráulio S. Archanjo, Carlos A. Achete, and Andrew J. Gellman. Assessment of a High-Throughput Methodology for the Study of Alloy Oxidation using Al_xFeyNi_{1-x-y} Composition Gradient Thin Films. *ACS Combinatorial Science*, 18(7):425–436, 2016.
- [187] John H Perepezko. The Hotter the Engine, the Better. *Science*, 326(5956):1068–1069, nov 2009.
- [188] S Pinchas, Brian L Silver, and I Laulicht. Infrared Absorption Spectra of the 18 O-Labeled Acetylacetonates of Cr(III) and Mn(III). *The Journal of Chemical Physics*, 46(4):1506–1510, feb 1967.

- [189] Antonio Pizzi and K.L. Mittal, editors. *Handbook of Adhesive Technology*. Marcel Dekker, New York, 2nd edition, 2003.
- [190] P. Platt, P. Frankel, M. Gass, R. Howells, and M. Preuss. Finite element analysis of the tetragonal to monoclinic phase transformation during oxidation of zirconium alloys. *Journal of Nuclear Materials*, 454(1-3):290–297, 2014.
- [191] Radislav A Potyrailo, Krishna Rajan, Klaus Stowe, Ichiro Takeuchi, Bret Chisholm, and Hubert Lam. Combinatorial and High-Throughput Screening of Materials Libraries : Review of State of the Art Combinatorial and High-Throughput Screening of Materials Libraries : Review of State of the Art. *ACS Combinatorial Science*, 13:579–633, 2011.
- [192] A. M. Racu, D. Menzel, J. Schoenes, and K. Doll. Crystallographic disorder and electron-phonon coupling in Fe_{1-x}Co_xSi single crystals: Raman spectroscopy study. *Physical Review B - Condensed Matter and Materials Physics*, 76(11), 2007.
- [193] A. M. Racu, D. Menzel, J. Schoenes, M. Marutzky, S. Johnsen, and B. B. Iversen. Phonon properties in narrow gap FeSi and FeSb₂ single crystals. *Journal of Applied Physics*, 103(7):101–104, 2008.
- [194] P. Rahulkumar, A. Jagota, S. J. Bennison, and S. Saigal. Cohesive element modeling of viscoelastic fracture: Application to peel testing of polymers. *International Journal of Solids and Structures*, 37(13):1873–1897, 2000.
- [195] R. Ramamoorthy, D. Sundararaman, and S. Ramasamy. Ionic conductivity studies of ultrafine-grained yttria stabilized zirconia polymorphs. *Solid State Ionics*, 123(1):271–278, 1999.
- [196] C V Raman and K S Krishnan. A new class of spectra due to secondary radiation Part I. *Indian Journal of Physics*, 2:399–419, jan 1928.
- [197] S Ranganathan. Alloyed pleasures: Multimetallc cocktails. *Current Science*, 85(10):10–12, 2003.
- [198] Sushila Rani, Atul K. Agrawal, and Vikas Rastogi. Failure analysis of a first stage IN738 gas turbine blade tip cracking in a thermal power plant. *Case Studies in Engineering Failure Analysis*, 8:1–10, 2017.

- [199] Dmitriy Rappoport and Filipp Furche. Lagrangian approach to molecular vibrational Raman intensities using time-dependent hybrid density functional theory. *Journal of Chemical Physics*, 126(20):1–5, 2007.
- [200] Fang Ren, Ronald Pandolfi, Douglas Van Campen, Alexander Hexemer, and Apurva Mehta. On-the-fly data assessment for high-throughput X-ray diffraction measurements. *ACS Combinatorial Science*, 19(6):377–385, 2017.
- [201] Xiaorui Ren and Wei Pan. Mechanical properties of high-temperature-degraded yttria-stabilized zirconia. *Acta Materialia*, 69:397–406, 2014.
- [202] Christina M Rost, Edward Sachet, Trent Borman, Ali Moballeghe, Elizabeth C Dickey, Dong Hou, Jacob L Jones, Stefano Curtarolo, and Jon-paul Maria. Entropy-stabilized oxides. *Nature Communications*, 6(1):8485, dec 2015.
- [203] David E Ruddell, Brian R Stoner, and Jeffrey Y Thompson. The effect of deposition parameters on the properties of yttria-stabilized zirconia thin films. *Thin Solid Films*, 445(1):14–19, nov 2003.
- [204] B. Saha, N. S. Das, and K. K. Chattopadhyay. Combined effect of oxygen deficient point defects and Ni doping in radio frequency magnetron sputtering deposited ZnO thin films. *Thin Solid Films*, 562:37–42, 2014.
- [205] J. Sainio, M. Aronniemi, O. Pakarinen, K. Kauraala, S. Airaksinen, O. Krause, and J. Lahtinen. An XPS study of CrO_x on a thin alumina film and in alumina supported catalysts. *Applied Surface Science*, 252(4):1076–1083, 2005.
- [206] Adib J. Samin and Christopher D. Taylor. An Analysis of Limiting Cases for the Metal Oxide Film Growth Kinetics Using an Oxygen Defects Model Accounting for Transport and Interfacial Reactions. *Journal of Non-Equilibrium Thermodynamics*, 43(4):317–326, 2018.
- [207] N. M. Sammes and Cai Zhihong. Ionic conductivity of ceria/yttria stabilized zirconia electrolyte materials. *Solid State Ionics*, 100(1-2):39–44, 1997.
- [208] S. Sarat, N. Sammes, and A. Smirnova. Bismuth oxide doped scandia-stabilized zirconia electrolyte for the intermediate temperature solid oxide fuel cells. *Journal of Power Sources*, 160(2):892–896, oct 2006.
- [209] Pierre Sarrazin, Alain Galerie, and Jacques Fouletier. *Mechanisms of High Temperature Corrosion: a kinetic approach*. Trans Tech Publications Ltd, Stafa-Zuerich, 2008.

- [210] Günter Sauerbrey. Verwendung von Schwingquarzen zur Wägung dünner Schichten und zur Mikrowägung. *Zeitschrift für Physik*, 155(2):206–222, apr 1959.
- [211] Patrick K. Schelling and Simon R. Phillpot. Mechanism of Thermal Transport in Zirconia and Yttria-Stabilized Zirconia by Molecular-Dynamics Simulation. *Journal of the American Ceramic Society*, 84(12):2997–3007, 2001.
- [212] S Schiller, K Goedicke, J Reschke, V Kirchhoff, S Schneider, and F Milde. Pulsed magnetron sputter technology. *Surf. Coat. Technol.*, 61:331–337, 1993.
- [213] K. W. Schlichting, N. P. Padture, and P. G. Klemens. Thermal conductivity of dense and porous yttria-stabilized zirconia. *Journal of Materials Science*, 36(12):3003–3010, 2001.
- [214] National Science and Technology Council (US). *Materials genome initiative for global competitiveness*. Executive Office of the President, National Science and Technology Council, 2011.
- [215] O. N. Senkov, J. M. Scott, S. V. Senkova, D. B. Miracle, and C. F. Woodward. Microstructure and room temperature properties of a high-entropy TaNbHfZrTi alloy. *Journal of Alloys and Compounds*, 509(20):6043–6048, 2011.
- [216] Antoine Seyeux, Vincent Maurice, and Philippe Marcus. Oxide film growth kinetics on metals and alloys i. physical model. *Journal of the Electrochemical Society*, 160(6), 2013.
- [217] E. A.G. Shillington and D. R. Clarke. Spalling failure of a thermal barrier coating associated with aluminum depletion in the bond-coat. *Acta Materialia*, 47(4):1297–1305, 1999.
- [218] M. Sillassen, P. Eklund, N. Pryds, N. Bonanos, and J. Bøttiger. Concentration-dependent ionic conductivity and thermal stability of magnetron-sputtered nanocrystalline scandia-stabilized zirconia. *Solid State Ionics*, 181(23-24):1140–1145, 2010.
- [219] M. Sillassen, P. Eklund, M. Sridharan, N. Pryds, N. Bonanos, and J. Bøttiger. Ionic conductivity and thermal stability of magnetron-sputtered nanocrystalline yttria-stabilized zirconia. *Journal of Applied Physics*, 105(10), 2009.
- [220] Michael Sillassen, Per Eklund, Nini Pryds, Erik Johnson, Ulf Helmersson, and Jørgen Bøttiger. Low-Temperature Superionic Conductivity in Strained Yttria-

- Stabilized Zirconia. *Advanced Functional Materials*, 20(13):2071–2076, may 2010.
- [221] Preetam Singh and John B. Goodenough. Monoclinic $\text{Sr}_{1-x}\text{NaxSiO}_{3-0.5x}$: New superior oxide ion electrolytes. *Journal of the American Chemical Society*, 135(27):10149–10154, 2013.
- [222] Donald L. Smith. *Thin-Film Deposition: Principles and Practice*. McGraw-Hill, New York, 1995.
- [223] A. A. Solovyev, N. S. Sochugov, S. V. Rabotkin, A. V. Shipilova, I. V. Ionov, A. N. Kovalchuk, and A. O. Borduleva. Application of PVD methods to solid oxide fuel cells. *Applied Surface Science*, 310:272–277, 2014.
- [224] Chunshan Song. Fuel processing for low-temperature and high-temperature fuel cells: Challenges, and opportunities for sustainable development in the 21st century. *Catalysis Today*, 77(1-2):17–49, 2002.
- [225] Bradley J. Sparks, Ethan F.T. Hoff, Latonya P. Hayes, and Derek L. Patton. Mussel-inspired thiol-ene polymer networks: Influencing network properties and adhesion with catechol functionality. *Chemistry of Materials*, 24(18):3633–3642, 2012.
- [226] Bradley J. Sparks, Ethan F.T. Hoff, Li Xiong, James T. Goetz, and Derek L. Patton. Superhydrophobic hybrid inorganic-organic thiol-ene surfaces fabricated via spray-deposition and photopolymerization. *ACS Applied Materials and Interfaces*, 5(5):1811–1817, 2013.
- [227] D. Stanoi, G. Socol, C. Grigorescu, F. Guinneton, O. Monnereau, L. Tortet, T. Zhang, and I. N. Mihailescu. Chromium oxides thin films prepared and coated in situ with gold by pulsed laser deposition. *Materials Science and Engineering B: Solid-State Materials for Advanced Technology*, 118(1-3):74–78, 2005.
- [228] D. W. Strickler and W. G. Carlson. Electrical Conductivity in the ZrO_2 -Rich Region of Several M_2O_3 — ZrO_2 Systems. *Journal of the American Ceramic Society*, 48(6):286–289, 1965.
- [229] DW Strickler and WG Carlson. Ionic conductivity of cubic solid solutions in the system CaO — Y_2O_3 — ZrO_2 . *Journal of the American Ceramic Society*, 47(3):122–127, 1964.

- [230] Weiguang Su, Jing Zhang, Zhaochi Feng, Tao Chen, Pinliang Ying, and Can Li. Surface phases of TiO₂ nanoparticles studied by UV raman spectroscopy and FT-IR spectroscopy. *Journal of Physical Chemistry C*, 112(20):7710–7716, 2008.
- [231] S. Swann. Magnetron sputtering. *Physics in Technology*, 19(2):67–75, 1988.
- [232] Akira Takeuchi and Akihisa Inoue. Classification of Bulk Metallic Glasses by Atomic Size Difference, Heat of Mixing and Period of Constituent Elements and Its Application to Characterization of the Main Alloying Element. *Materials Transactions*, 46(12):2817–2829, 2005.
- [233] Liang Tang. *Fundamentals of Nanotechnology (Hornyak, G.I., et al.) [Book reviews]*, volume 3. CRC Press, Boca Raton, FL, 1st ed. edition, 2009.
- [234] Shuhei Tazawa, Nobuhiko Ota, Masazumi Tamura, Yoshinao Nakagawa, Kazu Okumura, and Keiichi Tomishige. Deoxydehydration with Molecular Hydrogen over Ceria-Supported Rhenium Catalyst with Gold Promoter. *ACS Catalysis*, 6(10):6393–6397, 2016.
- [235] E. Terzini, G. Nobile, S. Loreti, C. Minarini, T. Polichetti, and P. Thilakan. Influences of Sputtering Power and Substrate Temperature on the Properties of RF Magnetron Sputtered Indium Tin Oxide Thin Films. *Japanese Journal of Applied Physics*, 38(Part 1, No. 6A):3448–3452, 1999.
- [236] S. Thienhaus, D. Naujoks, J. Pftzing-Micklich, D. König, and A. Ludwig. Rapid identification of areas of interest in thin film materials libraries by combining electrical, optical, X-ray diffraction, and mechanical high-throughput measurements: A case study for the system ni-al. *ACS Combinatorial Science*, 16(12):686–694, 2014.
- [237] Henryk Tomaszewski, Johan Haemers, Nico De Roo, Jurgen Denul, and Roger De Gryse. Ytria-stabilized zirconia thin films grown by r.f. magnetron sputtering from an oxide target. *Thin Solid Films*, 293(1-2):67–74, jan 1997.
- [238] Chung-jin Tong, Yu-liang Chen, Swe-kai Chen, Jien-wei Yeh, Tao-tsung Shun, Chun-huei Tsau, Su-jien Lin, and Shou-yi Chang. Microstructure Characterization of Al x CoCrCuFeNi High-Entropy Alloy System with Multiprincipal Elements. *Metallurgical and Materials Transactions A*, 36(April), 2005.
- [239] Ming-Hung Tsai, Chun-Wen Wang, Che-Wei Tsai, Wan-Jui Shen, Jien-Wei Yeh, Jon-Yiew Gan, and Wen-Wei Wu. Thermal Stability and Performance of Nb-

- SiTaTiZr High-Entropy Alloy Barrier for Copper Metallization. *Journal of The Electrochemical Society*, 158(11):H1161, 2011.
- [240] Ming-Hung Tsai and Jien-Wei Yeh. High-Entropy Alloys: A Critical Review. *Materials Research Letters*, 2(3):107–123, apr 2014.
- [241] Ming-Hung Tsai, Jien-Wei Yeh, and Jon-Yiew Gan. Diffusion barrier properties of AlMoNbSiTaTiVZr high-entropy alloy layer between copper and silicon. *Thin Solid Films*, 516(16):5527–5530, jun 2008.
- [242] George Tsilomelekis and Soghomon Boghosian. In situ raman and FTIR spectroscopy of molybdenum(VI) oxide supported on titania combined with $^{18}\text{O}/^{16}\text{O}$ exchange: Molecular structure, vibrational properties, and vibrational isotope effects. *Journal of Physical Chemistry C*, 115(5):2146–2154, 2011.
- [243] Chung-Chin Chin Tung, Jien-Wei Wei Yeh, Tao-tsung Tsung Shun, Swe-Kai Kai Chen, Yuan-Sheng Sheng Huang, and Hung-Cheng Cheng Chen. On the elemental effect of AlCoCrCuFeNi high-entropy alloy system. *Materials Letters*, 61(1):1–5, jan 2007.
- [244] Mohammad Vaezi and Masoud Soleymani. Creep Life Prediction of Inconel 738 Gas Turbine Blade. *Journal of Applied Sciences*, 9(10):1950–1955, oct 2009.
- [245] V. Vijaya Lakshmi, Ranjit Bauri, Ashutosh S. Gandhi, and S. Paul. Synthesis and characterization of nanocrystalline ScSZ electrolyte for SOFCs. *International Journal of Hydrogen Energy*, 36(22):14936–14942, 2011.
- [246] Tuan Vo-Dinh and Fei Yan. Surface-enhanced raman scattering. In *Optical Chemical Sensors*, pages 239–259. Springer, 2006.
- [247] Johannes G. de Vries and André H.M. de Vries. The Power of High-Throughput Experimentation in Homogeneous Catalysis Research for Fine Chemicals. *European Journal of Organic Chemistry*, 2003(5):799–811, 2003.
- [248] Michael A. Vuurman and Israel E. Wachs. In situ Raman spectroscopy of alumina-supported metal oxide catalysts. *Journal of Physical Chemistry*, 96(12):5008–5016, 1992.
- [249] Israel E. Wachs and Charles A. Roberts. Monitoring surface metal oxide catalytic active sites with Raman spectroscopy. *Chemical Society Reviews*, 39(12):5002–5017, 2010.

- [250] Eric Wachsman, Tatsumi Ishihara, and John Kilner. Low-temperature solid-oxide fuel cells. *Mrs Bulletin*, 39(9):773–779, 2014.
- [251] F. J. Walker and A. C. Anderson. Low-energy excitations in yttria-stabilized zirconia. *Physical Review B*, 29(10):5881–5890, 1984.
- [252] Chao Wang, Erdem Sasmaz, Cun Wen, and Jochen Lauterbach. Pd supported on SnO₂-MnO_x-CeO₂ catalysts for low temperature CO oxidation. *Catalysis Today*, 258:481–486, 2015.
- [253] Chao Wang, Cun Wen, Jochen Lauterbach, and Erdem Sasmaz. Superior oxygen transfer ability of Pd/MnO_x-CeO₂ for enhanced low temperature CO oxidation activity. *Applied Catalysis B: Environmental*, 206:1–8, 2017.
- [254] Ling Wang, Huizhu Zhou, Kui Liu, Yinlin Wu, Lei Dai, and R.V. Kumar. A CO₂ gas sensor based upon composite Nasicon/Sr-β-Al₂O₃ bielectrolyte. *Solid State Ionics*, 179(27-32):1662–1665, sep 2008.
- [255] Bert M. Weckhuysen, Jih-Mirn Jehng, and Israel E. Wachs. In Situ Raman Spectroscopy of Supported Transition Metal Oxide Catalysts: ¹⁸O₂ – ¹⁶O₂ Isotopic Labeling Studies. *The Journal of Physical Chemistry B*, 104(31):7382–7387, 2000.
- [256] Bert M. Weckhuysen and Israel E. Wachs. In Situ Raman Spectroscopy of Supported Chromium Oxide Catalysts: ¹⁸O₂ – ¹⁶O₂ Isotopic Labeling Studies. *The Journal of Physical Chemistry B*, 101(15):2793–2796, 1997.
- [257] Tao Wei, Preetam Singh, Yunhui Gong, John B. Goodenough, Yunhui Huang, and Kevin Huang. Sr₃-3xNa_{3x}Si₃O₉-1.5x (x = 0.45) as a superior solid oxide-ion electrolyte for intermediate temperature-solid oxide fuel cells. *Energy & Environmental Science*, 7(5):1680–1684, 2014.
- [258] J Will. Fabrication of thin electrolytes for second-generation solid oxide fuel cells. *Solid State Ionics*, 131(1-2):79–96, 2000.
- [259] Edgar Bright Wilson, John Courtney Decius, and Paul C Cross. *Molecular vibrations: the theory of infrared and Raman vibrational spectra*. Courier Corporation, 1980.
- [260] Michael R. Winter and David R. Clarke. Thermal conductivity of yttria-stabilized zirconia-hafnia solid solutions. *Acta Materialia*, 54(19):5051–5059, 2006.

- [261] Michael R. Winter and David R. Clarke. Oxide Materials with Low Thermal Conductivity. *Journal of the American Ceramic Society*, 90(2):533–540, feb 2007.
- [262] Grégoire Witz, Valery Shklover, Walter Steurer, Sharath Bachegowda, and Hans-Peter Peter Bossmann. Phase evolution in yttria-stabilized zirconia thermal barrier coatings studied by rietveld refinement of X-ray powder diffraction patterns. *Journal of the American Ceramic Society*, 90(9):2935–2940, sep 2007.
- [263] Yongjie Xi, Wenqiang Yang, Salai Cheettu Ammal, Jochen Lauterbach, Yomaira Pagan-Torres, and Andreas Heyden. Mechanistic study of the ceria supported, re-catalyzed deoxydehydration of vicinal OH groups. *Catalysis Science and Technology*, 8(22):5740–5752, 2018.
- [264] Shuibo Xie, Enrique Iglesia, and Alexis T. Bell. Effects of temperature on the raman spectra and dispersed oxides. *Journal of Physical Chemistry B*, 105(22):5144–5152, 2001.
- [265] Gang Xu, Ya-Wen Zhang, Chun-Sheng Liao, and Chun-Hua Yan. Doping and grain size effects in nanocrystalline ZrO₂-Sc₂O₃ system with complex phase transitions: XRD and Raman studies. *Physical Chemistry Chemical Physics*, 6(23):5410, 2004.
- [266] J. Xu. Nano measurer sem analysis software. Department of Chemistry, Fudan University, 2008.
- [267] Osamu Yamamoto. Solid oxide fuel cells: Fundamental aspects and prospects. *Electrochimica Acta*, 45(15-16):2423–2435, 2000.
- [268] Osamu Yamamoto, Yoshinori Arati, Yasuo Takeda, Nobuyuki Imanishi, Yasumobu Mizutani, Masayuki Kawai, and Yasuhisa Nakamura. Electrical conductivity of stabilized zirconia with ytterbia and scandia. *Solid State Ionics*, 79(C):137–142, 1995.
- [269] Yoshihiko Yamamura, Shinji Kawasaki, and Hiroaki Sakai. Molecular dynamics analysis of ionic conduction mechanism in yttria-stabilized zirconia. *Solid State Ionics*, 126(1):181–189, 1999.
- [270] Fan Yang, Xiaofeng Zhao, and Ping Xiao. Thermal conductivities of YSZ/Al₂O₃ composites. *Journal of the European Ceramic Society*, 30(15):3111–3116, 2010.

- [271] Hung Hua Yang, Wen Ta Tsai, Jui Chao Kuo, and Chih Chao Yang. Solid/liquid interaction between a multicomponent FeCrNiCoMnAl high entropy alloy and molten aluminum. *Journal of Alloys and Compounds*, 509(32):8176–8182, 2011.
- [272] X. Yang and Y. Zhang. Prediction of high-entropy stabilized solid-solution in multi-component alloys. *Materials Chemistry and Physics*, 132(2-3):233–238, 2012.
- [273] Masatomo Yashima, Masato Kakihana, and Masahiro Yoshimura. Metastable-stable phase diagrams in the zirconia-containing systems utilized in solid-oxide fuel cell application. *Solid State Ionics*, 86-88(PART 2):1131–1149, 1996.
- [274] Fuxing Ye, Hidetoshi Fujii, Takuya Tsumura, and Kazuhiro Nakata. Friction stir welding of Inconel alloy 600. *Journal of Materials Science*, 41(16):5376–5379, 2006.
- [275] J.-W. Yeh, S.-K. Chen, S.-J. Lin, J.-Y. Gan, T.-S. Chin, T.-T. Shun, C.-H. Tsau, and S.-Y. Chang. Nanostructured High-Entropy Alloys with Multiple Principal Elements: Novel Alloy Design Concepts and Outcomes. *Advanced Engineering Materials*, 6(5):299–303, may 2004.
- [276] Jien-Wei Yeh, Su-Jien Lin, Tsung-Shune Chin, Jon-Yiew Gan, Swe-Kai Chen, Tao-Tsung Shun, Chung-Huei Tsau, and Shou-Yi Chou. Formation of simple crystal structures in Cu-Co-Ni-Cr-Al-Fe-Ti-V alloys with multiprincipal metallic elements. *Metallurgical and Materials Transactions A*, 35(8):2533–2536, 2004.
- [277] Yaofan Yi, Ashok D. Rao, Jacob Brouwer, and G. Scott Samuelsen. Fuel flexibility study of an integrated 25 kW SOFC reformer system. *Journal of Power Sources*, 144(1):67–76, 2005.
- [278] D. J. Young and B. A. Pint. Chromium volatilization rates from Cr₂O₃ scales into flowing gases containing water vapor. *Oxidation of Metals*, 66(3-4):137–153, 2006.
- [279] Khaled M. Youssef, Alexander J. Zaddach, Changning Niu, Douglas L. Irving, and Carl C. Koch. A Novel Low-Density, High-Hardness, High-entropy Alloy with Close-packed Single-phase Nanocrystalline Structures. *Materials Research Letters*, 3(April 2015):1–5, dec 2014.

- [280] Yuan Yu, Jun Wang, Jinshan Li, Hongchao Kou, and Weimin Liu. Characterization of BCC phases in AlCoCrFeNiTix high entropy alloys. *Materials Letters*, 138:78–80, jan 2015.
- [281] F. Zhang, C. Zhang, S.L. Chen, J. Zhu, W.S. Cao, and U.R. Kattner. An understanding of high entropy alloys from phase diagram calculations. *Calphad*, 45:1–10, jun 2014.
- [282] P.X. Zhang, S.J. Huang, H.U. Habermeier, and G.M. Zhao. Isotope effect on Raman spectra of polycrystalline La_{0.67}Ca_{0.33}MnO₃. *Journal of Raman Spectroscopy*, 32(10):812–816, 2001.
- [283] Y. Zhang, Y. J. Zhou, J. P. Lin, G. L. Chen, and P. K. Liaw. Solid-solution phase formation rules for multi-component alloys. *Advanced Engineering Materials*, 10(6):534–538, 2008.
- [284] Y. W. Zhang, S. Jin, Y. Yang, G. B. Li, S. J. Tian, J. T. Jia, C. S. Liao, and C. H. Yan. Electrical conductivity enhancement in nanocrystalline (RE₂O₃)_{0.08}(ZrO₂)_{0.92} (RE=Sc, Y) thin films. *Applied Physics Letters*, 77(21):3409–3411, 2000.
- [285] Yong Zhang, Ting Ting Zuo, Zhi Tang, Michael C. Gao, Karin A. Dahmen, Peter K. Liaw, and Zhao Ping Lu. Microstructures and properties of high-entropy alloys. *Progress in Materials Science*, 61(October 2013):1–93, 2014.
- [286] Ji Cheng Zhao. Combinatorial approaches as effective tools in the study of phase diagrams and composition-structure-property relationships. *Progress in Materials Science*, 51(5):557–631, 2006.
- [287] Y. J. Zhou, Y. Zhang, Y. L. Wang, and G. L. Chen. Solid solution alloys of AlCoCrFeNi Tix with excellent room-temperature mechanical properties. *Applied Physics Letters*, 90(18), 2007.
- [288] C. Zhu, a. Javed, P. Li, F. Yang, G.Y. Liang, and P. Xiao. A study of the microstructure and oxidation behavior of alumina/yttria-stabilized zirconia (Al₂O₃/YSZ) thermal barrier coatings. *Surface and Coatings Technology*, 212:214–222, nov 2012.
- [289] Dong Yu Zhu, Guang Sheng Cao, Wen Lian Qiu, Min Zhi Rong, and Ming Qiu Zhang. Self-healing polyvinyl chloride (PVC) based on microencapsulated nucleophilic thiol-click chemistry. *Polymer (United Kingdom)*, 69:1–9, 2015.

- [290] J. M. Zhu, H. M. Fu, H. F. Zhang, a. M. Wang, H. Li, and Z. Q. Hu. Microstructures and compressive properties of multicomponent AlCoCrFeNiMox alloys. *Materials Science and Engineering A*, 527(26):6975–6979, 2010.
- [291] Elena E. Zvereva, Artur R. Shagidullin, and Sergey A. Katsyuba. Ab initio and DFT predictions of infrared intensities and raman activities. *Journal of Physical Chemistry A*, 115(1):63–69, 2011.

APPENDIX A

MPEA PHASE STABILIZATION APPENDIX

A.1 Ω AND δ VALUES FOR $(Al_xCu_yMo_{1-x-y})FeNiTiVZr$ LIBRARIES

Table A.1 shows the binary solubilities of the $(Al_xCu_yMo_{1-x-y})FeNiTiVZr$ constituent pairs. A majority of the pairs result in body-centered cubic (BCC) structures, while the varying compositions between Al, Mo, and Cu show three different structures. The Al-Mo pair results in a BCC structure, the Al-Cu pair favors a face-centered cubic (FCC) structure, and the Cu-Mo pair is mostly insoluble. Therefore, when observing the edges of pseudo-ternary diagram, destabilization effects can be predicted.

Table A.1: Solubility Table of Binary Constituent Pairs

Element <i>B</i>	Element <i>A</i>							
	Al	Cu	Mo	Fe	Ni	Ti	V	Zr
Al	FCC	FCC	BCC	BCC	$\frac{FCC}{B2}$	BCC	BCC	BCC
Cu		FCC	No Mix	$\frac{FCC}{BCC}$	FCC	$\frac{FCC}{BCC}$	BCC	BCC
Mo			BCC	BCC	$\frac{FCC}{BCC}$	BCC	BCC	BCC
Fe				$\frac{FCC}{BCC}$	$\frac{FCC}{BCC}$	BCC	$\frac{FCC}{BCC}$	BCC
Ni					FCC	$\frac{FCC}{BCC}$	$\frac{FCC}{BCC}$	$\frac{FCC}{BCC}$
Ti						$\frac{BCC}{HCP}$	$\frac{BCC}{HCP}$	$\frac{BCC}{HCP}$
V							BCC	BCC
Zr								$\frac{BCC}{HCP}$

Table A.2 is a collection of the predictive values for the 150 W high power (HP) and 50 W low power (LP) $(Al_xCu_yMo_{1-x-y})FeNiTiVZr$ continuous composition spread (CCS) libraries at points diffracted at the synchrotron. This collection of data is used in Figure 3.8 in order to determine where the libraries fall in relation to previously predicted regions of stability.

Table A.2: Predictive Values for Alloy Phase Stabilization

Sample	50 W Data				150 W Data			
	x	y	δ	Ω	x	y	δ	Ω
1	0.548	0.114	9.17	1.09	0.453	0.118	9.20	1.14
2	0.550	0.169	9.21	1.09	0.509	0.151	9.22	1.09
3	0.548	0.114	9.17	1.09	0.438	0.125	9.20	1.16
4	0.550	0.169	9.21	1.09	0.491	0.162	9.22	1.11
5	0.537	0.090	9.16	1.10	0.381	0.116	9.19	1.21
6	0.551	0.134	9.19	1.16	0.439	0.152	9.22	1.16
7	0.544	0.195	9.22	1.15	0.484	0.197	9.24	1.11
8	0.511	0.089	9.16	1.13	0.351	0.117	9.19	1.25
9	0.529	0.132	9.18	1.13	0.408	0.156	9.22	1.19
10	0.526	0.193	9.22	1.14	0.452	0.204	9.25	1.15
11	0.502	0.271	9.26	1.13	0.483	0.261	9.28	1.11
12	0.494	0.113	9.17	1.13	0.358	0.141	9.20	1.24
13	0.503	0.167	9.20	1.14	0.406	0.189	9.23	1.19
14	0.491	0.238	9.24	1.14	0.441	0.246	9.27	1.15
15	0.459	0.327	9.29	1.21	0.464	0.311	9.30	1.12
16	0.467	0.123	9.18	1.20	0.340	0.152	9.21	1.26
17	0.476	0.180	9.21	1.19	0.385	0.204	9.24	1.21
18	0.464	0.255	9.25	1.18	0.417	0.265	9.28	1.18

Sample	50 W Data				150 W Data			
	x	y	δ	Ω	x	y	δ	Ω
19	0.432	0.348	9.30	1.18	0.436	0.336	9.31	1.15
20	0.433	0.112	9.17	1.18	0.303	0.143	9.20	1.30
21	0.450	0.166	9.20	1.17	0.350	0.196	9.23	1.25
22	0.446	0.238	9.24	1.17	0.384	0.258	9.27	1.21
23	0.421	0.327	9.29	1.18	0.405	0.329	9.31	1.18
24	0.390	0.094	9.15	1.19	0.269	0.133	9.19	1.34
25	0.418	0.141	9.18	1.20	0.308	0.174	9.22	1.30
26	0.426	0.205	9.22	1.29	0.346	0.235	9.25	1.26
27	0.414	0.288	9.26	1.26	0.372	0.305	9.29	1.22
28	0.381	0.388	9.31	1.27	0.384	0.384	9.33	1.20
29	0.375	0.108	9.16	1.25	0.256	0.141	9.20	1.36
30	0.398	0.162	9.19	1.23	0.301	0.198	9.23	1.31
31	0.402	0.234	9.23	1.22	0.334	0.266	9.27	1.27
32	0.385	0.323	9.28	1.23	0.353	0.342	9.31	1.24
33	0.348	0.430	9.33	1.22	0.359	0.423	9.35	1.22
34	0.353	0.114	9.16	1.22	0.243	0.149	9.20	1.37
35	0.376	0.172	9.20	1.23	0.285	0.212	9.24	1.33
36	0.379	0.247	9.24	1.24	0.315	0.283	9.28	1.29
37	0.362	0.340	9.29	1.26	0.332	0.363	9.32	1.26
38	0.326	0.450	9.34	1.27	0.335	0.448	9.36	1.24
39	0.326	0.110	9.16	1.33	0.231	0.159	9.20	1.39
40	0.352	0.168	9.19	1.32	0.263	0.211	9.23	1.35
41	0.359	0.243	9.24	1.30	0.293	0.286	9.28	1.32
42	0.346	0.336	9.28	1.30	0.309	0.368	9.32	1.29

Sample	50 W Data				150 W Data			
	x	y	δ	Ω	x	y	δ	Ω
43	0.313	0.446	9.34	1.28	0.312	0.457	9.36	1.27
44	0.299	0.106	9.15	1.27	0.220	0.168	9.21	1.40
45	0.328	0.164	9.19	1.27	0.243	0.209	9.23	1.38
46	0.338	0.239	9.23	1.27	0.273	0.287	9.28	1.34
47	0.329	0.331	9.28	1.27	0.289	0.371	9.32	1.32
48	0.300	0.441	9.33	1.28	0.291	0.462	9.37	1.30
49	0.277	0.507	9.36	1.28	0.289	0.497	9.38	1.29
50	0.300	0.145	9.18	1.30	0.216	0.191	9.22	1.41
51	0.317	0.217	9.22	1.30	0.248	0.271	9.26	1.37
52	0.315	0.306	9.27	1.39	0.267	0.356	9.31	1.34
53	0.294	0.412	9.32	1.37	0.272	0.447	9.36	1.32
54	0.258	0.526	9.37	1.35	0.267	0.521	9.39	1.31
55	0.271	0.126	9.16	1.34	0.199	0.189	9.22	1.43
56	0.294	0.196	9.20	1.34	0.225	0.253	9.25	1.40
57	0.299	0.281	9.25	1.33	0.246	0.340	9.30	1.37
58	0.286	0.384	9.30	1.32	0.254	0.432	9.35	1.35
59	0.254	0.502	9.36	1.32	0.249	0.529	9.39	1.33
60	0.242	0.107	9.15	1.32	0.189	0.200	9.22	1.45
61	0.271	0.173	9.19	1.32	0.201	0.232	9.24	1.43
62	0.282	0.256	9.24	1.32	0.226	0.322	9.29	1.40
63	0.276	0.355	9.29	1.33	0.237	0.415	9.34	1.38
64	0.252	0.470	9.34	1.35	0.234	0.513	9.38	1.36
65	0.223	0.565	9.39	1.35	0.227	0.570	9.41	1.35
66	0.246	0.151	9.18	1.35	0.180	0.211	9.23	1.46

Sample	50 W Data				150 W Data			
	x	y	δ	Ω	x	y	δ	Ω
67	0.263	0.231	9.22	1.44	0.206	0.301	9.28	1.43
68	0.263	0.327	9.27	1.42	0.220	0.397	9.33	1.40
69	0.247	0.438	9.33	1.40	0.221	0.496	9.37	1.38
70	0.213	0.566	9.39	1.39	0.208	0.594	9.42	1.37
71	0.232	0.157	9.18	1.38	0.171	0.223	9.23	1.47
72	0.248	0.241	9.22	1.37	0.195	0.318	9.28	1.44
73	0.247	0.340	9.28	1.37	0.207	0.418	9.33	1.42
74	0.231	0.454	9.33	1.36	0.205	0.519	9.38	1.40
75	0.198	0.584	9.39	1.36	0.191	0.618	9.43	1.39
76	0.219	0.163	9.18	1.36	0.163	0.235	9.24	1.48
77	0.233	0.251	9.23	1.36	0.185	0.335	9.29	1.46
78	0.232	0.353	9.28	1.37	0.194	0.438	9.34	1.43
79	0.216	0.470	9.34	1.38	0.190	0.542	9.39	1.41
80	0.184	0.602	9.40	1.39	0.174	0.642	9.44	1.41
81	0.206	0.169	9.18	1.40	0.155	0.248	9.24	1.50
82	0.220	0.260	9.23	1.48	0.175	0.353	9.30	1.47
83	0.218	0.366	9.29	1.46	0.182	0.459	9.35	1.44
84	0.202	0.486	9.35	1.44	0.176	0.565	9.40	1.43
85	0.171	0.620	9.41	1.43	0.158	0.666	9.45	1.42
86	0.202	0.211	9.20	1.42	0.156	0.304	9.27	1.50
87	0.208	0.312	9.26	1.41	0.169	0.415	9.33	1.47
88	0.201	0.426	9.32	1.41	0.169	0.524	9.38	1.45
89	0.179	0.554	9.38	1.39	0.156	0.630	9.43	1.44
90	0.185	0.180	9.19	1.40	0.142	0.275	9.26	1.52

Sample	50 W Data				150 W Data			
	x	y	δ	Ω	x	y	δ	Ω
91	0.196	0.280	9.24	1.41	0.157	0.389	9.31	1.49
92	0.193	0.392	9.30	1.39	0.160	0.503	9.37	1.47
93	0.178	0.517	9.36	1.41	0.151	0.612	9.42	1.45
94	0.148	0.654	9.42	1.42	0.130	0.713	9.46	1.45
95	0.185	0.289	9.24	1.43	0.149	0.408	9.32	1.50
96	0.182	0.405	9.30	1.44	0.150	0.525	9.38	1.48
97	0.167	0.532	9.36	1.52	0.139	0.635	9.43	1.46
98	0.173	0.233	9.21	1.50	0.136	0.352	9.29	1.52
99	0.176	0.345	9.27	1.49	0.143	0.477	9.36	1.50
100	0.167	0.468	9.33	1.47	0.138	0.593	9.41	1.48
101	0.148	0.602	9.40	1.47	0.120	0.702	9.46	1.47
102	0.167	0.333	9.26	1.46	0.136	0.473	9.35	1.51
103	0.161	0.456	9.33	1.44	0.131	0.594	9.41	1.49
104	0.144	0.590	9.39	1.44	0.114	0.705	9.46	1.48
105	0.158	0.393	9.29	1.43	0.133	0.530	9.38	1.50
106	0.147	0.523	9.36	1.44	0.123	0.647	9.43	1.49
107	0.155	0.420	9.31	1.44	0.132	0.554	9.39	1.50

APPENDIX B

MPEA OXIDATION APPENDIX

B.1 Ω AND δ VALUES FOR THE $(\text{ALFENITIVZR})_{1-x}\text{CR}_x$ LIBRARY

Table B.1 shows the thermodynamic predictive values, Ω and δ based off of the previous heuristics outlined by [272]. Interestingly, sample 1 has a entropy/enthalpy ratio less than 1, but the diffraction patterns show that the structure still formed a single phase solid solution upon deposition and post vacuum anneal. There may be small discrepancies based off of extrapolation of the composition from WDS data, but it also shows how the heuristic is still an estimation.

Table B.1: Predictive Values
for Alloy Phase Stabilization

Sample	Cr at.%	δ	Ω
1	6.4	9.14	0.99
2	6.8	9.13	1.00
3	7.3	9.12	1.01
4	8.0	9.12	1.02
5	8.6	9.11	1.04
6	9.4	9.09	1.05
7	10.3	9.08	1.07
8	11.2	9.07	1.08
9	12.3	9.05	1.10
10	13.4	9.03	1.12

Sample	Cr at.%	δ	Ω
11	14.6	9.01	1.14
12	15.9	8.98	1.17
13	17.2	8.95	1.19
14	18.7	8.92	1.22
15	20.3	8.89	1.24
16	21.9	8.85	1.27
17	23.6	8.81	1.30
18	25.4	8.76	1.34
19	27.3	8.70	1.37
20	29.2	8.65	1.41
21	31.3	8.58	1.44
22	33.4	8.51	1.48
23	35.7	8.43	1.53

B.2 ADDITIONAL WATERFALL PLOTS OF THE POST-ANNEALED MPEA LIBRARY

Figure B.1 shows additional diffraction patterns in between major annealing times of the $(\text{AlFeNiTiVZr})_{1-x}\text{Cr}_x$ continuous composition spread (CCS) library. These plots show the furthered development of oxide structures as the samples anneal longer. The phase boundary distinction remains between 23.6 and 29.2 at.% Cr. The 6-hour anneal shows the existence of a passivating oxide layer as the differences between the two regions become distinct.

B.3 ADDITIONAL RAMAN SPECTRA OF THE MPEA LIBRARY

Additional Raman spectra were taken in order to track the oxide structures as annealing time increased. Figure B.2, shows the Raman spectrum of the as-deposited $(\text{AlFeNiTiVZr})_{1-x}\text{Cr}_x$. Since the metallic alloy does not show Raman structures due to the infinite polarizability of metals, the spectrum only shows the modes of natural surface oxidation due to library's exposure to the air. This spectrum is seen throughout the entirety of the composition spread.

Figures B.3, B.4, and B.5 show a heat map of the binary CCS library after 1, 6, and 18 hours of annealing in air respectively at 873 K. After annealing for 1 hour the, a sharp band developed at 920 cm^{-1} at Cr concentrations above 25 at.%. Additional bands form at the same region at 884 , 770 , 662 , and 380 cm^{-1} , which correspond well with CrO_3 . However, as mentioned in Chapter 4 it is unlikely this structure solely consists of CrO_3 , due to the multiple potential species seen in the diffraction data. As the sample anneals for up to 6 hours, the bands seen in the 1-hour anneal are still present, but at lower Cr concentrations two broad bands exist at 936 and 815 cm^{-1} , which is indicative of continued oxidation in that concentration region. After annealing the sample for 18 hours, in the region of lower Cr concentration, the broad bands at 600 and 1000 cm^{-1} increased in intensity. The sharp band at 920 cm^{-1} does not form until approximately 28 at.% Cr, indicating that the behavioral boundary had shifted as the sample endured a longer anneal.

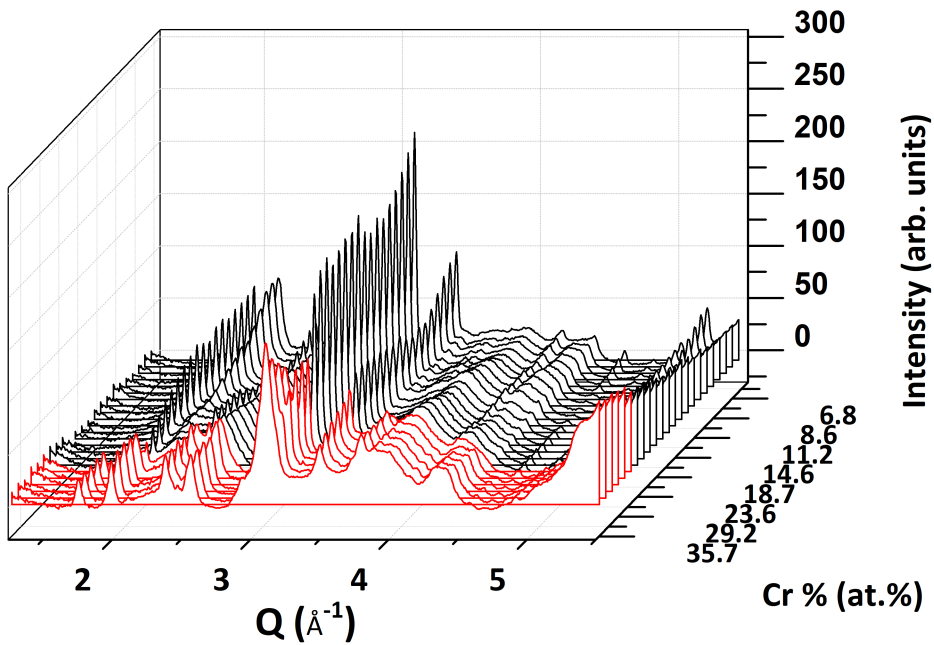
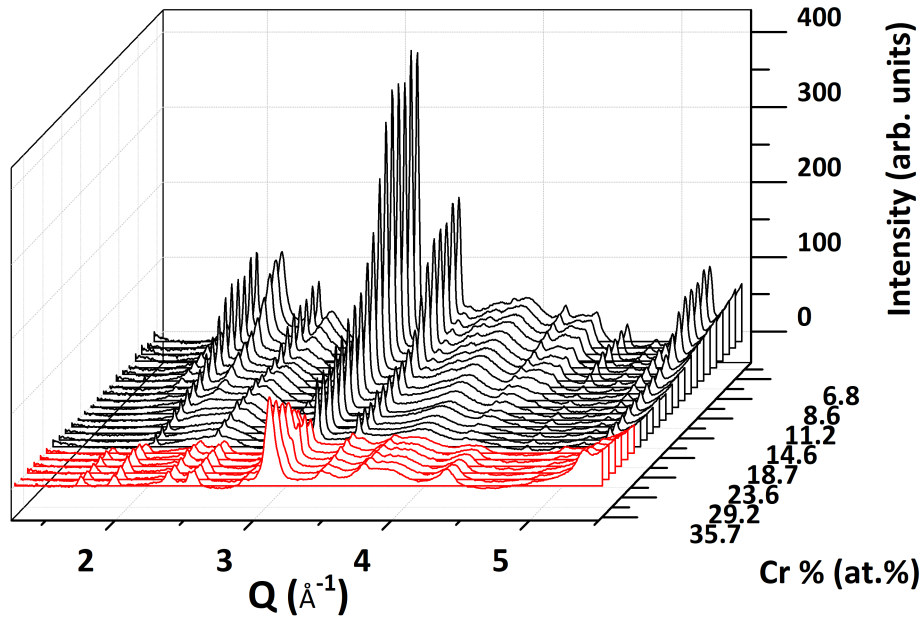


Figure B.1: Waterfall plots of the CCS library after annealing in air for 3 hours (Top) and 6 hours (bottom).

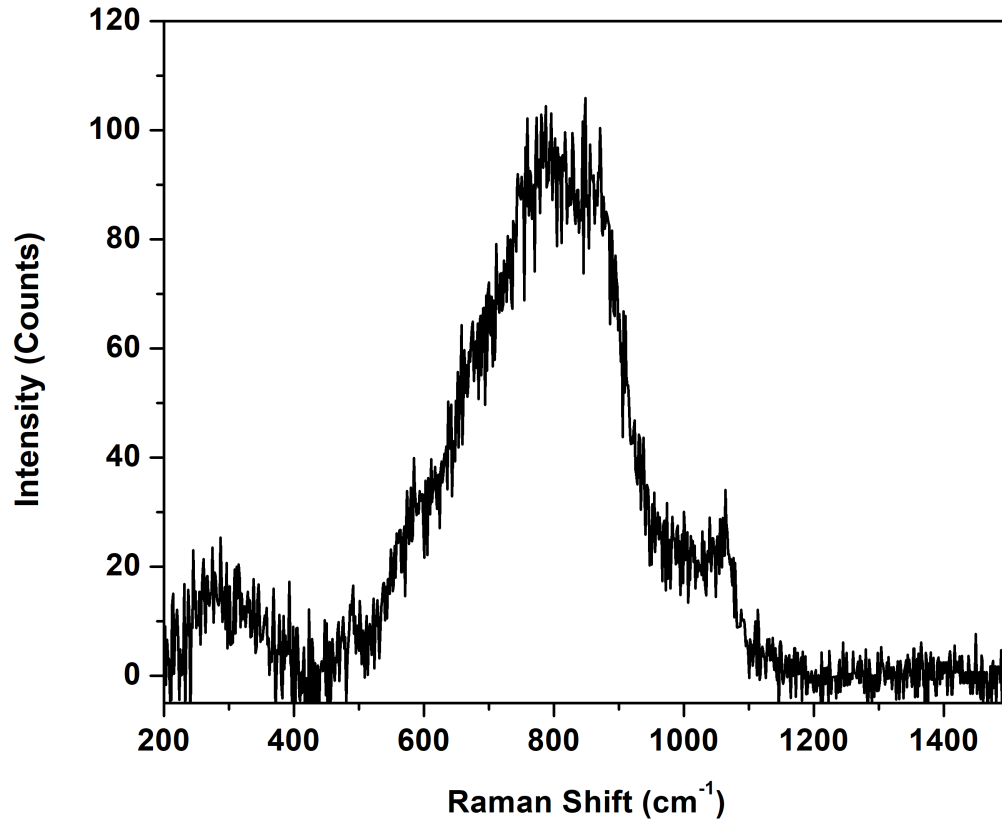


Figure B.2: The spectrum of the as-deposited $(\text{AlFeNiTiVZr})_{1-x}\text{Cr}_x$. The low intensity of the spectrum is due to the lack of oxides present on the sample surface.

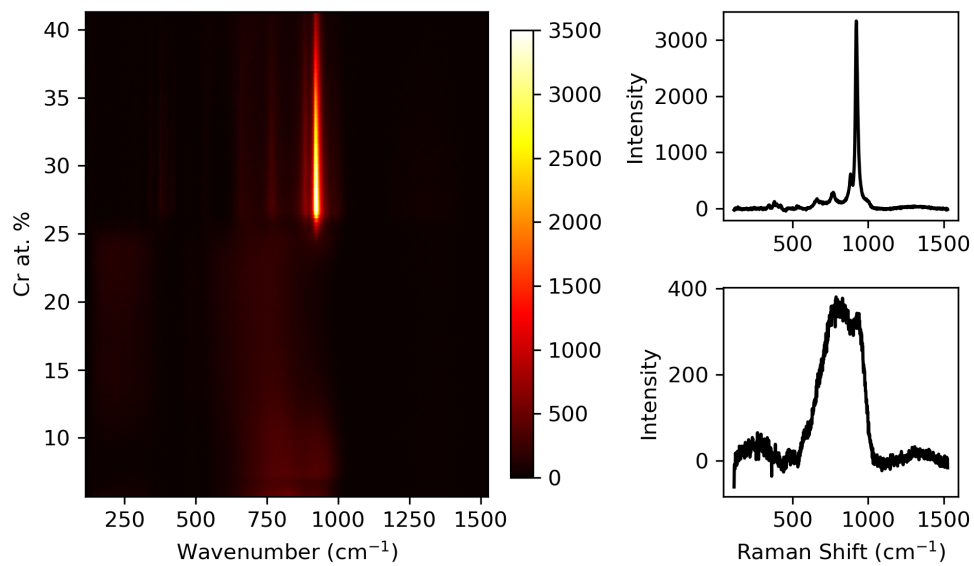


Figure B.3: Raman heat map and representative spectra of the CCS after 1 hour.

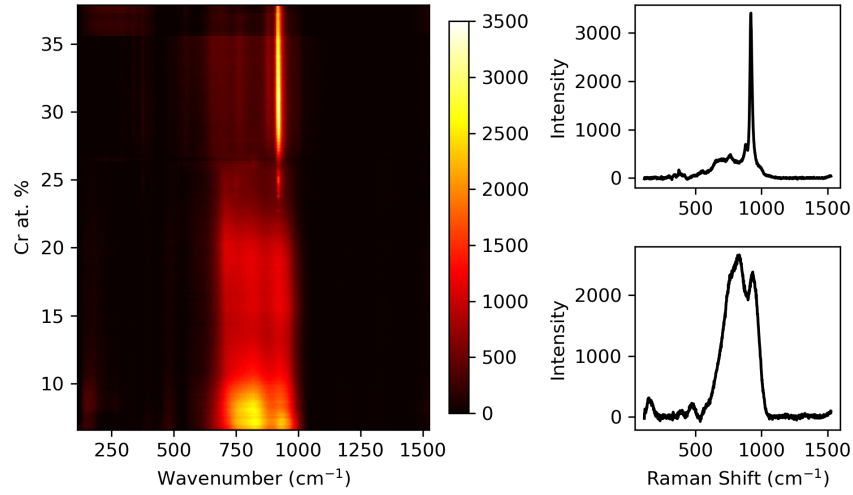


Figure B.4: Raman heat map and representative spectra of the CCS after 6 hours.

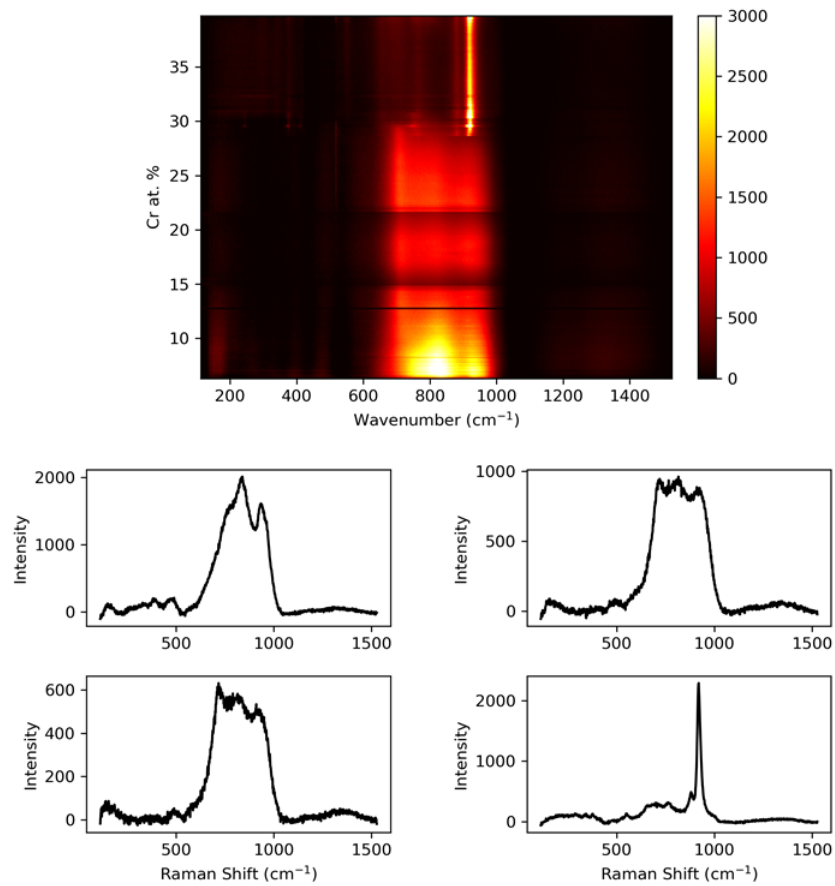


Figure B.5: Raman heat map and representative spectra of the CCS after 18 hours.

APPENDIX C

STABILIZED ZIRCONIA APPENDIX

C.1 DEPOSITED ScSZ SURFACE TOPOGRAPHY

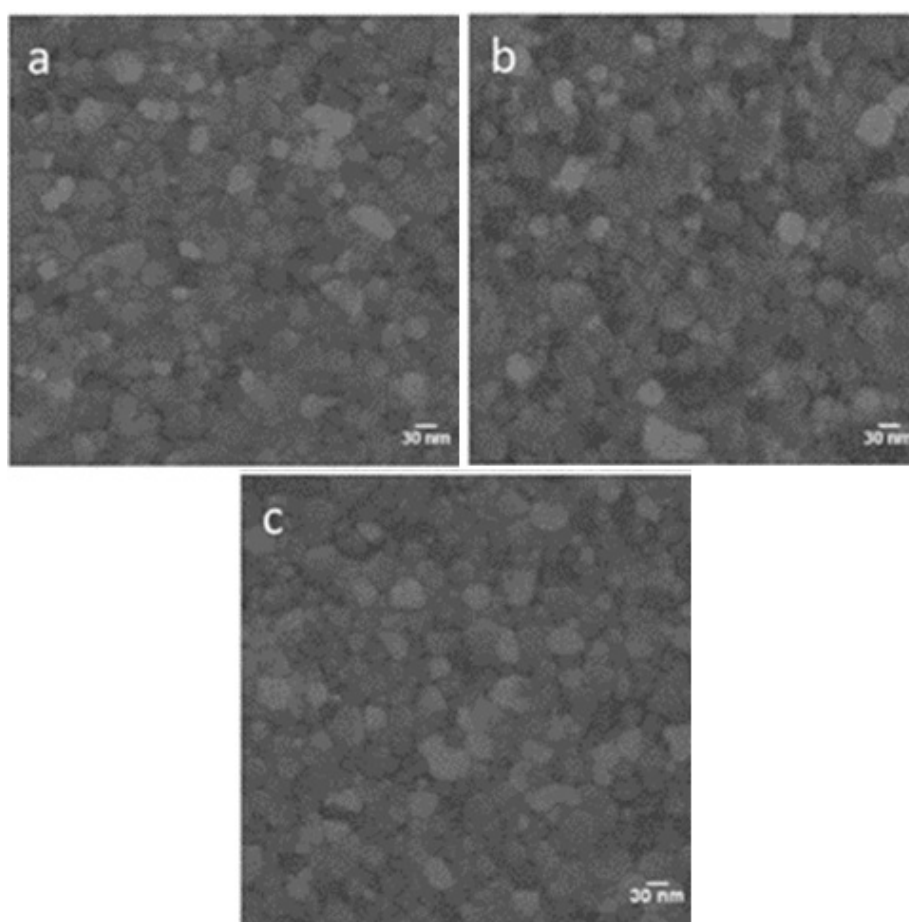


Figure C.1: SEM images of ScSZ samples deposited at 923 K, 65 W, and 10 vol.% O₂ concentration. (a)4 hour post-anneal, (b)8 hour post-anneal, (c)12 hour post-anneal.

In order to determine the grain size distribution seen in Figure 5.13, scanning electron microscopy (SEM) images were taken on the deposited ScSZ samples, seen

in Figure C.1. These micrographs were taken using a Zeiss Ultraplus Thermal Field Emission SEM with a 10 keV electron beam intensity, working distance of 4.6 nm, and secondary electron detector. The magnification scale bar seen in Figure C.1 is 30 nm. No major cracks or delamination was visible on the surfaces of any of the annealed samples. An image of the as-deposited film was excluded due to grains that were too small to resolve using the SEM.

APPENDIX D

$\text{ReO}_x/\text{CeO}_2$ APPENDIX

D.1 CATALYST DIFFRACTION DATA

A diffraction pattern of the $\text{ReO}_x/\text{CeO}_2$ catalyst powder can be seen in Figure D.1 and was taken using the Rigaku Miniflex II, which was briefly mentioned in 2.2. The measuring range was between $20\text{-}80^\circ 2\theta$ at a scan speed of $0.5^\circ/\text{minute}$ and a with resolution of 0.02° . From the pattern we see only peaks that correspond with cubic CeO_2 (PDF# 75-0390). No visible evidence of ReO_x could be detected, which is expected with the low percentage of ReO_x and the high dispersion across the support.

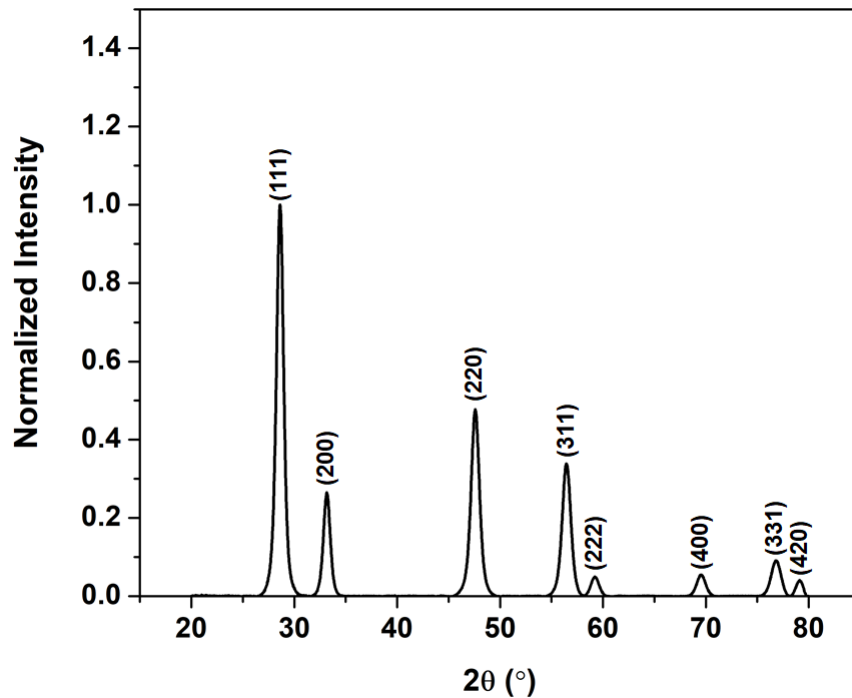


Figure D.1: The diffraction pattern of $\text{ReO}_x/\text{CeO}_2$.

D.2 RAMAN SPECTRA ANALYSIS VALIDATION

Raman spectra were taken in order to alleviate concerns about the measurement quality from the isotope exchange and validate previous measurements. The signal-to-noise ratio (SNR) of the spectrum in Figure 6.3a and 6.3b was 12.0 and 31.8 respectively. This led to some concerns that the ReO_x would sublime after several hours of exchange and annealing at 823 K, and the quality of the Raman signal would decrease. However, the SNR drop was most likely due to some challenges with the experimental equipment. The *in situ* cell for the Raman microscope requires the isotope oxygen to be manually attached to the cell, and this can cause slight movements in the positioning of the sample. While this can be a concern for some sample types, it can be reasonably assumed that the distribution of the ReO_x is even across the CeO_2 , and any movement would have caused a slight decrease in focus to the moved sample spot area. Figure D.2 is a spectral comparison between the 1 wt.% $\text{ReO}_x/\text{CeO}_2$ that was annealed in flowing Ar at the same time and temperature as the isotope exchange experimental conditions. For this measurement the sample remained undisturbed. From the spectra, we can see that the SNR of the main peak at 989 cm^{-1} decreased from 51.5 to 45.3 after heating for 3 hours at 823 K. While there was a drop in SNR of 12.0% that can be attributed to ReO_x sublimation, the drop seen in the isotope exchange was 62.3%, which is most likely due to sample perturbation.

The presence of a bending hydroxyl species, $\delta\text{-Re-OH}$, at 834 cm^{-1} required further investigation due to the uncommon sighting of the species. In order to verify that the Re-OH was appropriately assigned, the 700 cm^{-1} region was observed. This is a wavenumber range where the $\nu\text{-Re-OH}$ stretch is detectable. However, there were no detectable traces of the species at that wavenumber. While Raman measurements typically demand that all modes be visible to verify species assignment, the already low intensity of the bands detected at 834 cm^{-1} may imply other characteristic bands

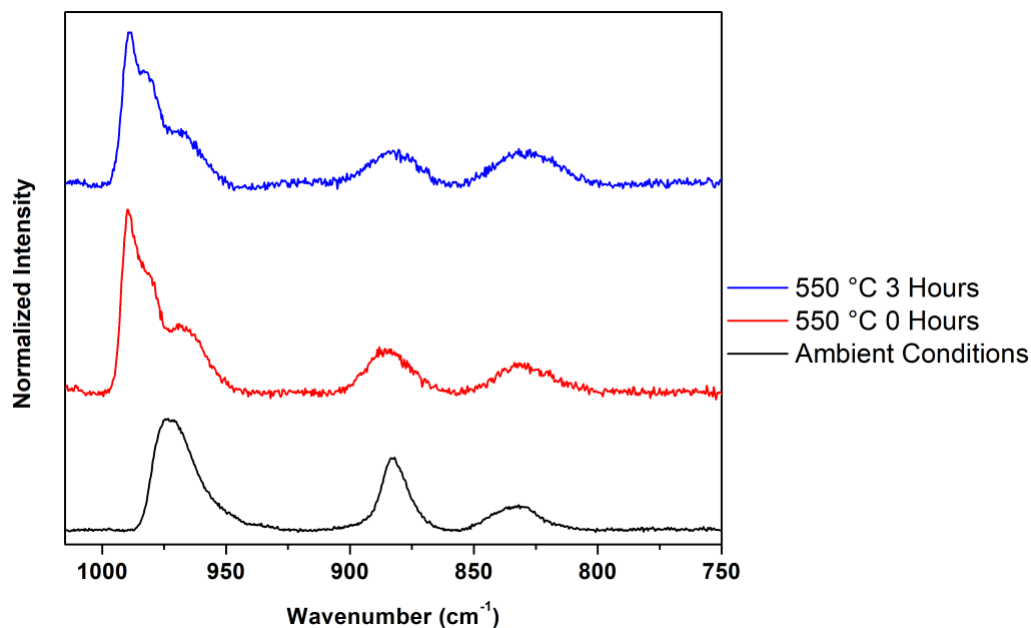


Figure D.2: A comparison of the SNR between Raman spectra at different points during heating.

of the Re–OH species at lower wavenumbers is indistinguishable from the background noise. Additionally, this stretch was only detected using FTIR in previous literature, which may imply that it is Raman inactive. However, the stretching band of Re–OH should theoretically be Raman active due to the lack of a center of symmetry for the species. Unfortunately, DRIFTS measurements were not reliable in the 700 cm^{-1} region due to the wavenumber range nearing the detection limit of the MCT detector. Additional Raman measurements were taken where $\nu\text{-O-H}$ bands are visible. This includes the 3700 cm^{-1} region seen in Figure D.3. A broad band that could be attributed to the $\nu\text{-O-H}$ stretch is visible, but the large background makes it difficult to process the data and make a firm verification of the species. Therefore, further testing is required for complete identification, but the initial band assignments are still applicable.

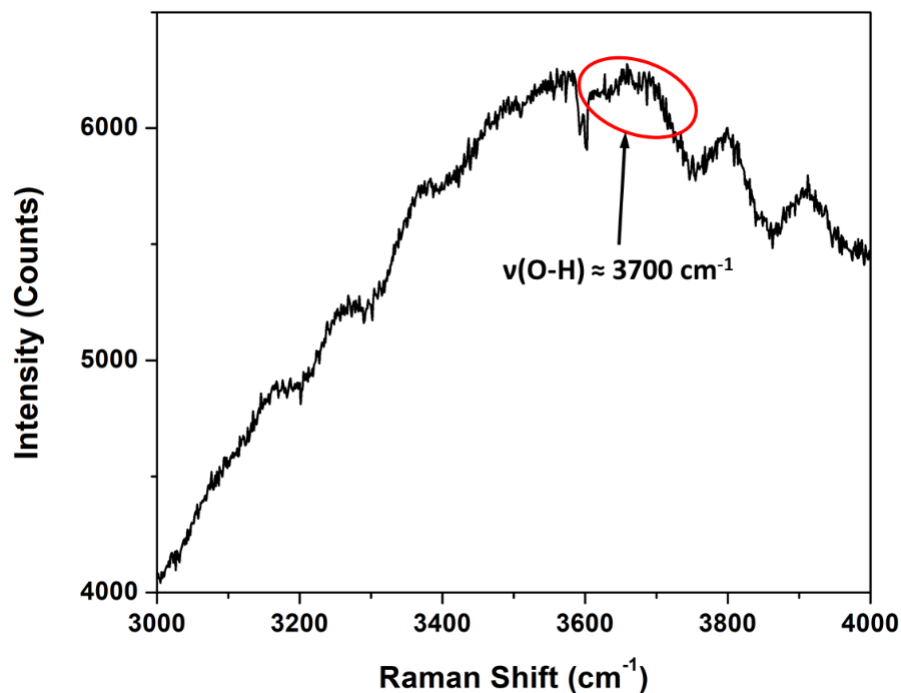


Figure D.3: A spectrum of the 1 wt.% ReO_x/CeO₂ between 3000 and 4000 wavenumbers. The O–H stretch has been observed near 3700 cm⁻¹, and a broad band is visible in the spectrum.

D.3 SELECTION RULE VALIDATION

When comparing the Raman spectra and DRIFTS of the 1 wt.% ReO_x/CeO₂, the selection rules between the two techniques must be obeyed. In Raman spectroscopy, the symmetric stretch must have greater or equivalent intensity to the asymmetric stretch, and the opposite is true when using FTIR spectral techniques. Solely observing the spectra of both the Raman and IR data would imply that the selection rules have been broken, because the peak intensity of the symmetric stretch is the greatest in both cases. However, the integrated peak intensity provides more information about the symmetric and asymmetric stretches. Table D.1 shows the integrated intensities of the di-oxo ReO_x stretches before and after the isotope exchange. The Raman symmetric to asymmetric ratio is greater than one, which is expected. As for

the DRIFTS, the ratio is slightly less than one, which is also expected. Therefore, the selection rules are upheld and the data band assignments are valid.

Table D.1: Integrated Intensities of the Di-Oxo ReO_x Stretch

	ν_s (O=Re=O)	ν_{as} (O=Re=O)	Sym/Asym Ratio
Raman (Pre-Exchange)	122.4	85.6	1.43
Raman (Post-Exchange)	123.6	86.5	1.43
DRIFTS (Pre-Exchange)	0.37	0.38	0.99
DRIFTS (Post-Exchange)	0.66	0.67	0.99

APPENDIX E

PEEL TEST APPENDIX

E.1 MEASURED ADHESION DATA

Table E.1 is a collection of the average adhesive strength of each sample condition. Each trial ran five samples and an average and standard error was measured. At the coldest condition of 10 °C (283 K), cure time often was required to be above 5 minutes before a peelable sample would form. Anytime a unfinished sample was developed it would be labeled with a zero for adhesive strength in the table. The TTT alkene monomer consistently held higher average adhesive strengths over the TMPTA monomer. The standard error for the samples was often between 10-20% of the average, with outliers reaching 50% of the peel strength.

Table E.1: Average Peel Strength of Thiol-Ene Sealant at the Measured Synthesis Conditions

Alkene	Time	Temp.	Filler	Peel Strength	Std. Err.
	min.	°C		N/mm	N/mm
TTT	3	10.0	None	0.138	0.013
TTT	3	10.0	Sand	0.189	0.028
TTT	3	10.0	Al ₂ O ₃	0.126	0.031
TTT	3	10.0	SiO ₂	0.060	0.009
TTT	3	15.6	None	0.000	0.000
TTT	3	15.6	Sand	0.161	0.026
TTT	3	15.6	Al ₂ O ₃	0.000	0.000

Alkene	Time	Temp.	Filler	Peel Strength	Std. Err.
	min.	°C		N/mm	N/mm
TTT	3	15.6	SiO ₂	0.000	0.000
TTT	5	10.0	None	0.129	0.014
TTT	5	10.0	Sand	0.000	0.000
TTT	5	10.0	Al ₂ O ₃	0.208	0.053
TTT	5	10.0	SiO ₂	0.170	0.008
TTT	5	15.6	None	0.192	0.032
TTT	5	15.6	Sand	0.077	0.009
TTT	5	15.6	Al ₂ O ₃	0.151	0.032
TTT	5	15.6	SiO ₂	0.180	0.023
TTT	7	10.0	None	0.144	0.034
TTT	7	10.0	Sand	0.146	0.021
TTT	7	10.0	Al ₂ O ₃	0.100	0.041
TTT	7	10.0	SiO ₂	0.109	0.023
TTT	7	15.6	None	0.099	0.015
TTT	7	15.6	Sand	0.000	0.000
TTT	7	15.6	Al ₂ O ₃	0.000	0.000
TTT	7	15.6	SiO ₂	0.424	0.059
TTT	10	10.0	None	0.000	0.000
TTT	10	10.0	Sand	0.109	0.011
TTT	10	10.0	Al ₂ O ₃	0.101	0.005
TTT	10	10.0	SiO ₂	0.000	0.000
TTT	10	15.6	None	0.000	0.000
TTT	10	15.6	Sand	0.192	0.033
TTT	10	15.6	Al ₂ O ₃	0.418	0.053

Alkene	Time	Temp.	Filler	Peel Strength	Std. Err.
	min.	°C		N/mm	N/mm
TTT	10	15.6	SiO ₂	0.340	0.038
TTT	10	21.1	None	0.208	0.032
TTT	10	21.1	Sand	0.280	0.084
TTT	10	21.1	Al ₂ O ₃	0.885	0.099
TTT	10	21.1	SiO ₂	0.846	0.116
TTT	20	10.0	None	0.172	0.054
TTT	20	10.0	Sand	0.144	0.058
TTT	20	10.0	Al ₂ O ₃	0.149	0.024
TTT	20	10.0	SiO ₂	0.137	0.026
TTT	20	15.6	None	0.220	0.038
TTT	20	15.6	Sand	0.207	0.053
TTT	20	15.6	Al ₂ O ₃	0.536	0.095
TTT	20	15.6	SiO ₂	0.214	0.056
TTT	20	21.1	None	0.409	0.070
TTT	20	21.1	Sand	0.367	0.039
TTT	20	21.1	Al ₂ O ₃	0.585	0.138
TTT	20	21.1	SiO ₂	0.568	0.070
TTT	40	10.0	None	0.286	0.015
TTT	40	10.0	Sand	0.765	0.081
TTT	40	10.0	Al ₂ O ₃	0.171	0.016
TTT	40	10.0	SiO ₂	0.248	0.039
TTT	40	15.6	None	0.355	0.011
TTT	40	15.6	Sand	0.231	0.065
TTT	40	15.6	Al ₂ O ₃	0.909	0.103

Alkene	Time	Temp.	Filler	Peel Strength	Std. Err.
	min.	°C		N/mm	N/mm
TTT	40	15.6	SiO ₂	0.505	0.113
TTT	40	21.1	None	0.262	0.009
TTT	40	21.1	Sand	0.713	0.134
TTT	40	21.1	Al ₂ O ₃	0.595	0.044
TTT	40	21.1	SiO ₂	1.225	0.321
TTT	60	10.0	None	0.589	0.081
TTT	60	10.0	Sand	0.603	0.133
TTT	60	10.0	Al ₂ O ₃	0.384	0.074
TTT	60	10.0	SiO ₂	0.448	0.106
TTT	60	15.6	None	1.050	0.220
TTT	60	15.6	Sand	0.355	0.018
TTT	60	15.6	Al ₂ O ₃	0.627	0.095
TTT	60	15.6	SiO ₂	0.427	0.128
TTT	60	21.1	None	1.448	0.289
TTT	60	21.1	Sand	1.098	0.418
TTT	60	21.1	Al ₂ O ₃	1.174	0.195
TTT	60	21.1	SiO ₂	1.038	0.204
TMPTA	3	10.0	None	0.000	0.000
TMPTA	3	10.0	Sand	0.000	0.000
TMPTA	3	10.0	Al ₂ O ₃	0.000	0.000
TMPTA	3	10.0	SiO ₂	0.000	0.000
TMPTA	3	15.6	None	0.000	0.000
TMPTA	3	15.6	Sand	0.083	0.006
TMPTA	3	15.6	Al ₂ O ₃	0.195	0.022

Alkene	Time	Temp.	Filler	Peel Strength	Std. Err.
	min.	°C		N/mm	N/mm
TMPTA	3	15.6	SiO ₂	0.136	0.041
TMPTA	5	10.0	None	0.000	0.000
TMPTA	5	10.0	Sand	0.000	0.000
TMPTA	5	10.0	Al ₂ O ₃	0.000	0.000
TMPTA	5	10.0	SiO ₂	0.000	0.000
TMPTA	5	15.6	None	0.074	0.029
TMPTA	5	15.6	Sand	0.090	0.024
TMPTA	5	15.6	Al ₂ O ₃	0.115	0.016
TMPTA	5	15.6	SiO ₂	0.129	0.007
TMPTA	7	10.0	None	0.000	0.000
TMPTA	7	10.0	Sand	0.000	0.000
TMPTA	7	10.0	Al ₂ O ₃	0.000	0.000
TMPTA	7	10.0	SiO ₂	0.000	0.000
TMPTA	7	15.6	None	0.146	0.023
TMPTA	7	15.6	Sand	0.176	0.006
TMPTA	7	15.6	Al ₂ O ₃	0.101	0.013
TMPTA	7	15.6	SiO ₂	0.124	0.008
TMPTA	10	10.0	None	0.000	0.000
TMPTA	10	10.0	Sand	0.000	0.000
TMPTA	10	10.0	Al ₂ O ₃	0.000	0.000
TMPTA	10	10.0	SiO ₂	0.000	0.000
TMPTA	10	15.6	None	0.183	0.052
TMPTA	10	15.6	Sand	0.142	0.019
TMPTA	10	15.6	Al ₂ O ₃	0.091	0.012

Alkene	Time	Temp.	Filler	Peel Strength	Std. Err.
	min.	°C		N/mm	N/mm
TMPTA	10	15.6	SiO ₂	0.177	0.013
TMPTA	10	21.1	None	0.182	0.022
TMPTA	10	21.1	Sand	0.171	0.008
TMPTA	10	21.1	Al ₂ O ₃	0.223	0.015
TMPTA	10	21.1	SiO ₂	0.214	0.047
TMPTA	20	10.0	None	0.107	0.023
TMPTA	20	10.0	Sand	0.158	0.029
TMPTA	20	10.0	Al ₂ O ₃	0.158	0.021
TMPTA	20	10.0	SiO ₂	0.141	0.010
TMPTA	20	15.6	None	0.118	0.024
TMPTA	20	15.6	Sand	0.124	0.015
TMPTA	20	15.6	Al ₂ O ₃	0.103	0.018
TMPTA	20	15.6	SiO ₂	0.079	0.012
TMPTA	20	21.1	None	0.172	0.029
TMPTA	20	21.1	Sand	0.161	0.024
TMPTA	20	21.1	Al ₂ O ₃	0.222	0.024
TMPTA	20	21.1	SiO ₂	0.154	0.022
TMPTA	40	10.0	None	0.116	0.008
TMPTA	40	10.0	Sand	0.138	0.013
TMPTA	40	10.0	Al ₂ O ₃	0.170	0.016
TMPTA	40	10.0	SiO ₂	0.140	0.034
TMPTA	40	15.6	None	0.263	0.020
TMPTA	40	15.6	Sand	0.156	0.016
TMPTA	40	15.6	Al ₂ O ₃	0.171	0.023

Alkene	Time	Temp.	Filler	Peel Strength	Std. Err.
	min.	°C		N/mm	N/mm
TMPTA	40	15.6	SiO ₂	0.217	0.042
TMPTA	40	21.1	None	0.224	0.017
TMPTA	40	21.1	Sand	0.196	0.025
TMPTA	40	21.1	Al ₂ O ₃	0.140	0.012
TMPTA	40	21.1	SiO ₂	0.159	0.032
TMPTA	60	10.0	None	0.122	0.025
TMPTA	60	10.0	Sand	0.131	0.013
TMPTA	60	10.0	Al ₂ O ₃	0.231	0.028
TMPTA	60	10.0	SiO ₂	0.260	0.033
TMPTA	60	15.6	None	0.189	0.019
TMPTA	60	15.6	Sand	0.157	0.016
TMPTA	60	15.6	Al ₂ O ₃	0.042	0.006
TMPTA	60	15.6	SiO ₂	0.090	0.017
TMPTA	60	21.1	None	0.219	0.023
TMPTA	60	21.1	Sand	0.141	0.007
TMPTA	60	21.1	Al ₂ O ₃	0.248	0.038
TMPTA	60	21.1	SiO ₂	0.161	0.020

E.2 3D RESPONSE SURFACE CONTOUR PLOTS

In addition to the 2D contour plots used in Figure 7.6, 3D response surface contour plots were generated alongside the average adhesive strength data points. The contour plots were developed using a second-order polynomial regression model. These plots are able to aid in visualization of the design space of interest for future experiments to optimize the adhesive strength of each system.

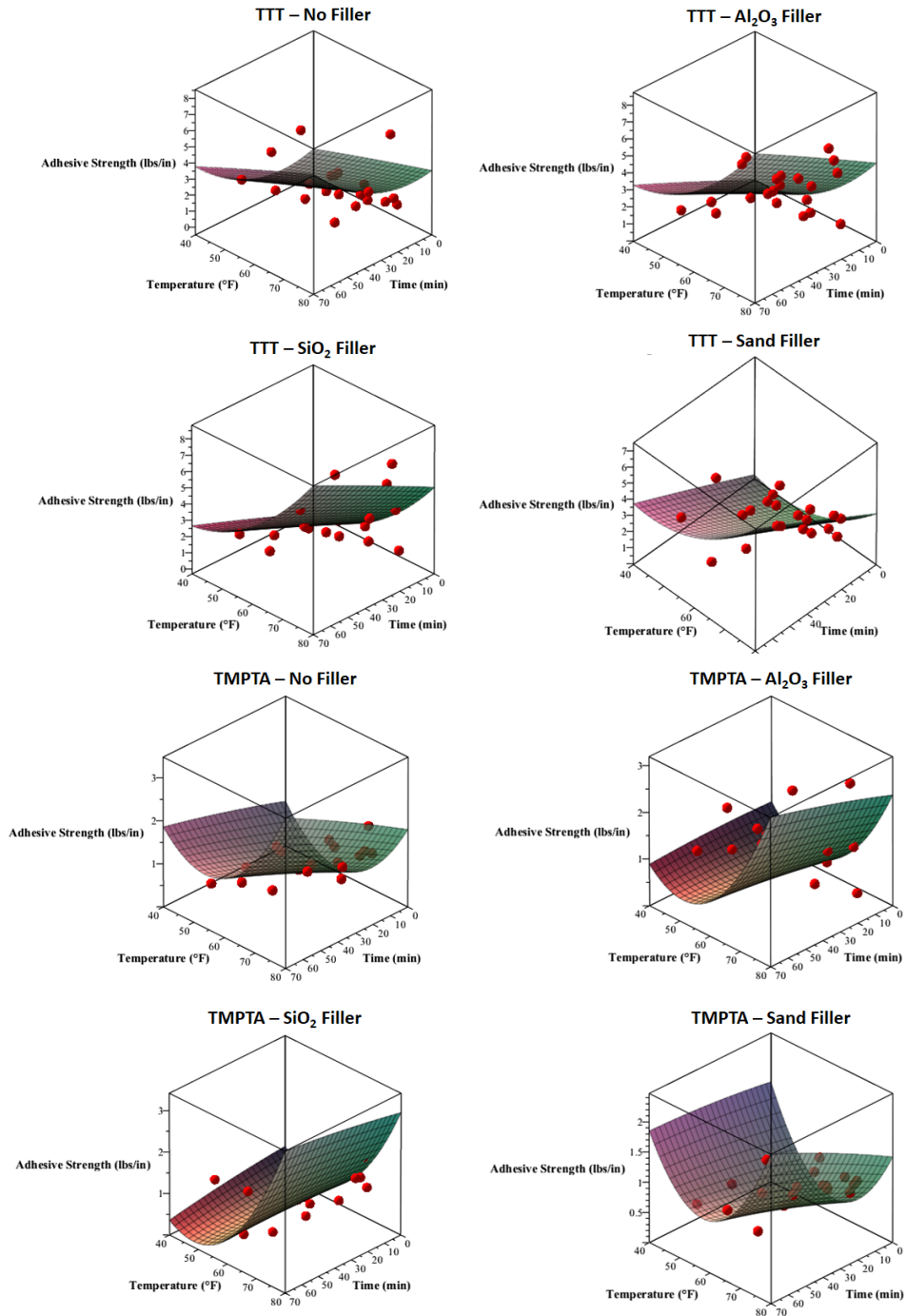


Figure E.1: 3D contour plots of the average adhesive strength. The plot was generated using a regression model that minimized the distance of the contour plot to the data points.

E.3 PROMOTER ADHESION

Standard adhesion strengths that are desired in the industry are typically an order of magnitude higher than what the current samples exhibited at any condition. A commercial promoter, (3-Mercaptopropyl)trimethoxysilane (MTMO) seen in Figure E.2, was applied to the Al substrate surface in an attempt to increase adhesion. However, no improvement could be seen in samples synthesized on the coated surface.

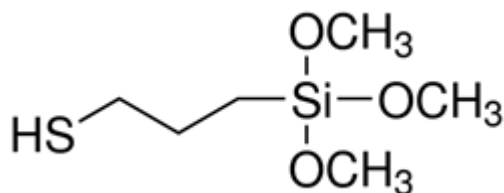


Figure E.2: The MTMO promoter. The silane end of the molecule is designed to bond with metal substrates, while the thiol end links with the sealant.

Scanning electron microscopy (SEM) and electron dispersive spectroscopy (EDS) was performed on a pairing of clean and coated substrates to compare the surface morphology and chemistry, as seen in Figure E.3. The MTMO is activated with an acid and binds to a metal surface via the silicon end, while the thiol functional group binds to a curable sealant. However, there is little evidence of the promoter binding to sample.

In order to verify if any of the MTMO bound with the Al substrate, the samples were measured using X-ray photoelectron microscopy (XPS). This is a highly sensitive technique that provides information on the oxidation state of the surface species. Outside the odd development of noise on the clean sample, which also exhibited an aluminum carbonate species, the Al 2p peaks showed shift of 0.65 eV toward higher binding energy after exposure to MTMO, which can be seen between Figures E.4(a) and (b). Additionally, there is evidence of silicon and sulfur post exposure as seen in Figures E.5(a) and (b). It seems that binding did occur between the aluminum

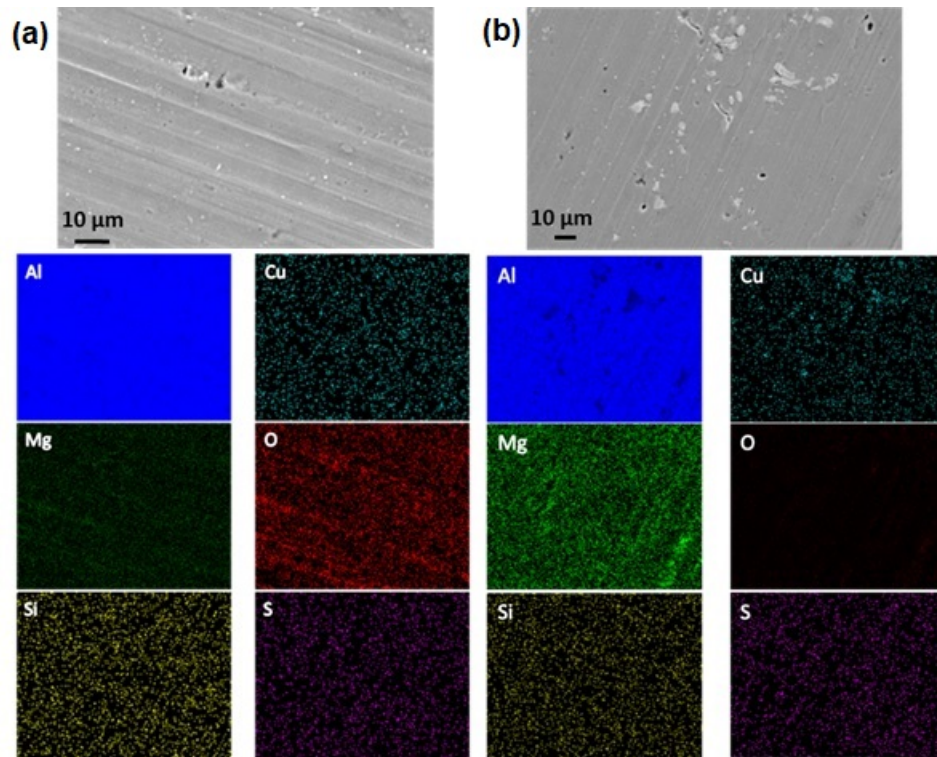


Figure E.3: SEM/EDS of the (a) clean Al substrate and (b) promoted Al substrate.

and silicon, but it is possible that the thiol species on the promoter was unable to cross-link with the sealant sample.

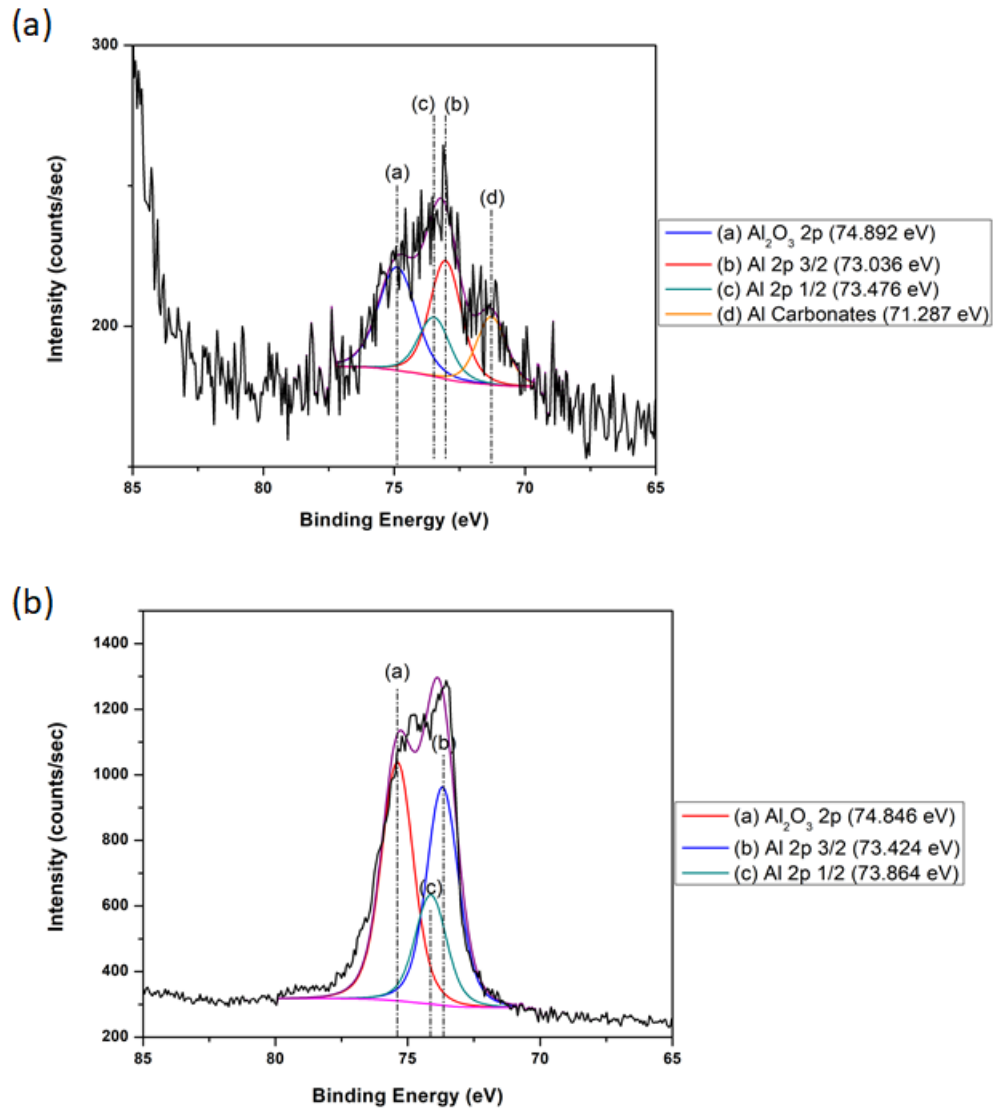


Figure E.4: XPS spectra of the (a) clean Al substrate and (b) promoted Al substrate.

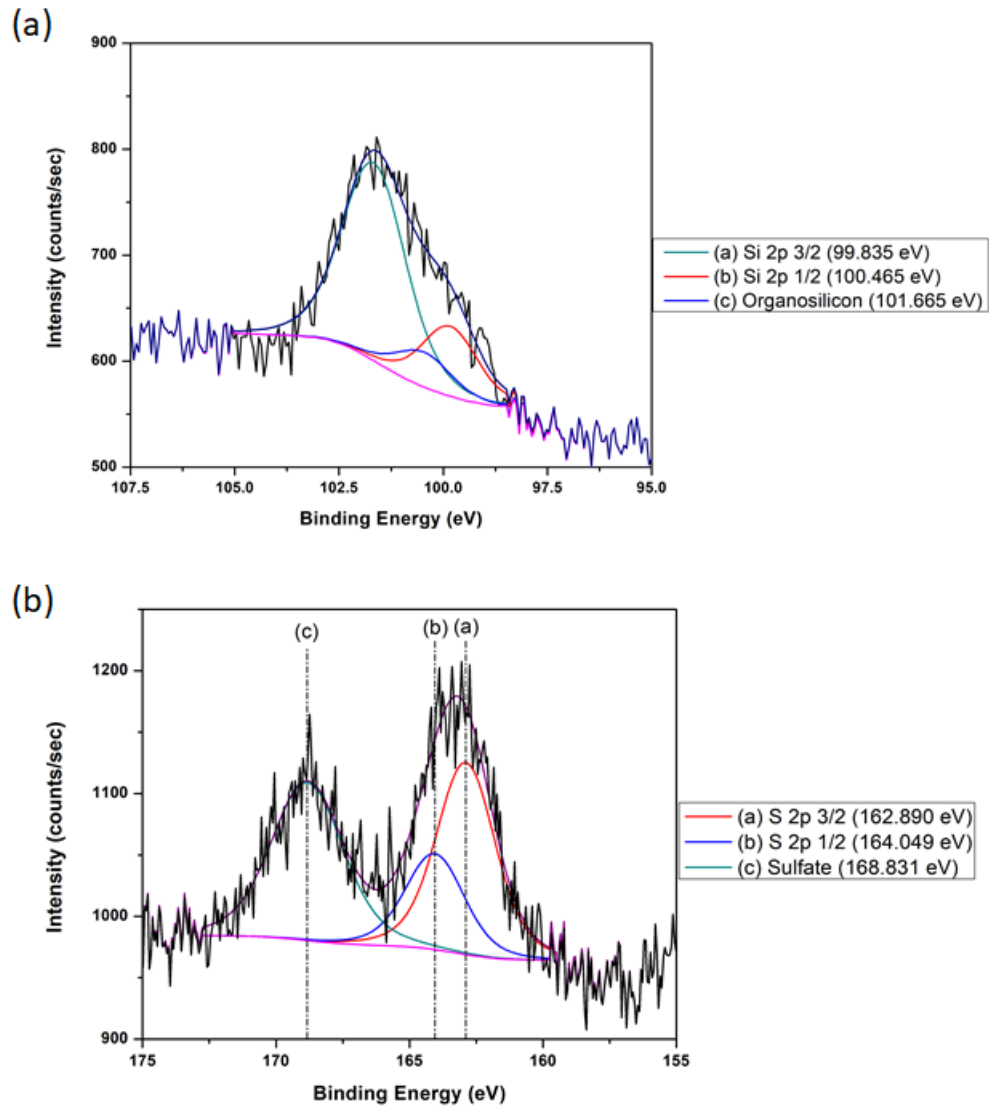


Figure E.5: XPS spectra of the (a) silicon and (b) sulfur on the promoted Al substrate.

APPENDIX F

COPYRIGHT PERMISSIONS

Thesis reprint permission

Kenneth Bunn <jkbunn@gmail.com>

Fri 6/12/2020 4:41 PM

To: RUIZ-YI, BENJAMIN <bruizyi@email.sc.edu>

Dear Benjamin Ruiz-Yi

In response for your request to republish data, figures, and information from my thesis titled:

Development of Novel High-Throughput Methodologies to Evaluate the Thermal Stability of High-Temperature Thin-Film Crystals for Energy Applications

I hereby grant you that permission and wish you luck on your thesis and defense.

Regards,
Jonathan Kenneth Bunn

Figure F.1: Copyright permission for J.K. Bunn, Development of Novel High-Throughput Methodologies to Evaluate the Thermal Stability of High-Temperature Thin-Film Crystals for Energy Applications. University of South Carolina, 2016

ACS Publications Most Trusted. Most Cited. Most Read.

Title: The Different Roles of Entropy and Solubility in High Entropy Alloy Stability

Author: Benjamin Ruiz-Yi, Jonathan Kenneth Bunn, Drew Stasak, et al

Publication: ACS Combinatorial Science

Publisher: American Chemical Society

Date: Sep 1, 2016

Copyright © 2016, American Chemical Society

LOGIN

If you're a copyright.com user, you can login to RightsLink using your copyright.com credentials. Already a RightsLink user or want to [learn more?](#)

Quick Price Estimate

Permission for this particular request is granted for print and electronic formats, and translations, at no charge. Figures and tables may be modified. Appropriate credit should be given. Please print this page for your records and provide a copy to your publisher. Requests for up to 4 figures require only this record. Five or more figures will generate a printout of additional terms and conditions. Appropriate credit should read: "Reprinted with permission from {COMPLETE REFERENCE CITATION}. Copyright {YEAR} American Chemical Society." Insert appropriate information in place of the capitalized words.

I would like to... reuse in a Thesis/Dissertation

Requestor Type Author (original work)

This service provides permission for reuse only. If you do not have a copy of the article you are using, you may copy and paste the content

Figure F.2: Copyright permission for B. Ruiz-Yi, J. K. Bunn, D. Stasak, A. Mehta, M. Besser, M. J. Kramer, I. Takeuchi, J. R. Hattrick-Simpers, (2016). The Different Roles of Entropy and Solubility in High Entropy Alloy Stability. ACS Combinatorial Science, 18(9), 596-603.

Reproduction of Materials from the NTSB Web Site and Publications

Text Content

Text appearing on NTSB Web pages, in reports, recommendation, and public dockets, unless otherwise noted, was prepared by employees of the United States Government as part of their official duties and, therefore, is not subject to copyright. By publishing its reports and recommendations and opening public dockets, the NTSB has placed the contents prepared by its staff in the public domain. This material may be freely copied and, at your discretion, credited to the NTSB with a "Courtesy: National Transportation Safety Board" notation. The Board requests that uses of its material be accurate and complete.

If copyrighted text is included on an NTSB Web page, in the docket, or in an NTSB publication, it should be specifically identified. Use by the NTSB of copyrighted material and publication on the NTSB Web site or in a printed report or other type of document does not constitute permission for the public to use the material without complying with copyright laws. It is the user's responsibility to contact copyright holders and obtain permission to use the material.

Graphics and Imagery

Permission to use and or reproduce the NTSB logo and the Seal of the NTSB is granted on a case by case basis. See 49 CFR 803. Granting permission to use or reproduce the NTSB logo and/or Seal of the NTSB does not explicitly or implicitly convey NTSB's endorsement of the site, publication or circumstance where it will be used by a requester. Once a requester receives confirmation from the NTSB that the Logo/NTSB shield may be used, the requester may, at his or her discretion, credit NTSB with a "Courtesy: National Transportation Safety Board" notation.

Alternatively, graphics which involve photographs, illustrations, and other pictorial materials and images found on the NTSB Web site, except where copyrighted, were prepared or created by the personnel of the NTSB and their publication indicates that the NTSB has placed them in the public domain.

In the case of copyrighted photographs, illustrations or other pictorial materials and images, although the NTSB may have placed the image in an NTSB public domain report, recommendation or other document, the NTSB's use does not constitute permission for the public, in turn, to use the material without complying with copyright laws. It is the user's responsibility to contact copyright holders and obtain permission to use the material. Therefore, with the exception of photographs, illustrations, and other pictorial materials and images created by the NTSB, copyrighted photographs, illustrations and other pictorial materials and images found on the NTSB web site should not be reused without permission.

Figure F.3: Copyright permission for National Transportation Safety Board. Aircraft accident report - In-flight breakup over the Atlantic Ocean Trans World Airlines Flight 800 Boeing 747-131, N93119, near East Moriches, New York, July 17, 1996. (Report No. PB2000-910403).

Order Completed

Thank you for your order.

This Agreement between University of South Carolina – Benjamin Ruiz-Yi ("You") and Elsevier ("Elsevier") consists of your license details and the terms and conditions provided by Elsevier and Copyright Clearance Center.

Your confirmation email will contain your order number for future reference.

License Number	4817831184796	Printable Details
License date	Apr 28, 2020	
Licensed Content		Order Details
Licensed Content Publisher	Elsevier	Type of Use
Licensed Content Publication	Acta Materialia	Portion
Licensed Content Title	Mechanical properties of high-temperature-degraded yttria-stabilized zirconia	Number of figures/tables/illustrations
Licensed Content Author	Xiaorui Ren,Wei Pan	Format
Licensed Content Date	May 1, 2014	Are you the author of this Elsevier article?
Licensed Content Volume	69	Will you be translating?
Licensed Content Issue	n/a	
Licensed Content Pages	10	
Journal Type	S&T	
About Your Work		Additional Data
Title	Solid Materials Discovery for Thin Films, Oxide Catalysts, and Polymer Sealants	Order reference number
Institution name	University of South Carolina	Portions
Expected presentation date	Aug 2020	
Requestor Location		Tax Details
Requestor Location	University of South Carolina 541 Main Street Horizon I Room 136 COLUMBIA, SC 29208 United States Attn: Benjamin Ruiz-Yi	Publisher Tax ID
Price		
Total	0.00 USD	

Total: 0.00 USD

Figure F.4: Copyright permission for X. Ren, W. Pan (2014). Mechanical properties of high-temperature-degraded yttria-stabilized zirconia. Acta Materialia, 69, 397-406.

Order Completed

Thank you for your order.

This Agreement between University of South Carolina -- Benjamin Ruiz-Yi ("You") and Elsevier ("Elsevier") consists of your license details and the terms and conditions provided by Elsevier and Copyright Clearance Center.

Your confirmation email will contain your order number for future reference.

License Number 4817840080603

[Printable Details](#)

License date Apr 28, 2020

Licensed Content

Licensed Content Publisher Elsevier
 Licensed Content Publication Solid State Ionics
 Licensed Content Title Metastable-stable phase diagrams in the zirconia-containing systems utilized in solid-oxide fuel cell application
 Licensed Content Author Masatomo Yashima, Masato Kakihana, Masahiro Yoshimura
 Licensed Content Date Jul 1, 1996
 Licensed Content Volume 86
 Licensed Content Issue n/a
 Licensed Content Pages 19
 Journal Type S&T

Order Details

Type of Use reuse in a thesis/dissertation
 Portion figures/tables/illustrations
 Number of figures/tables/illustrations 1
 Format both print and electronic
 Are you the author of this Elsevier article? No
 Will you be translating? No

About Your Work

Title Solid Materials Discovery for Thin Films, Oxide Catalysts, and Polymer Sealants
 Institution name University of South Carolina
 Expected presentation date Aug 2020

Additional Data

Order reference number Figure_YSZ_Phase
 Portions Figure 9

Requestor Location

Requestor Location University of South Carolina
 541 Main Street
 Horizon I
 Room 136
 COLUMBIA, SC 29208
 United States
 Attn: Benjamin Ruiz-Yi

Tax Details


Publisher Tax ID 98-0397604

\$ Price

Total 0.00 USD

Total: 0.00 USD

Figure F.5: Copyright permission for M. Yashima, M. Kakihana, M. Yoshimura, (1996). Metastable-stable phase diagrams in the zirconia-containing systems utilized in solid-oxide fuel cell application. Solid State Ionics, 86-88, 1131-1149.

 **In-Situ Oxygen Isotopic Exchange Vibrational Spectroscopy of Rhenium Oxide Surface Structures on Cerium Oxide**
Author: Blake MacQueen, Benjamin Ruiz-Yi, Michael Royko, et al
Publication: The Journal of Physical Chemistry C
Publisher: American Chemical Society
Date: Apr 1, 2020
Copyright © 2020, American Chemical Society

PERMISSION/LICENSE IS GRANTED FOR YOUR ORDER AT NO CHARGE

This type of permission/license, instead of the standard Terms & Conditions, is sent to you because no fee is being charged for your order. Please note the following:

- Permission is granted for your request in both print and electronic formats, and translations.
- If figures and/or tables were requested, they may be adapted or used in part.
- Please print this page for your records and send a copy of it to your publisher/graduate school.
- Appropriate credit for the requested material should be given as follows: "Reprinted (adapted) with permission from (COMPLETE REFERENCE CITATION). Copyright (YEAR) American Chemical Society." Insert appropriate information in place of the capitalized words.
- One-time permission is granted only for the use specified in your request. No additional uses are granted (such as derivative works or other editions). For any other uses, please submit a new request.

[BACK](#) [CLOSE WINDOW](#)

Figure F.6: Copyright permission for B. MacQueen, B. Ruiz-Yi, M. Royko, A. Heyden, Y.J. Pagan-Torres, C. Williams, J. Lauterbach, (2020). In-Situ Oxygen Isotopic Exchange Vibrational Spectroscopy of ReO_x Surface Structures on CeO_2 . The Journal of Physical Chemistry C, 124(13), 7174-7181.



Failure analysis of a first stage IN738 gas turbine blade tip cracking in a thermal power plant

Author: Sushila Rani, Atul K. Agrawal, Vikas Rastogi

Publication: Case Studies in Engineering Failure Analysis

Publisher: Elsevier

Date: April 2017

© 2016 The Author(s). Published by Elsevier Ltd.

Creative Commons Attribution-NonCommercial-No Derivatives License (CC BY NC ND)

This article is published under the terms of the [Creative Commons Attribution-NonCommercial-No Derivatives License \(CC BY NC ND\)](#).

For non-commercial purposes you may copy and distribute the article, use portions or extracts from the article in other works, and text or data mine the article, provided you do not alter or modify the article without permission from Elsevier. You may also create adaptations of the article for your own personal use only, but not distribute these to others. You must give appropriate credit to the original work, together with a link to the formal publication through the relevant DOI, and a link to the Creative Commons user license above. If changes are permitted, you must indicate if any changes are made but not in any way that suggests the licensor endorses you or your use of the work.

Permission is not required for this non-commercial use. For commercial use please continue to request permission via Rightslink.

BACK

CLOSE WINDOW

Figure F.7: Copyright permission for S. Rani, A.K. Agrawal, V. Rastogi, (2017). Failure analysis of a first stage IN738 gas turbine blade tip cracking in a thermal power plant. Case Studies in Engineering Failure Analysis, 8, 1-10.